Nonlinear Electromechanical Deformation of Isotropic and Anisotropic Electro-Elastic Materials

Seyul Son

Dissertation submitted to the faculty of the Virginia Polytechnic Institute and State University in partial fulfillment of the requirements for the degree of

Doctor of Philosophy
In
Mechanical Engineering

Nakhiah C. Goulbourne, Committee Chair

Daniel J. Inman
Donald J. Leo
Dennis Hong
Michael Philen

July 25th 2011
Blacksburg Virginia

Keywords: Electro-elastic material, Dielectric elastomer, polyconvexity, Finite element model and transducers

Nonlinear Electromechanical Deformation of Isotropic and Anisotropic Electro-Elastic Materials

Seyul Son

ABSTRACT

Electro-active polymers (EAPs) have emerged as a new class of active materials, which produce large deformations in response to an electric stimulus. EAPs have attractive characteristics of being lightweight, inexpensive, stretchable, and flexible. Additionally, EAPs are conformable, and their properties can be tailored to satisfy a broad range of requirements. These advantages have enabled many target applications in actuation and sensing. A general constitutive formulation for isotropic and anisotropic electro-active materials is developed using continuum mechanics framework and invariant theory. Based on the constitutive law, electromechanical stability of the electro-elastic materials is investigated using convexity and polyconvexity conditions. Implementation of the electro-active material model into a commercial finite element software (ABAQUS 6.9.1, PAWTUCKET, RI, USA) is presented. Several boundary and initial value problems are solved to investigate the actuation and sensing response of isotropic and anisotropic dielectric elastomers (DEs) subject to combined mechanical and electrical loads. The numerical response is compared with experimental results to validate the theoretical model.

For the constitutive formulation of the electro-elastic materials, invariants for the coupling between two families of electro-active fibers (or particles) and the applied electric field are introduced. The effect of the orientation of the electro-active fibers and the electric field on the

electromechanical coupling is investigated under equibiaxial extension. Advantage of the constitutive formulation derived in this research is that the electromechanical coupling can be illustrated easily by choosing invariants for the deformation gradient tensor, the electro-active fibers, and the electric field. For the electromechanical stability, it is shown that the stability can be controlled by tuning the material properties and the orientation of the electro-active fibers. The electromechanical stability condition is useful to build a stable free energy function and prevent the instabilities (wrinkling and electric breakdown) for the electro-elastic materials. The invariant-based constitutive formulation for the electro-elastic materials including the isotropic and anisotropic DEs is implemented into a user subroutine (UMAT in ABAQUS: user defined material) by using multiplicative decomposition of the deformation gradient and the applicability of the UMAT is shown by simulating a complicated electromechanical coupling problem in ABAQUS/CAE. Additionally, the static and dynamic sensing and actuation response of tubular DE transducers (silicone and polyacrylate materials) with respect to combined electrical and mechanical stimuli is obtained experimentally. It is shown that the silicone samples have better dynamic and static sensing characteristics than the polyacrylate. The theoretical modeling accords well with the experimental results.

ACKNOWLEDGEMENTS

A great number of people have lent their support to me throughout this endeavor. I owe my gratitude to all those who have made this dissertation possible as they have been with me throughout the entire journey to becoming a better engineer.

First of all, I would like to thank my advisor, Dr. Goulbourne, for her support and guidance on this research. Her invaluable encouragement and sometimes pushing me hard for publications have been vital in the completion of my Ph.D. degree. Specifically, I would like to thank for her numerous hours of editing papers with me. Again, thank you for challenging me and having confidence in me as well as being an excellent advisor. Special thanks are extended to the committee members, Dr. Inman, Leo, Hong, and Philen. For all your support and guidance, I will be eternally grateful.

I would like to express my gratitude to all members of the Smart Material Research Lab in University of Michigan and the Center for Intelligent material Systems and Structures in Virginia Tech. Several of my fellow SMRL and CIMSS colleagues have been instrumental in my success during graduate school.

Lastly, I would like to thank family members who have been encouraging and supportive of my efforts throughout this entire process. I owe much gratitude and appreciation to my mother and brother for their confidence and words of encouragement which were cherished. Specially, I would like to thank my fiancée Ju ng-hyun Huh for your support for five years. Your presence always inspires me with great confidence.

TABLE OF CONTENTS

LIST OF FIGURES

LIST OF TABLES

Chapter 1. Introduction

Electro-elastic materials are materials that can change their mechanical behavior in response to the applied electric field. Since their attractive characteristics are lightweight, stretchable, flexible, forming into any desired shape and controllable properties to satisfy a broad range of requirements, they have been subject of growing interest for their potential use in actuators for artificial muscles in robotics and for biomedical applications. This chapter presents basic introduction to electro-active materials along with the theoretical background required to model DE transducers. This dissertation consists of 4 main contributions: (1) Derivation of the generalized constitutive laws for electro-elastic materials (Chapter 2), (2) Examination of the polyconvexity conditions for the invariant-based electro-elastic free energy function for electro-elastic materials (Chapter 3), (3) Mathematical modeling of fiber containing dielectric elastomer (DE) systems (Chapters 4, 5 and 6), and (4) Implementation of the constitutive relationships for isotropic and anisotropic DE materials into the user subroutine (UMAT: User defined material) of a finite element modeling tool (ABAQUS 6.9.1, PAWTUCKET, R.I, USA) (Chapter 7).

A generalized constitutive formulation for electro-elastic materials undergoing large deformations, is derived using the continuum mechanics framework of Adkins and Rivlin [1, 2], Kydoniefs [3-5], Rajagopal and Wineman [6], Dorfmann and Ogden [7, 8] and Bustamante [9]. Using an invariant based formulation, the irreducible integrity bases for anisotropic electro-elastic materials are derived in general form for the first time based on the works of Spencer and Rivlin [10-12] and Pipkin and Rivlin [13]. Rajagopal and Wineman [6] and Dorfmann and Ogden [7, 8] derived a formulation for nonlinear and isotropic electro-elastic materials. Their formulation contains of an invariant-based free energy function, and the invariants for the isotropic electro-elastic material (essentially developed by Spencer, Pipkin and Rivlin [10-15])

are introduced in their work [6-8]. Bustamante [9] developed a theoretical constitutive law for transversely isotropic electro-elastic materials, consisting of the isotropic matrix and one family of the electro-active particles and the coupling between an electro-active directional vector (one family of the electro-active particles in his paper) and an applied electric field was described using Spencer's invariant theory [10]. The electromechanical stability of the electro-elastic materials is explored using polyconvexity conditions introduced by Ball [17], Schrőder [18, 19] and Rogers [20]. A method for the electro-elastic constitutive laws into a UMAT in ABAQUS is developed using the approaches of Weiss [21], Simo and Taylor [22-24], and Zhao and Suo [25-28]. Several boundary value problems are solved to investigate the actuation and sensing response of isotropic and anisotropic dielectric elastomers subject to combined mechanical and electrical loads. The numerical response is compared with experimental results to validate the theoretical model.

1.1. Electro-Active Polymers

Generally, electro-active polymers (EAPs) are defined as polymers that exhibit electromechanical coupling. Historically, the first EAP was likely first introduced by Roentgen's 1880 experiment where a rubber band with one fixed end and a mass attached at the other end was charged and discharged [29]. in the field of EAP materials has occurred in the last fifteen years, where materials that can produce over 300% electromechanical strains have emerged [30]. EAPs can be divided into two major classes: ionic and electronic. An electric field or Columbic forces drive electronic EAPs; these include electrostrictive, electrostatic, piezoelectric and ferroelectric materials which require high electric fields (> 100 $V/\mu m$) [31]. Ionic EAPs are materials whereby electromechanical coupling occurs due to ion movement within the polymer; these devices require 1–8 V for actuation.

1.1.1. Electronic EAP

A. Dielectric Elastomers

DEs offer various advantages in addition to large strains up to 300%, including simple fabrication techniques, low cost, repeatability, scalability, and shape conformability [30, 32, 33]. In principle, a DE is a three-component system consisting of a compliant elastomeric insulator sandwiched by two compliant electrodes. For DE actuators, an electric field applied on the electroded surfaces generates an electrostatic stress which creates in-plane and out-of-plane strain as shown in Figure 1.1. DE sensors are essentially compliant capacitors which have a capacitance that varies with mechanical strain as shown in Figure 1.1. Alternatively, the resistance can be monitored. More details about DEs will be provided in Section 1.2.

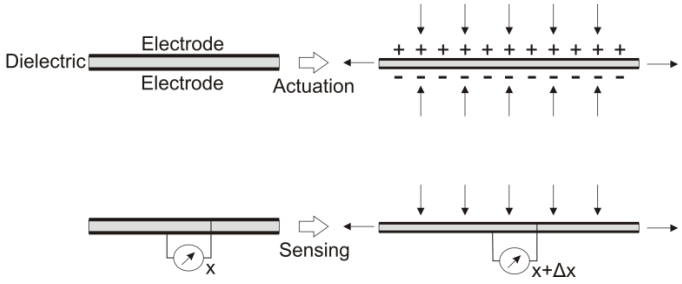

Figure 1.1. Principle of dielectric elastomer actuation and sensing.

B. Electrostrictive Graft Elastomers

Electrostrictive graft elastomers were introduced by NASA in 1998 [34]. These consist of two components: flexible macromolecule backbone chains and a grafted polymer crystal unit, which is described in Figure 1.2 [35]. The backbone and side chain crystal units can then form polarized monomers, which contain atoms with partial charges and generate dipole moments. When an electric field is applied to the elastomer, a force is applied to each partial charge and

causes rotation of the whole polymer unit. This rotation causes electrostrictive strain and deformation of the elastomer. Electrostrictive graft elastomers have obtained strain levels of up to 4% with a relatively higher mechanical modulus than electrostrictive polyurethane.

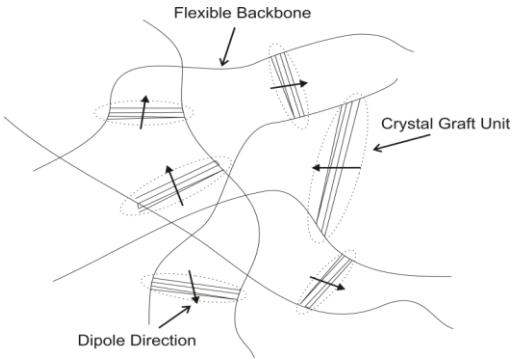

Figure 1.2. The structure of electrostrictive graft elastomers.

C. Ferroelectric Polymers

Piezoelectricity was discovered in 1880 by Pierre and Paul-Jacques Curie. They found that certain types of crystals compressed along certain axes produced a voltage on the surface of the crystal. Conversely, an application of a voltage leads to elongation of the crystal. When a non-conducting crystal or dielectric material exhibits spontaneous electric polarization, the phenomenon is called ferroelectricity [36]. In principle, ferroelectric polymers have a permanent electrical polarization that can be rotated repeatedly with respect to the orientation of applied electric field. The dipoles randomly oriented at the beginning can be aligned by applying an electric field. Ferroelectric polymers can be operated in air, and the most common is the poly(vinylidene fluoride), which is also known as PVDF or PVF2, and its copolymers.

1.1.2. Ionic EAPs

A. Ionic Gels

When a voltage is applied to ionic gels such as poly-acrylic acid, hydrogen ions move in and out of the gel, which becomes dense or swollen accordingly. In principle, under an applied voltage, the positively charged surfactant molecules move towards the cathode and form a complex with the negatively charged gel as shown in Figure 1.3 [37]. This causes contraction, bending the gel towards the anode. Since reversing the polarity of the electric field releases the surfactant molecules from the surface of the gel, the polymer gel flattens.

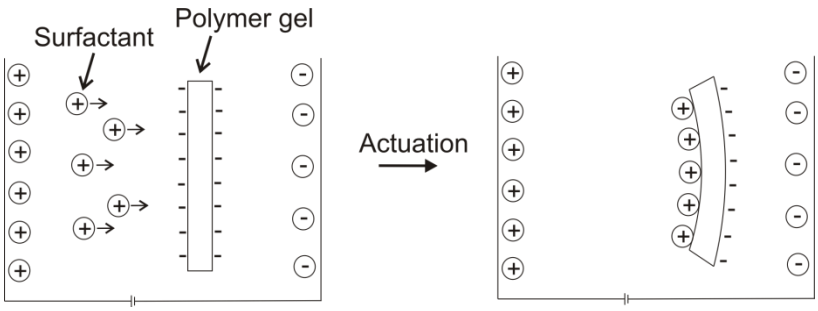

Figure 1.3. Principle of ionic polymer gels.

B. Ionic Polymer Metal Composites

An ionomeric polymer sandwiched by an interpenetrating conductive medium is called an ionic polymer-metal composite (IPMC). This material can exhibit large deformations (< 8.0%) if suitable electrodes are used and an electric field is applied [38]. In detail, an IPMC is a charged polymer-metal composite that is infused with a fluid and neutralized by mobile counterions. An applied electric field is responsible for the counterion redistribution shown in Figure 1.4. This redistribution of mobile counterions gives rise to a number of concurrent microscopic actuation mechanisms that lead to the macroscopic IPMC deformation. Conversely, an imposed mechanical deformation induces a redistribution of mobile counterions that leads to a charge stored at the IPMC electrodes.

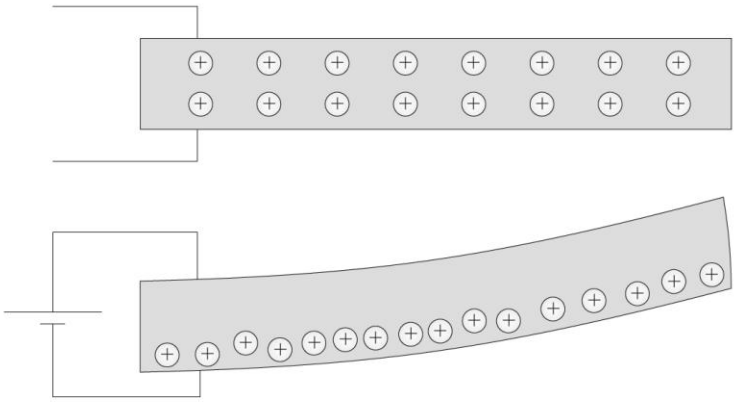

Figure 1.4. Principle of ionic polymer metal composites actuation.

C. Conductive Polymers

Conductive polymers (CPs) such as polypyrrole and polyaniline are materials that swell in response to an applied voltage as a result of oxidation or reduction, depending on the polarity, causing inclusion or exclusion of ions. The oxidation-reduction reaction induces a considerable volume change due to the exchange of ions with an electrolyte. Dimensional changes occur primarily due to ion insertion. Very high currents are required in order to operate at high power due to the low electromechanical coupling and low activation voltages [39].

1.2. Dielectric Elastomers

DE membranes are one of the most promising transducers for developing soft large strain sensors and actuators. Dielectric elastomers have been investigated theoretically and experimentally for over 20 years. Theoretically, Toupin presented the basic formulation of the electrically induced stress of a deformable elastic dielectric [40]. His formulation for the elastic dielectric was based on Green and Cauchy methods. Zhenyi *et al.* performed experiments on the electromechanical response of a soft polymer in 1994 [41]. They examined the thickness response of a polyurethane film (~25 μm) with respect to a high DC bias field and discovered that high static

strain could be produced by applying voltage. Additionally, they suggested that the electromechanical response measured was strongly reduced by the surface constraints imposed by the electrodes, because Tin Foil was used. In the late 1990's, the pioneering experimental investigation for DEs was carried out by a research group at SRI international. They coined the term dielectric elastomer and incorrectly proposed electrostriction as the coupling mechanism, it is now widely accepted that the mechanism is electrostatic. They fabricated thin uniform dielectric films by techniques such as spin coating, casting, dipping, and using off-the-shelf materials [33]. The dielectric materials they employed for the DEs include polyacrylate, polyurethane, silicone, fluorosilicone, ethylene propylene and isoprene. Among them, silicone polymers produced the highest in-plane strain (32%) at that time. At the same time, they developed various prototypes of the DE actuators to demonstrate the flexibility of the technology such as stretched film actuators, rolled actuators, tube actuators, and unimorph and bimorph actuators. In 2000, they showed that prestraining dielectric films further improves the electromechanical actuation performance [30]. Actuation strain up to 117% of linear strain was achieved with silicone (Dow Corning HS3 silicone) by prestraining 280% uniaxially and 158% of circular strain with acrylic elastomers (3M VHB 4910) by biaxial prestraining 300%.

DE research can be divided into two categories: (i) theoretical study and (ii) DE transducer development and applications. Most of the DE configurations are potential candidates for artificial muscle due to high energy densities, large strains, light weight, silent operation and the capability to operate as sensors and actuators. The drawbacks of these transducers include required high voltage causing the electrical breakdown and prestrain-supporting structure leading to unbalanced actuation and stress concentration. Several configurations of DEs have been employed by Son and Goulbourne [42, 43], Pelrine *et al.*[32, 44], Kornbluh *et al.* [45], Pei *et al.*

[46], Kofod *et al.* [47] and Carpi *et al.* [48, 49]. Goulbourne *et al.* developed a nonlinear static and dynamic model and performed experiments with a DE diaphragm with the view of potential application to a pump mechanism [50-52]. Son and Goulbourne investigated the electromechanical response of tubular DE transducers experimentally and numerically [42, 43]. The static and dynamic sensing and actuation performance of the tubular DE transducers were obtained and the DE transducers were employed to fabricate a fiber-reinforced electro-pneumatic transducer. Detail of this work is presented in Chapters 4, 5 and 6. Pelrine *et al.*[32, 44] and Kornbluh *et al.* [45] presented a bowtie, extender and rolled DE actuators being considered for artificial muscles. These actuators can be stacked in parallel to increase the force output, or chained in series to increase the stroke. They applied these actuators into several types of biomimetic robots [32, 44, 45]. Pei *et al.* introduced the multifunctional elastomer roll (MER) which is fabricated by rolling a prestrained elastomer film with patterned electrodes around a central compression spring [46]. The 2-DOF (degree of freedom) and 3-DOF spring rolls produced by patterning the electrodes exhibit both linear and bending actuation. In order to describe an application of the roll DE actuator, they fabricated a six legged robot [46]. Kofod *et al.* developed a stiff framed DE structure, consisting of a prestrained DE attached to a thin and flexible PET film [47]. Initially, the tension in the prestrained membrane causes the frame to curl up, and when a voltage is applied, the frame returns to its uncurled state, forming a useful bending actuator. The stiff framed DE can be applied to systems for manipulation, pumping and locomotion. Carpi *et al.* designed helical and contractile folded DE actuators which are very similar to stack-like configurations consisting of several layers of DEs [48, 49]. The helical and contractile folded DE actuators produce contractile actuation and overcame the fabrication technique difficulty of the stack-like configuration. The potential application of the helical and

contractile DE actuators includes hand splints for rehabilitation and lightweight flexible space structures.

Previously it has been reported that prestrain can improve the electromechanical behavior of DEs such as breakdown strength, actuation strain and efficiency [30, 53]. However, often the prestrain-supporting structure causes more weight and space than the polymers themselves, unbalanced actuation performance, and a short lifetime from the stress concentration at the interface between the soft polymer and the rigid structure. For setting the DEs free from the prestrain-supporting structure, additives have been introduced which enhance electromechanical actuation [54-58]. Ha *et al.* introduced diacrylate and trimethacrylate monomers into the prestrained VHB 4910, which act to preserve the prestrain [54]. Physically, VHB films are very soft (Young's modulus: ~500 *kPa*), consisting of the long chain and branched alkyl groups attached to the acrylate polymer chains. The flexible hexylene between the two acrylate end groups allows the polymer to stretch. When the polymer is stretched, adding either of the highly crosslinked polymers of HDDA (1,6 Hexanediol Diacrylate) or TMPTMA (Trifunctional trimethylolpropane trimethacrylate) results in a higher overall crosslink density and it was found that the prestrain of the polymer is preserved. They reported that VHB with poly(HDDA:18.3 wt %) preserves 275% prestrain and produces electromechanical actuation up to 233% in areal strain, and VHB with poly (TMPTMA:9.7 wt %) retains 244% prestrain and shows 300% of electromechanical areal strain.

Zhang *et al.* reported that EAP composites including an organic filler material (Metallophthalocyanine (MtPc) oligomer and copper-phthalocyanine (CuPc), dielectric constant: > 10,000) can possess a very high dielectric constant [55]. They fabricated an organic filler dispersed electrostrictive polymer matrix for enhancing dielectric constants while retaining the

flexibility of the matrix. Nguyen *et al.* [56] Gallon *et al.* [57] and Carpi *et al.* [58] reported that the dispersion of titanium dioxide powder in a silicone dielectric elastomer leads to a lower elastic modulus and higher dielectric permittivity and can produce a larger actuation.

Toupin [40] and Eringen [59] formulated a generalized theory for deformable elastic dielectrics by using Green and Cauchy's methods, respectively. Their formulations were theoretical frame works not limited to a specific electromechanical coupling, initial and boundary condition, material or application. Cauchy's method is to assume that the stress tensor is function of certain parameters and Green's method assumes the existence of a stored energy function. Toupin [40] and Eringen [59] assumed that the stress was a function of the displacement gradient, and polarization (or electric field or electric displacement). They presented the constitutive relationships for stress and the effective local field. In detail, Toupin and Eringen employed the principle of virtual work to yield field equations and boundary conditions along with equilibrium equations for the elastic dielectrics. Using the variational principle, a single scalar function of the variables of state is derived to characterize the mechanical and electrostatic properties of an electric dielectric. Without the energy principle, the same formal set of equations and boundary conditions can be derived but the constitutive equations for the stress and strain must be given separately in order to characterize the properties of the material. Differently from Toupin [40], Eringen applied his formulation to specific examples [59]. He presented the electro-elastic constitutive formulation for simple shear of an infinite homogeneous isotropic slab and uniform extension of a hollow cylindrical dielectric.

Theoretically, Pelrine *et al.* [33] modeled the electrostatic coupling between the applied electric field and the elastic dielectric as an effective pressure, which describes the electrostatic energy change per unit area and unit displacement in the thickness direction. The effective pressure is

exactly twice the pressure in a parallel-plate capacitor implying that the effective pressure is strongly dependent on the relative permittivity [33]. The actuation performance of the dielectric elastomer for the unloaded and unconstrained case is modeled analytically using a linear Hookean constitutive relation [33]. Though largely used due to its simplicity, it is not correct to represent the electrostatic stress as a pressure. Goulbourne *et al.* [52] derived the correct expression for the electrostatic stress tensor, which has been separately derived later by Suo *et al.* [27] and McMeeking [60].

Based on the approach in Pelrine *et al.* [33], Carpi and Rossi [61] and Wissler and Mazza [62-64] modeled the prestrained cylindrical and circular DE actuators using linear elasticity and hyperelasticity, respectively. Carpi and Rossi developed an analytical model for the cylindrical DE actuator assuming a linear elastic constitutive relationship and validated the modeling with the experimental results of the silicone samples (strain: < 5%) [61]. Wissler and Mazza [62-64] predicted the performance of a circular DE actuator by adopting a hyperelastic constitutive relation. The constitutive relationship was described by employing the hyperelastic strain energy potentials of Yeoh [65], Ogden [66] and Arruda-Boyce [67]. In [62], an analytical model was presented for analyzing a circular actuator in the case of dielectric elastomer. In [63, 64], finite element modeling for a circular DE actuator describing the time dependent response was developed employing a commercial software (ABAQUS 6.9.1). In ABAQUS, the effective pressure p is applied as a surface pressure and defined in a user's subroutine (UMAT: User defined material).

Goulbourne *et al.* [52, 68] derived a nonlinear large deformation model for DEs assuming that the stress as a point in the deformed medium is determined by the local elastic and electric fields, where the electrical effects of the system are described using Maxwell-Faraday electrostatics

[69]. They presented the electrical constitutive relationship for a homogenous and isotropic dielectric:

$$\begin{aligned} \boldsymbol{D} &= \varepsilon_0 \boldsymbol{e} + \boldsymbol{P} = \varepsilon_0 \varepsilon_r \boldsymbol{e}, \\ \boldsymbol{\sigma}_M &= \varepsilon_0 \varepsilon_r \boldsymbol{e} \otimes \boldsymbol{e} - \frac{\varepsilon_0 \varepsilon_r (\boldsymbol{e} \cdot \boldsymbol{e}) \boldsymbol{I}}{2} \end{aligned} \tag{1.1}$$

where $\boldsymbol{D}$ is the electric displacement, $\boldsymbol{P}$ is the polarization vector, $\boldsymbol{\sigma}_M$ is the Maxwell stress tensor, $\boldsymbol{I}$ is the identity tensor and $\otimes$ is the tensor product. They postulated that the Cauchy stress $\boldsymbol{\sigma}$ in the dielectric is the sum of the local elastic stress tensor and the Maxwell stress tensor giving

$$\boldsymbol{\sigma} = \boldsymbol{\sigma}_E + \boldsymbol{\sigma}_M, \tag{1.2}$$

where $\boldsymbol{\sigma}_E$ is the local elastic stress tensor which is obtained from a constitutive relationship using the Ogden [66] or Mooney-Rivlin [70] hyperelastic strain energy function. In order to validate the nonlinear mathematical formulation for the DEs, a boundary value problem (an inflatable DE membrane subject to prestrain, external pressure and applied electric field (potential cardiac pump application)) was presented and the numerical results compared well with the experimental results of the fluid pump in Tews *et al.* [71].

Suo *et al.* [27] derived a constitutive relation for an ideal dielectric elastomer using a variational approach which is identical to that proposed by Goulbourne *et al.* [52] previously in 2005. They assumed that the dielectric elastomer is attached with a weight and a battery, and then prescribed fields of virtual displacement and voltage [27]. Based on the approach of the virtual work for the weight, the inertia and the batteries, they defined the elastic stress and the electric displacement with respect to the deformation gradients and the gradient of electric potential, respectively. Based on the approach in Suo *et al.* [27], the electromechanical stability of the dielectric elastomer was investigated by Zhao [25, 26, 28]. This was done by using a general convexity condition, from which the Hessian matrix must be positive definite at the equilibrium state. A

literature review regarding electromechanical stability of dielectric elastomers will be presented in Chapter 3.

1.3. Large Electro-Elastic Deformations of Fiber-reinforced Elastomer Composites

In this research, the response of a DE transducer placed in contact with an axisymmetric tubular host system is investigated. Two such host systems are considered: a fiber-reinforced pneumatic actuator (in Chapters 4 and 5) and an arterial wall (in Chapter 6). The fiber reinforced tubular membrane is modeled as a thin cylindrical membrane with two families of fibers. Theoretical modeling of fiber-reinforced thin elastic membranes is based on the works of Adkins, Rivlin, and Green [1, 2, 72], Kydoniefs and Spencer [3-5] and Matsikoudi-Iliopoulou [73]. Fundamentally, Adkins, Rivlin, and Green developed a large deformation theory for pure thin membranes and fiber-reinforced elastic body and solved a series of axially symmetric problems [1, 2, 72]. They applied the theory of large elastic deformations of incompressible isotropic materials to the inflation of a circular diaphragm with a highly elastic material. In order to determine the deformation of axially symmetric problems (a circular diaphragm, a tube and a spherical shell), a numerical integration method using a truncated Taylor series expansion was employed [1, 72]. They indicated that if the deformation state at a point of the diaphragm is known, then the deformation state at all points of the inflated diaphragm could be calculated for any form of the strain energy function. In this research (Chapters 4, 5 and 6), the numerical integration scheme similar to Adkins, Rivlin, and Green [1, 72] are employed to solve the finite electro-elastic deformation of axisymmetric membrane under mechanical and electrical stimulus. In [2, 72], Adkins, Rivlin and Green employed the theory of large elastic deformation to the deformations

of elastic bodies reinforced with fibers. The fibers are assumed to be thin, flexible, and inextensible, and lie parallel and close together in smooth surfaces in the undeformed body. The elastic body is described using a hyperelastic strain energy function and the fibers are considered as structural components. The Cauchy stress is the sum of the elastic stress and stress from the fiber tension. The stress from the fiber tension was obtained by considering the geometry of the fibers on the elastic body. Based on the approach of Adkins, Rivlin, and Green [1, 2, 72], Kydoniefs and Spencer [3-5], and Matsikoudi-Iliopoulou [73] formulated a theory for the axisymmetric deformations of a cylindrical membrane and of a fiber-reinforced cylindrical membrane. Kydoniefs and Spencer considered an initially cylindrical membrane composed of an incompressible, homogenous, isotropic elastic material possessing a strain energy function [3, 5]. They obtained the exact solution of the deformation of a cylindrical membrane. The solution was obtained by solving the first order ordinary nonlinear differential equations formed by inserting the Cauchy stress into the equilibrium equations in the direction of the meridional and latitudinal directions of the cylindrical membrane. They illustrated their approach considering the inflation of a cylindrical membrane sealed at each end by rigid plugs. By using a numerical iterative process (which will be presented specifically in Chapter 4), the deformed profile of the cylindrical membrane was calculated numerically. Kydoniefs [4] and Matsikoudi-Iliopoulou [73] formulated the axisymmetric deformation of a fiber-reinforced cylindrical membrane with two families of inextensible fibers. Kydoniefs adopted his previous works [3, 5] on finite deformations of a cylindrical membrane to solve for the deformation profile of a fiber-reinforced cylindrical membrane and employed Adkins, Rivlin, and Green' work [1, 72] for formulating the fiber stress with fiber geometry [4]. The geometric consideration of two families of fibers on the elastic membrane in Kydoniefs' work [4] is employed in Chapters 4, 5 and 6 to obtain the

constitutive formulation of the fiber-reinforced axisymmetric membrane. However in Chapters 2 and 3, differently from the structural approach for the fibers, the continuum approach is employed to describe the constitutive formulation of the anisotropic continuum, which is described by using an invariant-based free energy function. The detail of the continuum approach will be given in Chapter 2. In comparison with Kydoniefs' work, Matsikoudi-Iliopoulou [73] considered finite deformations of a cylindrical membrane with one family of fibers by the application of a constant inner pressure and an external torque at the end of the membrane. Matsikoudi-Iliopoulou employed a Mooney-Rivlin strain energy function in the numerical examples. Matsikoudi-Iliopoulou's results indicated that the ratio between the initial length and radius of the cylindrical membrane is an important parameter for the deformation and the external torque on the ends of the membrane does not affect the deformation after the pressure reaches a certain value. Later, Shan *et al*. [74], Goulbourne [75] and Liu [76] adopted the approaches in Adkins, Rivlin and Green [1, 2, 72], Kydoniefs and Spencer [3-5] for solving problems considering an axisymmetric fiber-reinforced cylindrical membrane. In this research (Chapter 4, 5 and 6), a mathematical model for finite deformations of an axisymmetric fiber-reinforced cylindrical membrane with two families of fibers under internal pressure, axial loading and external electric field is derived. Details of the formulation are presented in Chapters 4, 5 and 6.

1.4. Scope of the Dissertation

The content of this dissertation can be subdivided as follows: (1) Formulation of a general constitutive relationship for electro-elastic materials using an invariant-based formulation (Chapter 2), (2) Examination of the polyconvexity conditions for the invariant-based electro-

elastic free energy function (Chapter 3), (3) Investigation of the sensing and actuation response of tubular DE transducers and application of the DE sensors to specific host systems (Chapters 4, 5 and 6), and (4) Implementation of an electro-elastic material into user subroutine (UMAT) in ABAQUS (Chapter 7). Both isotropic and anisotropic formulations are presented along. Finite electro-elastic deformation of axisymmetric DE transducers is fundamentally based on combining large deformation membrane theory and electrostatics.

1.5. References

1. Adkins, J.E. and R.S. Rivlin, *Large elastic deformations of isotropic materials -- IX. Deformation of thin shells.* Philosophical Transactions, 1952.
2. Adkins, J.E. and R.S. Rivlin, *Elastic Deformations of Isotropic Materials X. Reinforced by Inextensible Cords.* Philosophical Transactions of the Royal Society of London. Series A, 1955: p. 201-223.
3. Kydoniefs, A.D., *Finite Axisymmetric Deformations of an Initially Cylindrical Elastic Membrane Enclosing a Rigid Body,.* Quarterly Journal of Mechanics and Applied Mathematics, 1968: p. 319-331.
4. Kydoniefs, A.D., *FINITE AXISYMMETRIC DEFORMATIONS OF INITIALLY CYLINDRICAL REINFORCED MEMBRANES.* Rubber Chemistry and Technology, 1972: p. 1677-1683.
5. Kydoniefs, A.D. and A.J.M. Spencer, *Finite Axisymmetric Deformations of An Initially Cylindrical Elastic Membrane.* Quarterly Journal of Mechanics and Applied Mathematics, 1968: p. 87-95.
6. Rajagopal, K.R. and A. Wineman, *A constitutive equation for non-linear electro-active solids.* Acta Mechanica, 1999: p. 219-28.
7. Dorfmann, A. and R.W. Ogden, *Nonlinear electroelasticity.* Acta Mechanica, 2005: p. 167-83.
8. Dorfmann, A. and R.W. Ogden, *Nonlinear electroelastic deformations.* Journal of Elasticity, 2006: p. 99-127.
9. Bustamante, R., *Transversely isotropic non-linear electro-active elastomers.* Acta Mechanica, 2009: p. 237-259.
10. Spencer, A.J.M., *Theory of invariants*, in *Continuum Physics volume 1: Mathematics*. 1971, Academic: London, UK. p. 239-55.
11. Spencer, A.J.M. and R.S. Rivlin, *Isotropic integrity bases for vectors and second-order tensors.* Archive for Rational Mechanics and Analysis, 1962: p. 45-63.
12. Spencer, A.J.M., *Isotropic integrity bases for vectors and second-order tensors.* Archive for Rational Mechanics and Analysis, 1965: p. 51-82.

13. Pipkin, A.C. and R.S. Rivlin, *Electrical, thermal and magnetic constitutive equations for deformed isotropic materials.* Atti della Accademia Nazionale dei Lincei. Rendiconti, Classe di Scienze Fisiche, Matematiche e Naturali, 1966: p. 3-29.
14. Pipkin, A. and R. Rivlin, *The formulation of constitutive equations in continuum physics. I.* Archive for Rational Mechanics and Analysis, 1959: p. 129-144.
15. Spencer, A.J.M., *Continuum Theory of the Mechanics of Fibre-Reinforced Composites*. 1984, New York: Springer-Verlag.
16. Bustamante, R., A. Dorfmann, and R.W. Ogden, *Nonlinear electroelastostatics: A variational framework.* Zeitschrift fur Angewandte Mathematik und Physik, 2009: p. 154-177.
17. Ball, J.M., *Convexity conditions and existence theorems in nonlinear elasticity.* Archive for Rational Mechanics and Analysis, 1977: p. 337-403.
18. Schröder, J., *Anisotropie polyconvex energies*, in *Poly-, Quasi- and Rank-One Convexity in Applied Mechanics*, J. Schröder and P. Neff, Editors. 2010, Springer Vienna. p. 53-105.
19. Schroder, J. and P. Neff, *Invariant formulation of hyperelastic transverse isotropy based on polyconvex free energy functions.* International Journal of Solids and Structures, 2003: p. 401-45.
20. Rogers, R.C. and S.S. Antman, *Steady-state problems of nonlinear electro-magneto-thermo-elasticity.* Archive for Rational Mechanics and Analysis, 1986: p. 279-323.
21. Weiss, J.A., B.N. Maker, and S. Govindjee, *Finite element implementation of incompressible, transversely isotropic hyperelasticity.* Computer Methods in Applied Mechanics and Engineering, 1996: p. 107-28.
22. Simo, J.C., *A framework for finite strain elastoplasticity based on maximum plastic dissipation and the multiplicative decomposition. I. Continuum formulation.* Computer Methods in Applied Mechanics and Engineering, 1988: p. 199-219.
23. Simo, J.C. and R.L. Taylor, *PENALTY FUNCTION FORMULATIONS FOR INCOMPRESSIBLE NONLINEAR ELASTOSTATICS.* Computer Methods in Applied Mechanics and Engineering, 1982: p. 107-118.
24. Simo, J.C. and R.L. Taylor, *Quasi-incompressible finite elasticity in principal stretches. Continuum basis and numerical algorithms.* Computer Methods in Applied Mechanics and Engineering, 1991: p. 273-310.
25. Xuanhe, Z., H. Wei, and S. Zhigang, *Electromechanical hysteresis and coexistent states in dielectric elastomers.* Physical Review B (Condensed Matter and Materials Physics), 2007: p. 134113-1.
26. Xuanhe, Z. and S. Zhigang, *Method to analyze programmable deformation of dielectric elastomer layers.* Applied Physics Letters, 2008: p. 251902 (3 pp.).
27. Zhigang, S., Z. Xuanhe, and W.H. Greene, *A nonlinear field theory of deformable dielectrics.* Journal of the Mechanics and Physics of Solids, 2008: p. 467-86.
28. Xuanhe, Z. and S. Zhigang, *Method to analyze electromechanical stability of dielectric elastomers.* Applied Physics Letters, 2007: p. 061921-1.
29. Roentgen, W.C., *About the Changes in Shape and Volume of Dielectrics Caused by Electricity*, in *Annual Physics and Chemistry Series*. 1880, John Ambrosius Barth: Leipzig. p. 771-786.
30. Pelrine, R., et al., *High-speed electrically actuated elastomers with strain greater than 100%*. Science, 2000: p. 836-9.

31. Bar-Cohen, Y. *Electro-active polymers: Current capabilities and challenges*. in *Smart Structures and Materials 2002: Electroactive Polymer Actuators and Devices (EAPAD), March 18, 2002 - March 21, 2002*. 2002. San Diego, CA, United states: SPIE.
32. Pelrine, R., et al. *Dielectric elastomer artificial muscle actuators: toward biomimetic motion*. in *Smart Structures and Materials 2002. Electroactive Polymer Actuators and Devices (EAPAD), 18-21 March 2002*. 2002. USA: SPIE-Int. Soc. Opt. Eng.
33. Pelrine, R.E., R.D. Kornbluh, and J.P. Joseph. *Electrostriction of polymer dielectrics with compliant electrodes as a means of actuation*. in *IEEE Tenth Annual International Workshop on Micro Electro Mechanical Systems. An Investigation of Micro Structures, Sensors, Actuators, Machines and Robots, 26-30 Jan. 1997*. 1998. Switzerland: Elsevier.
34. Su, J., et al. *Electrostrictive graft elastomers and applications*. in *The 1999 MRS Fall Meeting- Symposium Electroactive Polymers, December 29, 1999 - January 1, 1999*. 2000. Boston, MA, USA: Materials Research Society.
35. Su, J., et al. *Electrostrictive graft elastomers and applications*. in *Electroactive Polymers (EAP). Symposium, 29 Nov.-1 Dec. 1999*. 2000. Warrendale, PA, USA: Mater. Res. Soc.
36. Bar-Cohen, Y., *Electroactive polymers as an enabling materials technology.* Proceedings of the Institution of Mechanical Engineers, Part G (Journal of Aerospace Engineering), 2007: p. 553-64.
37. Okuzaki, H. and Y. Osada, *A chemomechanical polymer gel with electrically driven motility.* Journal of Intelligent Material Systems and Structures, 1993: p. 50-3.
38. Shahinpoor, M. and K.J. Kim, *Ionic polymer-metal composites. I. Fundamentals.* Smart Materials and Structures, 2001: p. 819-33.
39. Kim, J., et al., *A comparative study of conductive polypyrrole and polyaniline coatings on electro-active papers.* Polymer Journal, 2006: p. 659-668.
40. Toupin, R.A., *The elastic dielectric.* Archive for Rational Mechanics and Analysis, 1956: p. 849-915.
41. Zhenyl, M., et al., *High field electrostrictive response of polymers.* Journal of Polymer Science, Part B (Polymer Physics), 1994: p. 2721-31.
42. Son, S. and N.C. Goulbourne, *Finite Deformations of Tubular Dielectric Elastomer Sensors.* Journal of Intelligent Material Systems and Structures, 2009: p. 2187-2199.
43. Son, S. and N.C. Goulbourne, *Dynamic response of tubular dielectric elastomer transducers.* International Journal of Solids and Structures, 2010: p. 2672-2679.
44. Pelrine, R., et al. *Applications of dielectric elastomer actuators*. in *Electroactive Polymer, Actuators and Devices-Smart Structures and Materials 2001-, March 5, 2001 - March 8, 2001*. 2001. Newport Beach, CA, United states: SPIE.
45. Kornbluh, R., et al. *Electroelastomers: Applications of dielectric elastomer transducers for actuation, generation and smart structures*. in *Smart Structures and Materials 2002: Industrial and Commercial Applications of Smart Structures Technologies, March 18, 2002 - March 21, 2002*. 2002. San Diego, CA, United states: SPIE.
46. Pei, Q., et al., *Multiple-degrees-of-freedom electroelastomer roll actuators.* Smart Materials and Structures, 2004: p. 86-92.
47. Kofod, G., M. Paajanen, and S. Bauer. *New design concept for dielectric elastomer actuators*. in *Smart Structures and Materials 2006: Electroactive Polymer Actuators and Devices (EAPAD), 27 Feb. 2006*. 2006. USA: SPIE - The International Society for Optical Engineering.

48. Carpi, F., et al., *Helical dielectric elastomer actuators.* Smart Materials and Structures, 2005: p. 1210-16.
49. Carpi, F., C. Salaris, and D. De Rossi, *Folded dielectric elastomer actuators.* Smart Materials and Structures, 2007: p. 300-5.
50. Fox, J.W. and N.C. Goulbourne, *On the dynamic electromechanical loading of dielectric elastomer membranes.* Journal of the Mechanics and Physics of Solids, 2008: p. 2669-2686.
51. Fox, J.W. and N.C. Goulbourne, *Electric field-induced surface transformations and experimental dynamic characteristics of dielectric elastomer membranes.* Journal of the Mechanics and Physics of Solids, 2009: p. 1417-1435.
52. Goulbourne, N., E. Mockensturm, and M. Frecker, *A nonlinear model for dielectric elastomer membranes.* Journal of Applied Mechanics, Transactions ASME, 2005: p. 899-906.
53. Kofod, G., *The static actuation of dielectric elastomer actuators: how does pre-stretch improve actuation?* Journal of Physics D: Applied Physics, 2008: p. 215405 (11 pp.).
54. Soon Mok, H., et al., *Interpenetrating networks of elastomers exhibiting 300% electrically-induced area strain.* Smart Materials and Structures, 2007: p. 280-7.
55. Zhang, Q.M., et al., *An all-organic composite actuator material with a high dielectric constant.* Nature, 2002: p. 284-7.
56. Huu Chuc, N., et al., *The effects of additives on the actuating performances of a dielectric elastomer actuator.* Smart Materials and Structures, 2009: p. 015006 (9 pp.).
57. Gallone, G., et al., *Dielectric constant enhancement in a silicone elastomer filled with lead magnesium niobate-lead titanate.* Materials Science & Engineering C, Biomimetic and Supramolecular Systems, 2007: p. 110-16.
58. Carpi, F. and D.D. Rossi, *Improvement of electromechanical actuating performances of a silicone dielectric elastomer by dispersion of titanium dioxide powder.* IEEE Transactions on Dielectrics and Electrical Insulation, 2005: p. 835-43.
59. Eringen, A.C., *Nonlinear Theory of Continuous Media*. 1962, New York: McGraw-Hill Book Company.
60. McMeeking, R.M. and C.M. Landis, *Electrostatic forces and stored energy for deformable dielectric materials.* Transactions of the ASME. Journal of Applied Mechanics, 2005: p. 581-90.
61. Carpi, F. and D. De Rossi, *Dielectric elastomer cylindrical actuators: Electromechanical modelling and experimental evaluation.* Materials Science and Engineering C, 2004: p. 555-562.
62. Wissler, M. and E. Mazza, *Modeling of a pre-strained circular actuator made of dielectric elastomers.* Sensors and Actuators A: Physical, 2005: p. 184-192.
63. Wissler, M. and E. Mazza, *Modeling and simulation of dielectric elastomer actuators.* Smart Materials and Structures, 2005: p. 1396-1402.
64. Wissler, M. and E. Mazza, *Mechanical behavior of an acrylic elastomer used in dielectric elastomer actuators.* Sensors and Actuators A: Physical, 2007: p. 494-504.
65. Yeoh, O.H., *Characterization of Elastic Properties of Carbon-Black-Filled Rubber Vulcanizates.* Rubber Chemistry and Technology, 1990: p. 792-805.
66. Ogden, R.W., *Large Deformation Isotropic Elasticity - On the Correlation of Theory and Experiment for Incompressible Rubberlike Solids.* Proceedings of the Royal Society of London. A. Mathematical and Physical Sciences, 1972: p. 565-584.

67. Arruda, E.M. and M.C. Boyce, *A three-dimensional constitutive model for the large stretch behavior of rubber elastic materials.* Journal of the Mechanics and Physics of Solids, 1993: p. 389-412.
68. Goulbourne, N.C., E.M. Mockensturm, and M.I. Frecker, *Electro-elastomers: Large deformation analysis of silicone membranes.* International Journal of Solids and Structures, 2007: p. 2609-2626.
69. Maxwell, J.C., *A Treatise on Electricity and Magnetism*. 1954, Oxford: Dover.
70. Mooney, M., *Theory of large elastic deformation.* Journal of Applied Physics, 1940: p. 582-592.
71. Tews, A.M., K.L. Pope, and A.J. Snyder. *Pressure-volume characteristics of dielectric elastomer diaphragms*. in *Smart Structures and Materials 2003. Electroactive Polymer Actuators and Devices (EAPAD), 3-6 March 2003*. 2003. USA: SPIE-Int. Soc. Opt. Eng.
72. Green, A.E. and J.E. Adkins, *Large Elastic Deformation*. 1970, London: Oxford University Press.
73. Matsikoudi-Iliopoulou, M., *Finite axisymmetric deformations with torsion of an initially cylindrical membrane reinforced with one family inextensible cords.* International Journal of Engineering Science, 1987: p. 673-80.
74. Shan, Y., et al., *Nonlinear-elastic finite axisymmetric deformation of flexible matrix composite membranes under internal pressure and axial force.* Composites Science and Technology, 2006: p. 3053-3063.
75. Goulbourne, N.C., *A mathematical model for cylindrical, fiber reinforced electro-pneumatic actuators.* International Journal of Solids and Structures, 2009: p. 1043-1052.
76. Liu, W. and C.R. Rahn, *Fiber-reinforced membrane models of McKibben actuators.* Transactions of the ASME. Journal of Applied Mechanics, 2003: p. 853-9.

Chapter 2. Constitutive Formulations for Anisotropic Electro-Elastic Materials

In this chapter, generalized constitutive relationships for anisotropic electro-elastic materials are formulated using continuum mechanics framework [1-7]. The constitutive relationship for an anisotropic electro-elastic material can be derived using an invariant-based theoretical approach. The invariants for the scalar valued stress function that is itself a function of the deformation gradient, directional vectors and the electric field are determined by using the approach and derivations of Spencer, Pipkin and Rivlin [8-13]. The anisotropic electro-elastic material consists of an isotropic continuum with electro-passive or active particles or fibers embedded in a certain direction. The particles or fibers are organized and have a certain orientation, consequently the material properties can change significantly by applying an electric field if the fibers (or particles) are electro-active. In this research, two families of fibers are considered in a 3-dimensional space. The particles are arranged in linear form and closely packed so they can be treated as fibers mathematically. Here, the particles are considered only in the electro-active case, hence there is no electrical interaction and physical connection among the particles without the applied field. Unlike fibers, the particles do not carry tension because they are not continuous without the electrical coupling induced by the electric field. Two families means that the fibers are in the isotropic matrix with two distinct angles forming each family. The angles could vary for a number of fibers in a given family where the variation is determined by a statistic distribution from the dominant angle.

The constitutive relationship for fiber-reinforced materials can be derived using a semi-structural approach or a purely invariant approach. For the structural approach, the fiber families are

considered as structural components in a matrix and a formulation can be obtained by describing the geometric relationship of the fibers and the matrix. In Chapters 4–6, the structural approach is employed for fiber-reinforced elastomers undergoing large deformations [14-16]. The anisotropic continuum is described by an invariant-based free energy function. Holzapfel *et al*. [17] and Gasser *et al*. [18] adopted this invariant approach to describe arterial layers containing a statistical distribution of collagen fiber angles.

In order to describe the local fiber and particle directions (electro-passive or active), a vector representing the material preferred direction is introduced as in Spencer [11]. When the fibers are not electro-active, they are described by electro-passive directional vectors and exert influence only on the zero field stiffness of the material. When they are electro-active, they are represented as electro-active directional vectors and affect the field dependent stiffness and deformation of the material. For electro-elastic materials, an applied electric field causes macroscopically observable deformations, which may include electromechanical coupling mechanisms such as electrostrictive and electrostatic effects. It is expected that the amount and nature of the electric coupling can be significantly dependent on the orientations of the electric directional vectors and polarity and magnitude of the applied electric field. In order to observe the dependence of the electric coupling on the electro-active directional vectors and the applied electric field, the coupling is investigated using an analytical method.

In the development of constitutive equations, one first determines the set of variables on which the constitutive function depends and it is convenient to have a method to reduce the possible forms of the constitutive function. Mathematically, we pose the problem of constructing the irreducible integrity basis for a scalar valued function that depends on any number of tensor and vectors. The reduction is carried out by satisfying requirements for material frame invariance,

material symmetry, and kinematic considerations. Spencer and Rivlin [8-10] obtained a finite integrity basis (invariant set) for an arbitrary number of vectors which are denoted as skew-symmetric 2nd order tensors and an arbitrary number of symmetric 2nd order tensors. They proved that the integrity basis under the proper orthogonal group consists of the integrity basis for the symmetric tensors only and the trace of the symmetric tensor products [8]. They tabulated the full class of integrity bases for an arbitrary number of symmetric 2nd order tensors, axial vectors, and polar vectors under the proper and full orthogonal groups [9]. Pipkin and Rivlin [13] derived the irreducible integrity bases, used to obtain the constitutive equations for several physical phenomena involving electric, magnetic, and temperature gradient fields. The stress is a function of the deformation gradient (2nd order tensor), a magnetic field (axial vector), and an electric field (polar vector) and a temperature gradient field (polar vector). The integrity bases for symmetric tensor and three polar vectors under the proper and the integrity bases for the symmetric tensor, two polar vectors and two axial vectors under full orthogonal groups in Pipkin and Rivlin's work [13] are presented in Appendix B. The characteristic group of the material symmetry of the anisotropic electro-elastic material is the proper orthogonal group [19, 20].

Constitutive formulations for general electro-elastic material have been developed in [1-4]. Dorfmann and Ogden [1, 2] and Rajagopal and Wineman [3] derived a formulation for nonlinear isotropic electro-elastic materials. Dorfmann and Ogden developed a constitutive relationship for isotropic electro-active materials using the invariants derived by Spencer [10] and applied the formulation to two different boundary value problems (homogenous simple shear and non-homogenous axial shear of a circular cylindrical tube) [1, 2]. Rajagopal and Wineman derived a constitutive relationship to describe the stress that develops in a deformed solid due to the

presence of an electric field by using the invariants presented by Spencer [10]. They presented two simple boundary value problems, triaxial extension and shear. Based on the approach developed by Dorfmann and Ogden [1, 2], Bustamante [4] developed a theoretical constitutive law for transversely isotropic electro-elastic materials, consisting of an isotropic matrix and one family of electro-active particles [10]. He showed that the coupling between the electric field and the electro-active particles can be controlled by aligning the electro-active directional vector in particular orientations with respect to the applied electric field [4]. The research presented here distinguishes itself from the works of Dorfmann and Ogden [1, 2], Rajagopal and Wineman [3] and Bustamante [4], by means of the following contributions: 1. Constitutive equations for an anisotropic material containing two electro-active fiber families are derived and explored in 3 dimensional space 2. The effect of the orientation of the directional vectors on the electromechanical coupling are investigated (the direction of the fiber direction and electric field is limited to the principal directions in Bustamante's work [4]). 3. The constitutive formulation in this research is a general formulation applicable to materials with the electro-active or passive fibers embedded.

In Sections 2.1–2.4, a constitutive formulation for anisotropic electro-elastic materials is presented. In Section 2.2, the invariants for the coupling between the electric directional vectors and electric field are derived. In Sections 2.3 and 2.4, total stress and tangent modulus equations are given. The coupling effect between the electric directional vectors and the electric field is investigated with simple examples (equi-biaxial extension and simple shear) in Section 2.5.

2.1. Geometry and Kinematics

We consider an electro-elastic solid continuum occupying and let Ω_0 denote the undeformed fixed reference configuration, which undergoes a large deformation to the deformed current configuration Ω. The transformation from the reference to the current configuration is denoted by χ, such that

$$\mathbf{x} = \chi(\mathbf{X}) \in \Omega, \text{ for each } \mathbf{X} \in \Omega_0. \tag{2.1}$$

The deformation gradient $\boldsymbol{F}$ is defined as

$$\boldsymbol{F} = \frac{\partial \chi(\mathbf{x})}{\partial \mathbf{X}}. \tag{2.2}$$

The Jacobian of the deformation gradient is

$$J = \det[\boldsymbol{F}], \tag{2.3}$$

with the convention that $J > 0$ for real materials to exist. The left and right Cauchy-Green tensors are written as

$$\boldsymbol{B} = \boldsymbol{F}\boldsymbol{F}^T, \boldsymbol{C} = \boldsymbol{F}^T\boldsymbol{F}. \tag{2.4}$$

For an incompressible material, the material is subject to the constraint

$$J = \det[\boldsymbol{F}] = 1. \tag{2.5}$$

2.2. Invariants for an Electro-Elastic Material

In order to describe the local fiber and particle directions which could be electro-passive or active, vectors $\boldsymbol{a}$ and $\boldsymbol{b}$ in the undeformed configuration is introduced in Equation (2.6) and it is required that the free energy depends on the vectors. The directional vectors are considered as one dimensional components, which are characterized by the fibers' angles in Equation (2.6). When a material undergoes deformation, the unit vectors $\boldsymbol{a}$ and $\boldsymbol{b}$ will deform along with the material. Their initial orientation is

$$\boldsymbol{a} = \cos\gamma\cos\alpha\,\hat{e}_1 + \cos\gamma\sin\alpha\,\hat{e}_2 + \sin\gamma\,\hat{e}_3,\ \boldsymbol{b} = \cos\gamma\cos\beta\,\hat{e}_1 + \cos\gamma\sin\beta\,\hat{e}_2 + \sin\gamma\,\hat{e}_3, \tag{2.6}$$

where $\{\hat{e}_1, \hat{e}_2, \hat{e}_3\}$ denote base vectors for a rectangular Cartesian coordinate system (see Figure 2.1), α and β are the angle between the vector and the X_1 direction on the X_1-X_2 plane and γ is the angle between the vector and the vector projection on the X_1-X_2 plane $(\alpha, \beta \in [-\pi, \pi], \gamma \in [-\pi/2, \pi/2])$. The nominal electric field vector $\boldsymbol{E}$ in Equation (2.7) is described in Figure 2.1

$$\boldsymbol{E} = E_1\,\hat{e}_1 + E_2\,\hat{e}_2 + E_3\,\hat{e}_3. \tag{2.7}$$

(Note that generally in this dissertation, $\boldsymbol{E}$ is used for the nominal electric field vector, but the rest of vectors are lowercase and bold).

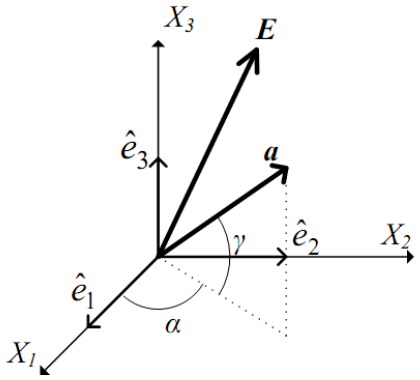

Figure 2.1. Direction vector *a* and nominal electric field *E* in the reference state.

We consider the anisotropic electro-elastic material under the electric field and the anisotropic continuum is described by an invariant-based free energy function. The invariants are constructed by using deformation gradient, directional vectors, $\boldsymbol{a}$ and $\boldsymbol{b}$ and electric field $\boldsymbol{E}$. The stress invariants for the deformation gradient $\boldsymbol{F}$, directional vectors $\boldsymbol{a}$ and $\boldsymbol{b}$ and electric field $\boldsymbol{E}$ are constructed using Pipkin, Rivlin, and Spencer's results [8-13]. They derived the integrity bases (invariants) for various symmetric groups. The selection of the invariants depends on number and type of tensors and vectors and type of orthogonal group. For the proper orthogonal

group, it is immaterial whether the vectors are axial or polar vectors. Since the proper orthogonal group consists of all rotations but no reflection, the axial and polar vectors are invariant under the proper orthogonal group. For the full orthogonal group, the distinction becomes important because the full orthogonal group includes all rotations and reflections in any plane. That is to say, since under the reflection a polar vector is transformed into its negative whereas the coordinates of an axial vector are unchanged by the reflection, the number of invariants under the full orthogonal group is dependent on whether the vectors are axial or polar. According to Eringen and Toupin [19, 20], since the anisotropic electro-elastic material is defined under the proper orthogonal group, the integrity basis for the proper orthogonal group is employed in this research and is given in Appendix B [13]. Since the anisotropic materials have fewer symmetries than isotropic material, they are defined under the proper orthogonal group. To use those results, it is important to identify the type of the vector (polar or axial vectors) needed. Electric field $\boldsymbol{E}$ and directional vectors $\boldsymbol{a}$ and $\boldsymbol{b}$ can be defined as polar vectors. The invariant groups for the polar and axial vectors under the proper and full orthogonal groups were derived by Pipkin and Rivlin [13]; a summary of the results is given in Appendix B.

The mechanical behavior of an elastic material is described by the stress which is a function of the deformation gradient $\boldsymbol{F}$. The principal invariants of the stress are expressed in terms of the right Cauchy-Green tensor $\boldsymbol{C}$ as

$$I_1 = \mathrm{tr}[\boldsymbol{C}], I_2 = \mathrm{tr}[\mathrm{cof}[\boldsymbol{C}]], I_3 = \det[\boldsymbol{C}], \tag{2.8}$$

where I_1, I_2 and I_3 represent the length, area and volume change of the solid. The quantities tr[$\boldsymbol{C}$] and cof[$\boldsymbol{C}$] are the trace and cofactor of the right Cauchy-Green tensor, respectively. If the material is incompressible, $I_3 = 1$.

The stress in an anisotropic material is a function of the deformation gradient and the fiber orientation (***a*** and ***b***). Spencer derived the following set of invariants for fiber reinforced elastic materials [11]

$$\begin{aligned} &I_4 = \boldsymbol{a}\cdot\boldsymbol{C}\cdot\boldsymbol{a},\ I_5 = \boldsymbol{a}\cdot\boldsymbol{C}^2\cdot\boldsymbol{a},\ I_6 = \boldsymbol{b}\cdot\boldsymbol{C}\cdot\boldsymbol{b},\ I_7 = \boldsymbol{b}\cdot\boldsymbol{C}^2\cdot\boldsymbol{b}, \\ &I_8 = \boldsymbol{a}\cdot\boldsymbol{C}\cdot\boldsymbol{b},\ I_9 = \boldsymbol{a}\cdot\boldsymbol{C}^2\cdot\boldsymbol{b}, \end{aligned} \tag{2.9}$$

in addition to I_1–I_3 from Equation (2.8). I_4 and I_6 are the fiber stretches in the direction of ***a*** and ***b***, I_5 and I_7 are higher order invariants for I_4 and I_5, and I_8 and I_9 are coupled invariants of the directional vectors ***a*** and ***b***. Since it is assumed that the fibers are inextensible in Chapters 4, 5 and 6 and I_4–I_9 are constant during the deformation.

The invariants associated with the electric field are

$$I_{10} = \boldsymbol{E}\cdot\boldsymbol{E},\ I_{11} = \boldsymbol{E}\cdot\boldsymbol{C}^{-1}\boldsymbol{E},\ I_{12} = \boldsymbol{E}\cdot\boldsymbol{C}^{-2}\boldsymbol{E}, \tag{2.10}$$

where I_{10} and I_{11} represent the quadratics of the nominal and true electric field ***E*** and ***e***, respectively. The true electric field ***e*** is expressed in terms of the nominal electric field ***E*** as

$$\begin{aligned} &\boldsymbol{e} = \boldsymbol{F}^{-1}\boldsymbol{E}, \\ &I_{11} = \boldsymbol{E}\cdot(\boldsymbol{F}^{\boldsymbol{T}}F)^{-1}\boldsymbol{E} = \boldsymbol{F}^{-1}\boldsymbol{E}\cdot(\boldsymbol{F}^{T}\boldsymbol{F})^{-1}\boldsymbol{E}\boldsymbol{F} = \boldsymbol{F}^{-1}\boldsymbol{E}\cdot\boldsymbol{F}^{-1}\boldsymbol{E} = \boldsymbol{e}\cdot\boldsymbol{e}. \end{aligned} \tag{2.11}$$

Additionally, there are coupled invariants between the nominal electric field and the two electro-active directional vectors,

$$\begin{aligned} &I_{13} = \boldsymbol{a}\cdot\boldsymbol{E},\ I_{14} = \boldsymbol{a}\cdot\boldsymbol{C}\boldsymbol{E},\ I_{15} = \boldsymbol{b}\cdot\boldsymbol{E},\ I_{16} = \boldsymbol{b}\cdot\boldsymbol{C}\boldsymbol{E}, \\ &I_{17} = (\boldsymbol{a}\times\boldsymbol{b})\cdot\boldsymbol{E},\ I_{18} = (\boldsymbol{a}\times\boldsymbol{b})\cdot\boldsymbol{C}\boldsymbol{E},\ I_{19} = (\boldsymbol{a}\times\boldsymbol{b})\cdot\boldsymbol{C}^2\boldsymbol{E}, \end{aligned} \tag{2.12}$$

where I_{13}–I_{16} represent the coupling between one electro-active directional vector and the nominal electric field and I_{17}–I_{19} represent the coupling between two electro-active vectors and the electric field. Since the electro-active fibers (or particles) are considered as one dimensional components and the coupling invariants between the fibers (or particles) and the nominal electric

field are defined as dot product of two vectors in Equation (2.12), there is no coupling when the directions of the fibers $\boldsymbol{a}$ and $\boldsymbol{b}$ are orthogonal to the nominal electric field $\boldsymbol{E}$. The choice of which invariants in Equation (2.12) to use in the formulation of a free energy function for an electro-elastic material is determined by whether the directional vectors $\boldsymbol{a}$ and $\boldsymbol{b}$ in the material are electro-active or passive.

2.3. Cauchy Stress for an Incompressible Material

If there exists a energy function W, meaning the system is conservative, then W also depends on $\boldsymbol{F}$, $\boldsymbol{a}$, $\boldsymbol{b}$, and $\boldsymbol{E}$. We postulate a free energy function that depends on $\boldsymbol{F}$, $\boldsymbol{a}$, $\boldsymbol{b}$, and $\boldsymbol{E}$ to describe the behavior of an anisotropic electro-elastic material. The free energy function is then a function of the set of invariants,

$$W = W(I_1, I_2, I_3, I_4, I_5, I_6, I_7, I_8, I_9, I_{10}, I_{11}, I_{12}, I_{13}, I_{14}, I_{15}, I_{16}, I_{17}, I_{18}, I_{19}). \tag{2.13}$$

For isotropic electro-elastic materials, the free energy function can be prescribed as

$$W = W(I_1, I_2, I_3, I_{10}, I_{11}, I_{12}). \tag{2.14}$$

If two families of the electro-passive fibers are embedded in an isotropic matrix, there is no coupling between the fibers and the electric field and the free energy function can be given as

$$W = W(I_1, I_2, I_3, I_4, I_5, I_6, I_7, I_8, I_9, I_{10}, I_{11}, I_{12}). \tag{2.15}$$

For anisotropic electro-elastic materials with two families of electro-active fibers or particles embedded, the free energy function is written as

$$W = W(I_1, I_2, I_3, I_4, I_5, I_6, I_7, I_8, I_9, I_{10}, I_{11}, I_{12}, I_{13}, I_{14}, I_{15}, I_{16}, I_{17}, I_{18}, I_{19}). \tag{2.16}$$

To simplify the constitutive formulations, higher order invariants with $\boldsymbol{C}^2$ (I_5, I_7, I_9, I_{12} and I_{19}) are not included and the free energy function for anisotropic electro-elastic materials is

$$W = W(I_1, I_2, I_3, I_4, I_6, I_8, I_{10}, I_{11}, I_{13}, I_{14}, I_{15}, I_{16}, I_{17}, I_{18}). \tag{2.17}$$

The 2nd Piola-Kirchhoff stress $\boldsymbol{S}$ is defined as

$$\boldsymbol{S} = 2\frac{\partial W}{\partial \boldsymbol{C}}. \tag{2.18}$$

By using the chain rule, the 2nd Piola-Kirchhoff stresses is obtained explicitly as

$$\boldsymbol{S} = 2\left(\begin{array}{l} \frac{\partial W}{\partial I_1}\frac{\partial I_1}{\partial \boldsymbol{C}} + \frac{\partial W}{\partial I_2}\frac{\partial I_2}{\partial \boldsymbol{C}} + \frac{\partial W}{\partial I_3}\frac{\partial I_3}{\partial \boldsymbol{C}} + \frac{\partial W}{\partial I_4}\frac{\partial I_4}{\partial \boldsymbol{C}} + \frac{\partial W}{\partial I_6}\frac{\partial I_6}{\partial \boldsymbol{C}} + \frac{\partial W}{\partial I_8}\frac{\partial I_8}{\partial \boldsymbol{C}} + \frac{\partial W}{\partial I_{10}}\frac{\partial I_{10}}{\partial \boldsymbol{C}} \\ + \frac{\partial W}{\partial I_{11}}\frac{\partial I_{11}}{\partial \boldsymbol{C}} + \frac{\partial W}{\partial I_{13}}\frac{\partial I_{13}}{\partial \boldsymbol{C}} + \frac{\partial W}{\partial I_{14}}\frac{\partial I_{14}}{\partial \boldsymbol{C}} + \frac{\partial W}{\partial I_{15}}\frac{\partial I_{15}}{\partial \boldsymbol{C}} + \frac{\partial W}{\partial I_{16}}\frac{\partial I_{16}}{\partial \boldsymbol{C}} + \frac{\partial W}{\partial I_{17}}\frac{\partial I_{17}}{\partial \boldsymbol{C}} \\ + \frac{\partial W}{\partial I_{18}}\frac{\partial I_{18}}{\partial \boldsymbol{C}} \end{array}\right), \tag{2.19}$$

where the first derivatives of the invariants in terms of the right Cauchy-Green tensor are

$$\begin{array}{l} \frac{\partial I_1}{\partial \boldsymbol{C}} = \boldsymbol{1},\ \frac{\partial I_2}{\partial \boldsymbol{C}} = I_1\boldsymbol{1} - \boldsymbol{C},\ \frac{\partial I_3}{\partial \boldsymbol{C}} = I_2\boldsymbol{1} - I_1\boldsymbol{C} + \boldsymbol{C}^2 = I_3\boldsymbol{C}^{-1}, \\ \frac{\partial I_4}{\partial \boldsymbol{C}} = \boldsymbol{a}\otimes\boldsymbol{a},\ \frac{\partial I_6}{\partial \boldsymbol{C}} = \boldsymbol{b}\otimes\boldsymbol{b},\ \frac{\partial I_8}{\partial \boldsymbol{C}} = \boldsymbol{a}\otimes\boldsymbol{b}, \\ \frac{\partial I_{10}}{\partial \boldsymbol{C}} = 0,\ \frac{\partial I_{11}}{\partial \boldsymbol{C}} = -\boldsymbol{C}^{-1}(\boldsymbol{E}\otimes\boldsymbol{C}^{-1}\boldsymbol{E}) = -\boldsymbol{C}^{-1}(\boldsymbol{e}\otimes\boldsymbol{e}), \\ \frac{\partial I_{13}}{\partial \boldsymbol{C}} = 0,\ \frac{\partial I_{14}}{\partial \boldsymbol{C}} = \boldsymbol{a}\otimes\boldsymbol{E},\ \frac{\partial I_{15}}{\partial \boldsymbol{C}} = 0,\ \frac{\partial I_{16}}{\partial \boldsymbol{C}} = \boldsymbol{b}\otimes\boldsymbol{E}, \\ \frac{\partial I_{17}}{\partial \boldsymbol{C}} = 0,\ \frac{\partial I_{18}}{\partial \boldsymbol{C}} = ((\boldsymbol{a}\times\boldsymbol{b})\otimes\boldsymbol{E}), \end{array} \tag{2.20}$$

where $\boldsymbol{1}$ is the 2nd identity tensor and $\otimes$ and $\times$ represent the tensor and cross products, respectively.

By inserting Equation (2.20) into (2.19), the 2nd Piola-Kirchhoff stress becomes

$$\begin{array}{l} \boldsymbol{S} = 2\{(W_1 + I_1W_2 + I_2W_3)\boldsymbol{1} - (W_2 + I_1W_3)\boldsymbol{C} + W_3\boldsymbol{C}^2 + W_4\boldsymbol{a}\otimes\boldsymbol{a} + W_6\boldsymbol{b}\otimes\boldsymbol{b} + W_8\boldsymbol{a}\otimes\boldsymbol{b} \\ - W_{11}\boldsymbol{C}^{-2}(\boldsymbol{E}\otimes\boldsymbol{E}) + W_{14}\boldsymbol{a}\otimes\boldsymbol{E} + W_{16}\boldsymbol{b}\otimes\boldsymbol{E} + W_{18}\boldsymbol{d}\otimes\boldsymbol{E}\}, \end{array} \tag{2.21}$$

where $W_i = \partial W / \partial I_i$, i = 1, 2, 4, 6, 8, 11, 14, 16 and 18, and $\boldsymbol{d} = \boldsymbol{a} \times \boldsymbol{b}$. With the assumption of material incompressibility (J = 1), the 2nd Piola-Kirchhoff stress is rewritten as

$$\begin{array}{l} \boldsymbol{S} = 2\{(W_1 + I_1W_2)\boldsymbol{1} - W_2\boldsymbol{C} + W_4\boldsymbol{a}\otimes\boldsymbol{a} + W_6\boldsymbol{b}\otimes\boldsymbol{b} + W_8\boldsymbol{a}\otimes\boldsymbol{b} \\ - W_{11}\boldsymbol{C}^{-2}(\boldsymbol{E}\otimes\boldsymbol{E}) + W_{14}\boldsymbol{a}\otimes\boldsymbol{E} + W_{16}\boldsymbol{b}\otimes\boldsymbol{E} + W_{18}\boldsymbol{d}\otimes\boldsymbol{E}\} + p\boldsymbol{C}^{-1}, \end{array} \tag{2.22}$$

where p is the hydrostatic pressure. By using the push-forward operator [21], the total Cauchy stress in the deformed configuration is

$$\begin{aligned}&\boldsymbol{\sigma} = \boldsymbol{F}\boldsymbol{S}\boldsymbol{F}^{T},\\&\boldsymbol{\sigma} = \{2(W_1 + W_2 I_1)\boldsymbol{B} - 2W_2\boldsymbol{B}^2 + 2W_4(\boldsymbol{F}\boldsymbol{a}\otimes\boldsymbol{F}\boldsymbol{a}) + 2W_6(\boldsymbol{F}\boldsymbol{b}\otimes\boldsymbol{F}\boldsymbol{b}) + 2W_8(\boldsymbol{F}\boldsymbol{a}\otimes\boldsymbol{F}\boldsymbol{b})\\&- 2W_{11}(\boldsymbol{e}\otimes\boldsymbol{e}) + 2W_{14}(\boldsymbol{F}\boldsymbol{a}\otimes\boldsymbol{B}\boldsymbol{e}) + 2W_{16}(\boldsymbol{F}\boldsymbol{b}\otimes\boldsymbol{B}\boldsymbol{e}) + 2W_{18}(\boldsymbol{F}\boldsymbol{d}\otimes\boldsymbol{B}\boldsymbol{e})\} + p\boldsymbol{1}.\end{aligned} \tag{2.23}$$

The total stress in Equation (2.23) can be expressed in index notation, where the summation convention is implied for repeated indices

$$\begin{aligned}\sigma_{ij} &= \{2(W_1 + W_2 I_1)B_{ij} - 2W_2 B_{ij}^2 + 2W_4(F_{ik}a_k F_{jl}a_l) + 2W_6(F_{ik}b_k F_{jl}b_l)\\&+ 2W_8(F_{ik}a_k F_{jl}b_l) - 2W_{11}(e_i e_j) + 2W_{14}(F_{ik}a_k B_{jl}e_l) + 2W_{16}(F_{ik}b_k B_{jl}e_l)\\&+ 2W_{18}(F_{ik}d_k B_{jl}e_l)\} + p\delta_{ij}.\end{aligned} \tag{2.24}$$

where i, j and k run from 1–3. If it is assumed that the free energy function is a linear combination of the invariants in Equations (2.8)–(2.11) and W_i is a material contant, W_1, W_2, W_4, W_6 and W_8 represent mechanical properties of the material and the fibers, which can be obtained using a uniaxial or biaxial extension test. W_{11} is an electrical property of the isotropic matrix and can be independently measured using a reference material, which electrical property is already known. W_{14}, W_{16} and W_{18} are electromechancial coupling coefficients between the fibers and the applied electric field, which also can be determined similarly to W_{11}.

If $\boldsymbol{E}$ = 0, there is no electro-active coupling and the material behavior is elastic. If $\boldsymbol{E} \neq 0$, specifically, well known electromechanical coupling mechanisms can be associated with the invariants and the electric charges will align towards the electric field. The Coulombic attraction between charged surfaces is described by the sixth term of Equation (2.24). $F_{ik}\,a_k\,B_{jl}\,e_l$ and $F_{ik}\,b_k$ $B_{jl}\,e_l$ represents the coupling between one electro-active directional vector ($\boldsymbol{a}$ and $\boldsymbol{b}$) and the applied true electric field ($\boldsymbol{e}$). $F_{ik}\,d_k\,B_{jl}\,e_l$ describes the coupling between two electro-active

directional vectors and the applied electric field. It is expected that the couplings are strongly dependent on the orientation and magnitude of $\boldsymbol{a}$, $\boldsymbol{b}$ and $\boldsymbol{e}$.

2.4. Tangent Modulus for an Incompressible Material

Application of the constitutive formulations in the previous section to a finite element method (ABAQUS 6.9-1) requires the derivation of the tangent modulus. The tangent modulus serves as an iterative operator for a finite element solver using a Newton-type method for the solution of nonlinear initial or boundary value problems. The detail of the implementation of the constitutive formulation for the electro-elastic material will be presented in Chapter 7.

The tangent modulus tensor is defined as

$$\boldsymbol{\mathcal{C}} = 4\frac{\partial^2 W}{\partial \boldsymbol{C}\partial \boldsymbol{C}} = 2\frac{\partial \boldsymbol{S}}{\partial \boldsymbol{C}}. \tag{2.25}$$

The tangent modulus in the reference state is obtained by inserting Equation (2.21) into (2.25),

$$\boldsymbol{\mathcal{C}} = 4\left\{\begin{array}{l} \boldsymbol{1}\otimes\frac{\partial W_1}{\partial \boldsymbol{C}} + \boldsymbol{1}\otimes W_2\frac{\partial I_2}{\partial \boldsymbol{C}} + \boldsymbol{1}\otimes I_1\frac{\partial W_2}{\partial \boldsymbol{C}} + \boldsymbol{1}\otimes I_2\frac{\partial W_3}{\partial \boldsymbol{C}} + \boldsymbol{1}\otimes W_3\frac{\partial I_2}{\partial \boldsymbol{C}} + W_3\frac{\partial \boldsymbol{C}^2}{\partial \boldsymbol{C}} \\ + \boldsymbol{C}^2\otimes\frac{\partial W_3}{\partial \boldsymbol{C}} - \boldsymbol{C}\otimes\frac{\partial W_2}{\partial \boldsymbol{C}} - W_2\frac{\partial \boldsymbol{C}}{\partial \boldsymbol{C}} - I_1W_3\frac{\partial \boldsymbol{C}}{\partial \boldsymbol{C}} - I_1\boldsymbol{C}\otimes\frac{\partial \boldsymbol{C}}{\partial \boldsymbol{C}} - W_3\boldsymbol{C}\otimes\frac{\partial I_1}{\partial \boldsymbol{C}} \\ + \boldsymbol{a}\otimes\boldsymbol{a}\otimes\frac{\partial W_4}{\partial \boldsymbol{C}} + \boldsymbol{b}\otimes\boldsymbol{b}\otimes\frac{\partial W_6}{\partial \boldsymbol{C}} + \boldsymbol{a}\otimes\boldsymbol{b}\otimes\frac{\partial W_8}{\partial \boldsymbol{C}} - \frac{\partial W_{11}}{\partial \boldsymbol{C}}\otimes\boldsymbol{C}^{-2}(\boldsymbol{E}\otimes\boldsymbol{E}) \\ - W_{11}\boldsymbol{C}^{-3}(\boldsymbol{E}\otimes\boldsymbol{E})\otimes\frac{\partial \boldsymbol{C}^{-1}}{\partial \boldsymbol{C}} + \boldsymbol{a}\otimes\boldsymbol{E}\otimes\frac{\partial W_{14}}{\partial \boldsymbol{C}} + \boldsymbol{b}\otimes\boldsymbol{E}\otimes\frac{\partial W_{16}}{\partial \boldsymbol{C}} + (\boldsymbol{d}\otimes\boldsymbol{E})\otimes\frac{\partial W_{18}}{\partial \boldsymbol{C}} \end{array}\right\}, \tag{2.26}$$

where

$$\begin{aligned} &\frac{\partial W_i}{\partial \boldsymbol{C}} = \sum_{j=1}^{18}\frac{\partial W_i}{\partial I_j}\frac{\partial I_j}{\partial \boldsymbol{C}}, \\ &= W_{i1}1 + W_{i2}(I_1 1 - \boldsymbol{C}) + W_{i3}I_3\boldsymbol{C}^{-1} + W_{i4}\boldsymbol{a}\otimes\boldsymbol{a} + W_{i6}\boldsymbol{b}\otimes\boldsymbol{b} + W_{i8}\boldsymbol{a}\otimes\boldsymbol{b} - W_{i11}\boldsymbol{C}^{-2}(\boldsymbol{E}\otimes\boldsymbol{E}) \\ &+ W_{i14}\boldsymbol{a}\otimes\boldsymbol{E} + W_{i16}\boldsymbol{b}\otimes\boldsymbol{E} + W_{i18}\boldsymbol{d}\otimes\boldsymbol{E}, \\ &W_{ij} = \frac{\partial^2 W}{\partial I_i\partial I_j}, (i \text{ and } j = 1,2,3,4,6,8,11,14,16 \text{ and } 18). \end{aligned} \tag{2.27}$$

The tangent modulus tensor in the deformed configuration is obtained using the push-forward operator,

$$\boldsymbol{c} = \frac{1}{J}\boldsymbol{F}\boldsymbol{F}\boldsymbol{C}\boldsymbol{F}^T\boldsymbol{F}^T. \tag{2.28}$$

The detailed formulation of the tangent modulus for an electro-elastic material is given in Appendix C.

2.5. Coupling Effect between the Fibers and the Electric Field

In this section, the coupling between the electro-active directional vectors and the electric field is investigated by using the constitutive formulation in Section 2.3. A maximum or minimum coupling effect can be generated by orienting the angles of the directional vectors and changing the polarity and magnitude of the electric field. The critical angles for the maximum or minimum coupling are obtained by using a simple second derivative test in Section 2.5.1. In Section 2.5.2, the constitutive formulation for an electro-elastic material with two electro-passive directional vectors is presented for the case of plane strain. In Sections 2.5.3 and 2.5.4, the coupling between a single active directional vector and the electric field and between 2 active directional vectors and the electric field are investigated respectively by using the second derivative test. To examine the dependence of coupling on the angles and electric field, simple examples (equi-biaxial extension and simple shear) are presented in Section 2.5.5 and 2.5.6.

2.5.1. Local Maxima and Minima for Electro-active Coupling

The local maximum and minimum of the coupling between the electro-active directional vectors and electric field are investigated using a simple second derivative test [22]. For a single fiber

family (α and γ), the critical values (α_1 and γ_1) can be obtained by taking the first partial derivatives of a given function f with respect to α and γ. The Hessian matrix of second partial derivatives of the function f with respect to α and γ is

$$H = \begin{bmatrix} \frac{\partial^2 f}{\partial \alpha^2} & \frac{\partial^2 f}{\partial \alpha \partial \gamma} \\ \frac{\partial^2 f}{\partial \alpha \partial \gamma} & \frac{\partial^2 f}{\partial \gamma^2} \end{bmatrix}, \qquad (2.29)$$

$$\text{where } D_1 = \frac{\partial^2 f}{\partial \alpha^2} \left(\text{or } \frac{\partial^2 f}{\partial \gamma^2} \right), D_2 = \det[\boldsymbol{H}].$$

$\frac{\partial^2 f}{\partial \gamma^2}$ has the same sign as $\frac{\partial^2 f}{\partial \alpha^2}$ at $D_2(\alpha_1, \gamma_1) > 0$,

$$\begin{aligned} D_2 &= \left(\frac{\partial^2 f}{\partial \alpha^2}\right)\left(\frac{\partial^2 f}{\partial \gamma^2}\right) - \left(\frac{\partial^2 f}{\partial \alpha \partial \gamma}\right)^2 > 0, \\ \left(\frac{\partial^2 f}{\partial \alpha^2}\right)\left(\frac{\partial^2 f}{\partial \gamma^2}\right) &> \left(\frac{\partial^2 f}{\partial \alpha \partial \gamma}\right)^2 > 0, \\ \left(\frac{\partial^2 f}{\partial \alpha^2}\right)\left(\frac{\partial^2 f}{\partial \gamma^2}\right) &> 0, \\ \therefore \text{ if } \frac{\partial^2 f}{\partial \alpha^2} > 0, \frac{\partial^2 f}{\partial \gamma^2} &> 0 \text{ and if } \frac{\partial^2 f}{\partial \alpha^2} < 0, \frac{\partial^2 f}{\partial \gamma^2} < 0, \end{aligned} \qquad (2.30)$$

so that $\frac{\partial^2 f}{\partial \gamma^2}$ or $\frac{\partial^2 f}{\partial \alpha^2}$ can be used as D_1.

The conditions for identifying a maximum, minimum , or saddle points are:

(i) If $D_1(\alpha_1, \gamma_1) > 0$ and $D_2(\alpha_1, \gamma_1) > 0$, then f *has* a local minimum at (α_1, γ_1),

(ii) If $D_1(\alpha_1, \gamma_1) < 0$ and $D_2(\alpha_1, \gamma_1) > 0$, then f has a local maximum at (α_1, γ_1),

(iii) In any other case where $D_2(\alpha_1, \gamma_1) < 0$, f has a saddle point at (α_1, γ_1).

2.5.2. Two Passive Directional Vectors and Electric Field

Let's consider two directional vectors which are not electro-active as may be the case for a material reinforced with passive fibers. Since the directional vectors are passive, the coupling invariants I_{13}–I_{19} are zero. The free energy function can now be simplified to

$$W = W(I_1, I_2, I_4, I_6, I_8, I_{10}, I_{11}). \tag{2.31}$$

The total stress in Equation (2.24) is also simplified:

$$\begin{aligned}\sigma_{ij} &= \{2(W_1 + W_2 I_1)B_{ij} - 2W_2 B_{ij}^2 + 2W_4(F_{ik}a_k F_{jl}a_l) + 2W_6(F_{ik}b_k F_{jl}b_l) \\ &+ 2W_8(F_{ik}a_k F_{jl}b_l) - 2W_{11}(e_i e_j)\} + p\delta_{ij}.\end{aligned} \tag{2.32}$$

Consider the electromechanical deformation in the X_1-X_2 plane of an anisotropic dielectric elastomer. It is assumed that there is no shear in the X_3 direction ($F_{13} = F_{23} = F_{31} = F_{32} = 0$), the fiber families exist in the X_1-X_2 plane ($\gamma = 0$) and the true electric field is applied in the X_3 direction ($e_1 = e_2 = 0$). In this case, the deformation gradient, directional vectors $\boldsymbol{a}$ and $\boldsymbol{b}$, and true electric field $\boldsymbol{e}$ are

$$\boldsymbol{F} = \begin{pmatrix} F_{11} & F_{12} & 0 \\ F_{12} & F_{22} & 0 \\ 0 & 0 & F_{33} \end{pmatrix},\ \boldsymbol{a} = \{\cos\alpha, \sin\alpha, 0\},\ \boldsymbol{b} = \{\cos\beta, \sin\beta, 0\},\ \boldsymbol{e} = \{0, 0, \boldsymbol{e}_3\}, \tag{2.33}$$

where the fibers $\boldsymbol{a}$ and $\boldsymbol{b}$ reside in the X_1-X_2 plane as shown in Figure 2.2. Figure 2.2 describes the geometry of the electro-elastic where L_1, L_2 and h_0 are reference dimensions in the X_1, X_2, and X_3 directions.

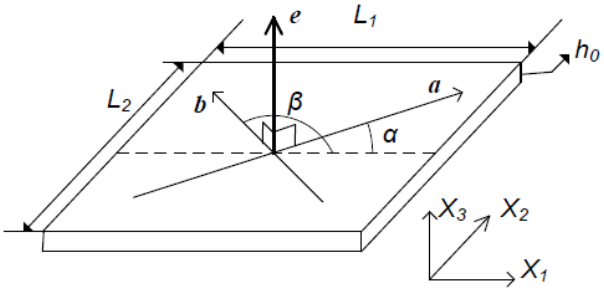

Figure 2.2. Schematic of anisotropic dielectric elastomer with two directional vectors *a* and *b* and true electric field *e* in the reference state.

There are no tractions normal to the surface, so we set σ_{33}=0 and the total stress is now written using Equations (2.32) and (2.33):

$$
\begin{aligned}
&\sigma_{11} = 2(W_1 + W_2 I_1)(B_{11} - B_{33}) - 2W_2(B_{11}^2 - B_{33}^2) + 2W_4(F_{11}\cos\alpha + F_{12}\sin\alpha)^2 \\
&+ 2W_6(F_{11}\cos\beta + F_{12}\sin\beta)^2 + 2W_8(F_{11}\cos\alpha + F_{12}\sin\alpha)(F_{11}\cos\beta + F_{12}\sin\beta) + 2W_{11}e_3^2, \\
&\sigma_{22} = 2(W_1 + W_2 I_1)(B_{22} - B_{33}) - 2W_2(B_{22}^2 - B_{33}^2) + 2W_4(F_{12}\cos\alpha + F_{22}\sin\alpha)^2 \\
&+ 2W_6(F_{12}\cos\beta + F_{22}\sin\beta)^2 + 2W_8(F_{11}\cos\alpha + F_{22}\sin\alpha)(F_{11}\cos\beta + F_{22}\sin\beta) + 2W_{11}e_3^2, \\
&\sigma_{12} = 2(W_1 + W_2 I_1)B_{12} - 2W_2 B_{12}^2 + 2W_4(F_{11}\cos\alpha + F_{12}\sin\alpha)(F_{12}\cos\alpha + F_{22}\sin\alpha) \\
&+ 2W_6(F_{11}\cos\beta + F_{12}\sin\beta)(F_{12}\cos\beta + F_{22}\sin\beta) + 2W_8(F_{11}\cos\alpha + F_{12}\sin\alpha)(F_{11}\cos\beta \\
&+ F_{22}\sin\beta), \\
&\sigma_{13} = \{2(W_1 + W_2 I_1)B_{13} - 2W_2 B_{13}^2,\ \sigma_{23} = \{2(W_1 + W_2 I_1)B_{23} - 2W_2 B_{23}^2,\ \sigma_{33} = 0,
\end{aligned}
\tag{2.34}
$$

where $\sigma_{13} = \sigma_{23} = 0$ because of $F_{13} = F_{23} = B_{13} = B_{23} = 0$.

Equation (2.34) can be applicable to the isotropic electro-elastic material or the anisotropic electro-elastic material with two families of the electro-passive fibers. According to Equation (2.34), the terms with W_4, W_6, and W_8 induce the stress from the electro-passive fibers during the deformation. However, for the electro-passive particles, since the electro-passive particles cannot carry the tension in the direction of the particles, the invariants (I_4, I_6, and I_8) for the directional vectors ***a*** and ***b*** should disappear.

2.5.3. One Electro-active Directional Vectors and Electric Field

Consider one electro-active vector ***a*** and a passive vector ***b***. Since there is coupling between ***a*** and ***e***, the free energy function becomes

$$W = W(I_1, I_2, I_3, I_4, I_6, I_8, I_{10}, I_{11}, I_{13}, I_{14}). \tag{2.35}$$

The total stress in Equation (2.24) is simplified with respect to the free energy function in Equation (2.35) to be

$$\begin{aligned}\sigma_{ij} = \{&2(W_1 + W_2 I_1)B_{ij} - 2W_2 B_{ij}^2 + 2W_4(F_{ik}a_k F_{jl}a_l) + 2W_6(F_{ik}b_k F_{jl}b_l) \\ &+ 2W_8(F_{ik}a_k F_{jl}b_l) - 2W_{11}(e_i e_j) + 2W_{14}(F_{ik}a_k B_{jl}e_l)\} + p\delta_{ij},\end{aligned} \tag{2.36}$$

where

$$\boldsymbol{a} = \{\cos\gamma\cos\alpha, \cos\gamma\sin\alpha, \sin\gamma\},\ \boldsymbol{b} = \{\cos\gamma\cos\beta, \cos\gamma\sin\beta, \sin\gamma\},\ \boldsymbol{e} = \{e_1, e_2, e_3\}. \tag{2.37}$$

Note that the fibers or aligned particles can take on a 3 dimensional character and are illustrated in Figure 2.3.

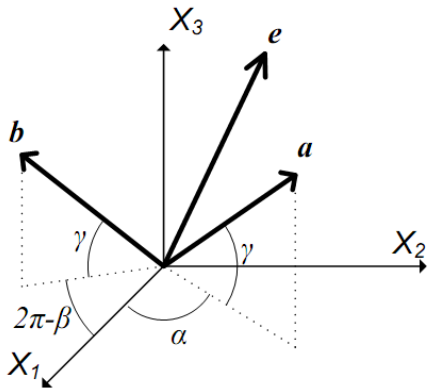

Figure 2.3. Two directional vectors *a* and *b* and true electric field *e* in 3 dimensional space.

When it is assumed that there is no surface traction in the X_3 direction, the total Cauchy stresses are derived as

$$\sigma_{ij} = 2\{(W_1 + W_2 I_1)(B_{ij} - B_{33}\delta_{ij}) - W_2(B_{ij}^2 - B_{33}^2\delta_{ij}) + W_4(F_{ik}a_k F_{jl}a_l - F_{3m}a_m F_{3n}a_n\delta_{ij})$$
$$+ W_6(F_{ik}b_k F_{jl}b_l - F_{3m}b_m F_{3n}b_n\delta_{ij}) + W_8(F_{ik}a_k F_{jl}b_l - F_{3m}a_m F_{3n}b_n\delta_{ij}) - W_{11}(e_i^2 - e_3^2)\delta_{ij} \quad (2.38)$$
$$+ W_{14}(F_{ik}a_k B_{jl}e_l - F_{3m}a_m B_{3n}e_n\delta_{ij})\},$$
$$(i = 1 \text{and } 2, k, l, m \text{ and } n = 1,2,3).$$

If W_i (i = 1, 2, 4,..., 18) are assumed to be prescribed parameters based on the electro-elastic materials (that is to say, W is a linear function of the invariants), the angles of the directional vector (α, β and γ) are controllable independent parameters for magnifying the coupling. Since the deformation gradient $\boldsymbol{F}$ and the electric field $\boldsymbol{e}$ are independent of the angles α, β and γ, the first and second derivatives of the coupling term in the principal stress (i = j) in Equation (2.33) with respect to the angles α, β, and γ are given as

$$\frac{\partial}{\partial\alpha}(F_{ik}a_k B_{il}e_l - F_{3m}a_m B_{3n}e_n) = F_{ik}\frac{\partial a_k}{\partial\alpha}B_{il}e_l - F_{3m}\frac{\partial a_m}{\partial\alpha}B_{3n}e_n,$$
$$\frac{\partial}{\partial\beta}(F_{ik}a_k B_{il}e_l - F_{3m}a_m B_{3n}e_n) = F_{ik}\frac{\partial a_k}{\partial\beta}B_{il}e_l - F_{3m}\frac{\partial a_m}{\partial\beta}B_{3n}e_n, \quad (2.39)$$
$$\frac{\partial}{\partial\gamma}(F_{ik}a_k B_{il}e_l - F_{3m}a_m B_{3n}e_n) = F_{ik}\frac{\partial a_k}{\partial\gamma}B_{il}e_l - F_{3m}\frac{\partial a_m}{\partial\gamma}B_{3n}e_n,$$

where

$$\frac{\partial\boldsymbol{a}}{\partial\alpha} = \{-\cos\gamma\sin\alpha, \cos\gamma\cos\alpha, 0\},\ \frac{\partial\boldsymbol{a}}{\partial\beta} = \{0,0,0\},\ \frac{\partial\boldsymbol{a}}{\partial\gamma} = \{-\sin\gamma\cos\alpha, -\sin\gamma\sin\alpha, \cos\gamma\}. \quad (2.40)$$

The critical angles for the maximum and minimum coupling are obtained when the first derivatives in Equation (2.39) are equal to zero. The critical angles corresponding to a maximum or minimum is determined by using the second derivatives per Equation (2.29) and conditions (i) and (ii),

$$\frac{\partial^2}{\partial\alpha^2}(F_{ik}a_k B_{il}e_l - F_{3m}a_m B_{3n}e_n) = F_{ik}\frac{\partial^2 a_k}{\partial\alpha^2}B_{il}e_l - F_{3m}\frac{\partial^2 a_m}{\partial\alpha^2}B_{3n}e_n,$$
$$\frac{\partial^2}{\partial\gamma^2}(F_{ik}a_k B_{il}e_l - F_{3m}a_m B_{3n}e_n) = F_{ik}\frac{\partial^2 a_k}{\partial\gamma^2}B_{il}e_l - F_{3m}\frac{\partial^2 a_m}{\partial\gamma^2}B_{3n}e_n, \quad (2.41)$$
$$\frac{\partial^2}{\partial\alpha^2}(F_{ik}a_k B_{jl}e_l) = F_{ik}\frac{\partial^2 a_k}{\partial\alpha^2}B_{jl}E_l,\ \frac{\partial^2}{\partial\gamma^2}(F_{ik}a_k B_{jl}E_l) = F_{ik}\frac{\partial^2 a_k}{\partial\gamma^2}B_{jl}e_l,$$

where

$$\frac{\partial^2 \boldsymbol{a}}{\partial \alpha^2} = \{-\cos\gamma\cos\alpha, -\cos\gamma\sin\alpha, 0\}, \frac{\partial^2 \boldsymbol{a}}{\partial \gamma^2} = \{-\cos\gamma\cos\alpha, -\cos\gamma\sin\alpha, -\sin\gamma\}. \tag{2.42}$$

2.5.4. Two Electro-Active Directional Vectors and Electric Field

Two electro-active directional vectors ***a*** and ***b*** and the electric field in Equations (2.6) and (2.7) are considered. Since there are couplings between both electro-active directional vectors (***a*** and ***b***) and the electric field, the free energy function becomes

$$W = W(I_1, I_2, I_3, I_4, I_6, I_8, I_{10}, I_{11}, I_{13}, I_{14}, I_{15}, I_{16}, I_{17}, I_{18}). \tag{2.43}$$

The total stress in Equation (2.24) is now simplified to

$$\begin{aligned}\sigma_{ij} &= \{2(W_1 + W_2 I_1)B_{ij} - 2W_2 B_{ij}^2 + 2W_4(F_{ik}a_k F_{jl}a_l) + 2W_6(F_{ik}b_k F_{jl}b_l) \\ &+ 2W_8(F_{ik}a_k F_{jl}b_l) - 2W_{11}(e_i e_j) + 2W_{14}(F_{ik}a_k B_{jl}e_l) + 2W_{16}(F_{ik}b_k B_{jl}e_l) \\ &+ 2W_{18}(F_{ik}d_k B_{jl}e_l)\} + p\delta_{ij},\end{aligned} \tag{2.44}$$

where

$$\boldsymbol{d} = \boldsymbol{a} \times \boldsymbol{b} = \{\cos\gamma\sin\gamma(\sin\alpha - \sin\beta), \cos\gamma\sin\gamma(\cos\beta - \cos\alpha), -\cos^2\gamma\sin(\alpha - \beta)\}. \tag{2.45}$$

For simplification, β is assumed to be $-\alpha$, which implies symmetric placement of the fibers and hence Equation (2.45) becomes,

$$\boldsymbol{d} = \{2\cos\gamma\sin\gamma\sin\alpha,\ 0,\ -\cos^2\gamma\sin 2\alpha\}. \tag{2.46}$$

The total Cauchy stresses in the X_1 and X_2 directions are expressed as

$$
\begin{aligned}
&\sigma_{ij} = 2\{(W_1 + W_2 I_1)(B_{ij} - B_{33}\delta_{ij}) - W_2(B_{ij}^2 - B_{33}^2\delta_{ij}) + W_4(F_{ik}a_k F_{jl}a_l - F_{3m}a_m F_{3n}a_n\delta_{ij}) \\
&+ W_6(F_{ik}b_k F_{jl}b_l - F_{3m}b_m F_{3n}b_n\delta_{ij}) + W_8(F_{ik}a_k F_{jl}b_l - F_{3m}a_m F_{3n}b_n) - W_{11}(e_i^2 - e_3^2)\delta_{ij} \\
&+ W_{14}(F_{ik}a_k B_{jl}e_l - F_{3m}a_m B_{3n}e_n\delta_{ij}) + W_{16}(F_{ik}b_k B_{jl}e_l - F_{3m}b_m B_{3n}e_n\delta_{ij}) \\
&+ W_{18}(F_{ik}d_k B_{jl}e_l - F_{3m}d_m B_{3n}e_n\delta_{ij})\}, \\
&(i = 1 \text{ and } 2;\ k, l, m \text{ and } n = 1,2,3).
\end{aligned}
\tag{2.47}
$$

For instance, if electro-active particles are embedded and no electric field is applied, there is no physical connection among the particles, which means that each family of the particles cannot carry the tension. The total Cauchy stresses for this case is

$$
\begin{aligned}
&E = 0, \\
&\sigma_{ij} = 2\{(W_1 + W_2 I_1)(B_{ij} - B_{33}\delta_{ij}) - W_2(B_{ij}^2 - B_{33}^2\delta_{ij})\}, \\
&(i = 1 \text{ and } 2,\ k, l, m \text{ and } n = 1,2,3).
\end{aligned}
\tag{2.48}
$$

However, if the electro-active fibers are embedded and no electric field is applied (or the direction of fibers is orthogonal to the direction of the applied electric field), there is no coupling between the fibers and the applied electric field but, each family of the fibers still carries the fiber tension. The total Cauchy stress for this case is

$$
\begin{aligned}
&E = 0, \\
&\sigma_{ij} = 2\{(W_1 + W_2 I_1)(B_{ij} - B_{33}\delta_{ij}) - W_2(B_{ij}^2 - B_{33}^2\delta_{ij}) + W_4(F_{ik}a_k F_{jl}a_l - F_{3m}a_m F_{3n}a_n\delta_{ij}) \\
&+ W_6(F_{ik}b_k F_{jl}b_l - F_{3m}b_m F_{3n}b_n\delta_{ij}) + W_8(F_{ik}a_k F_{jl}b_l - F_{3m}a_m F_{3n}b_n)\} \\
&(i = 1 \text{ and } 2,\ k, l, m \text{ and } n = 1,2,3).
\end{aligned}
\tag{2.49}
$$

The coupling term between directional vectors and the electric field in Equation (2.47) is now investigated to obtain the critical points to obtain a local maximum or minimum. Note that this value will depend on the deformation state. It is assumed that W_{18} is a prescribed constant. The first and second derivatives of the coupling term with respect to the angles α, β, and γ are given as

$$
\begin{aligned}
&i = j,\\
&\frac{\partial}{\partial\alpha}(F_{ik}d_kB_{il}e_l - F_{3m}d_mB_{3n}e_n) = F_{ik}\frac{\partial d_k}{\partial\alpha}B_{il}e_l - F_{3m}\frac{\partial d_m}{\partial\alpha}B_{3n}e_n,\\
&\frac{\partial}{\partial\gamma}(F_{ik}d_kB_{il}e_l - F_{3m}d_mB_{3n}e_n) = F_{ik}\frac{\partial d_k}{\partial\gamma}B_{il}e_l - F_{3m}\frac{\partial d_m}{\partial\gamma}B_{3n}e_n,\\
&i \neq j,\\
&\frac{\partial}{\partial\alpha}(F_{ik}d_kB_{il}e_l) = F_{ik}\frac{\partial d_k}{\partial\alpha}B_{il}e_l,\ \frac{\partial}{\partial\gamma}(F_{ik}d_kB_{il}e_l) = F_{ik}\frac{\partial d_k}{\partial\gamma}B_{il}e_l,
\end{aligned}
\tag{2.50}
$$

where

$$
\frac{\partial \boldsymbol{d}}{\partial\alpha} = \{2\cos\gamma\sin\gamma\cos\alpha, 0, -2\cos^2\gamma\cos 2\alpha\}, \frac{\partial \boldsymbol{d}}{\partial\gamma} = \{2\cos 2\gamma\sin\alpha, 0, \sin 2\gamma\sin 2\alpha\}. \tag{2.51}
$$

The critical angles are obtained using Equations (2.50) and (2.51) via the method described in Section 2.5.2:

$$
\begin{aligned}
&\frac{\partial^2}{\partial\alpha^2}(F_{ik}d_kB_{il}e_l - F_{3m}d_mB_{3n}e_n) = F_{ik}\frac{\partial^2 d_k}{\partial\alpha^2}B_{il}e_l - F_{3m}\frac{\partial^2 d_m}{\partial\alpha^2}B_{3n}e_n,\\
&\frac{\partial^2}{\partial\gamma^2}(F_{ik}d_kB_{il}e_l - F_{3m}d_mB_{3n}e_n) = F_{ik}\frac{\partial^2 d_k}{\partial\gamma^2}B_{il}e_l - F_{3m}\frac{\partial^2 d_m}{\partial\gamma^2}B_{3n}e_n,
\end{aligned}
\tag{2.52}
$$

where

$$
\begin{aligned}
&\frac{\partial^2 \boldsymbol{d}}{\partial\alpha^2} = \{-2\cos\gamma\sin\gamma\sin\alpha, 0, 8\cos^2\gamma\cos\alpha\sin\alpha\}, \frac{\partial^2 \boldsymbol{d}}{\partial\gamma^2} = \{-8\cos\gamma\sin\gamma\sin\alpha, 0, 2\cos 2\gamma\sin 2\alpha\},\\
&\frac{\partial^2 \boldsymbol{d}}{\partial\alpha\partial\gamma} = \{2\cos\alpha\cos 2\gamma, 0, 2\cos 2\alpha\sin\gamma\}.
\end{aligned}
\tag{2.53}
$$

2.5.5. Numerical Example 1: Equi-biaxial Extension

Consider equi-biaxial extension without shear ($F_{12} = F_{13} = F_{23} = 0$) with the incompressibility assumption in Equation (2.5). The deformation gradient $\boldsymbol{F}$, directional vectors $\boldsymbol{a}$ and $\boldsymbol{b}$ and true electric field $\boldsymbol{e}$ are given as

$$\boldsymbol{F}=\begin{pmatrix} F_{11} & 0 & 0 \\ 0 & F_{11} & 0 \\ 0 & 0 & 1/F_{11}^2 \end{pmatrix}, \tag{2.54}$$
$$\boldsymbol{a}=\{\cos\gamma\cos\alpha,\cos\gamma\sin\alpha,\sin\gamma\},\ \boldsymbol{b}=\{\cos\gamma\cos\beta,\cos\gamma\sin\beta,\sin\gamma\},\ \boldsymbol{e}=\{e_1,e_2,e_3\},$$

The critical angles inducing the minimum and maximum couplings between one or two electro-active directional vectors and the electric field are obtained by using the formulation in Sections 2.5.2 and 2.5.3 along with conditions (i) and (ii) in Section 2.5.1.

A. Coupling between one active directional vector and the electric field

For the coupling between one electro-active directional vector and the electric field, the critical angles for the principle directions $i = j = 1$ and 2 are obtained by solving Equation (2.39),

$$\begin{aligned} &i=j=1,\ -e_1F_{11}^3\cos\gamma\sin\alpha=0,\ -\frac{e_3\cos\gamma+e_1F_{11}^9\sin\gamma\cos\alpha}{F_{11}^6}=0, \\ &i=j=2,\ -e_1F_{11}^3\cos\gamma\cos\alpha=0,\ -\frac{e_3\cos\gamma+e_2F_{11}^9\sin\gamma\sin\alpha}{F_{11}^6}=0. \end{aligned} \tag{2.55}$$

The critical angles $\{\alpha_i, \gamma_i\}$ for $i = j = 1$ and 2 are

$$\{\alpha_1,\gamma_1\}=\{0,\tan^{-1}\left(-\frac{e_3}{e_1F_{11}^9}\right)\},\ \{\alpha_2,\gamma_2\}=\{\pi/2,\tan^{-1}\left(-\frac{e_3}{e_2F_{11}^9}\right)\}. \tag{2.56}$$

Whether the critical angles in Equation (2.56) produce a maximum or minimum coupling is determined by conditions (i) and (ii):

$$\begin{aligned} &D_1\big|_{\alpha=\alpha_1,\gamma=\gamma_1}=-\frac{e_1F_{11}^3}{\sqrt{1+\frac{e_1^2F_{11}^{18}}{e_3^2}}},\ D_2\big|_{\alpha=\alpha_1,\gamma=\gamma_1}=\frac{2e_1^2F_{11}^6}{1+\frac{e_1^2F_{11}^{18}}{e_3^2}}, \\ &D_1\big|_{\alpha=\alpha_2,\gamma=\gamma_2}=-\frac{e_2F_{11}^3}{\sqrt{1+\frac{e_1^2F_{11}^{18}}{e_3^2}}},\ D_2\big|_{\alpha=\alpha_2,\gamma=\gamma_2}=\frac{e_2(e_1+e_2)e_3^2F_{11}^6}{e_3^2+e_1^2F_{11}^{18}}. \end{aligned} \tag{2.57}$$

According to Equations (2.56) and (2.57), there are several possible scenarios depending on the polarity and magnitude of the applied electric field. They are:

Case 1) when $|e_1|$ and $|e_2| >> |e_3|$, $\{\alpha_1, \gamma_1\}=\{0, 0\}$ and $\{\alpha_2, \gamma_2\}=\{\pi/2, 0\}$, which induce maximum coupling (e_1 and $e_2 > 0$) and minimum coupling (e_1 and $e_2 < 0$) in the X_1 and X_2 direction,

Case 2) when $|e_3| >> |e_1|$ and $|e_2|$, $\gamma_1 = \gamma_2 = \pi/2$, which induce maximum coupling (e_1 and $e_2 > 0$ and $e_3 < 0$), and $\gamma_1 = \gamma_2 = -\pi/2$, which induce minimum coupling (e_1 and $e_2 < 0$ and $e_3 < 0$) in the X_1 and X_2 direction, and α is not defined at $\gamma = \pm\pi/2$,

Case 3) when $e_1 = 0, |e_2| >> |e_3|$ $\{\alpha_2, \gamma_2\}=\{\pi/2, 0\}$, which induce maximum coupling ($e_2 > 0$) and minimum coupling ($e_2 < 0$) in the X_2 direction,

Case 4) when $e_2 = 0, |e_1| >> |e_3|$ $\{\alpha_1, \gamma_1\}=\{0, 0\}$, which induce maximum coupling ($e_1 > 0$) and minimum coupling ($e_1 < 0$) in the X_2 direction.

The orientation of α and γ in the two cases are shown to Figure 2.4. The dash and solid lines represent the minimum and maximum coupling, respectively. According to conditions Case 1) – Case 2), the critical angles for the maximum and minimum coupling are significantly dependent on the polarity and magnitude of the applied electric field. The change of the electric polarity reverses the direction of the coupling. This result implies that when the electro-active directional vector aligns in the preferred direction for coupling, controlling the electric polarity leads to either positive or negative coupling.

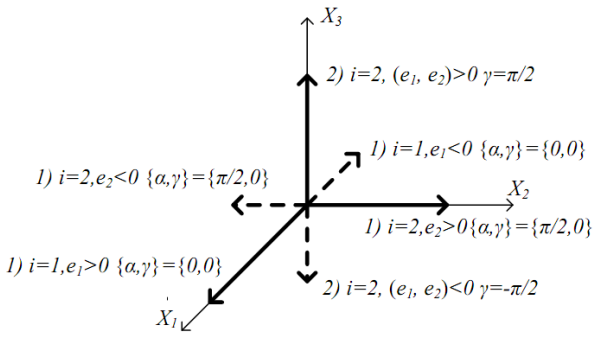

Figure 2.4. Orientation of the directional vector for the cases 1) and 2)

The coupling in Equation (2.38) is denoted as $\boldsymbol{Q}$ and can be normalized by $e_1F_{11}^3$ and $e_2F_{22}^3$ with assuming W_{14} = 1 and e_3 = 0 for $i = j$ = 1 and 2.

$$\begin{aligned} &Q_{11} = W_{14}(F_{1k}a_kB_{1l}e_l - F_{3m}a_mB_{3n}e_n),\ Q_{11} = e_1F_{11}^3\cos\alpha\cos\gamma,\ \frac{Q_{11}}{e_1F_{11}^3} = \cos\alpha\cos\gamma, \\ &Q_{22} = W_{14}(F_{2k}a_kB_{2l}e_l - F_{3m}a_mB_{3n}e_n),\ Q_{11} = e_2F_{22}^3\sin\alpha\cos\gamma,\ \frac{Q_{22}}{e_1F_{22}^3} = \sin\alpha\cos\gamma. \end{aligned} \tag{2.58}$$

The normalized couplings for $i = j$ = 1 and 2 are plotted in Figures 2.5 and 2.6.

Positive coupling means positive electric stress, which is induced by the coupling between one electro-active directional vector and the applied electric field. Consider Case 1) ($|e_1|$ and $|e_2| \gg |e_3|$). At the boundary in Figure 2.2, the force balance equation in the X_1 direction can be obtained using Equation (2.47)

$$\begin{aligned} &A\sigma_{11} = F, \\ &F = 2A\{(W_1 + W_2I_1)(B_{11} - B_{33}) - W_2(B_{11}^2 - B_{33}^2) + W_4((F_{11}a_1)^2 - (F_{33}a_3)^2) \\ &- W_{11}e_1^2 + W_{14}(F_{11}a_1B_{11}e_1)\}, \end{aligned} \tag{2.59}$$

where A and F represent the deformed cross-sectional area and the external force in the X_1 direction, respectively and the last term in Equation (2.59) is the coupling term Q_{11} in Equation (2.58). Equation (2.59) implies that a larger positive coupling Q_{11} ($e_1 > 0$) causes a larger Cauchy stress and more external force F is required. Conversely, the negative coupling Q_{11} ($e_1 <$

0) leads to a smaller Cauchy stress and improve the actuation response. Specifically, the effect of the negative coupling Q_{11} with respect to the orientation of the directional vector on the actuation response can be investigated using Figures 2.4 and 2.5. For example, the improvement of the actuation in the X_1 direction at $e_1 < 0$ can be maximized by aligning the directional vector in the X_1 direction ($\alpha = \gamma = 0°$) in Figures 2.4 and 2.5.

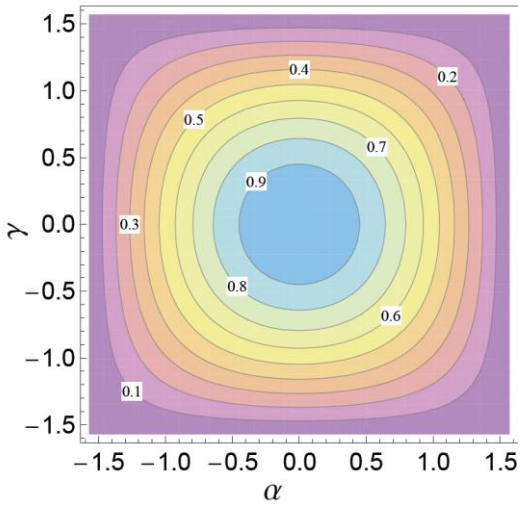

Figure 2.5. Contour plot for the coupling at $i = j = 1$ between one electro-active directional vector a and the electric field e with respect to α and γ.

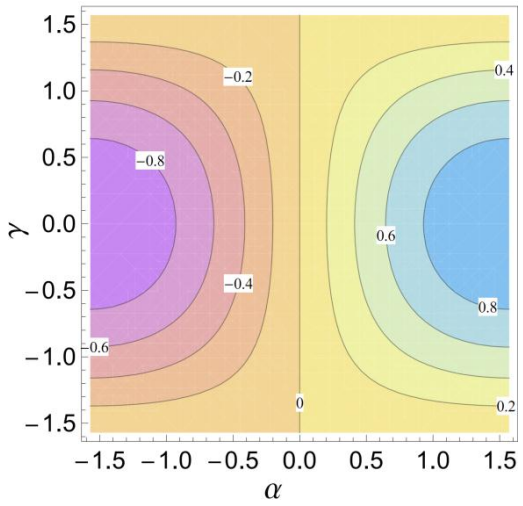

Figure 2.6. Contour plot for the coupling at $i = j = 2$ between one electro-active directional vector a and the electric field e with respect to α and γ.

B. Coupling between two active directional vectors and the electric field

For the coupling between two electro-active vectors and the electric field, the second derivative test is used to find the critical angles. The critical angles for the principal direction $i = j = 1$ are calculated by using Equation (2.39):

$$\{\alpha_1,\gamma_1\}_1=\{\cos^{-1}\Phi_1,\cos^{-1}\Phi_2\},\ \{\alpha_1,\gamma_1\}_2=\{-\cos^{-1}\Phi_1,\cos^{-1}\Phi_2\},$$
$$\{\alpha_1,\gamma_1\}_3=\{\cos^{-1}\Phi_1,-\cos^{-1}\Phi_2\},\ \{\alpha_1,\gamma_1\}_4=\{-\cos^{-1}\Phi_1,-\cos^{-1}\Phi_2\},$$
$$\beta=-\alpha,\Phi_1=\frac{e_3}{\sqrt{2e_3^2+e_1^2F_{11}^{18}}},\ \Phi_2=\sqrt{\frac{2e_3^2+e_1^2F_{11}^{18}}{2e_3^2+2e_1^2F_{11}^{18}}}, \tag{2.60}$$

where $\{\alpha_1, \gamma_1\}_n$ represents the nth critical angle for $i = j = 1$.

At $i = j = 1$, the critical angles are also dependent on the electric field e_1 and e_3.

To simplify D_1 and D_2, either e_1 or e_3 is assumed to be zero. Now, the critical angles become

$$\text{For } e_1=0,\ e_3\neq 0,\ \beta=-\alpha,\ \ \Phi_1=\frac{1}{\sqrt{2}},\ \Phi_2=1,$$
$$\{\alpha_1,\gamma_1\}_1=\{\alpha_1,\gamma_1\}_3=\{\frac{\pi}{4},0\},\ \{\alpha_1,\gamma_1\}_2=\{\alpha_1,\gamma_1\}_4=\{-\frac{\pi}{4},0\},$$
$$\text{For } e_3=0,\ e_1\neq 0,\ \beta=-\alpha,\ \ \Phi_1=0,\ \Phi_2=\frac{1}{\sqrt{2}}, \tag{2.61}$$
$$\{\alpha_1,\gamma_1\}=\{\frac{\pi}{2},\frac{\pi}{4}\},\ \{\alpha_1,\gamma_1\}_2=\{-\frac{\pi}{2},\frac{\pi}{4}\},\ \{\alpha_1,\gamma_1\}_3=\{\frac{\pi}{2},-\frac{\pi}{4}\},\{\alpha_1,\gamma_1\}_4=\{-\frac{\pi}{2},-\frac{\pi}{4}\}.$$

Whether the critical angles in Equation (2.61) produce a maximum or minimum coupling is determined by conditions (i) and (ii):

$$\text{For } e_1=0,\ e_3\neq 0,$$
$$D_1\big|_{\{\alpha_1,\gamma_1\}_1}=-\frac{8e_3}{F_{11}^6},\ D_2\big|_{\{\alpha_1,\gamma_1\}_1}=\frac{30e_3^2}{F_{11}^{12}},\ \ D_1\big|_{\{\alpha_1,\gamma_1\}_2}=\frac{8e_3}{F_{11}^6},\ \ D_2\big|_{\{\alpha_1,\gamma_1\}_2}=\frac{30e_3^2}{F_{11}^{12}},$$
$$\text{For } e_3=0,e_1\neq 0,$$
$$D_1\big|_{\{\alpha_1,\gamma_1\}_1}=D_1\big|_{\{\alpha_1,\gamma_1\}_4}=-2e_1F_{11}^3,\ D_2\big|_{\{\alpha_1,\gamma_1\}_1}=D_2\big|_{\{\alpha_1,\gamma_1\}_4}=16e_1^2F_{11}^6, \tag{2.62}$$
$$D_1\big|_{\{\alpha_1,\gamma_1\}_2}=D_1\big|_{\{\alpha_1,\gamma_1\}_3}=2e_1F_{11}^3,\ D_2\big|_{\{\alpha_1,\gamma_1\}_2}=D_2\big|_{\{\alpha_1,\gamma_1\}_3}=16e_1^2F_{11}^6.$$

According to Equation (2.62), the specific angles for the maximum or minimum coupling are decided by the polarity of the electric field e_1 and e_3. As expected, the direction of the coupling is reversed by changing the polarity.

For example, the coupling normalized by $e_1F_{11}^3$ and the orientation of the critical angles for $i = j = 1$ with $W_{18} = 1$ and $e_3 = 0$ in Equations (2.61) and (2.62) are plotted in the left of Figure 2.7.

The maximum coupling (solid lines: B and C to the right of Figure 2.7) exist at $\{\alpha, \beta, \gamma\} = \{\pi/2, -\pi/2, \pi/4\}$ and $\{-\pi/2, \pi/2, -\pi/4\}$ and minimum coupling (dotted lines: A and D in the right of Figure 2.7) at $\{\alpha, \beta, \gamma\} = \{-\pi/2, \pi/2, \pi/4\}$ and $\{\pi/2, -\pi/2, -\pi/4\}$, respectively. In detail, since the absolute value of the maximum and minimum coupling is identical mutually, the maximum coupling could be reversed by converting the electric polarity. According to right of Figure 2.7, since the critical angles of $\alpha = \pi/2$ (or $-\pi/2$) and $\gamma=\pi/4$ (or $-\pi/4$) leads to the maximization of the cross product of ***a*** and ***b*** along with the X_1 direction, the coupling is maximized (B and C on right of Figure 2.7). Differently from Coupling between one active directional vector and the electric field, the coupling between two electro-active directional vectors and the electric field is maximized when the electric field is orthogonal to the plane where ***a*** and ***b*** exist because the coupling is defined as the cross produce of ***a*** and ***b***. Additionally, the coupling is not affected directly by the mechanical properties of the electro-active fibers because the direction of the coupling is orthogonal to orientation of the fibers.

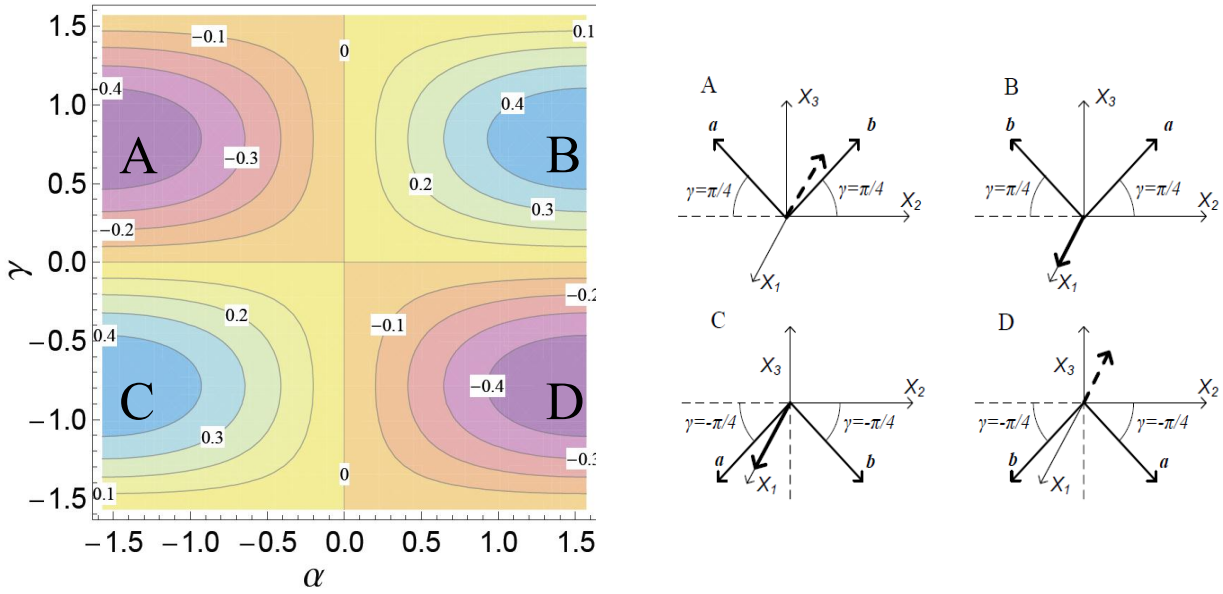

Figure 2.7. (Left) The maximum and minimum coupling between two directional vectors and electric field with respect to α and γ. (Right) see B and C for maximum coupling and A and D for minimum coupling, coupling vectors illustrated by solid and dotted lines.

2.5.6. Numerical Example 2: Simple Shear

Consider simple shear with the electric field in the X_1 direction. The deformation gradient $\boldsymbol{F}$, directional vectors $\boldsymbol{a}$ and $\boldsymbol{b}$ and true electric field $\boldsymbol{e}$ are given as

$$\boldsymbol{F}=\begin{pmatrix}1 & k & 0\\ 0 & 1 & 0\\ 0 & 0 & 1\end{pmatrix},\ \boldsymbol{a}=\{\cos\gamma\cos\alpha,\cos\gamma\sin\alpha,\sin\gamma\},\ \boldsymbol{b}=\{\cos\gamma\cos\beta,\cos\gamma\sin\beta,\sin\gamma\},\ \boldsymbol{e}=\{e_1,0,0\}, \tag{2.63}$$

where k represents a value of the shear. The critical angles inducing the minimum and maximum couplings between one or two electro-active directional vectors and the electric field are obtained using the same procedure outlined previously in Section 2.5.5.

A. Coupling between one active directional vector and the electric field

For the coupling between one electro-active directional vector and the electric field, the critical angles for the principle directions at $i = j = 1$ and 2 are obtained by solving Equation (2.39),

$$\begin{aligned} &i=j=1,\ \ e_1(1+k^2)\cos\gamma(k\cos\alpha-\sin\alpha)=0,\ -e_1(1+k^2)\sin\gamma(\cos\alpha+k\sin\alpha)=0,\\ &i=j=2,\ \ e_1 k\cos\gamma\cos\alpha=0,\ -e_1 k\sin\gamma\sin\alpha=0. \end{aligned} \tag{2.64}$$

The critical angles $\{\alpha_i, \gamma_i\}$ for $i = j = 1$ and 2 are

$$\{\alpha_1,\gamma_1\}=\{\tan^{-1}k,0\},\ \{\alpha_2,\gamma_2\}=\{\frac{\pi}{2},0\}. \tag{2.65}$$

Whether the critical angles in Equation (2.65) produce a maximum or minimum coupling is determined by conditions (i) and (ii):

$$
\begin{aligned}
&i = j = 1, \\
&D_1\big|_{\{\alpha_1,\gamma_1\}} = -e_1(1+k^2)^{3/2},\ D_2\big|_{\{\alpha_1,\gamma_1\}} = e_1^2(1+k^2)^3 > 0, \\
&i = j = 2, \\
&D_1\big|_{\{\alpha_2,\gamma_2\}} = -e_1 k,\ D_2\big|_{\{\alpha_2,\gamma_2\}} = e_1^2 k^2 > 0.
\end{aligned}
\tag{2.66}
$$

According to Equation (2.65), the critical angle at $i = j = 1$ is dependent only on the shear k which is shown in Figure 2.8. Figure 2.8 describes the coupling normalized by the applied true electric field e_1 for $i = j = 1$ at $k = 0.1$ and 0.6 *rad*. In the left of Figure 2.8 ($k = 0.1$), the critical angle exists near to the X_1 axis. This implies that the maximum or minimum coupling can be obtained by aligning the directional vector in the X_1 direction when the shear is small. However, according to the right of Figure 2.8 ($k = 0.6$), the critical angle is strongly dependent on the shear when the shear is not small. As expected, the minimum and maximum couplings are dependent on the polarity of the applied electric field e_1 (see D_1 in Equation (2.66)). For example, when the electro-active fibers or particles are embedded in a certain direction, positive e_1 could produce the contraction and negative e_1 leads to the extension in the X_1 direction. When $i = j = 2$, the critical angle always exists in the X_2 direction ($\{\alpha_2, \gamma_2\}=\{\pi/2, 0\}$) because the shear k is in the X_1 direction. The magnitude of the coupling for $i = j = 2$ is strongly dependent on the amount of shear k in Figure 2.9.

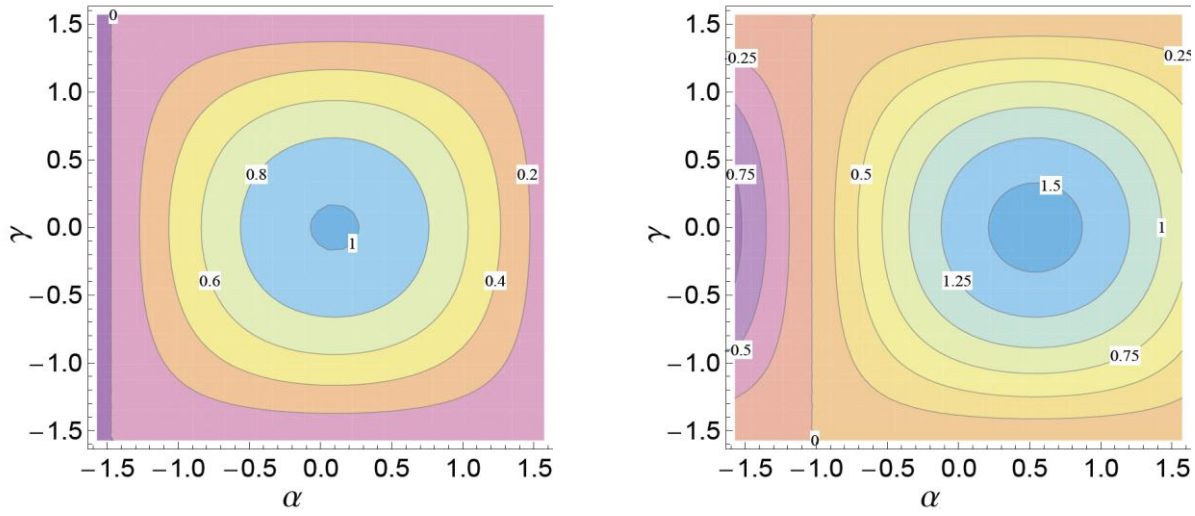

Figure 2.8. Contour plot for the coupling ($i = j = 1$) between one electro-active directional vector a and the electric field e with respect to α and γ for $k = 0.1$ (left) and $k = 0.6$ (right).

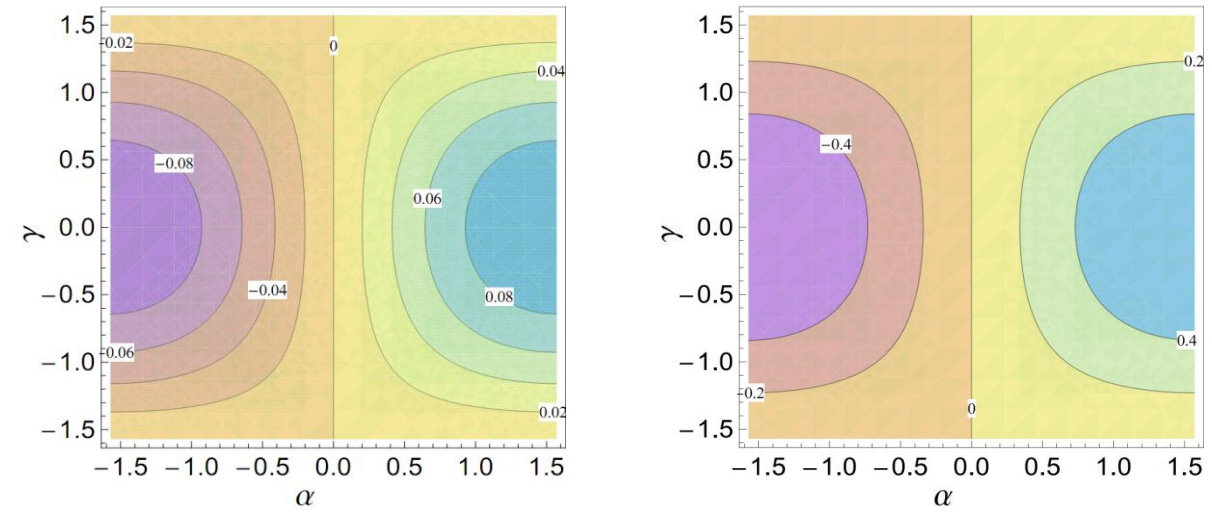

Figure 2.9. Contour plot for the coupling ($i = j = 2$) between one electro-active directional vector a and the electric field e with respect to α and γ for $k = 0.1$ (left) and $k = 0.6$ (right).

B. Coupling between two active directional vectors and the electric field

For the coupling between two electro-active vectors and the electric field, the second derivative test is applied to find the critical angles. The critical angles for the principle directions $i = j = 1$ are calculated using Equation (2.50):

$$\{\alpha_1,\gamma_1\}_1=\{\frac{\pi}{2},\frac{\pi}{4}\},\ \{\alpha_1,\gamma_1\}_2=\{-\frac{\pi}{2},\frac{\pi}{4}\},\ \{\alpha_1,\gamma_1\}_3=\{\frac{\pi}{2},-\frac{\pi}{4}\},\{\alpha_1,\gamma_1\}_4=\{-\frac{\pi}{2},-\frac{\pi}{4}\},$$
$$\beta=-\alpha, \tag{2.67}$$

where $\{\alpha_1, \gamma_1\}_n$ represents the nth critical angle (n = 1, 2, 3, and 4) for $i = j = 1$. Whether the critical angles in Equation (2.67) produce a maximum or minimum coupling is determined by the conditions (i) and (ii):

$$D_2\big|_{\{\alpha_1,\gamma_1\}_1}=D_2\big|_{\{\alpha_1,\gamma_1\}_2}=D_2\big|_{\{\alpha_1,\gamma_1\}_3}=D_2\big|_{\{\alpha_1,\gamma_1\}_4}=16e_1^2(1+k_1^2)^2>0,$$
$$D_1\big|_{\{\alpha_1,\gamma_1\}_1}=D_1\big|_{\{\alpha_1,\gamma_1\}_4}=-2e_1(1+k_1^2),\ D_1\big|_{\{\alpha_1,\gamma_1\}_2}=D_1\big|_{\{\alpha_1,\gamma_1\}_3}=2e_1(1+k_1^2), \tag{2.68}$$

According to Equations (2.66) and (2.67), the specific angles for the maximum or minimum coupling are decided by the polarity of the applied electric field. As expected in Equation (2.67), the direction of the coupling is reversed by changing the electric polarity. Similar to the result of the coupling in Section 2.5.5, the critical angles in Equation (2.66) maximizes the cross product of ***a*** and ***b*** along with the X_1 direction such that the magnitude of the coupling is maximized. Physically, the directional vectors ***a*** and ***b*** are not affected by the shear in the X_1 direction because ***a*** and ***b*** are aligned in the X_2 direction (α and $\beta = \pi/2$ (or $-\pi/2$)). Since the coupling is the cross product of ***a*** and ***b***, the critical angles for the coupling is not dependent on the shear k in the X_1 direction, which is shown in Figure 2.10. As expected, the magnitude of the coupling depends on the amount of shear k.

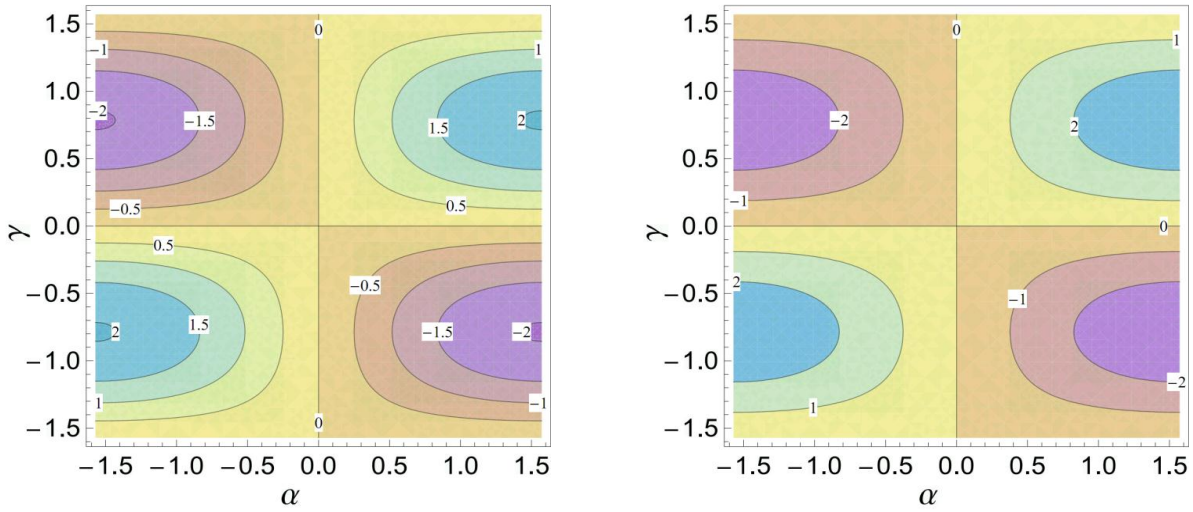

Figure 2.10. Contour plot for the coupling ($i = j = 1$) between two electro-active directional vector a and b and the electric field e with respect to α and γ for $k = 0.1$ (left) and $k = 0.6$ (right).

2.6. Conclusion

In this chapter, a nonlinear constitutive law for anisotropic electro-elastic materials is formulated by using a continuum mechanics framework. The anisotropic electro-elastic material is considered as an isotropic continuum with electro-active and passive fibers or particles embedded, which are defined by directional unit vectors. The free energy function for the electro-elastic material is assumed to be invariant-based. The invariants for describing the coupling between the electro-active directional vectors and electric field are developed by adopting the approach of Spencer and Rivlin [8-10] and Pipkin and Rivlin [13]. The coupling between the electro-active directional vectors and the applied electric field was analyzed with respect to the orientation of the directional vector and polarity and magnitude of the applied electric field. The conditions on the electro-active directional vectors and the applied electric field for maximizing and minimizing the coupling were investigated in two simple examples (equi-biaxial extension and simple shear). The results indicate that the magnitude and direction

of the coupling is significantly dependent on the boundary conditions, the orientation of the directional vectors, and the polarity of the applied electric field.

2.7. References

1. Dorfmann, A. and R.W. Ogden, *Nonlinear electroelasticity*. Acta Mechanica, 2005: p. 167-83.
2. Dorfmann, A. and R.W. Ogden, *Nonlinear electroelastic deformations.* Journal of Elasticity, 2006: p. 99-127.
3. Rajagopal, K.R. and A. Wineman, *A constitutive equation for non-linear electro-active solids.* Acta Mechanica, 1999: p. 219-28.
4. Bustamante, R., *Transversely isotropic non-linear electro-active elastomers.* Acta Mechanica, 2009: p. 237-259.
5. Green, A.E. and J.E. Adkins, *Large Elastic Deformation*. 1970, London: Oxford University Press.
6. Ogden, R.W., *Large Deformation Isotropic Elasticity - On the Correlation of Theory and Experiment for Incompressible Rubberlike Solids.* Philosophical Transactions of the Royal Society of London. Series A, 1972: p. 398-416.
7. Weiss, J.A., B.N. Maker, and S. Govindjee, *Finite element implementation of incompressible, transversely isotropic hyperelasticity.* Computer Methods in Applied Mechanics and Engineering, 1996: p. 107-28.
8. Spencer, A.J.M. and R.S. Rivlin, *Isotropic integrity bases for vectors and second-order tensors.* Archive for Rational Mechanics and Analysis, 1962: p. 45-63.
9. Spencer, A.J.M., *Isotropic integrity bases for vectors and second-order tensors.* Archive for Rational Mechanics and Analysis, 1965: p. 51-82.
10. Spencer, A.J.M., *Theory of invariants*, in *Continuum Physics volume 1: Mathematics*. 1971, Academic: London, UK. p. 239-55.
11. Spencer, A.J.M., *Continuum Theory of the Mechanics of Fibre-Reinforced Composites*. 1984, New York: Springer-Verlag.
12. Pipkin, A. and R. Rivlin, *The formulation of constitutive equations in continuum physics. I.* Archive for Rational Mechanics and Analysis, 1959: p. 129-144.
13. Pipkin, A.C. and R.S. Rivlin, *Electrical, thermal and magnetic constitutive equations for deformed isotropic materials.* Atti della Accademia Nazionale dei Lincei. Rendiconti, Classe di Scienze Fisiche, Matematiche e Naturali, 1966: p. 3-29.
14. Son, S. and N.C. Goulbourne, *Finite Deformations of Tubular Dielectric Elastomer Sensors.* Journal of Intelligent Material Systems and Structures, 2009: p. 2187-2199.
15. Son, S. and N.C. Goulbourne, *Dynamic response of tubular dielectric elastomer transducers.* International Journal of Solids and Structures, 2010: p. 2672-2679.
16. Son, S. and D.N.C. Goulbourne, *Large Strain Analysis of a Soft Polymer Electromechanical Sensor Coupled to an Arterial Segment.* Journal of Intelligent Material Systems and Structures, 2011: p. (Submitted).

17. Holzapfel, G.A., T.C. Gasser, and R.W. Ogden, *A new constitutive framework for arterial wall mechanics and a comparative study of material models.* Journal of Elasticity, 2000: p. 1-48.
18. Gasser, T.C., R.W. Ogden, and G.A. Holzapfel, *Hyperelastic modelling of arterial layers with distributed collagen fibre orientations.* Journal of the Royal Society Interface, 2006: p. 15-35.
19. Eringen, A.C., *Nonlinear Theory of Continuous Media*. 1962, New York: McGraw-Hill Book Company.
20. Toupin, R.A., *The elastic dielectric.* Archive for Rational Mechanics and Analysis, 1956: p. 849-915.
21. Marsden, J.E. and T.J.R. Hughes, *Mathematical Foundations of Elasticity*. 1983, Englewood Cliffs, NJ: Prentice-Hall.
22. Thomas, G.B.J. and R.L. Finney, *Calculus and Analytic Geometry*. 1992, Reading, MA: Addison-Wesley.

Chapter 3. Electromechanical Stability Conditions for Electro-Elastic Materials

The main objective of this section is to investigate the numerical stability of the proposed constitutive models for electro-elastic materials. When using finite element modeling, numerical stability is a crucial consideration in obtaining converged solutions of initial and boundary value problems. Stability is dependent on the mechanical and electrical material properties, the boundary conditions and external forces (mechanical or electrical stimulus). Stability therefore depends on the form of the strain energy function, which is oftentimes invariant based. The invariants can be either convex or non-convex, which ultimately will affect the stability of the strain energy function. In this chapter, only invariant-based free energy functions are considered and the stability of the electro-elastic material is examined using the concepts of convexity and polyconvexity.

The convexity of the invariants which are involved in the deformation gradient, the directional vectors and the electric field vector as well as the polyconvexity of the invariant-based free energy function for electro-elastic materials are examined using the convexity and the polyconvexity conditions, which have been developed formally by Hill [1] and Ball [2]. The conditions are mainly based on the direct method of the variational principle, finding a minimizing deformation of the electro-elastic strain energy subject to specified boundary conditions. The set of invariants, which are also called the irreducible integrity bases, are

obtained by adopting the invariant theoretical formulations previously derived by Spencer, Pipkin and Rivlin [3-7] described in Chapter 2.

The direct method in calculus of variations is used for proving the existence of equilibrium solutions of the free energy function $W(\boldsymbol{F})$ with given boundary conditions. If the function is finite-valued and continuous, an important relationship can be summarized

$$convexity \Rightarrow polyconvexity \Rightarrow quasiconvexity \Rightarrow rank-one\ convexity.$$

This says that a convex function is polyconvex, a polyconvex function is also quasiconvex, and a quasiconvex function is also rank-one convex, but the converse relationship is not true. A convex free energy function with respect to the deformation gradient $\boldsymbol{F}$ leads to a unique equilibrium solution under specific boundary conditions (the concept of convexity is presented in Section 3.1). In nonlinear elasticity, there is in general no unique solution to boundary-value problems, and it is also not guaranteed that solutions always exist. To examine the existence of solutions when considering finite deformations, Morrey introduced the concept of quasiconvexity. This was formulated as an integral inequality over an arbitrary domain subject to Dirichlet boundary conditions (the concept of quasiconvexity is introduced in Section 3.2) [8]. However, since quasiconvexity is formulated as an integral inequality, it is difficult to show the existence of solutions by using quasiconvexity. In order to overcome this limitation, Ball proposed the polyconvexity condition which is a more practical method for proving the existence of the equilibrium solutions [2]. According to Ball's approach, the polyconvexity of a free energy function is proven by showing that that function is convex with respect to the argument ($\boldsymbol{F}$, cof[$\boldsymbol{F}$] and det[$\boldsymbol{F}$]), which represent the mappings of the line, area and volume elements, respectively. Ball demonstrated the polyconvexity of several isotropic strain energy functions,

namely the *Neo*-Hookean, Mooney-Rivlin, and Ogden models [2]. He modified the class of strain energy functions $W(\boldsymbol{F})$ introduced by Ogden [9] to be

$$W(\boldsymbol{F}) = B + \sum_{k=1}^{M} b_k \psi(\alpha_k) + \sum_{k=1}^{N} c_k \chi(\beta_k)$$
$$\psi(\alpha) = F_{11}^{\alpha} + F_{22}^{\alpha} + F_{33}^{\alpha} - 3, \chi(\beta) = (F_{22}F_{33})^{\beta} + (F_{11}F_{33})^{\beta} + (F_{11}F_{22})^{\beta} - 3 \tag{3.1}$$

where $\alpha_1 \geq \cdots \geq \alpha_M \geq 1$, $\beta_1 \geq \cdots \geq \beta_N \geq 1$, B is arbitrary constant and F_{ij} is the component of the deformation gradient $\boldsymbol{F}$ (i and j = 1, 2 and 3). The polyconvexity condition for $W(\boldsymbol{F})$ was determined to be

$$\alpha_1 \geq 2, \ \frac{1}{\alpha_1} + \frac{1}{\beta_1} \leq 1. \tag{3.2}$$

The special cases, $B = 0$, $M = N = 1$, $\alpha_1 = \beta_1 = 2$ and $B = 0$, $c_k = 0$ represent the Mooney-Rivlin [10] and Ogden models, respectively.

For isotropic materials, Raoult [11], Steigmann [12], and Schrőder and Neff [13, 14] investigated polyconvexity of the free energy function for the material following Ball's approach. Raoult employed a Saint Venant-Kirchhoff model for a hyperelastic material,

$$W(\boldsymbol{F}) = a_1 \mathrm{tr}[\boldsymbol{F}^T\boldsymbol{F}] + a_2 \mathrm{tr}[\boldsymbol{F}^T\boldsymbol{F}]^2 + b_1 \mathrm{tr}[\mathrm{cof}[\boldsymbol{F}^T\boldsymbol{F}]]. \tag{3.3}$$

He showed that the Saint Venant-Kirchhoff model $W(\boldsymbol{F})$ is not polyconvex if $a_1 < 0$ but $W(\boldsymbol{F})$ is polyconvex if all coefficients a_1, a_2 and b_1 are nonnegative [11]. Steigmann inspected the convexity of the invariants for the isotropic material. He introduced a new set $\{i_k\}$ which is derived from the invariants for isotropic materials as

$$i_1 = \mathrm{tr}[\boldsymbol{U}], \ i_2 = \mathrm{tr}[\mathrm{cof}[\boldsymbol{U}]], \ i_3 = \mathrm{det}[\boldsymbol{U}], \tag{3.4}$$

where I_1, I_2 and I_3 have been introduced in Chapter 2 and $\boldsymbol{U}$ is the unique positive symmetric right stretch tensor and square root of $\boldsymbol{C}$ [12]. The convexity of i_1, i_2 and i_3 were established with respect to $\boldsymbol{F}$, cof[$\boldsymbol{F}$] and det[$\boldsymbol{F}$], respectively. Steigmann also proved the polyconvexity of an additive form of the invariant-based strain energy function

$$W(i_1, i_2, i_3) = W(i_1) + W(i_2) + W(i_3), \tag{3.5}$$

where $W(i_1)$, $W(i_2)$ and $W(i_3)$ are convex with respect to $\boldsymbol{F}$, cof[$\boldsymbol{F}$] and det[$\boldsymbol{F}$], respectively [12]. Schrőder and Neff proved the convexity of the invariants I_1, I_2 and I_3 by using Ball's approach [13, 14]. Also, they introduced several additive and multiplicative combinations of the invariants between I_1, I_2 and I_3 for developing polyconvex invariant-based strain energy functions.

For anisotropic materials, a polyconvex strain energy function was introduced by Schrőder and Neff [13, 14]. They proved the convexity of the invariants (I_4, I_5, I_6, I_7, I_8 and I_9) for anisotropic materials and developed a polyconvex anisotropic invariant-based strain energy function by taking a linear combination of the convex invariants. Based on the proposed polyconvex strain energy function, they derived a constitutive formulation for anisotropic materials, and two numerical examples were presented for describing the constitutive equations with specific boundary conditions (biaxial extension and a 3-dimensional tapered cantilever) [13, 14].

Rogers and Antman adopted Ball's approach to prove polyconvexity of the free energy function for electro-magneto-thermo-elastic materials [15]. According to their work, the polyconvex function for an electro-magneto-thermo elastic material is expressed as

$$W(\boldsymbol{F}, \boldsymbol{E}, \boldsymbol{H}) = g(\boldsymbol{F}, \mathrm{cof}[\boldsymbol{F}], \det[\boldsymbol{F}], \boldsymbol{E}, \boldsymbol{H}), \tag{3.6}$$

with g convex with respect to the independent variables $\boldsymbol{F}$, cof[$\boldsymbol{F}$], det[$\boldsymbol{F}$], $\boldsymbol{E}$ and $\boldsymbol{H}$, where $\boldsymbol{E}$ and $\boldsymbol{H}$ are electric and magnetic fields.

The numerical stability of dielectric elastomers (DEs) has been investigated by Zhao and Suo [16-18], Xu *et al.* [19] and Leng *et al.* [20]. Based on considerations of virtual work, they derived the elastic stress and the electric displacement with respect to the deformation gradients and the gradient of electric potential, respectively. The electromechanical stability of a dielectric elastomer (DE) was examined by using a general convexity condition, for which the Hessian

matrix must be positive definite in the equilibrium state [16-18]. Zhao and Suo showed that the free energy function for the DEs (an isotropic electro-elastic material) is typically non-convex and causes the material to undergo one of three possible unstable states such as wrinkling when two states coexist and a discontinuous transition is made from a thick to thin state. Based on Zhao and Suo's approach to electromechanical stability of DEs, Xu *et al.* [19] and Leng *et al.* [20] presented the critical nominal electric field, nominal stresses and principal stretches for the electromechanical stability of DEs under biaxial extension.

In this chapter, polyconvexity of invariant-based free energy functions for electro-elastic materials under equibiaxial extension is investigated using Ball's, and Rogers and Antman's approaches [2, 15]. In Sections 3.1 and 3.2, the concepts of convexity and quasiconvexity will be presented, respectively. In Section 3.3, the general and strict polyconvexity conditions for pure elastic and electro-elastic materials will be described. Based on the convexity condition in Section 3.1, convexity of the invariants for the nominal electric field and the electro-active directional vectors will be proved in Section 3.4. In Section 3.5, the polyconvexity conditions for isotropic and anisotropic electro-elastic materials will be obtained using the polyconvexity condition in Section 3.3.

3.1. Convexity Conditions

In order to find a minimizing deformation of the free energy $W(\boldsymbol{F})$ subject to specific boundary condition, the method of variations is the main mathematical treatment. A sufficient condition for the existence of minimizers can be obtained by using the concepts of convexity, quasiconvexity and polyconvexity. The convexity of a function with respect to its different arguments plays a major role in determining the mathematical stability of the function. Let us

first consider a scalar-valued function $f(x)$ depicted in Figure 1.2 The function $f(x)$ is convex with respect to x if

$$f(\lambda x_1 + (1-\lambda)x_2) \le \lambda f(x_1) + (1-\lambda) f(x_2), \tag{3.7}$$

where $(x_1, x_2) \subset x, x_1 \ne x_2, \lambda \in [0,1]$.

Figure 1.2describes the geometric interpretation of Equation (3.7). The point C which exists on a straight line between A and B is always above D. The geometry of each point is given as

$$A = f(x_1),\ B = f(x_2),\ C = \lambda A + (1-\lambda)B,\ D = f(\lambda x_1 + (1-\lambda)x_2). \tag{3.8}$$

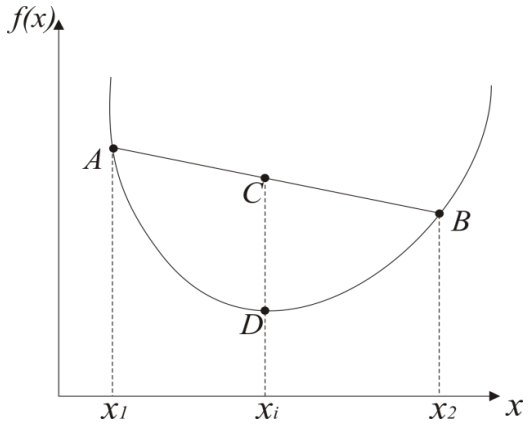

Figure 3.1. Geometric interpretation of the convexity condition.

If the first or second derivatives $f'(x)$ and $f''(x)$ exist for each x, the convexity condition can be reformulated from Figure 1.2

$$\begin{aligned} &\frac{f(x_2) - f(x_1)}{x_2 - x_1} \ge f'(x_1), \quad \frac{f(x_1) - f(x_2)}{x_1 - x_2} \ge f'(x_2) \\ &\{f'(x_1) - f'(x_2)\}(x_1 - x_2) \ge 0. \end{aligned} \tag{3.9}$$

Alternatively, Equation (3.9) becomes

$$f''(x) \ge 0. \tag{3.10}$$

Therefore, the twice differentiable scalar valued free energy function $W(\boldsymbol{F})$ is convex with respect to $\boldsymbol{F}$ if

$$W''(\boldsymbol{F}) \geq 0. \tag{3.11}$$

The convexity condition with respect to the deformation gradient $\boldsymbol{F}$ in Equation (3.11) guarantees the unique solution, which means that a local minimum is always a global minimum. A drawback of the convexity condition is that it is physically too restrictive. That is to say, since the convexity condition of the free energy function precludes instable solutions, the stability of problems cannot be analyzed. Therefore, W needs not be strictly convex for including the non-unique solution for the description of instability. One suitable condition is quasiconvexity, which was introduced by Morrey [8]. The concept of quasiconvexity is introduced in Section 3.2.

3.2. Quasiconvexity Conditions

The mathematical criterion of material stability states that it is impossible to release energy from a body made of a stable and homogeneous thermo-elastic material by an isothermal process if the body is fixed at the boundaries [8]. This condition can be formulated for the case of hyperelasticity as

$$\int_{t_0}^{t}\int_{\Omega} \frac{\partial W(\boldsymbol{F})}{\partial \boldsymbol{F}} : \frac{\partial \boldsymbol{F}}{\partial t}\, dV dt \geq 0, \tag{3.12}$$

with homogeneous Dirichlet boundary conditions, where Ω and $[t, t_0]$ represent the space and time domains.

The deformation gradient and free energy at the initial time t_0 over Ω are denoted as $\hat{\boldsymbol{F}}$ and $W(\boldsymbol{F},t_0)=W(\hat{\boldsymbol{F}})$. Performing the time integration, Equation (3.12) becomes

$$\int_\Omega W(\boldsymbol{F})dV-\int_\Omega W(\hat{\boldsymbol{F}})dV\geq 0. \tag{3.13}$$

The first term in Equation (3.13) describes a state at time *t*. The deformation gradient $\boldsymbol{F}$ at *t* can be rewritten using an arbitrary fluctuation field $\boldsymbol{w}$,

$$\boldsymbol{F}=\hat{\boldsymbol{F}}+\nabla\boldsymbol{w}. \tag{3.14}$$

where $\nabla\boldsymbol{w}$ represents the gradient of $\boldsymbol{w}$. By inserting Equation (3.14) into (3.13), the quasiconvexity condition which has been introduced by Morrey [8] is obtained,

$$\int_\Omega W(\hat{\boldsymbol{F}}+\nabla\boldsymbol{w})dV\geq\int_\Omega W(\hat{\boldsymbol{F}})dV. \tag{3.15}$$

Note that the inequality in Equation (3.15) holds for arbitrary fluctuations $\boldsymbol{w}$. The quasiconvexity condition in Equation (3.15) implies that any homogeneous body for any displacement boundary value problem allow a possible homogeneous strain which should be an absolute minimizer for the total energy. Morrey showed that if $W(\boldsymbol{x})$ is quasiconvex for every argument *x*, there exist minimizers for various boundary value problems [8]. This condition is relatively difficult to verify due to the fact that it characterizes an integral inequality, and a more tractable condition is required.

3.3. Polyconvexity Condition

Morrey introduced a more suitable condition than convexity (quasiconvexity), which ensures the minimizers of a function for various boundary value problems [8]. However, as already mentioned in Section 3.2, since the quasiconvexity condition in Equation (3.15) is a non-local integral inequality, proving quasiconvexity of an explicit free energy function is rather

complicated to handle. So, Ball introduced the notion of polyconvexity, which is more practical than quasiconvexity [2]. The polyconvexity condition is also equivalent to a sufficient condition for quasiconvexity given by Morrey [8].

Based on physical considerations, it is implied that extreme strains lead to infinite stress. That is to say, if a material is extremely compressed ($J \to 0$, where $J = \det[\boldsymbol{F}]$) or stretched ($J \to \infty$), large stresses is produced. This physical observation can be summarized using the arguments $\boldsymbol{F}$, cof[$\boldsymbol{F}$] and det[$\boldsymbol{F}$]

$$\begin{aligned} &W(\boldsymbol{F}) \to \infty, \ \text{ if } \det[\boldsymbol{F}] \to 0, \\ &W(\boldsymbol{F}) \to \infty, \ \text{ if } (\|\boldsymbol{F}\| + \|\text{cof}[\boldsymbol{F}]\| + \det[\boldsymbol{F}]) \to \infty, \\ &\|\boldsymbol{F}\| = \sqrt{\boldsymbol{F} : \boldsymbol{F}}, \ \ \|\text{cof}[\boldsymbol{F}]\| = \sqrt{\text{tr}[\text{cof}[\boldsymbol{F}]^T \cdot \text{cof}[\boldsymbol{F}]}. \end{aligned} \tag{3.16}$$

Equation (3.16) can be replaced by the coerciveness inequality

$$W(\boldsymbol{F}) \geq \alpha\{\|\boldsymbol{F}\|^p + \|\text{cof}[\boldsymbol{F}]\|^q + (\det[\boldsymbol{F}])^r\} + \beta, \tag{3.17}$$

where α, β, p, q and $r > 0$. Ball combined this result with the calculus of variations to establish the existence of minimizers for a free energy function [2]. According to Ball's approach [2], the free energy function of an elastic material is defined as

$$W = g(\boldsymbol{F}, \text{cof}[\boldsymbol{F}], \det[\boldsymbol{F}]), \tag{3.18}$$

where cof[$\boldsymbol{F}$] is the cofactor of the deformation gradient $\boldsymbol{F}$.

$W(\boldsymbol{F})$ is polyconvex if g is convex with respect to each variable ($\boldsymbol{F}$, cof[$\boldsymbol{F}$] and det[$\boldsymbol{F}$]).

In other words, by adopting Equation (3.7), polyconvexity of the free energy function $W(\boldsymbol{F})$ is satisfied if

$$\begin{aligned} &W(\lambda(\boldsymbol{F}_1, \text{cof}[\boldsymbol{F}_1], \det[\boldsymbol{F}_1]) + (1-\lambda)(\boldsymbol{F}_2, \text{cof}[\boldsymbol{F}_2], \det[\boldsymbol{F}_2])) \leq \lambda W(\boldsymbol{F}_1, \text{cof}[\boldsymbol{F}_1], \det[\boldsymbol{F}_1]) \\ &+ (1-\lambda) W(\boldsymbol{F}_2, \text{cof}[\boldsymbol{F}_2], \det[\boldsymbol{F}_2]), \end{aligned} \tag{3.19}$$

where $\boldsymbol{F}_1 \neq \boldsymbol{F}_2, \lambda \in [0,1]$.

It is further assumed that W can be decomposed into

$$W = g_1(\boldsymbol{F}) + g_2(\text{cof}[\boldsymbol{F}]) + g_3(\det[\boldsymbol{F}]). \tag{3.20}$$

Strictly, W is polyconvex if g_1, g_2 and g_3 are convex with respect to the independent variables $\boldsymbol{F}$, cof[$\boldsymbol{F}$] and det[$\boldsymbol{F}$], respectively [13, 14]. If the free energy function for an anisotropic material is assumed to be a linear combination of invariants, Equations (3.18) and (3.20) can be rewritten as

$$\begin{aligned} W &= g(I_1, I_2, I_3, I_4, I_5, I_6, I_7, I_8, I_9), \\ W &= g_1(I_1) + g_2(I_2) + g_3(I_3) + g_4(I_4) + g_5(I_5) + g_6(I_6) + g_7(I_7) + g_8(I_8) + g_9(I_9), \end{aligned} \tag{3.21}$$

where W is polyconvex if g_i, (i = 1,…,9) are convex with respect to the independent variables $\boldsymbol{F}$, cof[$\boldsymbol{F}$] and det[$\boldsymbol{F}$]. Note that I_2 and I_3 are functions of cof[$\boldsymbol{F}$] and det[$\boldsymbol{F}$], respectively, and the rest of the invariants (I_1, I_4, I_5, I_6, I_7, I_8 and I_9) are only functions of $\boldsymbol{F}$.

Rogers employed Ball's approach [2] for investigating polyconvexity of electro-elastic materials [15]. According to Rogers and Antman's work, the coerciveness inequality for the electro-elastic material becomes similar to Equation (3.17)

$$W(\boldsymbol{F}) \geq \alpha\{\|\boldsymbol{F}\|^p + \|\text{cof}[\boldsymbol{F}]\|^q + (\det[\boldsymbol{F}])^r + \|\boldsymbol{E}\|^s\} + \beta, \tag{3.22}$$

where α, β, p, q, r and $s > 0$. Therefore, W for isotropic electro-elastic materials is said to be polyconvex if it can be written in the form

$$W(\boldsymbol{F}, \boldsymbol{E}) = g(\boldsymbol{F}, \text{cof}[\boldsymbol{F}], \det[\boldsymbol{F}], \boldsymbol{E}), \tag{3.23}$$

with g convex for each independent variable $\boldsymbol{F}$, cof[$\boldsymbol{F}$], det[$\boldsymbol{F}$] and $\boldsymbol{E}$. Equation (3.23) represents the general polyconvexity condition for electro-elastic materials.

Under the assumption that the free energy function for an electro-elastic material is a linear combination of the invariants similar to Equation (3.21), Equation (3.23) becomes

$$\begin{aligned} W &= g(I_1, I_2, I_3, I_4, I_5, I_6, I_7, I_8, I_9, I_{10}, I_{11}, I_{12}, I_{13}, I_{14}, I_{15}, I_{16}, I_{17}, I_{18}, I_{19}), \\ W &= g_1(I_1) + g_2(I_2) + g_3(I_3) + \ldots + g_{17}(I_{17}) + g_{18}(I_{18}) + g_{19}(I_{19}), \end{aligned} \tag{3.24}$$

where W is polyconvex if g_i, (i = 1,…,19) are convex with respect to the independent variables $\boldsymbol{F}$, cof[$\boldsymbol{F}$], det[$\boldsymbol{F}$] and $\boldsymbol{E}$. Note that I_i, (i = 10,…,19) are functions of $\boldsymbol{F}$ and $\boldsymbol{E}$. Equation (3.24)

represents the strict polyconvexity condition for electro-elastic materials. If the invariant-based free energy function for electro-elastic material does not satisfy the strict polyconvexity condition in Equation (3.24), the general polyconvexity condition for the free energy function can be obtained using Equation (3.23). That is to say, since the strict polyconvexity in Equation (3.24) cannot be satisfied when non-convex invariants in the free energy function exist; the polyconvexity should be investigated by using the general polyconvexity condition in Equation (3.23).

Equations (3.18)–(3.24) can be adopted for investigating polyconvexity of electro-elastic materials which are described with an invariant-based free energy function. In the literature, the convexity of the general invariants for isotropic and transversely isotropic materials (I_i, (i = 1,…,9)) has been investigated and proven by Schrőder and Neff [13, 14], Steigmann [21] and Hartmann and Neff [22]. They developed a polyconvex strain energy function using a set of the convex invariants .

Based on the polyconvexity condition in Equations (3.23) and (3.24), the polyconvexity of the anisotropic free energy function $W = W(I_1, I_2, I_3, I_4,\ldots, I_{19})$ is investigated by proving the convexity of the invariants (I_i, (i = 1,…,19)) with respect to the independent variables ($\boldsymbol{F}$, cof[$\boldsymbol{F}$], det[$\boldsymbol{F}$] and $\boldsymbol{E}$). In Section 3.4, the convexity of the coupling invariants (I_i, (i = 10,…,19)) under equi-biaxial extension is investigated by using the convexity condition in Equation (3.11). Note that the independent variables ($\boldsymbol{F}$, cof[$\boldsymbol{F}$], det[$\boldsymbol{F}$] and $\boldsymbol{E}$) are dependent on the boundary conditions.

3.4. Convexity of Invariants

In this section, the convexity of the coupling invariants (I_i, (i = 1,…,19)) for electro-elastic materials, which were introduced in Chapter 2 is inspected. To simplifying the formulation, we consider equi-biaxial extension of an anisotropic electro-elastic material with two electro-active directional vectors $\boldsymbol{a}$, $\boldsymbol{b}$ and an applied nominal electric field $\boldsymbol{E}$. The deformation gradient, directional vectors, and nominal electric field under equi-biaxial extension with the assumption of material incompressibility are given as

$$\boldsymbol{F} = \begin{pmatrix} F_{11} & 0 & 0 \\ 0 & F_{11} & 0 \\ 0 & 0 & 1/F_{11}^2 \end{pmatrix}, \boldsymbol{a} = \{\cos\gamma\cos\alpha, \cos\gamma\sin\alpha, \sin\gamma\},\ \boldsymbol{b} = \{\cos\gamma\cos\beta, \cos\gamma\sin\beta, \sin\gamma\},\ \boldsymbol{E} = \{0,0,E_3\}, \tag{3.25}$$

where it is assumed that the angles α, β and γ are dependent and F_{11} and E_3 are independent variables for equi-biaxial extension. With Equation (2.54), the polyconvexity condition can be rewritten to state that W in Equation (3.24) is strictly polyconvex if g_i, (i = 1,…,19) are convex with respect to the independent variables F_{11} and E_3. Note that the polyconvexity condition and the independent variables are dependent on the boundary conditions. Since the convexity of (I_i, (i = 1,…,9)) has already been proved by Schrőder and Neff [13, 14], Steigmann [21] and Hartmann and Neff [22]. The convexity of I_i, (i = 1,…,19) will now be examined using the convexity condition in Equation (3.11). The invariants I_i, (i = 1,…,19) were introduced in Chapter 2.

The second derivative of the invariants $I_1,\ldots,I_9$ with respect to the independent variable F_{11} is written as

$$\frac{\partial^2 I_1}{\partial F_{11}^2} = 4 + \frac{20}{F_{11}^6} > 0, \quad \frac{\partial^2 I_2}{\partial F_{22}^2} = 12F_{11}^2 + \frac{12}{F_{11}^4} > 0,$$
$$\frac{\partial^2 I_4}{\partial F_{11}^2} = \frac{\partial^2 I_6}{\partial F_{11}^2} = \frac{\partial^2 I_8}{\partial F_{11}^2} = 2\cos^2\gamma + \frac{20\sin^2\gamma}{F_{11}^6} > 0, \tag{3.26}$$
$$\frac{\partial^2 I_5}{\partial F_{11}^2} = \frac{\partial^2 I_7}{\partial F_{11}^2} = \frac{\partial^2 I_9}{\partial F_{11}^2} = 12F_{11}^2\cos^2\gamma + \frac{72\sin^2\gamma}{F_{11}^{10}} > 0.$$

Equation (3.26) implies that $I_1,\ldots,I_9$ are convex with respect to F_{11}.

The second derivative of the invariants I_{10}, I_{11} and I_{12} with respect to the independent variables F_{11} and E_3 is written as

$$\frac{\partial^2 I_{10}}{\partial E_3^2} = 2 > 0,$$
$$\frac{\partial^2 I_{11}}{\partial \xi_i\, \partial \xi_j} = \begin{pmatrix} 12E_3^2F_{11}^2 & 8E_3F_{11}^3 \\ 8E_3F_{11}^3 & 2F_{11}^4 \end{pmatrix}, \det\left[\frac{\partial^2 I_{11}}{\partial \xi_i\, \partial \xi_j}\right] = -40E_3^2F_{11}^6 < 0, \tag{3.27}$$
$$\frac{\partial^2 I_{12}}{\partial \xi_i\, \partial \xi_j} = \begin{pmatrix} 56E_3^2F_{11}^6 & 16E_3F_{11}^7 \\ 16E_3F_{11}^7 & 2F_{11}^8 \end{pmatrix}, \det\left[\frac{\partial^2 I_{12}}{\partial \xi_i\, \partial \xi_j}\right] = -144E_3^2F_{11}^{14} < 0,$$
$$\xi_1 = F_{11},\ \xi_2 = E_3.$$

It is therefore seen that I_{10} is convex with respect to E_3, but I_{11} and I_{12} are not convex with respect to F_{11} and E_3. Except for I_{13}, I_{15} and I_{17}, the coupling invariants I_{14}, I_{16}, I_{18} and I_{19} are also not convex with respect to F_{11} and E_3:

$$
\begin{aligned}
&\xi_1 = F_{11},\ \xi_2 = E_3,\ \frac{\partial^2 I_{13}}{\partial E_3^2} = \frac{\partial^2 I_{15}}{\partial E_3^2} = \frac{\partial^2 I_{17}}{\partial E_3^2} = 0,\\
&\frac{\partial^2 I_{14}}{\partial \xi_i\, \partial \xi_j} = \frac{\partial^2 I_{16}}{\partial \xi_i\, \partial \xi_j} = \begin{pmatrix} \dfrac{20E_3 \sin\gamma}{F_{11}^6} & -\dfrac{4\sin\gamma}{F_{11}^5} \\ -\dfrac{4\sin\gamma}{F_{11}^5} & 0 \end{pmatrix},\ \det\left[\frac{\partial^2 I_{14}}{\partial \xi_i\, \partial \xi_j}\right] = \det\left[\frac{\partial^2 I_{16}}{\partial \xi_i\, \partial \xi_j}\right] = -\frac{16\sin^2\gamma}{F_{11}^{10}} < 0,\\
&\frac{\partial^2 I_{18}}{\partial \xi_i\, \partial \xi_j} = \begin{pmatrix} \dfrac{-20E_3\cos^2\gamma\sin(\alpha-\beta)}{F_{11}^5} & \dfrac{4\cos^2\gamma\sin(\alpha-\beta)}{F_{11}^5} \\ \dfrac{4\cos^2\gamma\sin(\alpha-\beta)}{F_{11}^5} & 0 \end{pmatrix}, \det\left[\frac{\partial^2 I_{18}}{\partial \xi_i\, \partial \xi_j}\right] = -\frac{16\cos^4\gamma\sin^2(\alpha-\beta)}{F_{11}^{10}} < 0,\\
&\frac{\partial^2 I_{19}}{\partial \xi_i\, \partial \xi_j} = \begin{pmatrix} \dfrac{-72E_3\cos^2\gamma\sin(\alpha-\beta)}{F_{11}^5} & \dfrac{4\cos^2\gamma\sin(\alpha-\beta)}{F_{11}^5} \\ \dfrac{4\cos^2\gamma\sin(\alpha-\beta)}{F_{11}^5} & 0 \end{pmatrix}, \det\left[\frac{\partial^2 I_{19}}{\partial \xi_i\, \partial \xi_j}\right] = -\frac{64\cos^4\gamma\sin^2(\alpha-\beta)}{F_{11}^{18}} < 0.
\end{aligned}
\tag{3.28}
$$

According to Equations (3.27) and (3.28), since the invariants for the electro-active directional vectors $\boldsymbol{a}$, $\boldsymbol{b}$ and nominal electric field $\boldsymbol{E}$ are not convex with respect to F_{11} and E_3 excepting for I_{10}, I_{13}, I_{15} and I_{17}, the polyconvexity of an invariant based free energy function which is a linear combination of I_1, I_2, I_3, I_4,…, I_{19} with respect to F_{11} and E_3 is not satisfied by using the strict polyconvexity condition in the second of Equation (3.24). Therefore, by applying the general polyconvexity condition in Equation (3.23), the general polyconvexity condition for the electro-elastic material under equi-biaxial extension is derived in Section 3.5.

3.5. Polyconvexity of Invariant-based Free Energy Functions

In order to ensure polyconvexity of a free energy function which is a linear combination of convex and non-convex invariants (I_{11}, I_{12}, I_{14}, I_{16}, I_{18} and I_{19}), an explicit condition can be

obtained by employing the general polyconvexity condition in Equation (3.23). The free energy function under equi-biaxial extension, in which the deformation gradients, the directional vectors and the electric field are defined in Equation (2.54) are given as

$$\begin{aligned} W &= W(I_1, I_2, I_3, I_4, I_5, I_6, I_7, I_8, I_9, I_{10}, I_{11}, I_{12}, I_{13}, I_{14}, I_{15}, I_{16}, I_{17}, I_{18}, I_{19}) \\ &= g(F_{11}, E_3), \end{aligned} \tag{3.29}$$

Similar to Equations (3.18) and (3.23), W is said to be polyconvex if g is convex with respect to F_{11} and E_3.

An explicit condition for the convexity of g under equibiaxial extension with respect to F_{11} and E_{n3} can be obtained by employing the general convexity condition in Equation (3.11):

$$H = \begin{bmatrix} \dfrac{\partial^2 W}{\partial F_{11}^2} & \dfrac{\partial^2 W}{\partial F_{11}\partial E_3} \\ \dfrac{\partial^2 W}{\partial F_{11}\partial E_3} & \dfrac{\partial^2 W}{\partial E_3^2} \end{bmatrix}, \det[H] = \frac{\partial^2 W}{\partial F_{11}^2}\frac{\partial^2 W}{\partial E_3^2} - \left(\frac{\partial^2 W}{\partial F_{11}\partial E_3}\right)^2 \geq 0, \tag{3.30}$$

where

$$\begin{aligned} &\frac{\partial^2 W}{\partial F_{11}^2} = \sum_{i=1}^{19} W_i \frac{\partial^2 I_i}{\partial F_{11}^2}, \ \frac{\partial^2 W}{\partial E_3^2} = W_{10}\frac{\partial^2 I_{11}}{\partial E_3^2} + W_{11}\frac{\partial^2 I_{11}}{\partial E_3^2} + W_{12}\frac{\partial^2 I_{12}}{\partial E_3^2}, \ \frac{\partial^2 I_1}{\partial F_{11}^2} = 4 + \frac{20}{F_{11}^6}, \\ &\frac{\partial I_{10}}{\partial F_{11}} = \frac{\partial I_{13}}{\partial F_{11}} = \frac{\partial I_{15}}{\partial F_{11}} = \frac{\partial I_{17}}{\partial F_{11}} = \frac{\partial^2 I_{10}}{\partial F_{11}^2} = \frac{\partial^2 I_{13}}{\partial F_{11}^2} = \frac{\partial^2 I_{15}}{\partial F_{11}^2} = \frac{\partial^2 I_{17}}{\partial F_{11}^2} = 0, \\ &\frac{\partial\ W}{\partial F_{11}\partial E_3} = W_{11}\frac{\partial^2 I_{11}}{\partial F_{11}\partial E_3} + W_{12}\frac{\partial^2 I_{12}}{\partial F_{11}\partial E_3} + W_{14}\frac{\partial^2 I_{14}}{\partial F_{11}\partial E_3} + W_{16}\frac{\partial^2 I_{16}}{\partial F_{11}\partial E_3} \\ &+ W_{18}\frac{\partial^2 I_{18}}{\partial F_{11}\partial E_3} + W_{19}\frac{\partial^2 I_{19}}{\partial F_{11}\partial E_3}, \end{aligned} \tag{3.31}$$

and the second derivatives of $I_1,\ldots, I_{19}$ with respect to F_{11} and E_3 are given in Equations (3.26), (3.27) and (3.28), where $W_i \equiv \partial W / \partial I_i$, $i = 1,\ldots,19$. When the condition in Equation (3.30) is satisfied, g is convex with respect to F_{11} and E_3. Therefore, the free energy function W is polyconvex when the convexity condition in Equation (3.30) is satisfied.

3.5.1. Polyconvexity: Isotropic Electro-Elastic Materials

Let us now consider the simplest case of an incompressible and isotropic electro-elastic material under equi-biaxial extension. The free energy function for an isotropic electro-elastic material is given as

$$W = W(I_1, I_2, I_{10}, I_{11}, I_{12}), \tag{3.32}$$

where all terms in $\boldsymbol{E}^2$ have been retained.

The polyconvexity condition for W with respect to F_{11} and E_3 in Equation (3. 31) is now formulated and solved for the nominal electric field E_3:

$$\begin{aligned} &8(W_{10} + F_{11}^4 W_{11} + F_{11}^8 W_{12})\{(5 + F_{11}^6)W_1 + E_3^2 F_{11}^8 (3W_{11} + 14F_{11}^4 W_{12}) \\ &+ 3F_{11}^2(1 + F_{11}^6)W_2\} \geq 64 E_3^2 F_{11}^{12}(W_{11} + 2F_{11}^4 W_{12})^2, \\ &\left|E_3\right| \leq \sqrt{\frac{(W_{10} + F_{11}^4 W_{11} + F_{11}^8 W_{12})\{(5 + F_{11}^6)W_1 + 3F_{11}^2(1 + F_{11}^6)W_2\}}{F_{11}^8(-3W_{10}W_{11} + 5F_{11}^4 W_{11}^2 - 14F_{11}^4 W_{10}W_{12} + 15F_{11}^8 W_{11}W_{12} + 18F_{11}^{12} W_{12}^2)}}. \end{aligned} \tag{3.33}$$

With the condition in Equation (3.33), the total free energy function in Equation (3.32) is polyconvex under equi-biaxial extension. The inequality in Equation (3.33) describes the magnitude of the applicable nominal electric field for retaining polyconvexity of the free energy function polyconvex. Equation (3.33) can be rewritten in terms of the ratio between the electrical and mechanical properties

$$\left|E_3\right| \le \sqrt{\frac{(R_{10}+F_{11}^4R_{11}+F_{11}^8R_{12})\{(5+F_{11}^6)+3F_{11}^2(1+F_{11}^6)R_2\}}{F_{11}^8(-3R_{10}R_{11}+5F_{11}^4R_{11}^2-14F_{11}^4R_{10}R_{12}+15F_{11}^8R_{11}R_{12}+18F_{11}^{12}R_{12}^2)}}, \qquad R_i=\frac{W_i}{W_1}, \tag{3.34}$$

where it is assumed that $0 < R_2 < 2$ and $0 < R_j$ (j = 10, 11 and 12) $< 10^{-12}$ because generally the electrical property is much smaller than the mechanical property (For polyacrylate (VHB 4905), W_1 = 16000, $W_{11} = \varepsilon_0\varepsilon_r/2 = 2.08\times10^{-10}$ and $R_{11}= 1.3\times10^{-14}$), where ε_0 and ε_r are vacuum and relative permittivity.

Figure 3.2 shows the effect of R_j (j = 10, 11 and 12) on the electromechanical stability of the isotropic electro-elastic materials. The area under each curve represents the electromechanical stable region along with the stretch ratio (1.0–7.0). In Figure 3.2, R_2 is given as 0.5 and R_{10}, R_{11} and R_{12} are assumed to be identical each other. Higher value of R_{10}, R_{11} and R_{12} represents higher electrical property of the material and leads to narrow electromechanical stable region. That is to say, higher R_{10}, R_{11} and R_{12} can induce larger electromechanical actuation, but cause electromechanical instability. Figure 3.3 shows the effect of the R_2 on the electromechanical stability. R_2 is varied between 0.1 and 2.0 and R_{10}, R_{11} and R_{12} are given as 1.0×10^{-14}. As R_2 increases, stiffer material enhances the electromechanical stability of the material.

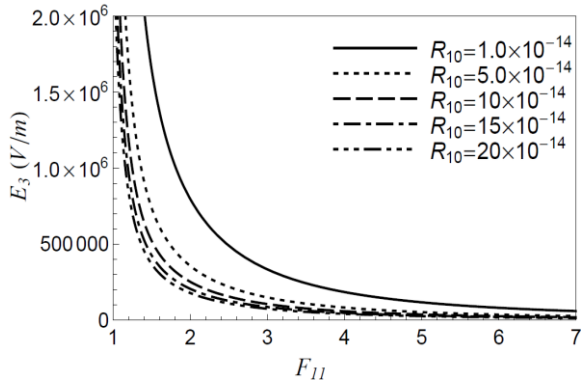

Figure 3.2. The effect of R_{10}, R_{11} and R_{12} on the electromechanical stability of the isotropic electro-elastic material.

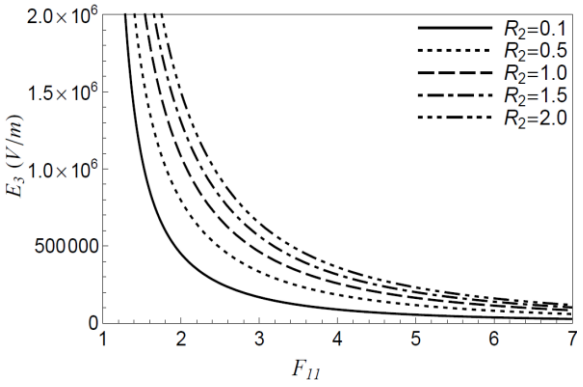

Figure 3.3. The effect of R_2 on the electromechanical stability of the isotropic electro-elastic material.

For example, let us consider an incompressible and isotropic dielectric elastomer described by an invariant based free energy function,

$$W = W(I_1, I_2, I_{11}). \tag{3.35}$$

For this case, Equation (3.33) can be simplified to be

$$\left|E_3\right| \le \sqrt{\frac{(5+F_{11}^6)+3F_{11}^2(1+F_{11}^6)R_2}{5F_{11}^8 R_{11}}}, \tag{3.36}$$

Equation (3.36) indicates that the applicable $\boldsymbol{E} = \{0, 0, E_3\}$ is therefore significantly dependent on the value of R_2 and R_{11}. When Mooney-Rivlin strain energy function [10] is employed, R_2 and R_{11} can be written in terms of the material properties

$$R_2 = \frac{W_2}{W_1} = \frac{C_2}{C_1},\ R_{11} = \frac{W_{11}}{W_1} = \frac{\varepsilon_0 \varepsilon_r}{C_1}, \tag{3.37}$$

where C_1 and C_2 are material constants for the Moony-Rivlin model.

Figure 3.4 describes the electromechanical stability region of the isotropic dielectric elastomer with respect to R_{11}, (R_2 = 0.5). Similarly to Figure 3.2, a lower value of R_{11} means large mechanical property (C_1) or small relative permittivity ε_r and leads to larger electromechanical

stability (wider range of stable ***E***), but can reduce the electromechanical actuation with respect to the ***E*** due to larger elastic stress or smaller Maxwell stress.

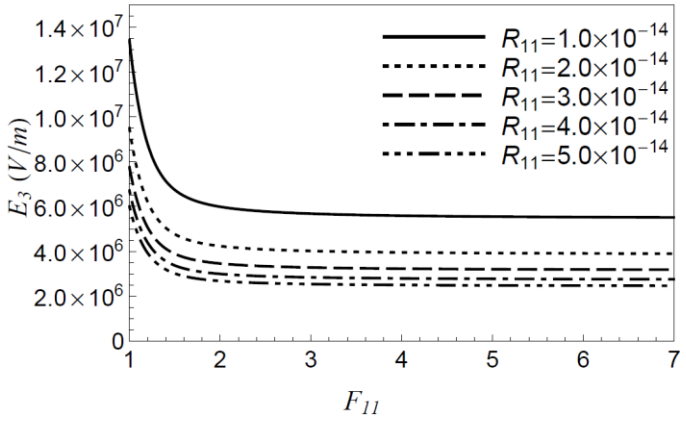

Figure 3.4. The effect of R_{11} on the electromechanical stability of isotropic dielectric elastomer (R_2 = 0.5).

Additionally, the range of R_{11} (W_{11}/W_1) for the isotropic dielectric elastomer can be obtained using Equations (3.30) and (3.31). Equation (3.38) describes the range of R_{11} for the electromechanical stability with respect to the given stretch F_{11} and the applied electric field E_3:

$$0 \le R_{11} \le \frac{5 + F_{11}^6 + 3F_{11}^2 R_2 + 3F_{11}^8 R_2}{5E_3^2 F_{11}^8}. \tag{3.38}$$

Figure 3.5 shows the range of R_{11} with respect to the stretch F_{11} and the applied electric field E_3. The area under each curve represents the boundary of R_{11} for the electromechanical stability. According to Figure 3.5, higher nominal electric field E_3 causes smaller range of R_{11}, which implies smaller region of the electromechanical stability.

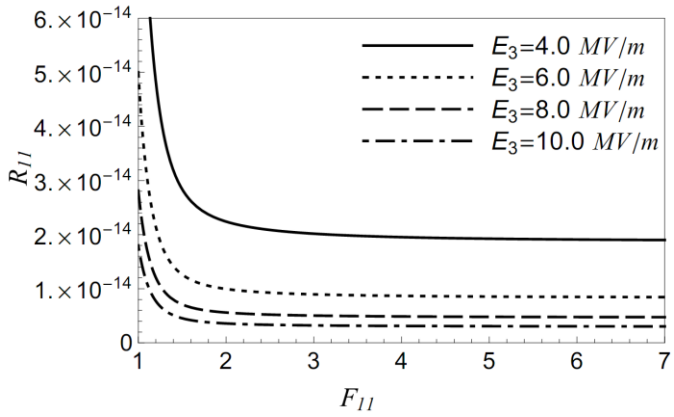

Figure 3.5. The boundary of R_{11} (W_{11}/W_1) with respect to the stretch F_{11} and applied electric field E_3.

3.5.2. Polyconvexity: Electro-Elastic Materials with Electro-Passive Fibers

For fiber-reinforced electro-elastic materials under equibiaxial extension which have two electro-passive directional vectors ***a*** and ***b***, the free energy function is given as

$$W = W(I_1, I_2, I_4, I_5, I_6, I_7, I_8, I_9, I_{10}, I_{11}, I_{12}). \tag{3.39}$$

The convexity condition for W with respect to F_{11} and E_3 is formulated as

$$\begin{aligned}
&\left|E_3\right| \le \frac{A_1}{\{2F_{11}^{12}(-3W_{10}W_{11} + 5F_{11}^4W_{11}^2 - 14F_{11}^4W_{10}W_{12} + 15F_{11}^8W_{11}W_{12} + 18F_{11}^{12}W_{12}^2)\}^{1/2}},\\
&A_1 = [(W_{10} + F_{11}^4W_{11} + F_{11}^8W_{12})\{10F_{11}^4W_1 + 2F_{11}^{10}W_1 + 6F_{11}^4W_2 + 6F_{11}^{12}W_2 + \cos^2\gamma(F_{11}^{10}(W_4\\
&+ 6F_{11}^2W_5)\cos^2\alpha + F_{11}^{10}(W_8 + 6F_{11}^2W_9)\cos\alpha\cos\beta + F_{11}^{10}(W_6 + 6F_{11}^2W_7)\cos^2\beta\\
&+ \sin^2\alpha(F_{11}^{10}W_4 + 6F_{11}^{12}W_5) + \sin\alpha\sin\beta(F_{11}^{10}W_8 + 6F_{11}^{12}W_9) + \sin^2\beta(F_{11}^{10}W_6 + 6F_{11}^{12}W_7))\\
&+ \sin^2\gamma(10F_{11}^4W_4 + 36W_5 + 10F_{11}^4W_6 + 36W_7 + 10F_{11}^4W_8 + 36W_9)\}]^{1/2}.
\end{aligned} \tag{3.40}$$

With the condition in Equation (3.40), the total free energy function for the fiber-reinforced electro-elastic materials with two families of the electro-passive fibers in Equation (3.39) is polyconvex under equibiaxial extension. Equation (3.40) can be rewritten

$$
\begin{aligned}
&\left|E_3\right| \le \frac{A_1}{\{2F_{11}^{12}(-3R_{10}R_{11}+5F_{11}^{4}R_{11}^{2}-14F_{11}^{4}R_{10}R_{12}+15F_{11}^{8}R_{11}R_{12}+18F_{11}^{12}R_{12}^{2})\}^{1/2}},\\
&A_1=[(R_{10}+F_{11}^{4}R_{11}+F_{11}^{8}R_{12})\{10F_{11}^{4}+2F_{11}^{10}+6F_{11}^{4}R_2+6F_{11}^{12}R_2+\cos^2\gamma(F_{11}^{10}(R_4\\
&+6F_{11}^{2}R_5)\cos^2\alpha+F_{11}^{10}(R_8+6F_{11}^{2}R_9)\cos\alpha\cos\beta+F_{11}^{10}(R_6+6F_{11}^{2}R_7)\cos^2\beta\\
&+\sin^2\alpha(F_{11}^{10}R_4+6F_{11}^{12}R_5)+\sin\alpha\sin\beta(F_{11}^{10}R_8+6F_{11}^{12}R_9)+\sin^2\beta(F_{11}^{10}R_6+6F_{11}^{12}R_7))\\
&+\sin^2\gamma(10F_{11}^{4}R_4+36R_5+10F_{11}^{4}R_6+36R_7+10F_{11}^{4}R_8+36R_9)\}]^{1/2},\\
&R_i=\frac{W_i}{W_1},\ (i=4,5,6,7,8,9),
\end{aligned}
\tag{3.41}
$$

where R_i represents the ratio between the fiber properties and the property of the isotropic matrix. When R_4, R_5, R_6, R_7, R_8 and R_9 are all zero which corresponds to an isotropic electro-elastic material, Equation (3.41) reduces to Equation (3.34) because no effects of the fibers are included. According to Equation (3.41), when the material properties are prescribed (not controllable), the applicable nominal electric field E_3 could be controlled by adjusting the orientation of the fibers (α, β and γ). That is to say, when the material properties are given, polyconvexity (stability) of an electro-passive fiber-reinforced electro-elastic material could be determined by the orientation of the fibers. Clearly, Figure 3.6 and Figure 3.7 show that the electromechanical stability can be controlled by adjusting the orientation of the electro-passive fibers with $\beta = -\alpha$, $R_2 = 0.5$, $R_4 = R_5 = R_6 = R_7 = R_8 = R_9 = 10.0$ and $R_{10} = R_{11} = R_{12} = 1.0\times10^{-14}$. According to Figure 3.6 and Figure 3.7, the fiber angle γ represents the angle between the electro-passive fiber and the X_1-X_2 plane and affects significantly on the electromechanical stability of the electro-elastic material with electro-passive fibers. As γ increases in Figure 3.6, the electromechanical stable region becomes narrow. When $\gamma = 90°$, there is no fiber-reinforcement in the X_1-X_2 plane.

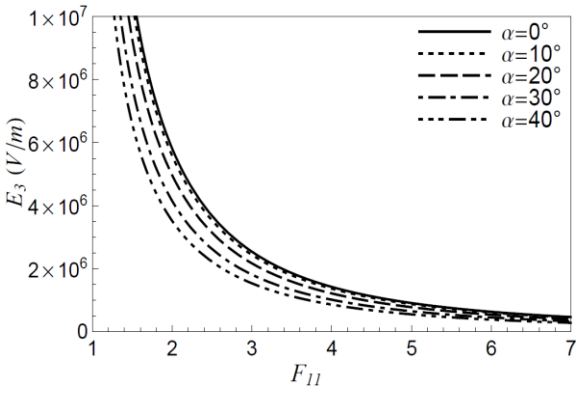

Figure 3.6. The effect of the fiber angles α and β on the electromechanical stability of electro-elastic material with two families of electro-passive fibers (γ = 0°).

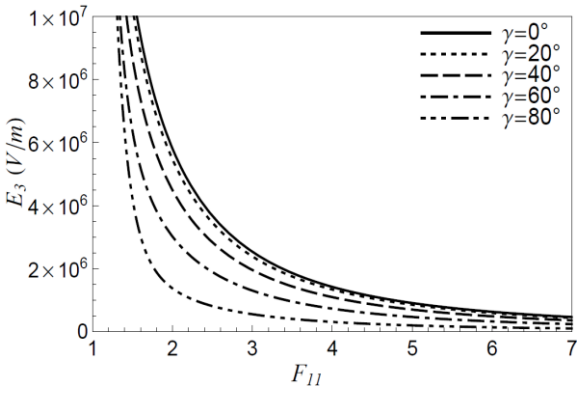

Figure 3.7. The effect of the fiber angle γ on the electromechanical stability of electro-elastic material with two families of electro-passive fibers ($\alpha = \beta$ = 0°).

Additionally, the range for R_{11} (W_{11}/W_1) of the anisotropic dielectric elastomer can be obtained using Equations (3.30) and (3.31):

$$0 \le R_{11} \le \frac{2(5+F_{11}^6)+6F_{11}^2R_2+F_{11}^6(R_4+R_6)+6F_{11}^8(R_2+R_5+R_7)+F_{11}^6(R_8+6F_{11}^2R_9)\cos 2\alpha}{10E_3^2F_{11}^8}. \quad (3.42)$$

Figures 3.8 and 3.9 show the range of R_{11} with respect to the applied electric field E_3 and the fiber's mechanical properties R_4 (W_4/W_1) at R_2 = 0.5, $R_5 = R_7 = R_9$ = 0.0 and $R_4 = R_6 = R_8$. The area under each curve represents the range of R_{11} for the electromechanical stability. Specifically in Figure 3.9, larger fiber mechanical properties (R_4, R_6 and R_8 >> 1: W_4, W_6 and W_8 >> W_1) lead to larger electromechanical stability. This result implies that the range of R_{11} (W_{11}/W_1) can be controlled by tuning the fiber's mechanical properties (W_4, W_6 and W_8).

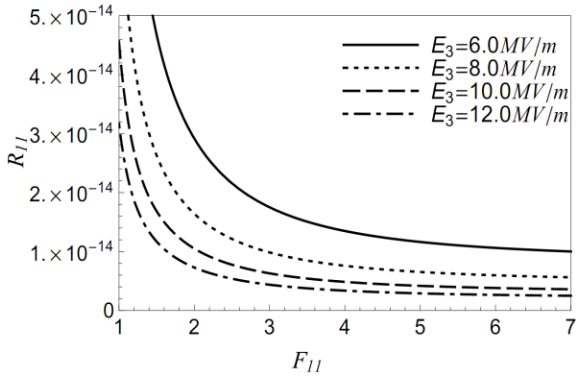

Figure 3.8. The boundary of R_{11} (W_{11}/W_1) with respect to the stretch F_{11} and applied electric field E_3 at $W_4 = W_6 = W_8 = 10.0$.

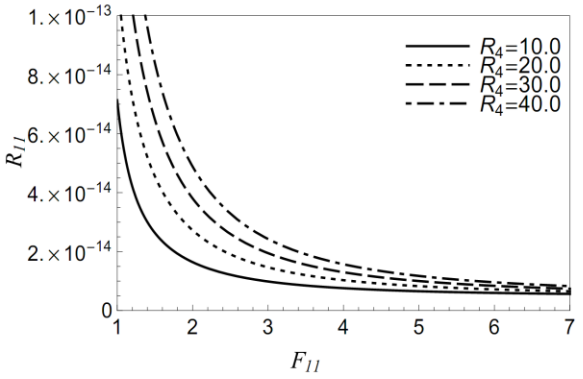

Figure 3.9. The boundary of R_{11} (W_{11}/W_1) with respect to the stretch F_{11} and R_4 (W_4/W_1) at 8.0 MV/m.

Note that the boundary for the other ratios R_i (i = 2, 3,…, 19) can be obtained solving Equations (3.30) and (3.31) for the ratios.

3.5.3. Polyconvexity: Anisotropic Electro-Elastic Materials

To simplify the polyconvexity condition, let's neglect the higher order invariants with $\boldsymbol{C}^2$ (I_5, I_7, I_9, I_{12} and I_{19}) in the free energy function:

$$W = W(I_1, I_2, I_3, I_4, I_6, I_8, I_{10}, I_{11}, I_{13}, I_{14}, I_{15}, I_{16}, I_{17}, I_{18}). \tag{3.43}$$

Equation (3.43) is now used to analyze 2 cases of coupling between electro-active fibers and the electric field.

A. Coupling between one active directional vector and the electric field

For an electro-elastic material which has one directional electro-active vector $\boldsymbol{a}$, the free energy function in Equation (3.43) is rewritten as

$$W = W(I_1, I_2, I_4, I_6, I_8, I_{10}, I_{11}, I_{14}). \tag{3.44}$$

The polyconvexity condition for this case is

$$
\begin{aligned}
&|E_3| \le \frac{\sin\gamma(10F_{11}^4W_{10}W_{14} + 26F_{11}^8W_{11}W_{14}) + A_2}{4F_{11}^{12}W_{11}(-3W_{10} + 5F_{11}^4W_{11})},\\
&A_2 = [\{\sin^2\gamma(10F_{11}^4W_{10}W_{14} + 26F_{11}^8W_{11}W_{14})^2 + 8F_{11}^{12}W_{11}(-3W_{10} + 5F_{11}^4W_{11})(2F_{11}^4(W_{10}\\
&+ F_{11}^4W_{11})((5 + F_{11}^6)W_1 + 3F_{11}^2(1 + F_{11}^6)W_2) - 4W_{14}^2\sin^2\gamma + (W_{10} + F_{11}^4W_{11})(F_{11}^{10}(W_4 + W_6\\
&+ W_8\cos(\alpha - \beta)\cos^2\gamma + 2(5F_{11}^4(W_4 + W_6 + W_8))\sin^2\gamma\}]^{1/2}.
\end{aligned}
\tag{3.45}
$$

Equation (3.45) is rewritten in terms of the ratio, $R_i = W_i/W_1$, (i = 2, 4, 6, 8, 10, 11 and 14)

$$
\begin{aligned}
&|E_3| \le \frac{\sin\gamma(10F_{11}^4R_{10}R_{14} + 26F_{11}^8R_{11}R_{14}) + A_2}{4F_{11}^{12}R_{11}(-3R_{10} + 5F_{11}^4R_{11})},\\
&A_2 = [\{\sin^2\gamma(10F_{11}^4R_{10}R_{14} + 26F_{11}^8R_{11}R_{14})^2 + 8F_{11}^{12}R_{11}(-3R_{10} + 5F_{11}^4R_{11})(2F_{11}^4(R_{10}\\
&+ F_{11}^4R_{11})((5 + F_{11}^6) + 3F_{11}^2(1 + F_{11}^6)R_2) - 4R_{14}^2\sin^2\gamma + (R_{10} + F_{11}^4R_{11})(F_{11}^{10}(R_4 + R_6\\
&+ (R_8 + 6F_{11}^2R_9)\cos(\alpha - \beta)\cos^2\gamma + 2(5F_{11}^4(R_4 + R_6 + R_8) + 18R_9)\sin^2\gamma\}]^{1/2}.
\end{aligned}
\tag{3.46}
$$

For γ = 0, the polyconvexity condition is:

$$
\begin{aligned}
&|E_3| \le \frac{A_3}{2F_{11}^{12}R_{11}(-3R_{10} + 5F_{11}^4R_{11})},\\
&A_3 = \{F_{11}^8(R_{10} + F_{11}^4R_{11})(4F_{11}^8R_{11}(-3R_{10} + 5F_{11}^4R_{11})(5 + F_{11}^6) + 3F_{11}^2(1 + F_{11}^6)R_2)\\
&+ 2F_{11}^{14}R_{11}(-3R_{10} + 5F_{11}^4R_{11})(R_4 + R_6 + (R_8\cos(\alpha - \beta)))\}^{1/2},
\end{aligned}
\tag{3.47}
$$

For $\gamma = \pi/2$, the polyconvexity condition is:

$$
\begin{aligned}
&|E_3| \le \frac{F_{11}^4R_{14}(5R_{10} + 13F_{11}^4R_{11}) + A_4}{2F_{11}^{12}R_{11}(-3R_{10} + 5F_{11}^4R_{11})},\\
&A_4 = \{F_{11}^8(R_{10} + F_{11}^4R_{11})(4F_{11}^8R_{11}(-3R_{10} + 5F_{11}^4R_{11})(5 + F_{11}^6) + 3F_{11}^2(1 + F_{11}^6)R_2)\\
&+ R_{10}(25R_{14}^2 - F_{11}^8R_{11}(R_4 + R_6 + R_8)) + F_{11}^4R_{11}(129R_{14}^2 + 20F_{11}^4R_{11}(5F_{11}^4(R_4\\
&+ R_6 + R_8))))\}^{1/2}.
\end{aligned}
\tag{3.48}
$$

According to Equations (3.47) and (3.48), since the directional vector $\boldsymbol{a}$ at γ = 0 exists in the X_1-X_2 plane and orthogonal to the electric field ($\boldsymbol{E}$ = {0, 0, E_3}), no electric coupling between $\boldsymbol{a}$ and the electric field $\boldsymbol{E}$ affects the polyconvexity condition. The effect of the electric coupling on the polyconvexity condition is maximized at $\gamma = \pi/2$. This result implies that the range of the nominal electric field for polyconvexity is controllable by orienting the directional vectors,

instead of changing the material parameters, similar to Section 3.5.2. Figure 3.7 shows the effect of the fiber angle γ on the electromechanical stable region with $\beta = -\alpha$, $R_2 = 0.5$, $R_4 = R_6 = R_8 = 10.0$, $R_{10} = R_{11} = 1.0\times10^{-14}$ and $R_{14} = 1.0\times10^{-4}$. According to Figure 3.7, as γ increases, the electromechanical stable region of the anisotropic electro-elastic material becomes wide. This is due to that higher electromechanical coupling between the electro-active fiber and the applied electric field ($\boldsymbol{E} = \{0, 0, E_3\}$) when the fiber exists out of the X_1-X_2 plane. Since the higher electromechanical coupling causes the higher total stress, the coupling enhances the overall stiffness of the material.

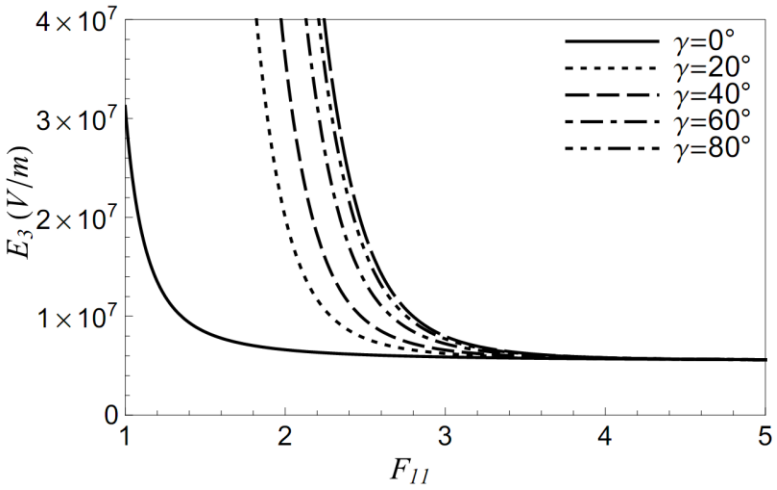

Figure 3.10. The effect of the fiber angle γ on the electromechanical stability of electro-elastic material with one family of electro-active fibers ($\alpha = \beta = 0°$).

B. Coupling between two active directional vectors and the electric field

For an electro-elastic material with two electro-active directional vectors and an applied electric field, the free energy function in Equation (3.43) is employed. The polyconvexity condition can be obtained by using Equation (3.30):

$$|E_3| \le \frac{F_{11}^4 W_{14}(5W_{10} + 13F_{11}^4 W_{11})(-W_{18}\cos^2\gamma\sin(\alpha-\beta) + (W_{14}+W_{16})\sin\gamma + A_5}{2F_{11}^{12}W_{11}(-3W_{10} + 5F_{11}^4 W_{11})},$$

$$\begin{aligned}
A_5 = \{&F_{11}^8(W_{10} + F_{11}^4 W_{11})(\cos^2\beta\cos^2\gamma(2F_{11}^4 W_{11}(-3W_{10} + 5F_{11}^4 W_{11})W_6 + (25W_{10} \\
&+ 129F_{11}^4 W_{11})W_{18}^2\sin^2\alpha\cos^2\gamma) + 2\cos\alpha\cos\beta\cos^2\gamma(F_{11}^{14}W_{11}(-3W_{10} + 5F_{11}^4 W_{11})W_8 \\
&- (25W_{10} + 129F_{11}^4 W_{11})W_{18}^2\sin\alpha\sin\beta\cos^2\gamma) + \cos^2\alpha\cos^2\gamma(2F_{11}^{14}W_{11}(-3W_{10} \\
&+ 5F_{11}^4 W_{11})W_4 + (25W_{10} + 129F_{11}^4 W_{11})W_{18}^2\sin^2\beta\cos^2\gamma) + 2F_{11}^8 W_{11}(-3W_{10} + 5F_{11}^4 W_{11}) \\
&(2(5 + F_{11}^5)W_1 + 6F_{11}^2(1 + F_{11}^6)W_2 + F_{11}^6\cos^2\gamma(W_4\sin^2\alpha + W_8\sin\alpha\sin\beta + W_6\sin^2\beta) \\
&- 2(25W_{10} + 129F_{11}^4 W_{11})(W_{14} + W_{16})W_{18}\cos^2\gamma\sin(\alpha-\beta)\sin\gamma + (5W_{10}(5(W_{14} + W_{16})^2 \\
&- 12F_{11}^8 W_{11}(W_4 + W_6 + W_8)) + F_{11}^4 W_{11}(129(W_{14} + W_{16})^2 + 100F_{11}^8 W_{11}(W_4 + W_6 + W_8))) \\
&\sin^2\gamma)\}^{1/2}.
\end{aligned} \tag{3.49}$$

Equation (3.49) is rewritten in terms of the ratio, $R_i = W_i/W_1$, (i = 2, 4, 6, 8, 10, 11, 14, 16 and 18)

$$|E_3| \le \frac{F_{11}^4 R_{14}(5R_{10} + 13F_{11}^4 R_{11})(-R_{18}\cos^2\gamma\sin(\alpha-\beta) + (R_{14}+R_{16})\sin\gamma + A_5}{2F_{11}^{12}R_{11}(-3R_{10} + 5F_{11}^4 R_{11})},$$

$$\begin{aligned}
A_5 = \{&F_{11}^8(R_{10} + F_{11}^4 R_{11})(\cos^2\beta\cos^2\gamma(2F_{11}^4 R_{11}(-3R_{10} + 5F_{11}^4 R_{11})R_6 + (25R_{10} \\
&+ 129F_{11}^4 R_{11})R_{18}^2\sin^2\alpha\cos^2\gamma) + 2\cos\alpha\cos\beta\cos^2\gamma(F_{11}^{14}R_{11}(-3R_{10} + 5F_{11}^4 R_{11})R_8 \\
&- (25R_{10} + 129F_{11}^4 R_{11})R_{18}^2\sin\alpha\sin\beta\cos^2\gamma) + \cos^2\alpha\cos^2\gamma(2F_{11}^{14}R_{11}(-3R_{10} \\
&+ 5F_{11}^4 R_{11})R_4 + (25R_{10} + 129F_{11}^4 R_{11})R_{18}^2\sin^2\beta\cos^2\gamma) + 2F_{11}^8 R_{11}(-3R_{10} + 5F_{11}^4 R_{11}) \\
&(2(5 + F_{11}^5) + 6F_{11}^2(1 + F_{11}^6)R_2 + F_{11}^6\cos^2\gamma(R_4\sin^2\alpha + R_8\sin\alpha\sin\beta + R_6\sin^2\beta) \\
&- 2(25R_{10} + 129F_{11}^4 R_{11})(R_{14} + R_{16})R_{18}\cos^2\gamma\sin(\alpha-\beta)\sin\gamma + (5R_{10}(5(R_{14} + R_{16})^2 \\
&- 12F_{11}^8 R_{11}(R_4 + R_6 + R_8)) + F_{11}^4 R_{11}(129(R_{14} + R_{16})^2 + 100F_{11}^8 R_{11}(R_4 + R_6 + R_8))) \\
&\sin^2\gamma)\}^{1/2}.
\end{aligned} \tag{3.50}$$

For γ = 0, Equation (3.50) becomes

$$|E_3| \le \frac{-F_{11}^4(5R_{10} + 13F_{11}^4 R_{11})R_{18}\sin(\alpha-\beta) + A_6}{2F_{11}^{12}R_{11}(-3R_{10} + 5F_{11}^4 R_{11})},$$

$$\begin{aligned}
A_6 = \{&\frac{1}{2}F_{11}^8(R_{10} + F_{11}^4 R_{11})(8F_{11}^4 R_{11}(-3R_{10} + 5F_{11}^4 R_{11})(5 + F_{11}^5) + 3F_{11}^2(1 + F_{11}^6)R_2) \\
&+ 25R_{10}R_{18}^2 + F_{11}^4 R_{11}(129R_{18}^2 + 425F_{11}^4 R_{11}(-3R_{10} + 5F_{11}^4 R_{11})R_8\cos(\alpha-\beta) - (25R_{10} \\
&+ 129F_{11}^4 R_{11})R_{18}^2\cos 2(\alpha-\beta))\}^{1/2}.
\end{aligned} \tag{3.51}$$

For $\gamma = 0$, the parameters R_{14} and R_{16} disappear because I_{14} and I_{16} do not exist when the directional vectors $\boldsymbol{a}$ and $\boldsymbol{b}$ exist on the X_1-X_2 plane orthogonal to the electric field $\boldsymbol{E} = \{0, 0, E_3\}$. This means that the electro-active fibers act like electro-passive because of the orientation of the electric field ($\boldsymbol{E} = \{0, 0, E_3\}$). Similarly to the electro-elastic material with the electro-passive fibers in Figure 5, the electromechanical stable region can be controlled by changing α and β.

For $\gamma = \pi/2$, Equation (3.50) becomes

$$
\begin{aligned}
&|E_3| \le \frac{F_{11}^4(5R_{10} + 13F_{11}^4R_{11})(R_{14} + R_{16}) + A_7}{2F_{11}^{12}R_{11}(-3R_{10} + 5F_{11}^4R_{11})}, \\
&A_7 = \{(F_{11}^8(R_{10} + F_{11}^4R_{11})(2F_{11}^8R_{11}(-3R_{10} + 5F_{11}^4R_{11})(2(5 + F_{11}^5) + 6F_{11}^2(1 + F_{11}^6)R_2) \\
&+ 5R_{10}(5(R_{14} + R_{16})^2 - 12F_{11}^8R_{11}(R_4 + R_6 + R_8)) + F_{11}^8R_{11}(129(R_{14} + R_{16})^2 \\
&+ 100F_{11}^8R_{11}(R_4 + R_6 + R_8)))))\}^{1/2}
\end{aligned}
\tag{3.52}
$$

For $\gamma = \pi/2$, since the directional vectors $\boldsymbol{a}$ and $\boldsymbol{b}$ converge to a unit vector in the X_3 direction, I_{18} disappears ($\boldsymbol{a} \times \boldsymbol{b} = 0$). In this case, the range of the nominal electric field for the polyconvexity is strongly dependent on the ratios (R_i, $i = 1, 2, \ldots, 16$), but not controllable by the orientation of the fibers (α and β).

3.6. Conclusion

In this Chapter, the polyconvexity condition for electro-elastic materials was investigated adopting Ball's and Rogers and Antman's approach [2, 15]. Note that the polyconvexity and convexity conditions are affected by the boundary conditions. Electro-elastic materials were described by employing an invariant-based free energy function. First, the convexity of the invariants for the electro-active directional vectors and nominal electric field under equi-biaxial extension were inspected using the general convexity condition in Section 3.1. According to the investigation, the invariants (I_{11}, I_{12}, I_{14}, I_{16}, I_{18} and I_{19}) are not convex with respect to the

independent variables F_{11} and E_3. Therefore, the polyconvexity of an invariant based free energy function which is a linear combination of I_1, I_2, I_3, I_4,…, I_{19} with respect to F_{11} and E_3 is not guaranteed by using the strict polyconvexity condition in Equation (3.24). By applying the general polyconvexity condition in Equation (3.23), an explicit polyconvexity condition for an electro-elastic material under equi-biaxial extension was obtained. The polyconvexity condition is expressed by setting a range for the applicable nominal electric field, and this range represents electromechanical stability of an electro-elastic material.

For an isotropic electro-elastic material (e.g, an isotropic DE), the applicable $\boldsymbol{E}$ is significantly dependent on the ratio R_{11} which is the ratio between the electrical (permittivity) and mechanical (stiffness) properties. For example, a higher permittivity ($R_{11} >> 0$) causes a narrow range of applicable $\boldsymbol{E}$ values and a higher stiffness ($W_1 >> W_{11}$) leads to a wide range of applicable $\boldsymbol{E}$ values. However, higher stiffness of the material leads to lower electromechanical actuation of the material due to the higher elastic stress. For anisotropic electro-elastic materials, it was indicated that the applicable $\boldsymbol{E}$ could be controlled by adjusting the orientation of the electro-active or passive directional vectors without tuning the material properties.

3.7. References

1. Hill, R., *On uniqueness and stability in the theory of finite elastic strain.* Journal of the Mechanics and Physics of Solids, 1957: p. 229-241.
2. Ball, J.M., *Convexity conditions and existence theorems in nonlinear elasticity.* Archive for Rational Mechanics and Analysis, 1977: p. 337-403.
3. Pipkin, A. and R. Rivlin, *The formulation of constitutive equations in continuum physics. I.* Archive for Rational Mechanics and Analysis, 1959: p. 129-144.
4. Pipkin, A.C. and R.S. Rivlin, *Electrical, thermal and magnetic constitutive equations for deformed isotropic materials.* Atti della Accademia Nazionale dei Lincei. Rendiconti, Classe di Scienze Fisiche, Matematiche e Naturali, 1966: p. 3-29.
5. Spencer, A.J.M. and R.S. Rivlin, *Isotropic integrity bases for vectors and second-order tensors.* Archive for Rational Mechanics and Analysis, 1962: p. 45-63.

6. Spencer, A.J.M., *Isotropic integrity bases for vectors and second-order tensors.* Archive for Rational Mechanics and Analysis, 1965: p. 51-82.
7. Spencer, A.J.M., *Theory of invariants*, in *Continuum Physics volume 1: Mathematics*. 1971, Academic: London, UK. p. 239-55.
8. Morrey, C.B., *Quasi-convexity and the lower semicontinuity of multiple integrals.* Pacific J. Math, 1952: p. 25-53.
9. Ogden, R.W., *Large Deformation Isotropic Elasticity - On the Correlation of Theory and Experiment for Incompressible Rubberlike Solids.* Proceedings of the Royal Society of London. A. Mathematical and Physical Sciences, 1972: p. 565-584.
10. Mooney, M., *Theory of large elastic deformation.* Journal of Applied Physics, 1940: p. 582-592.
11. Raoult, A., *Non-polyconvexity of the stored energy function of a Saint Venant-Kirchhoff material.* Applications of Mathematics, 1986: p. 417-419.
12. Steigmann, D.J., *On Isotropic, Frame-Invariant, Polyconvex Strain-Energy Functions.* The Quarterly Journal of Mechanics and Applied Mathematics, 2003: p. 483-491.
13. Schröder, J., *Anisotropie polyconvex energies*, in *Poly-, Quasi- and Rank-One Convexity in Applied Mechanics*, J. Schröder and P. Neff, Editors. 2010, Springer Vienna. p. 53-105.
14. Schroder, J. and P. Neff, *Invariant formulation of hyperelastic transverse isotropy based on polyconvex free energy functions.* International Journal of Solids and Structures, 2003: p. 401-45.
15. Rogers, R.C. and S.S. Antman, *Steady-state problems of nonlinear electro-magneto-thermo-elasticity.* Archive for Rational Mechanics and Analysis, 1986: p. 279-323.
16. Xuanhe, Z., H. Wei, and S. Zhigang, *Electromechanical hysteresis and coexistent states in dielectric elastomers.* Physical Review B (Condensed Matter and Materials Physics), 2007: p. 134113-1.
17. Xuanhe, Z. and S. Zhigang, *Method to analyze programmable deformation of dielectric elastomer layers.* Applied Physics Letters, 2008: p. 251902 (3 pp.).
18. Xuanhe, Z. and S. Zhigang, *Method to analyze electromechanical stability of dielectric elastomers.* Applied Physics Letters, 2007: p. 061921-1.
19. Bai-Xiang, X., et al., *On electromechanical stability analysis of dielectric elastomer actuators.* Applied Physics Letters, 2010: p. 162908 (3 pp.).
20. Jinsong, L., et al., *Electromechanical stability of dielectric elastomer.* Applied Physics Letters, 2009: p. 211901 (3 pp.).
21. Steigmann, D.J., *Frame-invariant polyconvex strain-energy functions for some anisotropic solids.* Mathematics and Mechanics of Solids, 2003: p. 497-506.
22. Hartmann, S. and P. Neff, *Polyconvexity of generalized polynomial-type hyperelastic strain energy functions for near-incompressibility.* International Journal of Solids and Structures, 2003: p. 2767-2791.

Chapter 4. Finite Deformations of Tubular Dielectric Elastomer Sensors

(This was published in Journal of Intelligent Material Systems and Structures (Son and Goulbourne [1]))

Seyul Son and N. C. Goulbourne
Center for Intelligent Material Systems and Structures
Virginia Polytechnic Institute and State University, Blacksburg, VA 24060

4.1. Abstract

This paper describes a numerical model validated with experimental results for a large stretch tubular sensor. The sensor is a dielectric elastomer (DE) membrane with electrical properties that can be accurately correlated with mechanical strain, for strains well over 50%. The DE sensor is a passive capacitive sensor. To illustrate the concept, the sensor is attached to the inner surface of a fiber reinforced elastomer actuator, which serves as the host substrate. Fiber reinforced elastomers configured for pneumatic operation are employed as actuators in robotic, prosthetic, and morphing applications. An electromechanical model for the two-layer composite consisting of the fiber reinforced elastomer and the sensor is derived. For several illustrative loading profiles, the model yields a strain output for an input capacitance value. Using identical loading cases, an experimental setup was designed to measure sensor output for two different sensor materials: silicone and polyacrylate. The sensitivity of the DE sensor was also evaluated for varying geometrical parameters and is mainly dependent on the initial thickness. Comparison of experimental data and numerical results is very good with an overall error of 3–6%. This work shows that the model is robust in the large strain range and furthermore predicts nonlinear strain behavior.

4.2. Introduction

The ultimate goal of this research is the development of sophisticated tactile sensory capabilities for soft robotics, prosthetic devices, and adaptive structures. The tactile sensors are based on dielectric elastomers. Dielectric elastomer sensors are essentially compliant passive sensors, which have a capacitance that varies with mechanical strain, or alternatively, the resistance can be monitored. Consider the placement of a dielectric elastomer sensor in direct contact with the inner surface of a McKibben actuator, which is a fiber reinforced pneumatic actuator that contracts when inflated in Figure 4.1. McKibben actuators have a high force to weight ratio and have been considered for decades as a potential artificial muscle for prosthetic limbs and devices. If it is assumed that the actuator/sensor system undergoes the same motion and that the sensor is structurally negligible, then the sensor output will be a measure of the corresponding mechanical strain.

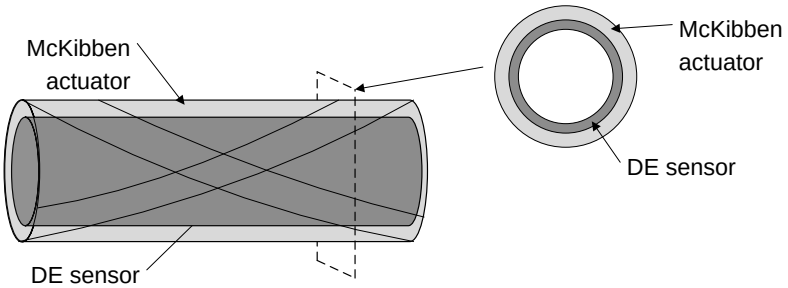

Figure 4.1. McKibben Actuators with tubular DE sensor.

This paper has two objectives. The first objective is to derive a mathematical model to describe axisymmetric deflections of a tubular dielectric elastomer sensor attached to a host or substrate (here: McKibben actuator) as well as demonstrate the robustness of the approach by comparing the results with experimental data. The second objective is to describe the electromechanical sensing response of the tubular dielectric elastomer, which can be used to monitor the strains of

the McKibben actuator. McKibben actuators have been chosen as a host structure to illustrate the capability of the large strain sensor model under representative loading scenarios. McKibben actuators are being investigated to enable the continually evolving technological fields of flexible control surfaces for aircrafts or aquatic vehicles, compliant limbs and graspers for robots, as well as for human-augmenting systems. McKibben actuators were first developed in the 1950's for an orthotic limb system. Since then, different models of the pneumatic actuator have been proposed over the years most notably by Baldwin [2], Chou *et al* [3], Klute [4, 5], Repperger et al [6, 7], and Schulte [8] and Nakamura [9]. The lack of sufficiently accurate and reproducible models and low precision of operation are two limiting issues [2]. McKibben actuators consist of a cylindrical rubber bladder enclosed by an inextensible braided shell. When the bladder is subjected to an internal inflation pressure the actuator contracts axially [3]. The inextensible fibers restrain axial extensions and allow axial contraction. This motion enables the actuator to mimic the behavior of biological muscles thus making it applicable to highly technological fields such as soft robotics, orthotics, and prosthetics [10-14]. McKibben actuators can also be configured for a variety of functions using different kinematic arrangements for example as antagonistic actuator pairs [7].

The McKibben actuator is modeled as a thin elastic cylindrical membrane undergoing axisymmetric deformations with geometric constraints imposed by fiber inextensibility. Green and Adkins' proposed a general approach to the study of such a fiber reinforced elastic cylinder [15]. For large elastic deformations, Adkins and Rivlin [16, 17], Kydoniefs [18-20], and Matsikoudi-Iliopoulou [21] among others have made very notable contributions. Specifically, Adkins and Rivlin formulated a large deformation theory for thin membranes and solved a series of axially symmetric problems [16, 17]. Kydoniefs investigated the axisymmetric deformation

of an initially cylindrical membrane with two families of inextensible fibers [18-20]. Matsikoudi-Iliopoulou used a reinforced cylindrical membrane with one family of fibers to model torsion, inflation, and extension [21]. Recently, Liu and Rahn used a continuum approach to model inflation and contraction of McKibben actuators [22] – they employed Kydoniefs' model to describe McKibben actuators. In Liu and Rahn's results, a Mooney-Rivlin model was employed for the rubber bladder and the material constants were given assumed values in the numerical calculations. Employing an equivalent approach, we have found the membrane model to be very sensitive to the material model employed. This has previously been noted by Hart-Smith and Crisp [23]. To compare the results of the numerical model with our experimental data the material constants of the constitutive model were determined experimentally as opposed to presuming a value. Mooney-Rivlin and Ogden models were fit to experimental data from simple tension tests on rectangular samples. Simple tension tests using rectangular specimens were found to be a poor qualitative predictor of the multi-axial loading state in the boundary value problem. In this paper, uniaxial extension tests using tubular samples are used to determine Ogden material constants, which lead to excellent correlation with experimental data within 3%. The robustness of the modeling approach is demonstrated by varying several experimental parameters.

An introduction to dielectric elastomer sensors is given in the next section, followed by an outline of the continuum mechanics based model for elastic tubular membrane. In previous research, Goulbourne *et al*. [24, 25] derived a finite deformation model for dielectric elastomer membranes in actuation mode. Dynamic characterization of edge-clamped DE membrane actuators was conducted using an experimental approach [26, 27]. Wakimoto, Suzumori and Kanda [28] conducted experiments to study an internal rubber displacement sensor patch for a

McKibben actuator using changes in electrical resistance induced by the deformation of the actuator. The main contribution of their work was to demonstrate the concept of using a deformable sensor for in situ strain sensing. In this paper, a robust model for in situ large strain sensing is developed and validated by a series of experiments under varying loading conditions. Later, a mathematical model is derived to predict the capacitance versus stretch relationship for cylindrically symmetric deformations of dielectric elastomer sensors. If the sensor is presumed to maintain its cylindrical shape during deformation, then only a single stretch ratio is needed to completely describe the deformed state. In this case, a simple model is derived by combining elastic membrane theory and electrostatics. This geometrical restraint could be relaxed so that axisymmetric but not necessarily perfectly cylindrical shapes can be considered. To demonstrate the validity of the modeling approach a comparison of numerical and experimental results is performed. The results of a series of parametric studies performed to test the robustness of the model are presented.

4.3. Dielectric Elastomer Sensor Response

Dielectric elastomer sensors are large strain electromechanical transducers. The dielectric elastomer sensor is a three-component system consisting of a compliant elastomeric insulator sandwiched by two compliant electrodes. Dielectric elastomers offer various advantages as large strain sensors including: simple fabrication techniques, low cost, repeatability, scalability, and shape conformability, just to name a few. Traditional sensor materials are comparatively stiff and fail at low strains. This is not the case for dielectric elastomer sensors which are highly compliant and have a large strain range. Mechanical strains are detected by measuring one of two electrical parameters: capacitance or resistance. These sensors are ideal for large strain

sensing applications due to the ability to retain electrical conductivity at the strains – even up to 100%. A schematic of a tubular dielectric elastomer in sensing mode is given in Figure 4.2.

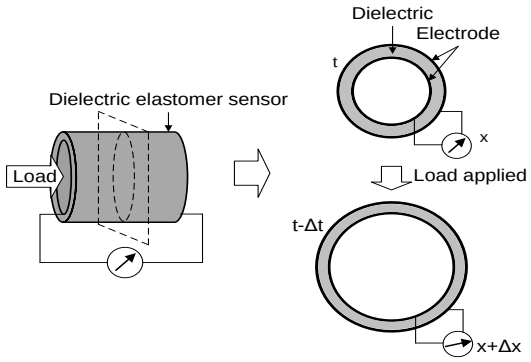

Figure 4.2. Schematic of pressure/strain sensing using a dielectric elastomer sensor.

The two most common types of dielectric elastomers used in fabricating sensors are acrylic rubber and silicone rubber [29, 30]. Failure of a typical specimen of 3M VHB 4905 does not occur until a stretch ratio of 8, thus making dielectric elastomer sensors ideal for large stretch applications. Applying compliant electrodes to the major surfaces of prestretched dielectric elastomer specimens completes the fabrication process. We have previously conducted an experimental evaluation of the large stretch response of different electrodes: carbon grease, silver grease, graphite powder, and graphite spray. The experimental results indicate that carbon grease and silver grease are the best compliant electrodes of the four that were tested; carbon grease has a slightly better performance overall and is also less costly [31].

4.4. Theoretical Model for Fiber-Reinforced Tubular Membrane

4.4.1. Formulation of the Boundary Value Problem

In this section, a theoretical model to describe the deformation response of fiber-reinforced tubular membranes based on Green and Adkins' work. The theory so derived is applicable to McKibben actuators. By relaxing the deformation constraints imposed by the inextensible fibers, the theory can be modified and used to model unreinforced tubular membranes such as the dielectric elastomer sensor. This approach is outlined in more detail in the following section. From the symmetry of the problem and the assumption that the membrane is very thin compared with its radius, the state of stress is considered nearly constant throughout the thickness (elastic membrane theory assumption). A set of cylindrical polar coordinates (R, Θ, η) at the midplane are employed in the undeformed state (Figure 4.3). The meridian length of the cylindrical membrane is denoted η in the undeformed state and ξ in the deformed state. The inextensible fibers on the membrane forms a constant angle $\pm\alpha$ with the z-axis and the initial length and radius of the cylindrical membrane are given by L_0 and R. It follows that the principal directions at any point in the deformed membrane coincides with the deformed coordinates (r, θ, z) and the principal extension ratios are denoted as λ_1, λ_2 and λ_3. Specifically, λ_1 and λ_2 are the meridional and latitudinal stretch ratios that define the deformation and λ_3 is the thickness stretch ratio. Mathematically, the deformed coordinates and stretch ratios are given as

$$\begin{aligned} &r = r(\xi),\ \theta = \Theta,\ z = z(\xi), \\ &\lambda_1 = \frac{d\xi}{d\eta},\ \lambda_2 = \frac{r}{R},\ \lambda_3 = \frac{h}{h_0}, \end{aligned} \tag{4.1}$$

where $2h_0$ and $2h$ are the undeformed and deformed thickness of the membrane.

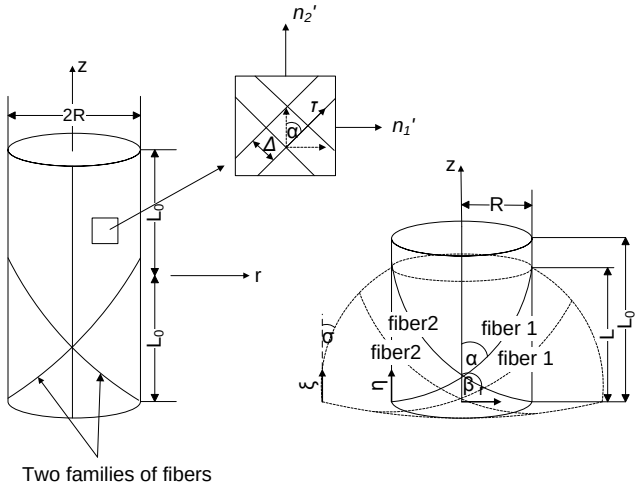

Figure 4.3. A reinforced cylindrical membrane with two families of fibers (left). Half of the undeformed and deformed membrane (right).

Let the elements of length in the undeformed and deformed states be denoted by ds_0 and ds and the geometrical relation between them given by

$$\left(\frac{ds}{ds_0}\right)^2 = \lambda_1^2 \cos^2\alpha + \lambda_2^2 \sin^2\alpha, \tag{4.2}$$

where α is the angle between an individual fiber and the z axis. In the direction of the fiber, ds_0 is equal to ds because it is assumed that the fiber is inextensible, so that Equation (4.2) becomes

$$\lambda_1^2 \cos^2\alpha + \lambda_2^2 \sin^2\alpha = 1. \tag{4.3}$$

Let β be the angle formed between the z axis and ds in the deformed state as shown in Figure 4.3. The geometry and fiber inextensibility can be used to determine β as

$$\begin{aligned} \cos\beta &= \lambda_1 \cos\alpha, \\ \sin\beta &= \lambda_2 \sin\alpha. \end{aligned} \tag{4.4}$$

Since the material is incompressible, the stretch invariant, I_3 is given as

$$I_3 = \lambda_1 \lambda_2 \lambda_3 = 1. \tag{4.5}$$

Hence, the strain energy function is a function of the stretch invariants, I_1 and I_2,

$$W = W(I_1, I_2), \tag{4.6}$$

which are defined by

$$I_1 = \lambda_1^2 + \lambda_2^2 + \lambda_3^2, \qquad I_2 = \lambda_1^{-2} + \lambda_2^{-2} + \lambda_3^{-2}. \tag{4.7}$$

For a fiber reinforced membrane, the total stress resultants are derived from the force required to deform the elastic membrane alone and from the tension in the fibers. Therefore, the total stress resultants, N_i' can be decomposed into two parts

$$N_i' = n_i' + t_i, \tag{4.8}$$

where n_i' is the stress resultant required to deform the membrane itself and t_i is the tension due to the inextensible fibers ($i=1,2$ and 3). In accordance with Adkins and Rivlins solution approach, we presume that the applied forces normal to the cylindrical surfaces are negligible in comparison to the in-plane stresses and set n_3=0. The stress components of the membrane are then given by

$$n_1 = 2\left(\lambda_2^2 - \frac{1}{\lambda_1^2\lambda_2^2}\right)\left(\frac{\partial W}{\partial I_1} + \lambda_1^2\frac{\partial W}{\partial I_2}\right), \qquad n_2 = 2\left(\lambda_1^2 - \frac{1}{\lambda_1^2\lambda_2^2}\right)\left(\frac{\partial W}{\partial I_1} + \lambda_2^2\frac{\partial W}{\partial I_2}\right), \qquad n_3 = 0, \tag{4.9}$$

where n_1, n_2, and n_3 are the latitudinal, meridional, and normal stress components. In the deformation, the initial thickness $2h_0$ of the membrane becomes $2\lambda_3 h_0$ and the stress resultants are obtained by integrating over the deformed thickness of the membrane

$$\begin{aligned} n'_1 &= 2\lambda_3 h_0 n_1 = 4\lambda_3 h_0\left(\lambda_2^2 - \frac{1}{\lambda_1^2\lambda_2^2}\right)\left(\frac{\partial W}{\partial I_1} + \lambda_1^2\frac{\partial W}{\partial I_2}\right), \\ n'_2 &= 2\lambda_3 h_0 n_2 = 4\lambda_3 h_0\left(\lambda_1^2 - \frac{1}{\lambda_1^2\lambda_2^2}\right)\left(\frac{\partial W}{\partial I_1} + \lambda_2^2\frac{\partial W}{\partial I_2}\right). \end{aligned} \tag{4.10}$$

Resolving the tensions of the two family fibers in the latitudinal and meridional directions yield

$$t_1 = 2\tau\left(\frac{\lambda_2 \sin^2\alpha}{\lambda_1\Delta}\right), \qquad t_2 = 2\tau\left(\frac{\lambda_1 \sin^2\alpha}{\lambda_2\Delta}\right), \tag{4.11}$$

where τ is the tension in the fiber and Δ is the constant distance between two different fibers on the undeformed circumference. Therefore, the total stress resultants for a reinforced membrane with two family fibers are

$$N_1' = n'_1 + t_1 = 4\lambda_3 h_0 \left(\lambda_2^2 - \frac{1}{\lambda_1^2 \lambda_2^2} \right) \left(\frac{\partial W}{\partial I_1} + \lambda_1^2 \frac{\partial W}{\partial I_2} \right) + 2\tau \left(\frac{\lambda_2 \sin^2 \alpha}{\lambda_1 \Delta} \right),$$
$$N_2' = n'_2 + t_2 = 4\lambda_3 h_0 \left(\lambda_1^2 - \frac{1}{\lambda_1^2 \lambda_2^2} \right) \left(\frac{\partial W}{\partial I_1} + \lambda_2^2 \frac{\partial W}{\partial I_2} \right) + 2\tau \left(\frac{\lambda_1 \cos^2 \alpha}{\lambda_2 \Delta} \right). \tag{4.12}$$

By employing the Ogden strain energy function and dividing the stress resultant by $4\mu_1 h_0$ the non-dimensional stress resultants become

$$N_1 = \frac{1}{2\lambda_1 \lambda_2} \left\{ \left(\lambda_2^{k_1} - \left(\frac{1}{\lambda_1 \lambda_2} \right)^{k_1} \right) + \beta_2 \left(\lambda_2^{k_2} - \left(\frac{1}{\lambda_1 \lambda_2} \right)^{k_2} \right) + \beta_3 \left(\lambda_2^{k_3} - \left(\frac{1}{\lambda_1 \lambda_2} \right)^{k_3} \right) \right\} + \frac{2T(1-\lambda_1^2 \cos^2 \alpha)}{\lambda_1 \lambda_2},$$
$$N_2 = \frac{1}{2\lambda_1 \lambda_2} \left\{ \left(\lambda_1^{k_1} - \left(\frac{1}{\lambda_1 \lambda_2} \right)^{k_1} \right) + \beta_2 \left(\lambda_1^{k_2} - \left(\frac{1}{\lambda_1 \lambda_2} \right)^{k_2} \right) + \beta_3 \left(\lambda_1^{k_3} - \left(\frac{1}{\lambda_1 \lambda_2} \right)^{k_3} \right) \right\} + \frac{2T\lambda_1 \cos^2 \alpha}{\lambda_2}, \tag{4.13}$$

where $T=\tau/4\mu_1 h_0 \Delta$, $\beta_2 = \mu_1/\mu_2$ and $\beta_3 = \mu_2/\mu_3$.

The equilibrium equations for axisymmetric deformations of a membrane are

$$\frac{d(\lambda_2 N_2)}{d\lambda_2} = N_1,$$
$$\frac{N_1 \cos \sigma}{\lambda_2} + N_2 \frac{d \cos \sigma}{d\lambda_2} = p, \tag{4.14}$$

where $p=PR/4\mu_1 h_0$ and σ is the angle between the deformed membrane and the z axis. Only half of the deformed membrane is considered due to symmetry considerations. If an axial load F is applied to the distal end of the membrane so that contraction forces can be measured, then the boundary conditions at $\xi = L$ and $\xi = 0$ become

$$\lambda_2(1) = 1, \pi r(0)^2 P = 2\pi r(0) n_2(0) - F, \; N_2(0) = \frac{\lambda_2(0) p}{2} + \frac{f}{\lambda_2(0)}, \; \sigma(0) = 0, \tag{4.15}$$

where $f=F/8\pi\mu_1 R h_0$.

From the second expression of Equation (4.14), we have

$$\frac{d}{d\lambda_2}(\lambda_2 N_1 \cos\sigma) = PR\lambda_2 . \tag{4.16}$$

By integrating Equation (4.16) and using the boundary conditions (Equation (4.15)), we obtain the following:

$$\begin{aligned} N_1\lambda_2\cos\sigma &= p\frac{\lambda_2}{2} + f, \\ \cos\sigma &= \frac{p\lambda_2}{2N_1} + \frac{f}{N_1\lambda_2}. \end{aligned} \tag{4.17}$$

Inserting the total stress resultants into the first nondimensional equilibrium equation, a nonlinear ordinary differential equation with independent variable, $\lambda_2(\xi)$, is obtained. By guessing τ, $\lambda_1(\xi)$ and $\lambda_2(\xi)$ are calculated. An iterative numerical solution procedure is applied until the calculated value of the initial length, l_0 using Equation (4.18) is compared with the initial length, l_0. This procedure is repeated until the correct initial length, l_0 is obtained:

$$l_0 = \frac{L_0}{R} = -\int_{\lambda_2(0)}^{1} \frac{d\lambda_2}{\lambda_1 \sin\sigma} . \tag{4.18}$$

The deformed length of half of the membrane is then obtained by

$$z(\lambda_2) = \frac{L}{R} = -\int_{\lambda_2(0)}^{1} \cot\sigma \, d\lambda_2 . \tag{4.19}$$

4.4.2. Constitutive Relationship for McKibben Actuator Tubes

The bladder of a McKibben actuator is made of a rubbery elastic material such as latex and silicone and is considered to be incompressible and isotropic. There are numerous strain energy functions that have been proposed to describe elastomeric materials, including Mooney-Rivlin, neo-Hookean, Blatz-Ko, and Ogden formulations. Axial extension experiments were conducted on 3 tubes. Figure 4.4 shows the force versus stretch results for tubular latex samples. The three samples were tested 5 times each, the average of these tests are represented by the dashed line (--) in Figure 4.4. A nonlinear fit of the data using Mooney-Rivlin and Ogden formulations are

shown in the figure. The results indicate that the Mooney-Rivlin material model only captures the stretch behavior up to ~1.75. The Ogden model is much better fit for the entire stretch range. Therefore, in this paper, an Ogden strain energy function [32] is employed for describing the stress-strain behavior of the rubbery material. The Ogden strain energy function has the form,

$$W = \sum_{i=1}^{m} \frac{\mu_i}{k_i} (\lambda_1^{k_i} + \lambda_2^{k_i} + \lambda_3^{k_i} - 3), \tag{4.20}$$

where k_i are dimensionless constants, μ_i are the dimensional Ogden material constants and λ_1, λ_2 and λ_3 are the three principal stretch ratios. Theoretical predictions of the Ogden model with $m = 3$ generates satisfactory results especially for multi-axial stress states [33]. The constants of the Ogden strain energy function, k_i and μ_i (i = 1,2 and 3), are determined from uniaxial extension tests on tubular samples supporting a uniformly distributed axial load. The Ogden constants for tubular samples are μ_1 = 2.79 *MPa*, μ_2 = 30.4 *kPa*, μ_3 = -1.69 *kPa*, k_1 = 0.078, k_2 = 3.33 and k_3 = -7.31.

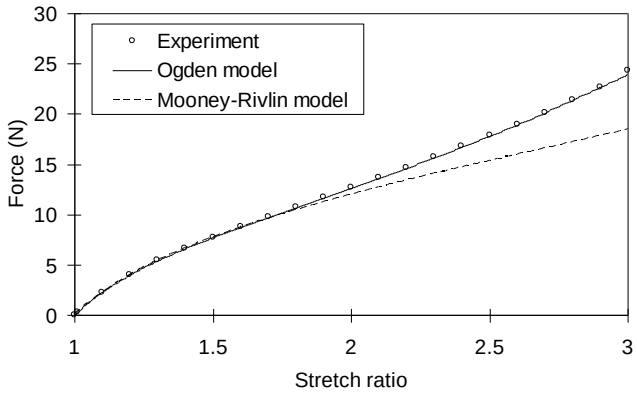

Figure 4.4. Force versus stretch data for tubular rubber samples compared with material models.

4.5. Electromechanical Model for Tubular DE Sensors

In this section, a capacitance versus stretch relationship is derived for tubular dielectric elastomer sensors. The expression for the capacitance is derived from basic electrostatics and the sensor deformation is described by modifying the membrane theory presented in the previous section (i.e. fiber constraints removed). Conventional sensor materials are relatively stiff and fail at low strains. Unlike traditional sensors such as strain gages and piezoelectric ceramics, low modulus dielectric elastomers do not fail at large strains and are hence a viable option for large strain applications. Dielectric elastomer sensors offer various other advantages such as simple fabrication, low cost, low weight, repeatability and shape compliance [34]. In the proposed hybrid McKibben actuator system, a tubular dielectric elastomer sensor is attached directly to the inner cylindrical surface of the actuator. Dielectric elastomers are fabricated by electroding an elastomeric material (3M VHB) with compliant electrodes (carbon grease). Since the dielectric elastomer is much more compliant than the rubbery actuator tube, it is assumed that the tubular dielectric elastomer layer is structurally negligible and hence considered to undergo the same deformation as the McKibben actuator. Three different loading scenarios for the tubular sensor and the hybrid McKibben actuator will be considered in the following section: (i) extension of the sensor, (ii) inflation and extension of the sensor and (iii) inflation and extension of the sensor/actuator composite in Figure 4.5.

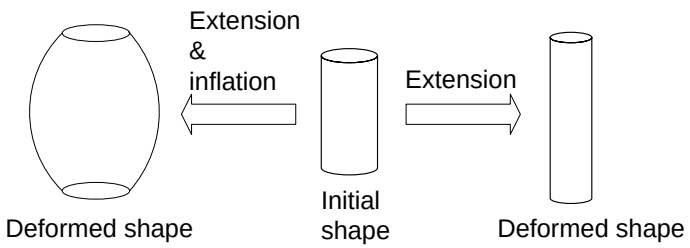

Figure 4.5. Deformed shapes of the tubular sensors and McKibben actuator.

4.5.1. Loading Case I: Sensor Extension

The DE is essentially a cylindrical membrane without inextensible fibers, which in the undeformed state is of length L_0, a deformed length L, an initial radius R in the mid-plane of the cross-sectional surface and thickness, h_0. It has outer and inner radii R_{out} and R_{in} respectively in the undeformed state and r_{in} and r_{out} in the deformed state. We assume that the membrane is stretched by a uniform extension ratio λ_1, parallel to the z axis without increase of internal pressure such that the deformations are cylindrically symmetric. We can apply the theoretical model outlined in the previous section to the unreinforced dielectric elastomer by making a few simplifications. First of all, the deformation constraints previously imposed by the fibers are removed. Secondly, if the deformed membrane is a perfect cylinder, then the angle between the membrane and the z axis, σ, is equal to zero. Therefore, there is a single nonzero curvature expression and the second equilibrium equation, Equation (4.14) can be rewritten as

$$\frac{N_2}{\lambda_2} = p. \tag{4.21}$$

From the second equilibrium equation, Equation (4.21), the pressure difference, P is obtained as

$$P = \frac{2\mu_1 h_0}{R\lambda_1\lambda_2^2}\left\{\left(\lambda_2^{k_1} - \left(\frac{1}{\lambda_1\lambda_2}\right)^{k_1}\right) + \beta_2\left(\lambda_2^{k_2} - \left(\frac{1}{\lambda_1\lambda_2}\right)^{k_2}\right) + \beta_3\left(\lambda_2^{k_3} - \left(\frac{1}{\lambda_1\lambda_2}\right)^{k_3}\right)\right\}. \tag{4.22}$$

Using the boundary conditions, ($\lambda_1(0)= \lambda_2(0)=1$), P is equal to be zero, which is constant during the deformation because the internal pressure is zero. Then, the relationship between λ_1 and λ_2 are obtained using Equation (4.22)

$$\lambda_2 = \lambda_1^{-1/2}. \tag{4.23}$$

To determine the capacitance of the deformed cylindrical membrane, expressions for the coaxial electric field and the potential difference between inner and outer surfaces are

$$E = \frac{Q}{2\pi L \varepsilon_0 \varepsilon_r r},$$
$$V = -\int_{r_{in}}^{r_{out}} E dr = -\frac{Q}{2\pi L \varepsilon_0 \varepsilon_r}\int_{r_{in}}^{r_{out}} \frac{1}{r} dr = \frac{Q}{2\pi L \varepsilon_0 \varepsilon_r} \ln\left(\frac{r_{out}}{r_{in}}\right), \tag{4.24}$$

where r is a radial coordinate, Q is the charge, ε_r is the relative permittivity and ε_0 is the vacuum permittivity and L is the deformed length of cylinder. The capacitance of the dielectric elastomer is the ratio between the electrical charge and the potential difference

$$C = \frac{Q}{V} = \frac{\varepsilon_0 \varepsilon_r 2\pi L}{\ln\left(r_{out} / r_{in}\right)}. \tag{4.25}$$

The capacitance of the tubular dielectric elastomer can then be rewritten and expressed in terms of only the initial dimensions and the stretch ratios

$$C = \frac{\varepsilon_0 \varepsilon_r 2\pi L_0}{\ln\left(\dfrac{R\lambda_2 + h_0 / \lambda_1\lambda_2}{R\lambda_2 - h_0 / \lambda_1\lambda_2}\right)} \lambda_1. \tag{4.26}$$

Then by substituting Equation (4.23), we can simplify Equation (4.26) for the case of pure extension of the sensor as

$$C = \frac{\varepsilon_0 \varepsilon_r 2\pi L_0}{\ln\left(\dfrac{R + h_0}{R - h_0}\right)} \lambda_1. \tag{4.27}$$

From Equation (4.27), the relationship between the total capacitance and extension ratio λ_1 is linear and the capacitance depends on the geometrical dimensions and relative permittivity of the tubular dielectric elastomer.

Using the expressions derived above, a parametric study can be conducted to determine the most effective operating regimes for the sensor. In other words, identify regions that will have high

sensitivity. Figure 4.6 gives capacitance as a function of the initial sensor dimensions, which is obtained by numerical computation. For the numerical computation, Equation (4.27) is used with a relative permittivity (3M VHB), ε_r of 4.7. The effect of thickness and radius (varied from 0.2 to 1.0 *mm* and from 4.0 to 10.0 *mm*) for a constant length of 20.0 *mm* on the capacitance is shown in Figure 4.6. The slope of the curve below the thickness, 0.4 *mm*, becomes very steep with decreasing thickness, and ever so slightly increases for increasing radius. This means that the capacitance sensitivity can be improved by using very thin sensors, that is to say, operating in the steep regions of the surface. Figure 4.7 shows capacitance as a function of length and radius (10–30.0 *mm* and 4–10.0 *mm*) for a constant thickness of 0.50 *mm*. When the length and radius are varied, only the initial capacitance is increased without a significant change in slope. In summary, the geometrical parameters affect the initial capacitance of the sensor (as expected). Most importantly, sensor thickness has the most significant impact on sensor performance since it can be varied to improve sensor sensitivity. Furthermore, in reality the length and radius of the sensor are limited by the configuration of a host system.

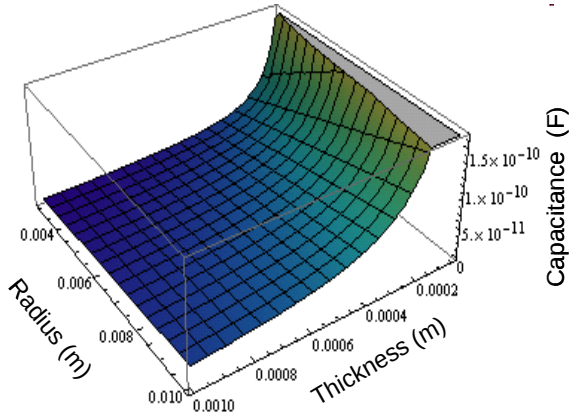

Figure 4.6 The effective regime of thickness and radius for the tubular dielectric elastomer sensor (3M VHB).

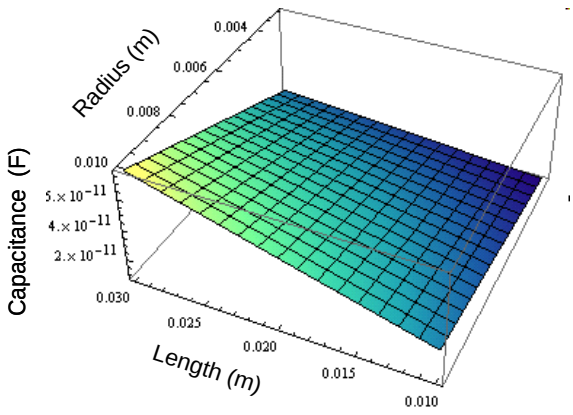

Figure 4.7. The effective regime of length and radius for the tubular dielectric elastomer sensor (3M VHB).

4.5.2. Loading Case II: Sensor Inflation and Extension

For the second loading scenario, an axial force and an internal pressure are applied to the sensor. Due to the nonzero inflation pressure, the cylindrical membrane does not deform as a perfect cylinder but rather inflates axisymmetrically as illustrated in Figure 4.5. Using the condition that there are two nonzero curvatures, all Equations (4.1)–(4.20) except for the equations involving the inextensible fibers can be used to model the unreinforced tube. For completeness, the equilibrium equations are repeated here

$$\begin{aligned} &\frac{d(\lambda_2 N_1)}{d\lambda_2} = N_2, \\ &\frac{N_2 \cos\sigma}{\lambda_2} + N_1 \frac{d\cos\sigma}{d\lambda_2} = p, \end{aligned} \tag{4.28}$$

where $p=PR/4\mu_1 h_0$.

Using the first equilibrium equation and the constitutive equations for the stress resultants, N_1 and N_2 from Equation (4.13), a relationship between λ_1 and λ_2 is obtained. The boundary conditions are identical to those applied previously in modeling the McKibben actuator and Equations (4.16)–(4.19) apply.

In addition, a new capacitance expression needs to be formulated since the membrane is no longer deforms as a perfect cylinder. A schematic of the deformed shape of the cylindrical membrane is shown in Figure 4.8.

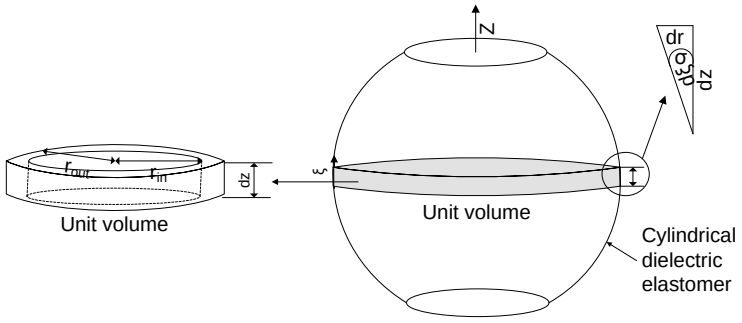

Figure 4.8. Deformed tubular dielectric elastomer sensor.

The capacitance of a unit volume of the sensor, *dC*, in Figure 4.6 can be obtained as,

$$dC = \frac{\varepsilon_0 \varepsilon_r 2\pi}{\ln\left(r_{out}/r_{in}\right)} dz = \frac{\varepsilon_0 \varepsilon_r 2\pi}{\ln\left(r_{out}/r_{in}\right)} \frac{1}{\tan\sigma} dr,$$
$$r_{out} = R_0\lambda_2 + h_0 \frac{1}{\lambda_1\lambda_2}, \quad r_{in} = R_0\lambda_2 - h_0 \frac{1}{\lambda_1\lambda_2}. \tag{4.29}$$

The total capacitance for the inflated tubular membrane is formulated by integrating Equation (4.29) with respect to z axis, yielding

$$C = \varepsilon_0 \varepsilon_r 2\pi R_0 \int_1^{\lambda_2(0)} \frac{1}{\ln\left(\dfrac{R_0\lambda_2 + h_0 \dfrac{1}{\lambda_1\lambda_2}}{R_0\lambda_2 - h_0 \dfrac{1}{\lambda_1\lambda_2}}\right)} \frac{1}{\tan\sigma} d\lambda_2. \tag{4.30}$$

An iterative numerical procedure is needed to solve this system of equations. Initially, the internal pressure (*P*) and initial dimensions of the sensor are known. The first step is to guess an axial loading *F* and $\lambda_2(0)$ and obtain $\lambda_1(0)$ by using the appropriate boundary conditions (Equation (4.15)). The second step is to insert the relationship between λ_1 and λ_2 from Equation (4.28) as well as Equation (4.17) into Equation (4.30). The third step is to obtain a numerical capacitance C_{num} by using Equation (4.30) and compare it with the given capacitance. The trial value for $\lambda_2(0)$ is changed until the values match. When the values match, a numerical initial length L_{num} is obtained from Equation (4.18) and compared with the given initial length. The trial value for the axial loading *F* is changed until the values are identical. Conversely, the pressure can be calculated by employing an identical numerical procedure.

4.5.3. Sensor/Actuator Composite: Inflation and Extension

In the previous two subsections, the sensor was studied in the absence of a substrate. In this section, we consider a sensor attached to a pneumatic actuator. The tubular sensor is placed in

contact directly with the inner surface of an actuator. The initial assumption is that the deformation of the sensor is identical to the actuator's. Therefore, the deformation is governed by the actuator, so that the model for the pneumatic actuator outlined in the previous section can be used without accounting for an additional layer. That is to say that, although physically there is a two-layer structure, only the dominant actuator layer is modeled. For a pneumatic actuator, the curvature in the meridional direction is nonzero (not a perfect cylinder) during deformation, hence the capacitance expression derived in Equation (4.30) can be applied. By measuring the capacitance change during the deformation, the deformed dimensions and axial loading or internal pressure applied can be predicted by using the following iterative procedure. Initially, a trial value of τ and $\lambda_2(0)$ are given. The second step is to obtain the numerical capacitance using Equation (4.30). When the numerical capacitance is matched with the measured value, the initial length l_0 is calculated using Equation (4.18), which is compared with the initial length, l_0. When matched, the axial loading or internal pressure is obtained using the boundary conditions, Equation (4.15). This procedure is repeated until the correct numerical capacitance and initial length, l_0 are obtained.

4.6. Experimental and Numerical Results

In this section, experimental results conducted to observe the static sensing response of tubular DE sensors are presented and discussed. The numerical results are generated using the mathematical model derived in the previous sections. The results are divided into two subsections. In the first subsection, the experimental setup is described. The response of polyacrylate DE sensors and silicone DE sensors with extension is analyzed in the first

subsection. In the second subsection, the response of a sensor integrated with a McKibben actuator is analyzed. In each section, experimental and numerical results are compared.

4.6.1. Pure Extension (Polyacrylate and Silicone Films)

For the first set of experiments, five different DE sensors using 3M VHB (Samples 1–5) were fabricated. Each sample was tested five times. The initial dimensions of each sample are given in Table 4.1. The sensor is clamped at both circular ends and a uniform longitudinal extension is applied to the sample using a linear displacement stage (NLS4 Series linear stage, Newmark systems, INC). The capacitance is measured throughout the deformation using a very sensitive capacitance meter (GLK model 3000, resolution: 0.001 *pF* to 0.1 *nF*). A schematic of the experimental setup is shown in Figure 4.9. It is expected that the relationship between capacitance and the stretch ratio is linear and the sensitivity of the sensor is dependent on the initial dimensions and the relative permittivity of the material (Equation (4.28)). The Ogden material constants are μ_1=70.3 *kPa*, μ_2=9.57 *kPa*, μ_3=-0.91 *kPa*, k_1=0.4293, k_2=0.4293 and k_3=-5.9555.

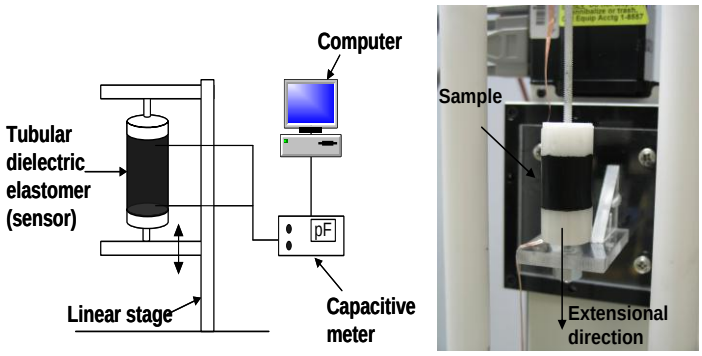

Figure 4.9. Experimental setup of the pure extension test for tubular dielectric elastomer sensor (Left), and picture of fabricated sensor (Right).

Table 4.1. Initial dimensions of tubular dielectric elastomer sensor (3M VHB & Siliccone).

Sensor (3M VHB)	**1**	**2**	**3**	**4**	**5**
$L_0/R_0/t_0$ (*mm*)	10.9/9.57/0.5	17.15/9.57/0.5	20.83/9.57/0.5	17.66/3.6/0.5	21/3.6/0.5
Sensor (Silicone)	**6**	**7**	**8**	**9**	**10**
$L_0/R_0/t_0$ (*mm*)	10.5/9.57/0.09	17.1/9.57/0.09	21/9.57/0.09	17.15/3.6/0.09	21/3.6/0.09

Figure 4.10 shows that the relationship between the capacitance and the stretch ratio in the longitudinal direction is linear. The effect of the initial length of the samples on the capacitance sensitivity is also shown in Figure 4.10. As the length increases, the slope increases. This implies that a longer sensor is more sensitive as can be seen by examining Equation (4.27). Previous experimental results had also indicated that increasing the prestretch increases the sensitivity of the sensor [35]. Therefore, the trade-off in size can be countered by optimizing the prestretch. Figure 4.11 shows the influence of the initial outer radius on the capacitance sensitivity. As the initial radius increases, the slope of the curve also increases. An increase in slope means higher sensor sensitivity. The curves for the numerical results compare well with the experimental results within 3% error.

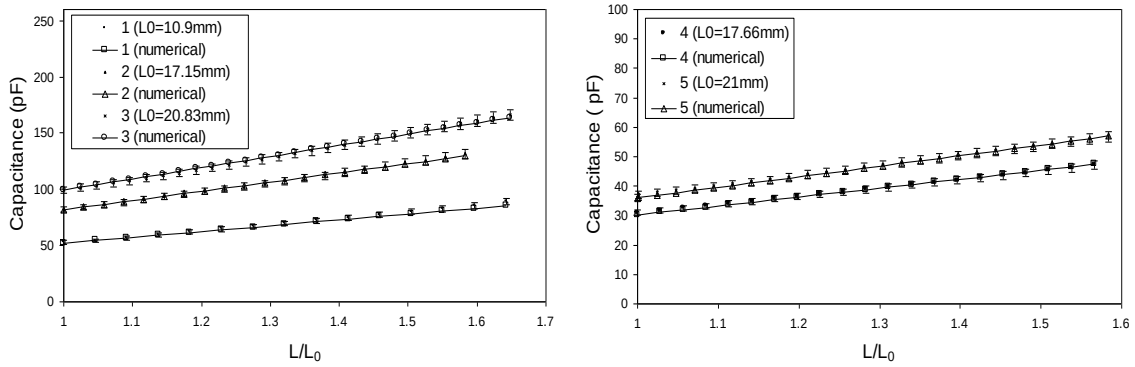

Figure 4.10. Effect of the length on the capacitance sensitivity (3M VHB).

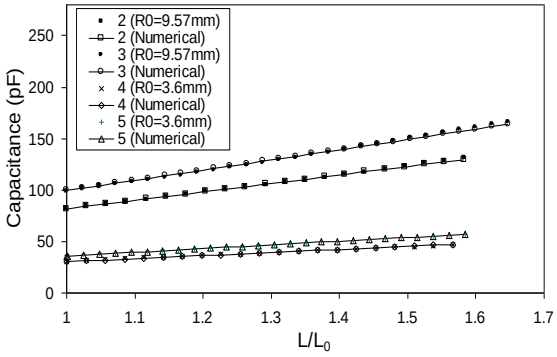

Figure 4.11. Effect of outer radius on the capacitance sensitivity (3M VHB).

As is expected from Equation (4.27), the relationship between the capacitance and the extension ratio is linear and the results indicate that the initial dimensions of the dielectric elastomer affect the sensitivity. The changes of the slope are summarized in Table 4.2. Sample 3, which has the largest initial radius and length, has the highest slope among the 3M VHB samples (Table 4.2).

Table 4.2. Slopes (Capacitance / Axial stretch) of the experimental results for samples 1~10.

Sample (3M VHB)	**1**	**2**	**3**	**4**	**5**
Slope of curve (*pF*/Axial stretch)	56.42	84.62	104.62	28.32	34.39
Sample (Silicone)	**6**	**7**	**8**	**9**	**10**
Slope of curve (*pF*/Axial stretch)	146.56	206.15	304.75	113.93	121.93

In the second set of experiments, five silicone DE sensors (Samples 6–10) were fabricated by spincoating two-part solutions of silicone (CF 19-2186) using the spin coater (Model P6700, Specialty coating systems. IMC). This method allows more refined control of initial sensor thickness.

The initial dimensions of each sample are given in Table 4.1. Each sample was tested 5 times using the setup in Figure 4.9. The Ogden material constants of silicone sensors are μ_1=22.9 *kPa*, μ_2=31.3 *kPa*, μ_3=-0.11 *kPa*, k_1=0.268, k_2=0.263 and k_3=-13.44.

Figure 4.12 shows the relationship between the capacitance and axial stretch for different initial dimensions (length and radius) of the sensors. These results show the same trend as those in

Figure 4.10 and Figure 4.11. The slopes of the curves are shown in Table 4.2. The numerical results compare well with the experimental results within an overall error of 6%. From these results we can conclude that silicone sensors have better sensitivity because of the initial thickness value. In both cases (3M VHB and Silicone), the results show linearity over the test region (Stretch ratio, 1~1.7).

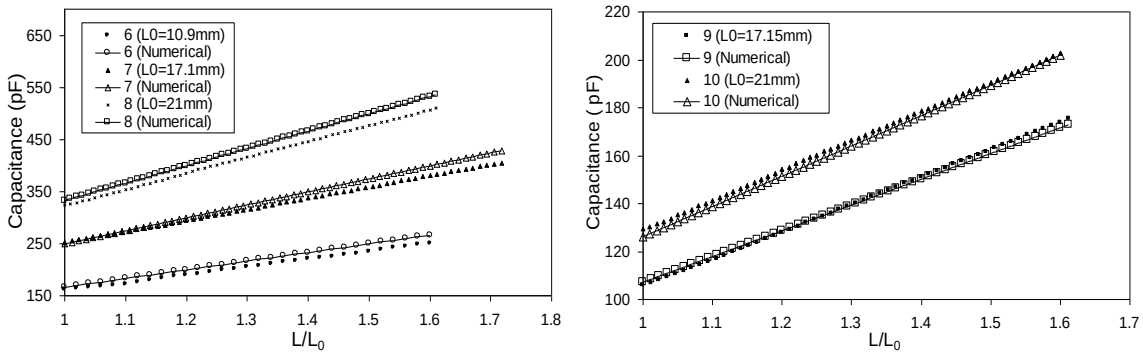

Figure 4.12. Effect of the length of the samples on the capacitance sensitivity (Silicone DE samples).

4.6.2. Inflation and Extension of Sensor/Actuator Composite

For these experiments, tubular dielectric elastomer sensors (VHB 4905 and silicone) are fabricated and placed directly in contact with the inner surface of a McKibben actuator. The initial dimensions of the tested specimens are given in Table 4.3. The fiber angle refers to the initial fiber angle of the braided shell of the McKibben actuator. In this set of experiments, the composite is subject to combined axial and inflation loads. The experimental setup consists of a pneumatic source to inflate the actuator, a capacitance-meter for the sensor, and a linear stage to apply axial loads. A schematic of the experimental setup is given in Figure 4.13. It is considered that the initial shape of the specimen is a perfect cylinder and its deformed shape does not remain perfectly cylindrical.

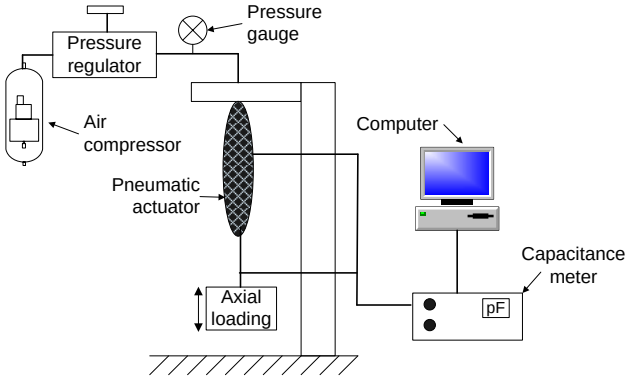

Figure 4.13. Experimental setup for a pneumatic actuator with attached tubular sensor.

Table 4.3. Initial dimensions of pneumatic actuator with tubular dielectric elastomer sensor (3M VHB (V1~V5) and Silicone film (S1~S3)).

Sample	L_0 (*mm*)	R_0 (*mm*)	t_0 (*mm*): tube	t_0 (*mm*): sensor	Fiber angle (°)
V1	65	6.4	1.2	0.5	20
V2	65	6.4	1.2	0.5	25
V3	65	6.4	1.2	0.5	30
V4	50	6.4	1.2	0.5	30
V5	60	6.4	1.2	0.5	30
S1	65	6.4	1.2	0.09	20
S2	65	6.4	1.2	0.09	25
S3	65	6.4	1.2	0.09	30

Figure 4.14 and Figure 4.15 show the experimental and numerical results for 3M VHB DE sensors (V1–V3) and silicone DE sensors (S1–S3) for a pure internal pressure test. The inflation pressure is varied from 0 to 160 *kPa*. The relationship between capacitance and pressure is nonlinear and the nonlinearity is shifted to a higher pressure range when the fiber angle decreases. The DE sensor is not inherently nonlinear. The nonlinearity arises from the nonlinear relationship between pressure and stretch of the McKibben actuator. To illustrate, consider Figure 4.16 and Figure 4.17, which show the relationship between pressure and deformed dimensions of the actuator. The observed plateau region in the curves is due to constrained motion as opposed to sensor insensitivity. In Figure 4.15, the initial capacitance value is higher

and the slope is also much larger than for the VHB samples (Figure 4.14) since the silicone sensors are thinner. These results also show that the fiber angle has significant effects on the actuation response which is coupled into the capacitance measurements. The curves for the numerical results compare well with the experimental results within 6% error in Figures 4.14–4.17.

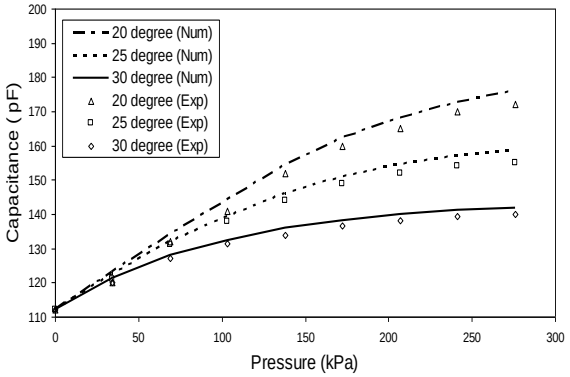

Figure 4.14. Capacitance change with applied pressure V1~V3 (3M VHB).

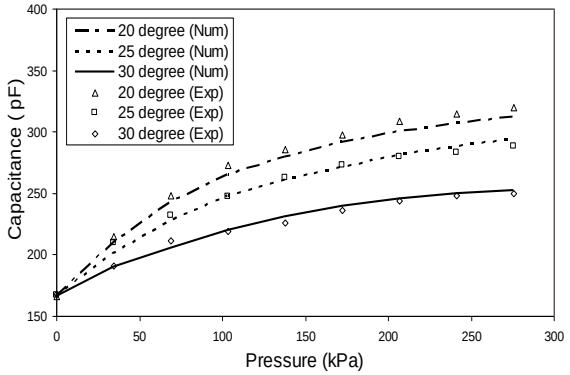

Figure 4.15. Capacitance change with applied pressure S1~S3 (Silicone).

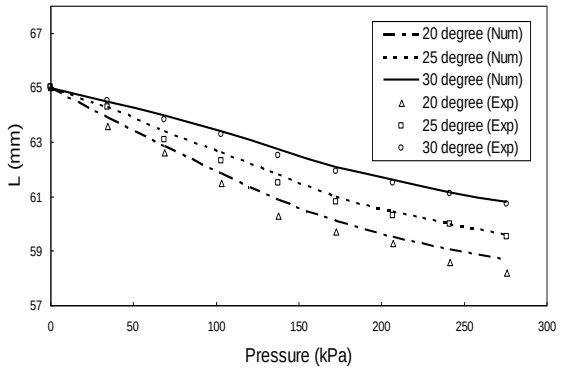

Figure 4.16. Deformed length with applied pressure V1~V3 (3M VHB).

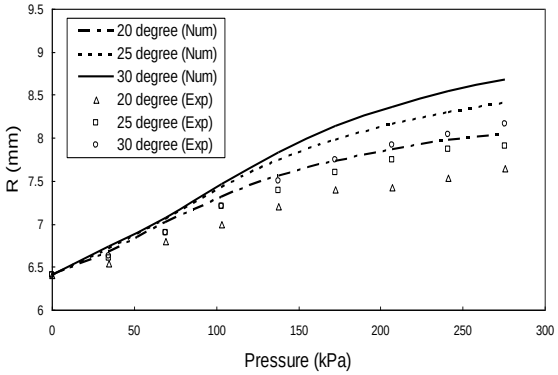

Figure 4.17. Deformed radius with applied pressure V1~V3 (3M VHB).

In Figure 4.18, the effect of the axial loading on the capacitance of the actuator is given for constant pressure values. The internal pressure is kept constant at 137 *kPa* & 207 *kPa* and the axial loading is varied between 0–650 *g*. The relationship between axial loading and capacitance is linear in the test range (0–650 *g*). Since the inextensible fibers constrain the overall deformation, the capacitance decreases when the axial load increases.

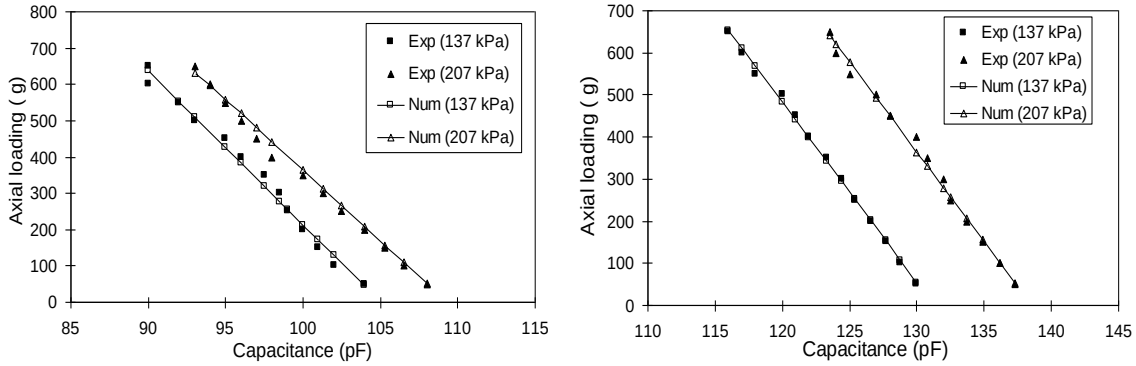

Figure 4.18. The effect of axial loading on the capacitance of VHB DE sensors (V4 and V5).

4.7. Summary

In this paper, a numerical model for tubular dielectric elastomer sensors is derived using large deformation membrane theory and electrostatics. Specifically, numerical models for tubular dielectric elastomer sensors and a pneumatic actuator with sensor integration are formulated. An Ogden material model is used to describe the rubber elastic tube of the actuator and the dielectric elastomers. The constitutive models are integrated into the boundary value problem so that numerical results for three different loading conditions can be studied. A comparison of numerical results and experimental results are presented for (i) the DE sensor and (ii) the sensor/actuator composite. Results for simple extension of 3M VHB and silicone DE sensors indicate that the relationship between the capacitance and extension ratio is linear and sensor sensitivity is affected by the initial dimensions of DE, particularly thickness can be used to significantly improve sensitivity. When the silicone DE sensors are used, the sensitivity is increased due to lower thickness values. For the actuator with the integrated DE sensor, it is observed that the relationship between pressure and capacitance is nonlinear due to the inextensible fibers. The relationship between axial load and capacitance, however, is linear.

Overall, the sensor is viable for a stretch range of 1–1.6. The experimental data for the tubular dielectric elastomer sensor shows good correlation with the numerical modeling results with 3~6% overall error. Therefore, the modeling approach, which is a combination of large deformation theory of fiber reinforced elastomers and electrostatics is a good tool for predicting DE sensor response. It should be noted that the model predicts both axial loading and the deformation state (simultaneously) for a known inflation pressure. Furthermore, this is the first large stretch sensor model for DE sensors.

4.8. References

1. Son, S. and N.C. Goulbourne, *Finite Deformations of Tubular Dielectric Elastomer Sensors*. Journal of Intelligent Material Systems and Structures, 2009. **vol 20**: p. 2187-2199.
2. Baldwin, H.A. *Muscle-like contractive devices*. in *Bionics Symposium*. 1963. Aeronautical Sys. Div./Aerospace Med. Div. Wright-Patterson AFB.
3. Chou, C. and B. Hannaford. *Measurement and Modeling of McKibben Pneumatic Artificial Muscles*. in *IEEE Transactions on Robotica and Automation*. 1996.
4. Klute, G., *Accounting for Elastic Energy Storage in McKibben Artificial Muscle Actuators*. Transactions of ASME, Journal of Dynamic Systems, Measurement, and Control, 2000. **122**: p. 386-388.
5. Klute, G., J. Czerniecki, and B. Hannaford. *McKibben Artificial Muscles: Pneumatic Actuators with Biomechanical Intelligence*. in *IEEE/ASME International Conference on advanced intelligent mechatronics*. 1999. atlanta.
6. Repperger, D.W., et al. *A study of pneumatic muscle technology for possible assistance in motility*. in *Proceeding of the IEEE EMBS*. 1997. Chicago.
7. Reynolds, D.B., et al., *Modeling the Dynamic Characteristics of Pneumatic Muscle*. Annals of Biomedical Engineering, 2003. **31**: p. 310-317.
8. Schulte, H.F., *The Application of External Power in Prosthetics and Orthotics: The Characteristics of the McKibben Artificial Muscle* N.A.o.S.-N.R. Council, Editor. 1961. p. 94-115.
9. Nakamura, T., N. Saga, and K. Yaegashi. *Development of a Pneumatic Artificial Muscle based on Biomechanical Characteristics*. in *IEEE Transactions on* 2003. Maribor.
10. Takuma, T., et al. *Design of Self-Contained Biped Walker with Pneumatic Actuators*. in *SICE Annual Conference* 2004. Sapporo.
11. Mangan, E., et al., *A biologically Inspired Gripping Device*. Industrial Robot: An International Journal, 2005. **32**(1): p. 49-54.

12. Mangan, E., et al. *Development of a Peristaltic Endoscope*. in *Proceedings IEEE: International Conference on Robotics and Automation*. 2002. Washington DC.
13. Vaidyanathan, R., H. Chiel, and R. Quinn, *A hydrostatic robot for marine applications.* Robotics and Autonomous Systems, 2000. **30**: p. 103-113.
14. Kopecny, L. *Producing of Tactile Feedback via Pneumatic Muscles*. in *IEEE ICIT*. 2003. Maribor.
15. Green, A.E., and Adkins, J. E., *Large Elastic Deformations*. 1970, London: Oxford University Press.
16. Adkins, J.E. and R.S. Rivlin, *Large elastic deformations of isotropic materials -- IX. Deformation of thin shells.* Philosophical Transactions, 1952. **244(888)**(505-531).
17. Adkins, J.E. and R.S. Rivlin, *Large elastic deformations of isotropic materials X. Reinforced by in extensible cords.* Royal Society of London -- Philosophical Transactions Series A, 1955. **2418**(201-223).
18. Kydoniefs, A.D., *Finite Axisymmetric Deformations of an Initially Cylindrical Elastic Membrane Enclosing a Rigid Body,.* Quarterly Journal of Mechanics and Applied Mathematics, 1968. **22**: p. 319-331.
19. Kydoniefs, A.D. and A.J.M. Spencer, *Finite Axisymmetric Deformations of An Initially Cylindrical Elastic Membrane.* Quarterly Journal of Mechanics and Applied Mathematics, 1968. **22**: p. 87-95.
20. Kydoniefs, A.D., *Finite Axisymmetric Deformations of an Initially Cylindrical Membrane Reinforced with Inextensible Cords.* Quarterly Journal of Mechanics and Applied Mathematics, 1969. **23**: p. 481-488.
21. Matsikoudi-Iliopoulou, M., *Finite axisymmetric deformations with torsion of an initially cylindrical membrane reinforced with one family inextensible cords.* International Journal of Engineering Science, 1987. **25**(6): p. 673-80.
22. Liu, W. and C.R. Rahn, *Fiber-Reinforced Membrane Models of McKibben Actuators.* Journal of Applied Mechanics, Transactions ASME, 2003. **70**(6): p. 853-859.
23. Hart-Smith, L.J. and J.D.C. Crisp, *Large elastic deformations of thin rubber membranes.* International Journal of Engineering Science, 1967. **5**(1): p. 1-24.
24. Goulbourne, N., E. Mockensturm, and M. Frecker, *A nonlinear model for dielectric elastomer membranes.* Journal of Applied Mechanics, Transactions ASME, 2005. **72**(6): p. 899-906.
25. Goulbourne, N.C., E.M. Mockensturm, and M.I. Frecker, *Electro-elastomers: Large deformation analysis of silicone membranes.* International Journal of Solids and Structures, 2007. **44**(9): p. 2609-2626.
26. Fox, J.W. and N.C. Goulbourne, *On the dynamic electromechanical loading of dielectric elastomer membranes.* Journal of the Mechanics and Physics of Solids, 2008. **56**(8): p. 2669-2686.
27. Fox, J.W., *Electromechanical Characterization of the Static and Dynamic Response of Dielectric Elastomer Membranes*, in *Mechanical Engineering*. 2007, Virginia Polytechnic Institute and State University: Blackburg.
28. Wakimoto, S., K. Suzumori, and T. Kanda. *Development of intelligent McKibben actuator with built-in soft conductive rubber sensor*. in *TRANSDUCERS '05. The 13th International Conference on Solid-State Sensors, Actuators and Microsystems. Digest of Technical Papers, 5-9 June 2005*. 2005. Piscataway, NJ, USA: IEEE.

29. Yang, G., et al. *The Strain Response of Silicone Dielectric Elastomer Actuators*. in *International Conference on Smart Materials Structures and Systems*. 2005. Bangalore.
30. Pelrine, R., R. Kornbluh, and G. Kofod, *High-Strain Actuator Materials Based on Dielectric Elastomers.* Advanced Materials, 2000. **12**(16): p. 1223-1225.
31. Fox, J.W. and N.C. Goulbourne. *A Study on the Effect of Flexible Electrodes and Passive Layers on the performance of dielectric Elastomer Membranes*. in *Proceedings ASME IMECE*. 2006. Chicago.
32. Ogden, R.W., *Large Deformation Isotropic Elasticity - On the Correlation of Theory and Experiment for Incompressible Rubberlike Solids.* Philosophical Transactions of the Royal Society of London. Series A, 1972. **326**(565-584): p. 398-416.
33. Ogden, R.W., G. Saccomandi, and I. Sgura, *Fitting hyperelastic models to experimental data*. Computational Mechanics, 2004. **34**(6): p. 484-502.
34. Rosenthal, M., et al. *Applications of dielectric elastomer EPAM sensors*. 2007. San Diego, CA, United States: SPIE, Bellingham WA, WA 98227-0010, United States.
35. Goulbourne, D.N.C., S. Son, and J.W. Fox. *Self-sensing McKibben actuators using dielectric elastomer sensors*. 2007. San Diego, CA, United States: SPIE, Bellingham WA, WA 98227-0010, United States.

Chapter 5. Dynamic Response of Tubular Dielectric Elastomer Transducers

(This was published in International Journal of Solids and Structures (Son and Goulbourne [1]))

Seyul Son[a,b] **N. C. Goulbourne**[b]
[a]Center for Intelligent Material Systems and Structures, Virginia Polytechnic Institute and State University, Blacksburg, VA, 24060
[b]Soft Material Research Lab, Department of Aerospace Engineering, University of Michigan, Ann Arbor, MI, 48109-2140

5.1. Abstract

In this paper, a numerical model for the dynamic response of tubular dielectric elastomer transducers is presented and validated with experimental results for the first time. Dielectric elastomers (DE) are soft polymer based smart materials that can be potentially employed in applications such as actuation, sensing and energy harvesting [2-4]. In our previous work, the quasi-static response of tubular DE transducers was studied [5, 6]. Here, a numerical model is developed to predict the dynamic response of tubular DE transducers. Inertia effects are included in our previous static model which yields a system of partial differential equations. The results of the dynamic response of the tubular DE transducers are obtained by numerically solving the simplified partial different equations using a finite difference scheme. The capacitance change induced by the dynamic deformation of the tubular DE is also calculated by a simple electrostatic model, illustrating dynamic passive sensing.

Several tubular DE transducer samples (VHB 4905 and silicone) were fabricated and an experimental setup was developed to investigate the dynamic response by measuring capacitance

and radial deformation. In the sensing experiments, a sweep of dynamic pressure profiles (0–5*Hz*) is applied. It is observed that silicone transducers have a larger dynamic sensing range. In the actuation experiments, the deformation of the silicone actuator is monitored while a voltage signal (4.5kV) is applied from 0–30*Hz*. The silicone actuator shows a good actuation response. The comparison between numerical and experimental results for the DE transducers shows an overall error of 3%.

5.2. Introduction

The purpose of this research is to study the dynamic response of tubular dielectric elastomer transducers using both an experimental and numerical modeling approach. Dielectric elastomers can be employed as actuators, large strain sensors and for energy harvesting [2-4, 7]. Dielectric elastomer sensors are essentially compliant capacitors, which have a capacitance that varies with mechanical strain, or alternatively, the resistance can be monitored. In general, conventional sensor materials are relatively stiff and fail at low strains within 2.5–5.0%. Dielectric elastomer sensors provide various advantages such as large strain range, simple fabrication, low cost, low weight, repeatability and shape compliance [8, 9]. Dielectric elastomer actuators are large strain electro-active polymers with areal strains up to 300% [10].

In the previous work, a finite deformation model for dielectric elastomer membranes in actuation mode was derived [11]. In this paper, a dynamic model for tubular configurations is derived by combining a modified large deformation membrane theory that accounts for the coupling electromechanical effect in actuation commonly referred to as the Maxwell stress and the dynamic capacitance change under finite strains which accounts for passive sensing is calculated. The equations are simplified with the assumption that the inertia effect in the

meriodinal direction is negligible. The dynamic model consists of a set of PDEs (Partial differential equations). A finite difference scheme (forward difference method) is used to simulate the dynamic response of the tubular DE transducer. The numerical method is general and can readily be employed for other axisymmetric configurations, and has a moderate computing time. The running time for the numerical method can be reduced by optimizing the finite difference algorithm.

Dynamic characterization of edge-clamped DE membrane actuators in a diaphragm configuration was conducted using an experimental approach in [12, 13]. The static response of tubular DE sensors was studied and numerical results were validated with experiments in [5, 14]. Tubular DE transducers have been previously analyzed by [9, 15]. Carpi *et al*. proposed a static model for actuation which was validated within the small strain range (0–5.0%). The model was based on the linear elasticity theory [15]. An actuation characterization of spring roll DE actuators has been conducted using analysis techniques [9]. The previous works have focused on the static actuation response and was limited to small strains. In this paper, a finite deformation model is used to describe the dynamic response of these transducers in both actuation and sensing modes [16]. For large elastic deformations, the developments by Adkins and Rivlin [16, 17], Kydoniefs [18-20], and Matsikoudi-Iliopoulou [21] are most notable. The dynamic mechanical response of elastic membranes has been studied by Jenkins [22], Tüzel [23] and Verron [24, 25] to name a few. Specifically, Jenkins *et al*. applied dynamic approaches to the dynamic inflation field while considering the membrane's inertia [22] and Tüzel studied the dynamic response of an isotropic hyperelastic membrane tube, subjected to a dynamic extension at one end [23]. Verron applied the Mooney-Rivlin model or non-linear viscoelastic Christensen's model to the dynamic inflation of spherical membranes [24, 25]. The dynamic

response of planar dielectric elastomer actuators was investigated in [26] by measuring current change while a high voltage (~6kV) was applied and the strain decrease of the DE actuator presumed due to material viscoelasticity was presented [27]. Here the dynamic inflation of tubular membrane in the presence of an electric field is considered.

Experimental results are obtained to validate the proposed dynamic modeling approach. The experimental procedure is devised to measure the dynamic deformation and capacitance of the DE membrane in sensing mode, in actuation mode, and in simultaneous sensing and actuation mode. For dynamic sensing the electromechanical response is measured while a dynamic pressure was applied for various frequencies, 0–5.0Hz. The tubular DE sensors are prepared with 3M VHB 4905 and silicone films (NuSil Technology: CF 19-2186), which are commercially available and spincoated in situ, respectively. They are electroded with carbon grease (Carbon Conductive Grease, M.G. Chemicals). Two end cylindrical shapes (Radius=9.5 and Length=10mm) of the transducers are made of fluoropolymers (Teflon® PTFE, McMaster-Carr Supply Company). The dynamic pressure is generated for low frequencies (~2.5Hz) and higher frequencies (2.5–5.0Hz). A comparison between the dynamic behavior of the VHB and silicone sensors is presented. For the dynamic actuation behavior of tubular DEs, radial deformations of the tubular DE actuator are monitored while a dynamic voltage signal is applied with various frequencies, 0~30Hz. In the actuation experiments, since VHB with radial prestretch did not show good actuation response while high voltage (4.5kV) is applied, only silicone DEs are used in the actuation experiments.

5.3. Principle of Dielectric Elastomer Transducer

Dielectric elastomers are large strain electromechanical transducers. The dielectric elastomer transducer is a three-component system consisting of a compliant elastomeric insulator sandwiched between two compliant electrodes. For the sensing configuration, mechanical strains are detected by measuring one of two electrical parameters: capacitance or resistance. These sensors are ideal for large strain sensing applications due to the ability to retain electrical conductivity at large strains – even up to 100%. For actuation, electrostatic forces are induced by applying an electric field to the dielectric elastomer. This results in thickness reduction and an areal expansion in the in-plane directions due to an effect that is amplified by the softness of the material and material incompressibility. A schematic of the typical assembly of a dielectric elastomer transducer as well as depiction of its sensing and actuation mode is given in Figure 5.1 and Figure 5.2.

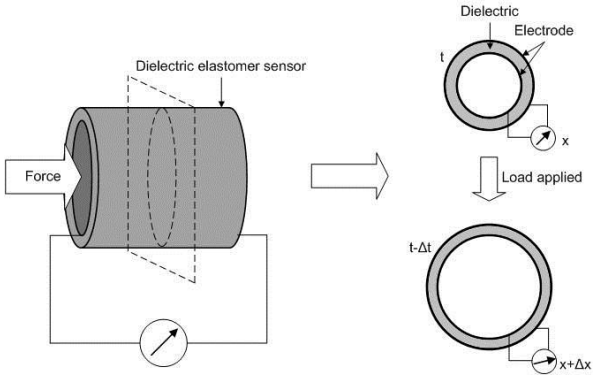

Figure 5.1. Schematic of pressure/strains sensing using a dielectric elastomer.

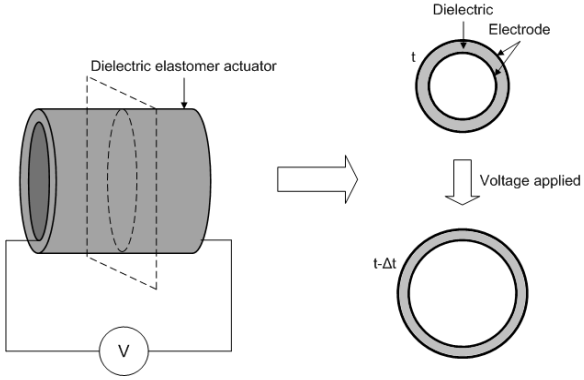

Figure 5.2. Schematic of actuation using a dielectric elastomer.

The two most common types of dielectric elastomers used in fabricating transducers are polyacrylates and silicone elastomers [28, 29]. Failure of a typical specimen of 3M VHB 4905 (polyacrylate) does not occur until a stretch ratio of 8. Applying compliant electrodes to the major surfaces of prestretched dielectric elastomer specimens completes the fabrication process.

We have conducted an experimental evaluation of the large stretch response of different electrodes: carbon grease, silver grease, graphite powder, and graphite spray. The experimental results indicate that carbon grease and silver grease are the best compliant electrodes of the four that were tested; carbon grease has a slightly better overall performance and is also less costly [30].

5.4. Electro-Elastic Model

In this section, the modeling approach for the dynamic response of tubular DE transducer is presented. Specifically, the previous large deformation model for the electromechanical response of DE membranes is augmented to account for dynamic effects.

5.4.1. Geometric Relationships: Coordinates

In this section, a theoretical model to describe the deformation response of tubular DE transducer based on Green and Adkins' work on unreinforced elastic tubes is briefly derived. The tubular DE transducers are modeled as an elastic cylindrical membrane as shown in Figure 5.3. From the symmetry of the problem and the assumption that the membrane is very thin compared with the cylinder's radius, the state of stress is considered nearly constant throughout the thickness (elastic membrane theory assumption). A set of cylindrical polar coordinates (R, Θ, η) at the midplane are employed in the undeformed state. The initial length and radius of the cylindrical membrane are given by L_0 and R respectively. The deformations of the tubular transducer are considered to be entirely symmetric with respect to the z-axis. The meridian length of the cylindrical membrane is denoted η in the undeformed state and ξ in the deformed state. It

follows that the principal directions at any point in the deformed membrane coincides with the deformed coordinates (r, θ, z), and the principal extension ratios are denoted as λ_1, λ_2, and λ_3. Specifically, λ_1 and λ_2 are the meridional and latitudinal stretch ratios that define the deformation and λ_3 is the thickness stretch ratio.

$$r = r(\xi),\ \theta = \Theta,\ z = z(\xi)$$
$$\lambda_1 = \frac{d\xi}{d\eta},\ \lambda_2 = \frac{r}{R},\ \lambda_3 = \frac{h}{h_0}, \tag{5.1}$$

where $2h_0$ and $2h$ are the undeformed and deformed thickness of the membrane.

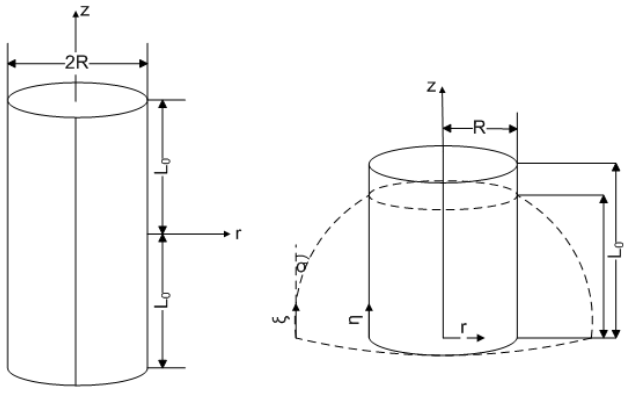

Figure 5.3. An undeformed cylindrical membrane (Left) Half of the undeformed and deformed membrane (Right).

5.4.2. Material Modeling: Electroelastic Stress and Strain Energy Function

It is assumed that the elastic dielectric material is homogenous, isotropic and electrically linear, so that there is no direct coupling between the mechanical and the electrical response. We hypothesize that the stress for the material can be written as the sum of the elastic and Maxwell stresses. Therefore, the total stresses are divided into the two parts, mechanical and electrical portion. The mechanical portion is determined by an elastic strain energy function (Mooney-Rivlin function). The electrical portion is given by the Maxwell stress. In accordance with

Adkins' and Rivlin's solution approach, we presume that the applied forces normal to the cylindrical surfaces are negligible in comparison to the in-plane stresses and set n_3=0. The stress components of the membrane are then given by

$$
\begin{aligned}
n_1 &= 2\left(\lambda_2^2 - \frac{1}{\lambda_1^2\lambda_2^2}\right)\left(\frac{\partial W}{\partial I_1} + \lambda_1^2\frac{\partial W}{\partial I_2}\right) - \frac{1}{2}\left(\varepsilon_0\varepsilon_r\left(\frac{V}{h\lambda_3}\right)^2\right), \\
n_2 &= 2\left(\lambda_1^2 - \frac{1}{\lambda_1^2\lambda_2^2}\right)\left(\frac{\partial W}{\partial I_1} + \lambda_2^2\frac{\partial W}{\partial I_2}\right) - \frac{1}{2}\left(\varepsilon_0\varepsilon_r\left(\frac{V}{h\lambda_3}\right)^2\right), \\
n_3 &= 0,
\end{aligned}
\tag{5.2}
$$

where n_1, n_2, and n_3 are the meridional, radial, and thickness stress components and W is a Mooney-Rivlin energy function.

Figure 5.4 shows the fit of the strain energy function with experimental uniaxial data for 3M VHB 4905. The Mooney-Rivlin model fits well with experimental data up to a stretch ratio around 4.

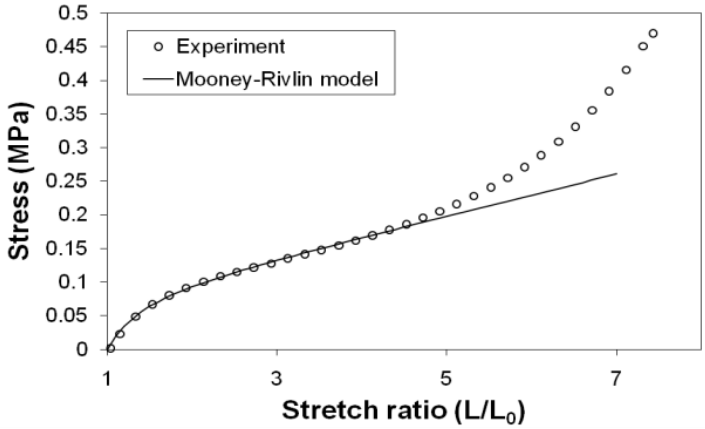

Figure 5.4. Stress vs stretch data for VHB 4905 samples compared with Mooney-Rivlin model.

For simplification of the partial differential equations using the finite difference scheme, the Mooney-Rivlin function is employed for describing the stress-strain behavior of dielectric elastomers (VHB 4905 & Silicone). The Mooney-Rivlin function has the form,

$$W = C_1(I_1 - 3) + C_2(I_2 - 3), \tag{5.3}$$

where I_1 and I_2 are strain invariants and C_i (i=1 and 2) are Mooney-Rivlin constants determined from uniaxial extension tests on rectangular samples supporting a uniformly distributed axial load (Table 5.1) [6].

Table 5.1. Mooney-Rivlin constants for VHB 4905 and Silicone.

Mooney-Rivlin constants	C_1 (kPa)	C_2 (kPa)
VHB 4905	16	7.3
Silicone	163	34.2

During deformation, the initial thickness $2h_0$ of the membrane becomes $2\lambda_3 h_0$ and the stress resultants are obtained by integrating over the deformed thickness

$$\begin{aligned} \mathrm{N}_1 &= 2\lambda_3 \mathrm{h}_0 \mathrm{n}_1 = 2\lambda_3 \mathrm{h}_0 \left\{ 2\left(\lambda_2^2 - \frac{1}{\lambda_1^2 \lambda_2^2} \right)\left(\frac{\partial W}{\partial I_1} + \lambda_1^2 \frac{\partial W}{\partial I_2} \right) - \frac{1}{2}\left(\varepsilon_0 \varepsilon_\mathrm{r} \left(\frac{V}{h\lambda_3} \right)^2 \right) \right\}, \\ \mathrm{N}_2 &= 2\lambda_3 \mathrm{h}_0 \mathrm{n}_2 = 2\lambda_3 \mathrm{h}_0 \left\{ 2\left(\lambda_1^2 - \frac{1}{\lambda_1^2 \lambda_2^2} \right)\left(\frac{\partial W}{\partial I_1} + \lambda_2^2 \frac{\partial W}{\partial I_2} \right) - \frac{1}{2}\left(\varepsilon_0 \varepsilon_\mathrm{r} \left(\frac{V}{h\lambda_3} \right)^2 \right) \right\}. \end{aligned} \tag{5.4}$$

5.4.3. Equations of Motion for Tubular DE Membranes

The equations of motion in the meridional and radial directions are expressed as,

$$\begin{aligned} &\frac{dN_1}{d\xi} + \frac{N_1}{r}\frac{dr}{d\xi} - \frac{N_2}{r}\frac{dr}{d\xi} = 2h_0 \rho R \frac{d^2\xi}{dt^2}, \\ &P - \kappa_1 N_1 - \kappa_2 N_2 = 2h_0 \rho R \frac{d^2 r}{dt^2}. \end{aligned} \tag{5.5}$$

where κ_1 and κ_2 are the principal curvatures given by,

$$\kappa_1 = \frac{-d^2 r / d\xi^2}{(1 - (d^2 r / d\xi^2)^2)^{1/2}} \text{ and } \kappa_2 = \frac{1}{r}(1 - (dr / d\xi)^2)^{1/2}. \tag{5.6}$$

For simplification, it is assumed that inertia effects in the meriodinal direction are negligible. Therefore, the first equation of motion in Equation (5.5) becomes an equilibrium equation due to $d^2\xi/dt^2=0$ and results in only the second equation of motion in Equation (5.6) to solve.

The independent variable ξ in the deformed state is rewritten as the independent variable η in the undeformed state by using the chain rule.

$$\begin{aligned}&\frac{dr}{d\xi}=\frac{R}{\lambda_1}\frac{d\lambda_2}{d\eta},\\&\frac{d^2r}{d\xi^2}=\frac{d}{d\xi}\left(\frac{R}{\lambda_1}\frac{d\lambda_2}{d\eta}\right)=\frac{1}{\lambda_1}\frac{d}{d\eta}\left(\frac{R}{\lambda_1}\frac{d\lambda_2}{d\eta}\right).\end{aligned} \tag{5.7}$$

Therefore, Equation (5.5) and (5.6) can be rewritten using Equation (5.7)

$$\begin{aligned}&\frac{dN_1}{d\xi}+\frac{N_1}{r}\frac{dr}{d\xi}-\frac{N_2}{r}\frac{dr}{d\xi}=0,\\&P-\kappa_1N_1-\kappa_2N_2=2h_0\rho R\frac{d^2\lambda_2}{dt^2}.\end{aligned} \tag{5.8}$$

$$\kappa_1=-\frac{\left(\frac{1}{\lambda_1}\frac{d}{d\eta}\left(\frac{R}{\lambda_1}\frac{d\lambda_2}{d\eta}\right)\right)^2}{\sqrt{\left(1-\left(Rd\lambda_2/\lambda_1 d\eta\right)^2\right)}},\ \kappa_2=\sqrt{\frac{1}{\lambda_2}\left(\frac{1}{R^2}-\left(\frac{1}{\lambda_1}\frac{d\lambda_2}{d\eta}\right)^2\right)}. \tag{5.9}$$

For dynamic solutions, the initial conditions are the radial deformation and deformation rate which are defined at t = 0. Boundary conditions are defined at one end and the mid-length of the cylinder. At the fixed end, the radial deformation is equal to zero and the curvature in the meridional direction at the middle of the membrane is zero.

$$\lambda_2(\eta,0)=\lambda_2(\eta),\quad \frac{d\lambda_2}{dt}(\eta,0)=0. \tag{5.10}$$

$$\lambda_2(L_0,t)=1,\quad \kappa_1=-\left.\frac{\left(\frac{1}{\lambda_1}\frac{d}{d\eta}\left(\frac{R}{\lambda_1}\frac{d\lambda_2}{d\eta}\right)\right)^2}{(1-\left(Rd\lambda_2/\lambda_1 d\eta\right)^2)^{1/2}}\right|_{\eta=0}=0. \tag{5.11}$$

The capacitance of the deformed tubular sensor is modeled by utilizing large deformation membrane theory and electrostatics. The approach is based on the assumption that the membrane is very thin compared with the tubular sensor's radius, as well as axisymmetric deformation [14]. The capacitance of the unit volume of the deformed tubular membrane is calculated using electrostatics. The total capacitance of the tubular membrane is obtained by integrating the capacitance of the unit volume with respect to the axis. The capacitance for an axisymmetric tubular membrane is

$$C = \varepsilon_0 \varepsilon_r 2\pi R \int_1^{\lambda_2(0)} \frac{1}{\ln\left(\dfrac{R\lambda_2 + h_0 \dfrac{1}{\lambda_1\lambda_2}}{R\lambda_2 - h_0 \dfrac{1}{\lambda_1\lambda_2}}\right)} \frac{1}{\tan\sigma} d\lambda_2. \tag{5.12}$$

where σ is the angle between membrane curve and vertical direction in Figure 5.3, ε_r is the relative permittivity and ε_0 is the vacuum permittivity.

5.4.4. Numerical Solution Procedure

In order to obtain the numerical solutions for the dynamic response of tubular DE transducers, a finite different scheme (forward difference method) is employed. The equation of motion, Equation (5.8) is second order in time and space and thus impossible to solve analytically. The first and second derivatives with respect to time and space are

$$\begin{aligned}
&\lambda_1 = \lambda_{1,i}^j, \lambda_2 = \lambda_{2,i}^j, \\
&\frac{d\lambda_1}{d\eta} = \frac{\lambda_{1,i+1}^j - \lambda_{1,i}^j}{h}, \frac{d\lambda_2}{d\eta} = \frac{\lambda_{2,i+1}^j - \lambda_{2,i}^j}{h}, \\
&\frac{d^2\lambda_2}{d\eta^2} = \frac{\lambda_{2,i+2}^j - 2\lambda_{2,i+1}^j + \lambda_{2,i}^j}{h^2}, \\
&\frac{d^2\lambda_2}{dt^2} = \frac{\lambda_{2,i}^{j+2} - 2\lambda_{2,i}^{j+1} + \lambda_{2,i}^j}{k^2}.
\end{aligned} \tag{5.13}$$

where *i* and *j* are the space and time indices respectively as well as *h* and *k* are space and time increments.

The parameters *h* and *k* are defined as

$$h = \frac{L_0}{n}, k = \frac{T}{m}. \tag{5.14}$$

where *n* and *m* are the space and time component number and *T* is the time period.

The equation of motion, initial conditions, and boundary conditions are rewritten by using the finite different method as

$$P - \kappa_1 N_1 - \kappa_2 N_2 = 2h_0 \rho R \frac{\lambda_{2,i}^{j+2} - 2\lambda_{2,i}^{j+1} + \lambda_{2,i}^{j}}{k^2}. \tag{5.15}$$

$$\lambda_2(\eta,0) = \lambda_{2,i}^0, \frac{d\lambda_2}{dt}(\eta,0) = \frac{\lambda_{2,i}^1 - \lambda_{2,i}^0}{k} = 0. \tag{5.16}$$

$$\lambda_{2,n}^j = 1, \kappa_1 = -\left. \frac{\left(\frac{1}{\lambda_{1,0}^j} \frac{d}{d\eta} \left(\frac{R}{\lambda_{1,0}^j} \frac{\lambda_{2,1}^j - \lambda_{2,0}^j}{h} \right) \right)^2}{(1 - \left(\frac{R}{\lambda_{1,0}^j} \frac{\lambda_{2,1}^j - \lambda_{2,0}^j}{h} \right)^2)^{1/2}} \right|_{\eta=0} = 0. \tag{5.17}$$

In the case of *j*=0, Equation (5.15) by inserting Equation (5.16) becomes

$$\lambda_{2,i}^2 = \frac{k^2}{2h_0 \rho R} \left(P - \kappa_1 N_1 - \kappa_2 N_2 \right) + \lambda_{2,i}^1. \tag{5.18}$$

To ensure convergence of the solution, the *k* value is changed until $\lambda_{2,n}^2$ converges to 1, which matches with boundary condition, Equation (5.16). Considering *j* = 1, Equation (5.15) becomes

$$\lambda_{2,i}^3 = \frac{k^2}{2h_0 \rho R} \left(P - \kappa_1 N_1 - \kappa_2 N_2 \right) + 2\lambda_{2,i}^2 - \lambda_{2,i}^1. \tag{5.19}$$

Similarly, the solution at *j* = 1 is obtained when $\lambda_{2,n}^2$ is converged to 1 by changing the *k* value. By repeating the previous steps for *j* = 2,3,4,…, *m*, numerical solutions are obtained.

5.5. Experimental and Numerical Results

In this section, the dynamic characteristics of tubular VHB and silicone transducers are presented. In Section 5.5.1, the experimental setup for the dynamic response is described. In Section 5.5.2, the sensing response is analyzed. Specifically, the frequency response is monitored while dynamic pressure is applied at various frequencies. In Section 5.5.3, the actuation response is described. The response is measured while dynamic high voltage is applied with various frequencies. For the validation of our modeling approach, the experimental results are compared with the numerical results, which are simulated using finite difference scheme, described in Section 5.5.4.

5.5.1. Experimental Setup

In this section, the sample preparation procedure and experimental setup are presented. Polyacrylate and silicone films are used to make tubular DE samples. 3M VHB is commercially available and silicone films are fabricated using a spincoater [6] and the initial dimensions are given in Table 5.2. For a length to radius ratio of one, the edge constraints could limit the radial deformation of the middle cross-section of the sample. Figure 5.5 shows the effect of the length-radius ratio (L/R) on the radial deformation. According to Figure 5.5, the effect of L/R is negligible within pressure range considered in this research ($0–2000Pa$).

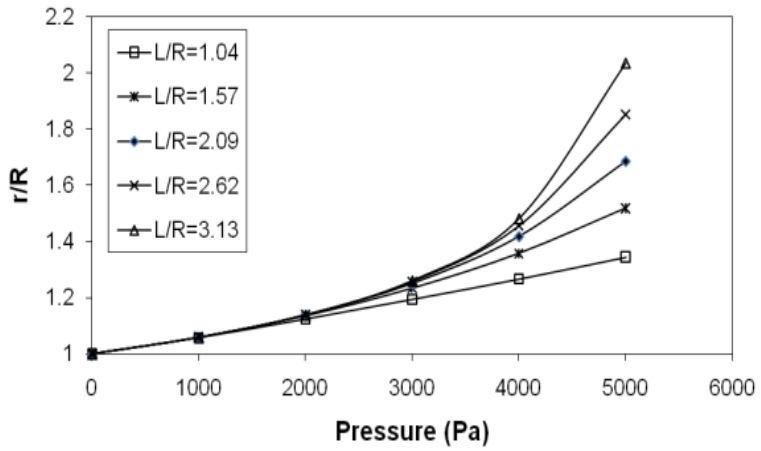

Figure 5.5. The effect of *L/R* on the radial deformation of the sample.

In the experimental setup (Figure 5.6), dynamic responses of tubular DE sensor/actuator are obtained by measuring the capacitance and the radial deformation at the midpoint of the transducer, which are measured by a capacitance meter (Model 3000, GLK) and a triangular optical laser sensor (Model LTC-050-20, MTI INSTRUMENT, INC). Dynamic pressure is used to inflate the tubular sensor and actuator by a combination of a syringe (140*CC*), linear stage (NLS4 Series linear stage, Newmark systems, INC) and solenoid valves (SY3340-SGZ, SMC), and measured by a pressure sensor (163PC01D36, OMEGA). A high voltage dynamic signal is applied by supplying a LabVIEW generated signal to an amplifier (Model 610E, Trek, INC).

Table 5.2. The initial dimensions of tubular DE sensor and actuator (VHB 4905 and silicone film).

Sample	R (*mm*)	L (*mm*)	t (*mm*)
VHB sensor	9.56	20	0.5
Silicone sensor	9.56	20	0.1
Silicone actuator	9.56	20	0.2

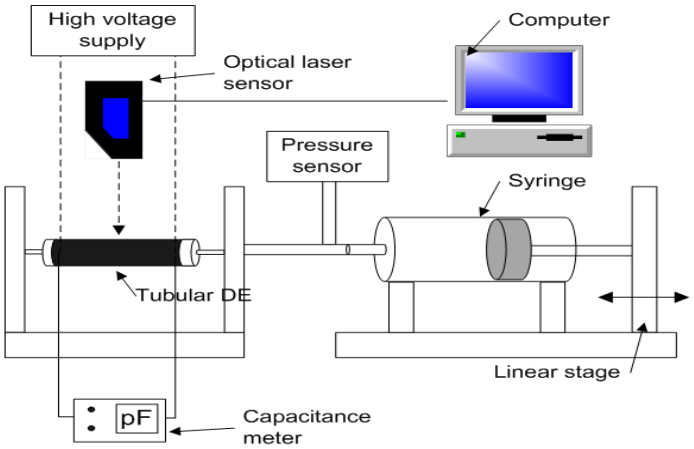

Figure 5.6. Experimental setup for dynamic response of tubular DE sensors and actuators.

For the tubular DE sensor experiment, the fabricated tubular samples are attached to a frame (Figure 5.6) and a dynamic pressure (1400 and 2000*Pa*) is applied with excitation frequencies ranging from 0–5.0*Hz*. Higher frequencies (2.5–5.0*Hz*) are generated by opening and closing the solenoid valves. For the tubular DE actuator experiment, the linear stage and syringe provide a static pressure (2000*Pa*) and a dynamic voltage (4.5*kV*) is applied with excitation frequencies ranging from 0–30*Hz*. In each of these experiments, 3 tests for 4 each samples are performed.

5.5.2. Dynamic Response of Tubular DE Sensors with Dynamic Pressure Input

The initial capacitance value of the VHB sensor is 85 *pF* and the initial dimensions of the sensor are given in Table 5.2. Figure 5.7 and 5.8 show the capacitance change and deformed radius of the tubular VHB sensor while a dynamic pressure (2000*Pa*) is applied at 0.3 *Hz*. At a low frequency (0.3 *Hz*), there is no delay between the pressure signal, the measured capacitance, and deformed radius. The maximum values of the measured capacitance and deformed radius are consistently measured to be 107 *pF* and 11 *mm* as shown in Figure 5.7 and Figure 5.8. That is to

say, the VHB sensor has a good quasi-static sensing response Figure 5.9 and Figure 5.10 show the sensing response of the VHB sensor at 2.0 *Hz*. For a 2.0 *Hz* signal of amplitude 2000 *Pa*, the capacitance signal is not identical to the dynamic pressure signal and the maximum value of capacitance decays with time. To understand the output signal further, which exhibits a definite rise and decay time, a comparison between the radial deformation and the input pressure is conducted. Figure 5.10 shows that the mechanical response (radial deformation) of the VHB sensor at 2.0 *Hz* is identical to the pressure signal and there is no delay. Therefore, the dissimilarity between the capacitance and the pressure signal is electrical in nature. There is an apparent time required for charging/discharging the VHB sensor. That is to say, the VHB tubular sensor is capacitive in nature. Additionally, the amplitude of the radial deformation decreases as the cycle is repeated. This is due to the material viscoelasticity. VHB sensors do not have a linear dynamic response at frequencies above 2.0 *Hz*. The sensor has good quasi-static behavior, but a poor dynamic response above 2.0 *Hz*.

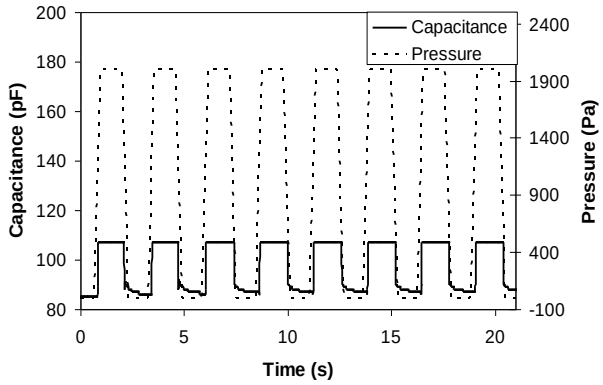

Figure 5.7. Dynamic capacitance of a VHB sensor at 0.3 *Hz*.

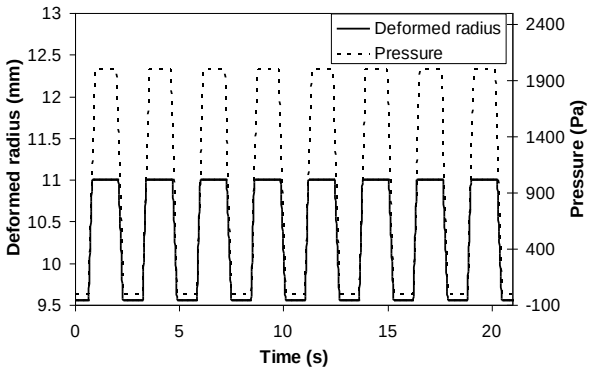

Figure 5.8. Radial deformation of a tubular VHB sensor at 0.3 *Hz*.

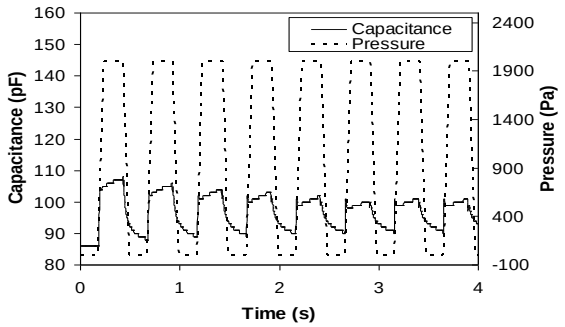

Figure 5.9. Dynamic capacitance of a VHB sensor at 2.0 *Hz*.

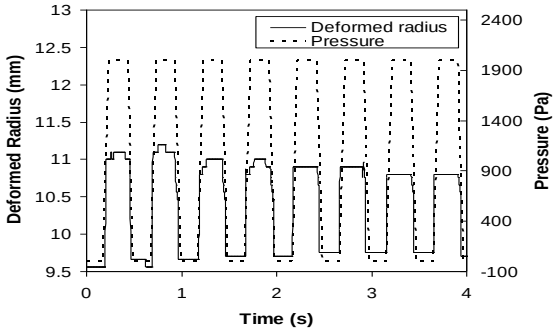

Figure 5.10. Radial deformation of a tubular VHB sensor at 2.0 *Hz*.

Between the frequency ranges of 0 to 5.0 *Hz*, the capacitance change and radial deformation of the tubular silicone sensor are monitored while a dynamic pressure is applied. Initially, the capacitance value of the depressurized sensor is 435 *pF*. Initial dimensions of the sensor are given in Table 5.2. It should be noted that the dynamic pressure profile is not a perfect rectangular shape. It is expected that the dynamic response of the silicone sensor shows linearity in proportion to the dynamic pressure. In Figure 5.11 and Figure 5.12, the somewhat quasi-static response of a silicone sensor (0.17 *Hz*) is shown. In detail, Figure 5.11 shows that the measured capacitance is identical to the dynamic pressure signal and the dynamic maximum value of the capacitance is 485 *pF*. That is to say, the silicone sensor shows a linear relationship between the mechanical input and the electrical output. Comparatively, Figure 5.12 shows the deformation of the membrane corresponding to the measured capacitance in Figure 5.11. Figure 5.13 and Figure 5.14 illustrates the dynamic response of the silicone sensor at 4.7 *Hz*. In Figure 5.13, it is shown that the maximum value of the capacitance is 485 *pF*, but there is a slight delay between the mechanical input and the electrical output. Similarly in Figure 5.14, the maximum radial deformation is 10.30 *mm* at a pressure of 1400 *Pa* but, there is almost no delay or time lag between the mechanical input and the output. Therefore, the delay in Figure 5.13 exists only

between the mechanical input and the electrical output. This appears to be related to the electrical charging and discharging time for the silicone sensor.

In summary, both VHB and silicone sensors show good quasi-static sensing behavior. The experimental analysis indicates that the maximum capacitance value of the VHB sensor at 2.0 *Hz* decays in time and the electrical output signal is delayed due to charging/discharging time (around 0.3s at 2.0 *Hz*), so that the VHB sensor shows poor dynamic response. On the other hand, the silicone sensor outputs a non-decaying signal and the charging/discharging time is significantly less around 0.05s at 4.7 *Hz*. Therefore, it can be concluded that the silicone sensor has a wider dynamic range in comparison to VHB sensors.

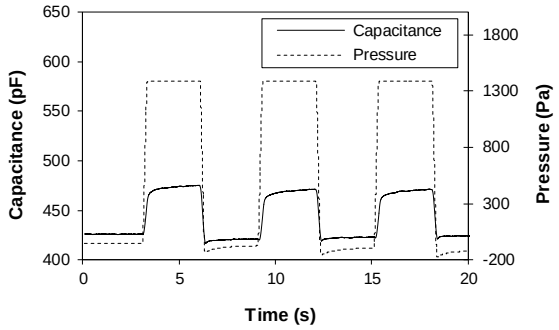

Figure 5.11. Capacitance change of a tubular silicone sensor at 0.17 *Hz*.

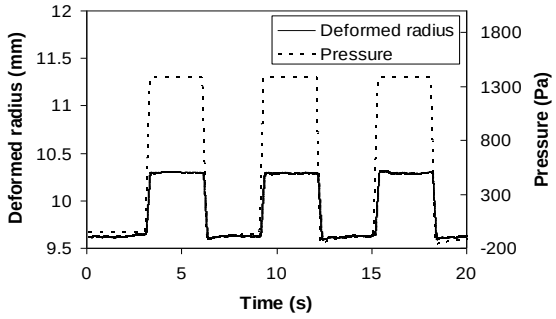

Figure 5.12. Radial deformation of a tubular silicone sensor at 0.17 *Hz*.

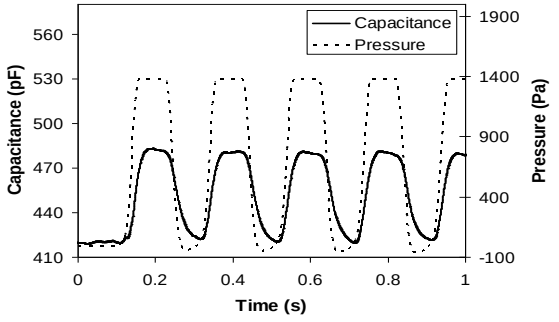

Figure 5.13. Capacitance change of a tubular silicone sensor at 4.7 *Hz*.

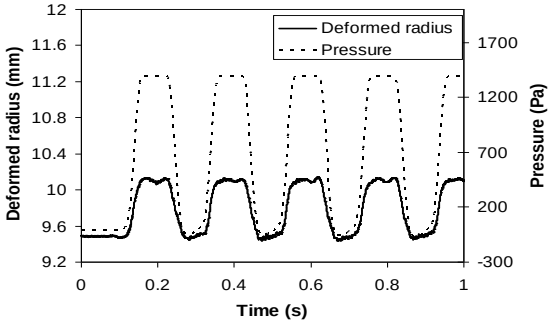

Figure 5.14. Radial deformation of a tubular silicone sensor at 4.7 *Hz*.

Figure 5.15 and 5.16 show a comparison between numerical and experimental results for the silicone sensor at 1400 *Pa* at 5.0 *Hz*. In Figure 5.15 and 5.16, there are differences between the numerical (rectangular) and experimental results (close to trapezoid), although the minimum and maximum values have a good correlation. The trapezoidal curve of the experimental capacitance results in Figure 5.15 is due to the discharging and charging time for the silicone sensor as well as the trapezoidal shape of the dynamic pressure input. Also, the measured radial deformation in Figure 5.16 comes from the trapezoidal shape of the experimental pressure input. Since these factors in the experiment are not included in the theoretical model, the differences in the results are expected. The comparison between maximum/minimum values of numerical and experimental capacitance and radial deformation in Figure 10 shows within 3% overall error.

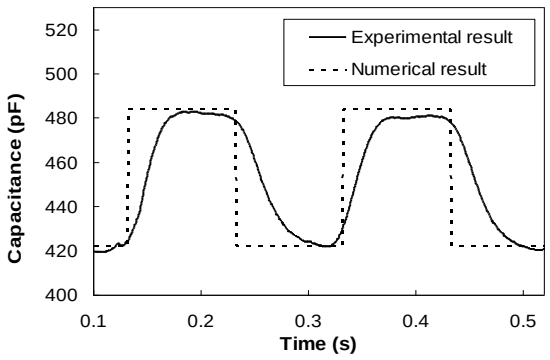

Figure 5.15. Comparison of numerical and experimental results for capacitance sensing (5.0 *Hz*).

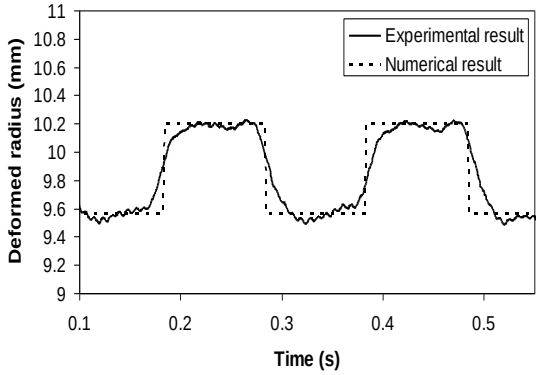

Figure 5.16. Comparison of radial deformation between numerical and experimental results (5.0 *Hz*).

5.5.3. Dynamic Response of Tubular DE Actuators with Dynamic Voltage Input

A series of experiments were conducted in which a dynamic voltage input between 0 and 30 *Hz* with an amplitude of 4.5 *kV* was applied to the tubular membrane. The initial dimensions of the

transducers are given in Table 2. Radial deformation of the initially pressurized tubular silicone actuator (2000 *Pa*) is measured while a dynamic voltage is applied. The radius of the tubular silicone actuator with the static pressure is 10.80 *mm*. Figure 5.17 and Figure 5.18 describe the relationship between the electrical input (voltage) and the mechanical output (radial deformation) for the given frequency values. Since there is a linear relationship and no delay between electrical input and mechanical output, good dynamic actuation responses of the tubular silicone actuator are shown. The normalized maximum amplitudes ((Deformed radius-10.80)/(10.80–9.56)) for 3 sets of voltage sweeps (1–30 *Hz*) are shown in Figure 5.19. The maximum amplitude averages around 0.5 below 15 *Hz*, and reaches 0.6 at 20–22 *Hz* and then steadily declines with increasing frequency.

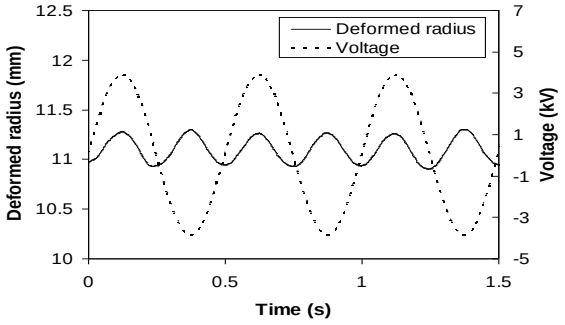

Figure 5.17. Radial deformation of tubular silicone actuator at 2.0 *Hz*.

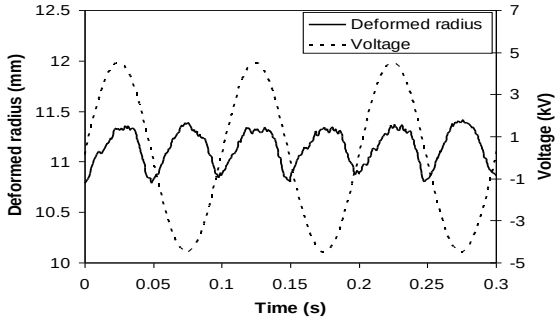

Figure 5.18. Radial deformation of tubular silicone actuator at 10 *Hz*.

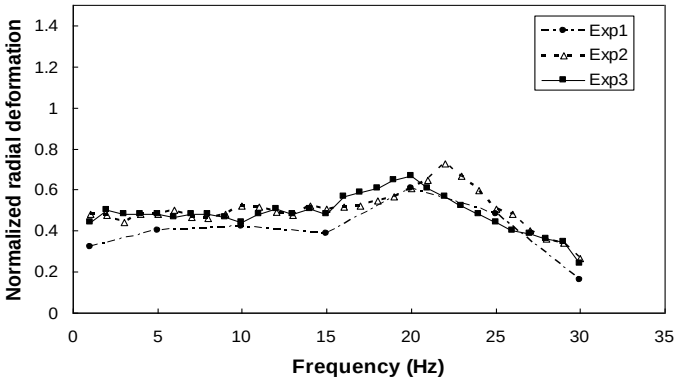

Figure 5.19. Dynamic actuation peak amplitudes for voltage frequencies, 1~30 *Hz*.

Figures 5.20 and 5.12 show the comparison between numerical and experimental results for a 4.5 *kV* signal at 2.0 *Hz* and 10 *Hz*. The experimental curves in Figures 5.20 and 5.21 accord well with the numerical results. The correlation between numerical and experimental results are within 3% overall error. Therefore, the modeling approach that is proposed in this paper is validated by these experimental results.

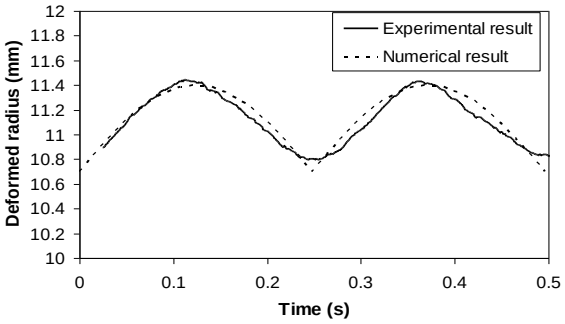

Figure 5.20. Comparison between numerical and experimental results (2.0 *Hz*).

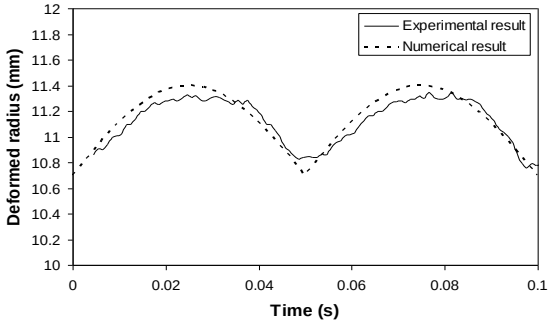

Figure 5.21. Comparison between numerical and experimental result (10 *Hz*).

5.6. Summary

In this paper, the dynamic actuation and sensing response of tubular dielectric elastomers was discussed. A theoretical background for the dynamic model based on a large deformation theory for DE membranes and electrostatics was presented. Numerical results were obtained by employing a finite difference scheme to solve the PDEs. The experiments indicate that both VHB and silicone sensors have good quasi-static sensing behavior. However, for the dynamic response within a limited frequency range, the VHB sensor shows poor response after 2.0 *Hz* and 13% radial strain under an applied dynamic pressure. The tubular silicone sensor shows good sensing response at higher frequencies up to 5.0 *Hz* and 8% radial strain. Tubular silicone actuators were assembled and dynamically actuated with a voltage signal (4.5 *kV*) at 0–30 *Hz*. From the results it can be concluded that tubular silicone transducers have a better dynamic sensing and actuation response in the frequency range analyzed in this research. Comparison

between the maximum values of numerical and experimental results for the silicone sensor and actuator shows good agreement with 3% overall error. This shows that the dynamic model and solution approach based on the finite difference method is a good tool for predicting the finite dynamic deformation of tubular DE sensors and actuators.

5.7. References

1. Son, S. and N.C. Goulbourne, *Dynamic response of tubular dielectric elastomer transducers.* International Journal of Solids and Structures, 2010. **47**(20): p. 2672-2679.
2. Waki, M., et al. *Electric power from artificial muscles*. in *OCEANS 2008 MTS/IEEE Kobe Techno-Ocean, 8-11 April 2008*. 2008. Piscataway, NJ, USA: IEEE.
3. Kornbluh, R., *Dielectric elastomer artificial muscle for actuation, sensing, generation, and intelligent structures.* Materials Technology, 2004. **19**(4): p. 216-224.
4. Carpi, F., et al., *Helical dielectric elastomer actuators.* Smart Materials and Structures, 2005. **14**(Copyright 2005, IEE): p. 1210-16.
5. Goulbourne, D.N.C., S. Son, and J.W. Fox. *Self-sensing McKibben actuators using dielectric elastomer sensors*. 2007. San Diego, CA, United States: SPIE, Bellingham WA, WA 98227-0010, United States.
6. Son, S. and N.C. Goulbourne, *Finite Deformations of Tubular Dielectric Elastomer Sensors.* Journal of Intelligent Material Systems and Structures, 2009. **vol 20**: p. 2187-2199.
7. Carpi, F., et al., *DIELECTRIC ELASTOMERS AS ELECTROMECHANICAL TRANSDUCERS. Fundamentals, Materials, Devices, Models and Applications of an Emerging Electroactive Polymer Technology*. 2008: Oxford: ELSEVIER. 344.
8. Rosenthal, M., et al. *Applications of dielectric elastomer EPAM sensors*. 2007. San Diego, CA, United States: SPIE, Bellingham WA, WA 98227-0010, United States.
9. Pei, Q., et al., *Multiple-degrees-of-freedom electroelastomer roll actuators.* Smart Materials and Structures, 2004. **13**(5): p. 86-92.
10. Pelrine, R., et al., *High-speed electrically actuated elastomers with strain greater than 100%*. Science, 2000. **287**(5454): p. 836-9.
11. Goulbourne, N., E. Mockensturm, and M. Frecker, *A nonlinear model for dielectric elastomer membranes.* Journal of Applied Mechanics, Transactions ASME, 2005. **72**(6): p. 899-906.
12. Fox, J.W. and N.C. Goulbourne, *On the dynamic electromechanical loading of dielectric elastomer membranes.* Journal of the Mechanics and Physics of Solids, 2008. **56**(8): p. 2669-2686.
13. Fox, J.W., *Electromechanical Characterization of the Static and Dynamic Response of Dielectric Elastomer Membranes,* in *Mechanical Engineering*. 2007, Virginia Polytechnic Institute and State University: Blackburg.

14. Goulbourne, N.C. and S. Son. *Numerical and experimental analysis of McKibben actuators and dielectric elastomer sensors*. 2008. Seattle, WA, United States: American Society of Mechanical Engineers, New York, NY 10016-5990, United States.
15. Carpi, F. and D. De Rossi, *Dielectric elastomer cylindrical actuators: Electromechanical modelling and experimental evaluation.* Materials Science and Engineering C, 2004. **24**(4): p. 555-562.
16. Adkins, J.E. and R.S. Rivlin, *Large elastic deformations of isotropic materials X. Reinforced by in extensible cords.* Royal Society of London -- Philosophical Transactions Series A, 1955. **2418**(201-223).
17. Adkins, J.E. and R.S. Rivlin, *Large elastic deformations of isotropic materials -- IX. Deformation of thin shells.* Philosophical Transactions, 1952. **244(888)**(505-531).
18. Kydoniefs, A.D., *Finite Axisymmetric Deformations of an Initially Cylindrical Elastic Membrane Enclosing a Rigid Body,.* Quarterly Journal of Mechanics and Applied Mathematics, 1968. **22**: p. 319-331.
19. Kydoniefs, A.D., *Finite Axisymmetric Deformations of an Initially Cylindrical Membrane Reinforced with Inextensible Cords.* Quarterly Journal of Mechanics and Applied Mathematics, 1969. **23**: p. 481-488.
20. Kydoniefs, A.D., *FINITE AXISYMMETRIC DEFORMATIONS OF INITIALLY CYLINDRICAL REINFORCED MEMBRANES.* Rubber Chemistry and Technology, 1972. **45**(6): p. 1677-1683.
21. Matsikoudi-Iliopoulou, M., *Finite axisymmetric deformations with torsion of an initially cylindrical membrane reinforced with one family inextensible cords.* International Journal of Engineering Science, 1987. **25**(6): p. 673-80.
22. Jenkins, C.H., *Nonlinear dynamic response of membranes: State of the art - update.* Applied Mechanics Reviews, 1996. **49**(10 pt 2): p. 41-48.
23. Tüzel, V.H. and H.A. Erbay, *The dynamic response of an incompressible non-linearly elastic membrane tube subjected to a dynamic extension.* International Journal of Non-Linear Mechanics, 2004. **39**(4): p. 515-537.
24. E. Verron, R.E.K., A. Derdouri and B. Peseux, *Dynamic inflation of hyperelastic spherical membranes.* Journal of Rheology, 1999. **43**(5): p. 1083-1097.
25. Verron, E., G. Marckmann, and B. Peseux, *Dynamic inflation of non-linear elastic and viscoelastic rubber-like membranes.* International Journal for Numerical Methods in Engineering, 2001. **50**(5): p. 1233-1251.
26. Sommer-Larsen, P., et al. *Response of dielectric elastomer actuators*. 2001. Newport Beach, CA: Society of Photo-Optical Instrumentation Engineers.
27. Pei, Q., et al. *Multifunctional electroelastomer roll actuators and their application for biomimetic walking robots*. 2003. San Diego, CA, United States: The International Society for Optical Engineering.
28. Yang, G., et al. *The Strain Response of Silicone Dielectric Elastomer Actuators*. in *International Conference on Smart Materials Structures and Systems*. 2005. Bangalore.
29. Pelrine, R., R. Kornbluh, and G. Kofod, *High-Strain Actuator Materials Based on Dielectric Elastomers.* Advanced Materials, 2000. **12**(16): p. 1223-1225.
30. Fox, J.W. and N.C. Goulbourne. *A Study on the Effect of Flexible Electrodes and Passive Layers on the performance of dielectric Elastomer Membranes*. in *Proceedings ASME IMECE*. 2006. Chicago.

Chapter 6. Large Strain Analysis of a Soft Polymer Electromechanical Sensor Coupled to an Arterial Segment

(This was submitted in Journal of Intelligent Material Systems and Structures)

Seyul Son[a,b] **N. C. Goulbourne**[b]
[a]Center for Intelligent Material Systems and Structures, Virginia Polytechnic Institute and State University, Blacksburg, VA, 24060
[b]Soft Material Research Lab, Department of Aerospace Engineering, University of Michigan, Ann Arbor, MI, 48109-2140

6.1. Abstract

Dielectric elastomer (DE) membranes are one of the most promising transducers for developing soft large strain sensors. In this paper, we describe the sensor response for a potential biomedical application. It is widely accepted that diseased arteries at various stages have a unique constitutive response. This means that ideally the output of an in situ artery sensor would have distinct profiles corresponding to various stages of unhealth. An in situ sensor can potentially allow access to information about the mechanical state of the artery that is not currently available. Furthermore, the potential to combine the functions of providing structural support (stent) and monitoring the mechanical state (sensor) is appealing. Traditional sensors such as strain gages and piezoelectric sensors are stiff and fail at low strains (< 1%) whereas some dielectric elastomers are viable at strains up to and even surpassing 100%. Investigating the electromechanical response of a deformable tube sensor sandwiched between a pulsating pressure source and a nonlinear elastic distensible thick wall has not been attempted before now.

The successful development of a multiphysics model that correlates the electrical output of a pulsatile membrane sensor to its state of strain would be a significant breakthrough in medical diagnostics. The artery is described using a structural model for a tubular membrane reinforced with two families of initially crimped fibers subject to a pulsating pressure profile. In this paper, the fundamental mechanics associated with electromechanical coupling during dynamic finite deformations of DEs is derived. A continuum model for the dynamic response of tubular dielectric elastomer membranes configured for sensing is presented. The pressure profile leads to a nonlinear response of the artery-sensor due to the nonlinear deformation behavior of the arterial wall. At pressures above $13kPa$, the artery undergoes infinitesimal deformation which leads to very small changes in the sensor signal. In this range, fabricating thinner sensors and synthesizing hybrid polymers with higher dielectric constants can enhance the sensitivity.

Keywords: artery, dielectric elastomer, sensor.

6.2. Introduction

The main purpose of this paper is to describe a structural model for an arterial segment and to use the model to describe the response of a soft in situ sensor subject to pulsatile loads. Arteries will have a unique constitutive response at various stages of disease progression due to local mechanical changes in the tissue. It is then expected that an implanted sensor would detect distinct profiles corresponding to various stages of unhealthy conditions. Unhealthy arteries can be caused by the blockage of the artery by plaque, calcification and hardening of the biological membrane. There are a variety of tests to detect heart disease such as electrocardiogram, stress test, echocardiography, computerized tomography and coronary angiography via cardiac

catheterization. In advanced cases, stent deployment is one of the commonly employed procedures to correct artery blockage. Once the stent is deployed, there is no means of locally tracking the state of that arterial segment. A multifunctional stent, one restoring structural integrity to the artery as well providing local state information, would be of utmost value. The DE sensor is a soft sensor that is easily fabricated, has low cost, low weight, repeatability, shape compliance, and operable at large strains [1, 2]. In this paper, we seek to understand the response of an in situ tubular DE sensor placed in contact with an arterial segment. Specifically, a numerical model of the electromechanical response of a tubular DE sensor placed in contact with the artery is studied.

The artery is a highly deformable material that shows a nonlinear constitutive response for a physiological pressure range (normal blood pressure: $16/10 kPa$). One modeling approach is to initially consider the artery as a hyper-elastic membrane with an anisotropic contribution due to the embedded wavy collagen fibrils, which can be modeled as crimping fibers in the undeformed state that are straightened during the deformation. The gradual straightening of the originally undulated fibers has been studied by [3-8]. Comninou and Yannas and Lanir developed the structural theory for the crimping collagen fibers with a sinusoidal wave, which correlated reasonably well with experimental data [3, 4]. Freed and Doehring considered the wavy collagen fibers as a three-dimensional structure wave form (which is a helical spring) on the geometry of a cylindrical helix and their model allowed compression [7, 8]. In the present model, the crimping collagen fibers in the reference configuration is represented by sinusoidal curves similar to the approaches in [3, 4] and it is assumed that when the fibers are undulated they do not carry any tension and hence do not contribute structurally to the overall material stress, which is dominated by the isotropic membrane in that phase. Once the fibers are straightened, they carry a tension.

This is equivalent to phenomenological treatments whereby the fiber constitutive response is represented by an exponential function making the fiber contribution negligible in the low strain range of the overall tissue response.

Collectively, the artery is represented as a fiber-reinforced tubular membrane and our approach is based on the work of Green, Adkins, and Rivlin [9-11]. Adkins and Rivlin formulated a large deformation theory for thin membranes and solved a series of axially symmetric problems for fiber reinforced membranes [9, 12]. The general formulation for fiber-reinforced elastic tubular membranes has also been treated by Kydoniefs and Matsikoudi-Iliopoulou [13-16]. Kydoniefs investigated the axisymmetric deformation of an initially tubular membrane with two families of inextensible fibers [13-15]. Matsikoudi-Iliopoulou described a reinforced membrane with one family of fibers to model torsion, inflation, and extension [16]. The general concept of a fiber-reinforced constitutive model for the artery was first introduced by Holzapfel *et al*. [17]. In their model, the structure of the artery is reduced from a three layered fibrous structure to an isotropic tubular non-collagen layer and two families of collagen fibers to represent the artery. The effect of the fibers is incorporated through the definition of an anisotropic strain energy function. In the strain energy function proposed by Holzapfel *et al.* [17], the non-collagen part of the arterial adventitia is mechanically viewed as an isotropic *Neo*-Hookean material. The strain energy function is disassociated into isotropic and anisotropic parts [18]. In the proposed model in this paper, the isotropic part of the artery (non-collagen part: Adventitia) is described using an isotropic strain energy function (*Neo*-Hookean model) and the two families of fibers are considered as structural components that place restraints on the overall deformation when they are straightened.

In principle, DE sensors are compliant capacitors, which have a capacitance that varies with mechanical strain; alternatively, the resistance can be monitored. The varying capacitance induced by the deformation of the tubular DE sensors is used as a measure of the deformation state. In this paper, a numerical model for the DE sensor is based on elastic membrane theory and electrostatics. In our previous work, a finite deformation model for DE membranes in actuation mode was derived [19] and a quasi-static model for a tubular DE sensor was derived in [20]. The quasi-static model for tubular DE sensors was validated with experiments in [20] whereby a fiber-reinforced membrane was employed as the host. The fiber-reinforced membrane consists of a rubbery elastic membrane bladder wrapped with a helical two-family fiber mesh. Here, we consider a model for a tubular DE sensor placed in contact with the inner surface of an artery as shown in Figure 6.1. It is assumed that the DE sensor does not inhibit the behavior of the artery and hence undergoes equivalent deformations. [21-23]

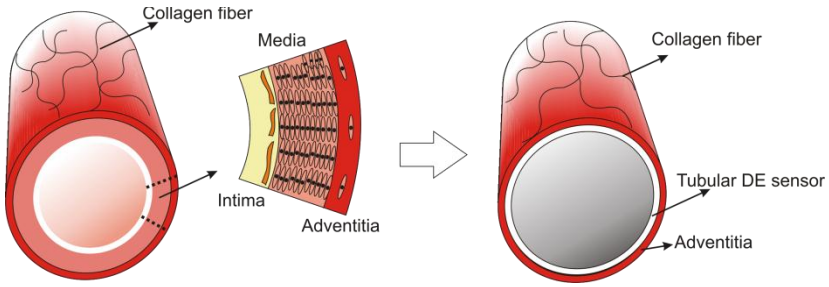

Figure 6.1. Schematic of an arterial segment with tubular DE sensor.

In this paper, numerical results are presented to validate the proposed modeling approach for the artery-DE sensor composite. This is a structural approach (see [20]) which differs from semi-structural and phenomenological approaches employed by [17, 18, 24, 25] amongst others in modeling the artery. Quasi-static results for the pulsatile response of the artery with physiologically valid pressures and frequencies (1–2*Hz*) are presented. Furthermore, with the sensor in contact with the membrane, the dynamic electromechanical response (capacitance

change) is calculated for physiologically valid pressures and frequencies. Based on large deformation membrane theory and electrostatics, a numerical model for the large strain sensing response of the tubular DE sensor is presented and solved.

In Section 6.3, the mathematical modeling for the quasi-static and dynamic response of the artery and tubular DE sensor is outlined. Based on the modeling in Section 6.3, numerical results are obtained for pressures from 0–20 *kPa* in the 1–2 *Hz* frequency range in Section 6.4. Specifically, the mechanical deformation of the artery and the electromechanical response of the tubular DE sensor are discussed in Section 6.4.

6.3. Modeling Approach for the Artery

In this section, a continuum mechanics based modeling approach for the quasi-static response of an artery in contact with a soft sensor is presented. The mathematical formulation is based on a combination of large deformation elastic membrane theory and electrostatics. Geometric relationships for the artery referred to a cylindrical coordinate system are established and geometric relationship of the crimping fibers in the undeformed state is explained in Section 6.3.1. The constitutive stress strain relationships for the artery which is considered as a fiber-reinforced tubular membrane are described in Section 6.3.2. Specifically, the isotropic portion is modeled as a *Neo*-Hookean material and two families of fibers are regarded as structural components. The governing equations are provided in Section 6.3.3. An expression for the capacitance of the tubular DE sensor with respect to the deformation of the artery is derived in Section 6.3.4.

6.3.1 Geometric Relationships for the Isotropic Membrane and Crimping Fibers

In this section, a theoretical model to describe the deformation response of the artery based on Green and Adkins' work on fiber-reinforced tubular membrane is briefly outlined. As shown in Figure 6.2, the artery is modeled as an elastic tubular membrane. From the symmetry of the problem and the assumption that the membrane is very thin compared with the tube's radius, the state of stress is considered nearly constant throughout the thickness (elastic membrane theory assumption). A set of cylindrical coordinates (R, Θ, η) at the midplane are employed in the undeformed state. The initial length and radius of the cylindrical membrane are given by L_0 and R_0. The deformations are considered to be entirely symmetric with respect to the z-axis. The meridian length of the artery is denoted η in the undeformed state and ξ in the deformed state. It follows that the principal directions at any point in the deformed membrane coincides with the deformed coordinates (r, θ, z), and the principal extension ratios are denoted by λ_1, λ_2 and λ_3. Specifically, λ_1 and λ_2 are the meridional and latitudinal stretch ratios that define the deformation and λ_3 is the thickness stretch ratio.

$$r = r(\xi), \theta = \Theta, z = z(\xi),$$
$$\lambda_1 = \frac{d\xi}{d\eta}, \lambda_2 = \frac{r}{R}, \lambda_3 = \frac{h}{h_0}, \tag{6.1}$$

where $2h_0$ and $2h$ are the undeformed and deformed thickness of the membrane. There are two fiber families: the initial angles of the fibers are $\alpha_1 = \alpha_2 = 39.98°$, $49.98°$ and $59.98°$ (chosen to be physiologically consistent) [24] and once deformed are located at the deformed angle β as shown in Figure 6.2. Two families of fibers are undulated in the reference state with the mean initial fiber angles α_1 and α_2 and the straightened fiber length L_f. The arterial wall deforms without

fiber tensions until the fibers are straightened at the deformed fiber angle β_1 *and* β_2 in Figure 6.2 (Right). Subsequently, the arterial wall deforms with the fiber tensions engaged.

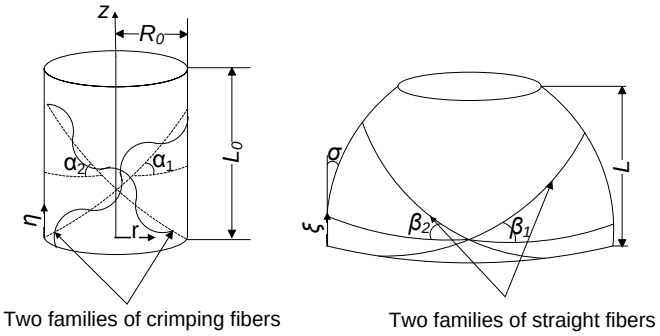

Figure 6.2. Half of the undeformed artery (symmetry presumed) with crimping fibers (Left) and the deformed artery with straight fibers (Right).

Let's assume that the crimping fibers in Figure 6.2 (Left) are continuous with all the same shape and natural lengths and there is no relative motion between the isotropic membrane and the fibers. The shape of the crimping fibers is regarded as a sinusoidal waveform (in Equation (6.2) and Figure 6.3) with respect to the undeformed membrane length ($L_0/sin\alpha_i$), (i=1 and 2) in the direction of the mean fiber angle α_i Note that dx initially coincides with $d\eta/sin\alpha_i$.

$$y = A\sin\left(2\pi\left(\frac{2\sin\alpha}{L_0}x\right)\right). \tag{6.2}$$

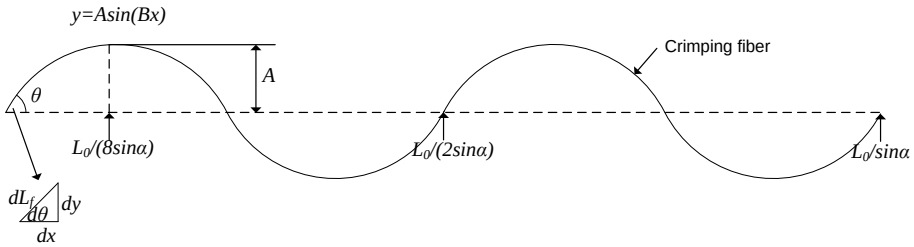

Figure 6.3. Schematic of a crimping fiber.

The straightened fiber length L_f can be obtained by using simple geometric relations from Figure 6.3,

$$
\begin{aligned}
&d\theta = \tan^{-1}\left(\frac{dy}{dx}\right) = \tan^{-1}(AB\cos Bx),\\
&x = \frac{\eta}{\sin\alpha_i},\quad dx = \frac{d\eta}{\sin\alpha_i},\quad B = \frac{4\pi\sin\alpha_i}{L_0},\\
&dL_f = \frac{d\eta/\sin\alpha_i}{\cos(d\theta)} = \frac{d\eta/\sin\alpha_i}{\cos(\tan^{-1}(AB\cos(B\eta/\sin\alpha_i)))},\\
&L_f = \int_0^{L_0} \frac{d\eta}{\sin\alpha\cos(\tan^{-1}(AB\cos(B\eta/\sin\alpha_i)))}.
\end{aligned}
\tag{6.3}
$$

The amplitude A in Equations (6.2) and (6.3) can be considered a crimping parameter of the fibers. For instance, if the fibers in the reference state are straight then A=0. At $A\neq 0$, the fibers are undulated in the undeformed configuration and there will be no fiber tension until the fibers are straightened. For a fixed natural length, the amplitude then describes the degree of crimping of the fibers. At some point during the deformation of the membrane, the fibers will become straight. To determine when the fibers become straight during the deformation, Equations (6.4)-(6.7) are employed. The undeformed and deformed lengths at the mean fiber angle α_i and β_i are dS and ds, respectively. The stretch ratio in the fiber direction (an arc length along the membrane) can be expressed as,

$$
\left(\frac{ds}{dS}\right)^2 = I_4 = \lambda_1^2\sin^2\alpha_i + \lambda_2^2\cos^2\alpha_i = 1. \tag{6.4}
$$

The relationship between the fiber angles α_i and β_i is obtained by geometric inspection of Figure 6.2,

$$
\begin{aligned}
&\cos(\frac{\pi}{2}-\beta)ds = \lambda_1\cos(\frac{\pi}{2}-\alpha_i)dS,\\
&\sin\beta_i = \lambda_1\sin\alpha_i\,\frac{dS}{ds} = \lambda_1\sin\alpha_i\,(I_4)^{-1/2},\\
&\beta = \sin^{-1}(\lambda_1\sin\alpha_i\,(I_4)^{-1/2}).
\end{aligned}
\tag{6.5}
$$

The deformed membrane length l_m in the z axis (Figure 6.4) is calculated as,

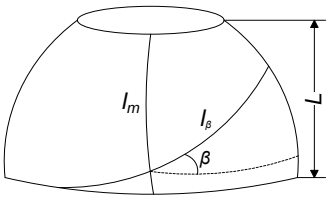

Figure 6.4. Geometric relationship between membrane length l_f and l_β.

$$l_m = \int_0^{L_0} \lambda_1 d\eta. \tag{6.6}$$

Then, the deformed membrane length l_β at the fiber direction β_i (i=1 and 2) (Figure 4) can be obtained by using a geometric relationship in Figure 6.4,

$$l_\beta = \frac{l_m}{\sin \beta_i}. \tag{6.7}$$

Therefore, when l_β is equal to L_f in Equation (6.3) (which is the straightened fiber length), the fiber is straightened and lies along the fiber angle β_i. It is assumed that all fibers straighten at the same moment and are parallel and closely spaced. Note that Gasser *et al*. [24] have proposed formulations that account for a statistical distribution of the fiber angle, which could be employed as an alternate approach to the sensor model developed later in the paper [24].

6.3.2. Material Modeling: Elastic Stress and Strain Energy Function

The artery is modeled as a tubular membrane with two families of crimping collagen fibers. Thus, the total stress resultants N_{ij} are derived from the force required to deform the elastic membrane alone in addition to the tension in the straightened collagen fibers. Recall that the effect of the crimping fibers is included in the reference state, there is no fiber tension until the

fibers are straight ($L_f = l_\beta$). Therefore, there are only stress resultants from the elastic membrane when the fibers are crimped,

$$N_{ij} = n_{ij}\,, \tag{6.8}$$

where n_{ij} is the stress resultant required to deform the membrane itself, (i and j = 1,2 and 3).

After the fibers are straight, the total stress, N_{ij} can be decomposed into two parts

$$N_{ij} = n_{ij} + t_i\,, \tag{6.9}$$

where t_i is the tension due to the collagen fibers (i and j=1,2 and 3).

The decomposition in Equation (6.9) is consistent with Green and Adkins and Rivlins' fiber reinforced membrane model [10, 11]. Employing a similar solution approach, we presume that the applied forces normal to the tubular surfaces are small in comparison to the in-plane stresses and set n_{33}=0. In the deformation, the initial thickness $2h_0$ of the membrane becomes $2\lambda_3 h_0$ and the stress resultants are obtained by integrating the stress components over the deformed thickness. Hence,

$$\begin{aligned} &n_{11} = 4\lambda_3 h_0\left(\lambda_1^2 - \frac{1}{\lambda_1^2\lambda_2^2}\right)\left(\frac{\partial W}{\partial I_1} + \lambda_2^2\frac{\partial W}{\partial I_2}\right), \quad n_{22} = 4\lambda_3 h_0\left(\lambda_2^2 - \frac{1}{\lambda_1^2\lambda_2^2}\right)\left(\frac{\partial W}{\partial I_1} + \lambda_1^2\frac{\partial W}{\partial I_2}\right), n_{ij} = 0,\ i \neq j, \\ &I_1 = \lambda_1^2 + \lambda_2^2 + \lambda_3^2, I_2 = \lambda_1^{-2} + \lambda_2^{-2} + \lambda_3^{-2}, I_3 = \lambda_1^2\lambda_2^2\lambda_3^2 = 1, \lambda_3 = 1/\lambda_1\lambda_2. \end{aligned} \tag{6.10}$$

where W is a strain energy function.

The collagen fiber tensions in the meridional and latitudinal directions are determined to be

$$t_1 = 2\frac{\tau}{\Delta}\left(\frac{\lambda_1 \sin^2\alpha}{\lambda_2}\right), \qquad t_2 = 2\frac{\tau}{\Delta}\left(\frac{\lambda_2 \cos^2\alpha}{\lambda_1}\right), \tag{6.11}$$

where τ is the tension in the fiber and Δ is the constant distance between two different fibers on a single circle of latitude. Δ is given as $5\mu m$ taken from measurements using transmitted light microscopic (TLM) images of stained adventitia samples and experimentally verified [26]. In the model presented here, only the *Neo*-Hookean model in Equation (6.12) is employed for the isotropic tubular membrane and fiber effects are modeled using a structural representation, which is already described in Equations (6.8)–(6.11).

$$W_{NH} = \frac{C}{2}(I_1 - 3), \tag{6.12}$$

where *C* is a *Neo*-Hookean material constant for the isotropic tubular membrane.

We compare the structural model described in this section to the semi-structural approach of the Holzapfel-Gasser-Ogden model (HGO model: [17]) in Equation (6.13). In their formulation, a strain energy function is proposed for the artery that contains an expression for the non-collagen part and a term for the two families of collagen fibers, which leads to a strongly nonlinear response in the large strain domain. The proposed strain energy function is an exponential type reminiscent of the well-known Fung type model for soft biological materials [27, 28],

$$W_{HGO} = \frac{C}{2}(I_1 - 3) + \frac{k_1}{k_2}\{\exp[k_2(I_4 - 1)^2] - 1\}, \tag{6.13}$$

where C is a *Neo*-Hookean constant for the isotropic non-collagen part, k_1 is a material parameter, k_2. The material parameters are given in Table 6.1. Note that any suitable material model for the artery can be used in the sensor framework that will be outlined in Section 6.4.

Table 6.1. Material parameters for the artery model [24].

C (kPa)	k_1 *(kPa)*	k_2
7.64	996.6	524.6

6.3.3. Governing Equations and Boundary Conditions for Static Response

The membrane governing equations for a tube subjected to an inflation pressure are expressed in the meridional and latitudinal directions as,

$$\begin{aligned} &\frac{dN_{11}}{d\xi}+\frac{N_{11}}{r}\frac{dr}{d\xi}-\frac{N_{22}}{r}\frac{dr}{d\xi}=2h_0\rho\frac{d^2\xi}{dt^2}, \\ &P-\kappa_1 N_{11}-\kappa_2 N_{22}=2h_0\rho\frac{d^2r}{dt^2}, \end{aligned} \tag{6.14}$$

where κ_1 and κ_2 are the principal curvatures in the meridional and latitudinal directions given by,

$$\kappa_1=-\frac{d^2r/d\xi^2}{(1-\left(dr/d\xi\right)^2)^{1/2}} \text{ and } \kappa_2=\frac{1}{r}(1-\left(dr/d\xi\right)^2)^{1/2}. \tag{6.15}$$

The derivation of the membrane equations from the Cauchy equilibrium equations is somewhat involved and can be found in Green and Adkins [9-11]. For an arterial segment of length L_0, the boundary conditions at $z=L_0$ and $z=0$ are fixed and given in Equation (6.16-1)) where symmetry about the midpoint of the membrane has been employed. The force balance in the axial direction yields at z=0 the expression given in Equation (6.16-2). The angle σ between the deformed membrane and the z axis is zero at the midpoint of the tube (z=0) and expressed in Equation (6.16-3),

$$\lambda_2(L_0)=1, \qquad \pi r(0)^2P=2\pi r(0)N_{11}(0), \qquad \sigma(0)=0. \tag{6.16}$$

In particular, the non-dimensional undeformed length l_0 is obtained by

$$l_0=\frac{L_0}{R}=-\int_{\lambda_2(0)}^{1}\frac{d\lambda_2}{\lambda_1\sin\sigma}. \tag{6.17}$$

The angle σ represents the angle between the deformed membrane and the z axis.

$$\sigma=\cos^{-1}(\kappa_2 r). \tag{6.18}$$

If the length is allowed to change (both ends of the tube not fixed), the deformed length of half of the membrane is obtained in the following manner

$$\begin{aligned} \tan\sigma &= \frac{dr}{dz} = \frac{R d\lambda_2}{dz}, \\ \frac{dz}{R} &= \cot\sigma d\lambda_2, \\ l &= \frac{L}{R} = -\int_{\lambda_2(0)}^{1} \cot\sigma \, d\lambda_2. \end{aligned} \tag{6.19}$$

For the quasi-static analysis, the right hand side of Equation (6.14) is set equal to be zero. Calculation of the numerical deformation profile of the artery is obtained using the following numerical procedure: Initially, trial values of τ and $\lambda_2(0)$ are given. The second step is to obtain $\lambda_2(L_0)$ using a Runge-Kutta algorithm. The value of $\lambda_2(L_0)$ is matched with the boundary condition, $\lambda_2(L_0)=1$ (Equation (6.17)) and the numerical deformation profile is calculated. If the value of $\lambda_2(L_0)$ does not match the boundary condition, the procedure is repeated until the correct value of $\lambda_2(L_0)$ ($\lambda_2(L_0)$=1)is obtained.

For the dynamic analysis, Equation (6.14) is simplified by assuming that inertial effects in the meridional direction are negligible. Therefore, the first equation of motion in Equation (6.14) becomes a static equilibrium equation where $d^2\xi/dt^2=0$ (Note that the current representation does not include viscous effects). The initial conditions are the deformed radius and deformation rate,

$$\lambda_2(z,0) = \lambda_2(z), \quad \frac{d\lambda_2}{dt}(z,0) = 0. \tag{6.20}$$

Numerical solutions for the dynamic response of the artery wall are obtained using a finite different scheme. Further details of the computational scheme are described in [29]. At first, the equation of motion, initial conditions, and boundary conditions in Equations (6.14), (6.16) and (6.20) are discretized by using the finite different method (forward difference method) for time and space domains. At the first time step, the deformed profile is calculated by using the initial

conditions. For the following time steps, the deformed profiles are obtained in the same manner as the procedure for the quasi-static solution.

6.3.4. Capacitance Formulation for Tubular Dielectric Elastomer Sensors

In this section, the sensing equation for the DE transducer is briefly derived. Consider a tubular DE in the undeformed state of length $2L_0$, and outer and inner radii R_{out}, and R_{in} respectively. To determine the capacitance of the tubular membrane, expressions for the coaxial electric field and the potential difference between the inner and outer surfaces are obtained using

$$\begin{aligned} E &= \frac{Q}{2\pi L \varepsilon_0 \varepsilon_r r}, \\ V &= -\int_{r_{in}}^{r_{out}} E dr = -\frac{Q}{2\pi L \varepsilon_0 \varepsilon_r} \int_{r_{in}}^{r_{out}} \frac{1}{r} dr = \frac{Q}{2\pi L \varepsilon_0 \varepsilon_r} \ln\left(\frac{r_{out}}{r_{in}}\right), \end{aligned} \tag{6.21}$$

where r is a radial coordinate, r_{in} and r_{out} are the inner and outer radii of the cylinder, Q is the charge, ε_r is the relative permittivity and ε_0 is the vacuum permittivity and $2L$ is the current length of the cylinder.

The capacitance of a unit volume of the tubular DE in Figure 6.5 is the ratio between the electrical charge and the potential difference

$$dC = \frac{Q}{V} = \frac{\varepsilon_0 \varepsilon_r 2\pi}{\ln\left(r_{out} \big/ r_{in}\right)} dz, \tag{6.22}$$

where dz is of unit length.

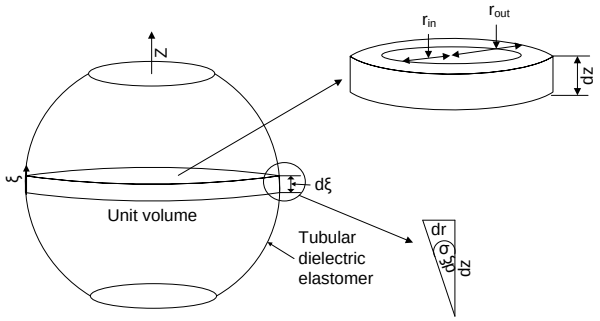

Figure 6.5. Unit element of a deformed tubular DE sensor.

Therefore, the total capacitance is calculated by integrating Equation (6.23) with respect to the *z* axis, which yields

$$C = \varepsilon_0 \varepsilon_r 4\pi R_0 \int_1^{\lambda_2(0)} \frac{1}{\ln\left(\dfrac{Rs_0\lambda_2 + \dfrac{t_0}{2\lambda_1\lambda_2}}{Rs_0\lambda_2 - \dfrac{t_0}{2\lambda_1\lambda_2}}\right)} \frac{1}{\tan\sigma} d\lambda_2. \tag{6.23}$$

where Rs_0 and t_0 are the radius and thickness of the tubular DE sensor. To calculate the capacitance value of a tubular DE sensor, we will assume that the deformation of the sensor is identical to that of the artery. Therefore, the sensing response can be calculated using Equation (6.23) for a known deformation profile of the artery wall (outlined in the previous section).

6.4. Quasi-static and Dynamic Response of the Large Strain Sensor

Consider a tubular sensor placed in contact with the inner surface of the arterial wall. It is assumed in this first approximation that the sensor does not structurally influence the behavior of the arterial wall, thereby undergoing equivalent deformations. By means of the numerical modeling approach described in the previous section, the deformation response of the artery and subsequent electromechanical coupling of the DE sensors is obtained. It is assumed that the uniformly distributed collagen fibers are initially crimped about a mean initial fiber angle α and then become aligned and straight during the deformation. The quasi-static and dynamic response

of the arterial wall with physiologically valid pressure and frequency ranges applied are presented in this section. The initial dimensions of the arterial wall and the tubular DE sensor (silicone) are given in Table 6.2 and Table 6.3, respectively. The initial fiber angle α=49.98° and artery dimensions given in the table are physiologically representative [30].

Table 6.2. The initial dimensions of the artery.

	R_0 (mm)	$2h_0$ (mm)	$2L_0$ (mm)	α (°)
Artery	4.745	0.43	20	39.98, 49.98 and 59.98

6.4.1. Comparison between the Structural Model and HGO Model

To validate the proposed numerical model for the artery, the static constitutive deformation of the artery wall is compared with Gasser *et al.*'s numerical results [24], which was validated with experimental results [31]. The parameters for the strain energy function and initial dimensions of the artery are given in Table 6.1 and Table 6.2 for the collagen fiber angle of 49.98°. One circular end of the artery is fixed, the other is free, and an internal pressure is applied. Figures 6.6 and 6.7 show comparisons of radial and longitudinal arterial deformations using the present model (SG) and the HGO model, in which κ is equal to 0. The difference between the two models are within 3% overall, which provides validation for the proposed approach. The error between the two numerical results are calculated by

$$\text{Error}(\%) = \frac{\text{HGO model} - \text{SG model}}{\text{HGO model}} \times 100. \tag{6.24}$$

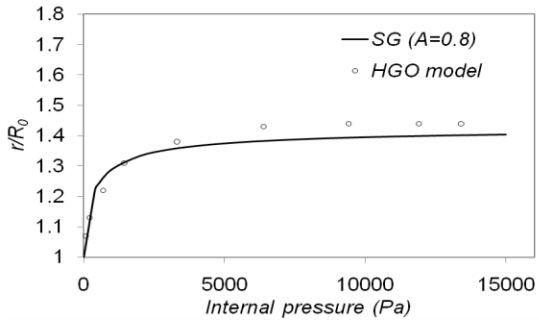

Figure 6.6. Comparison of radial deformation as a function of pressure.

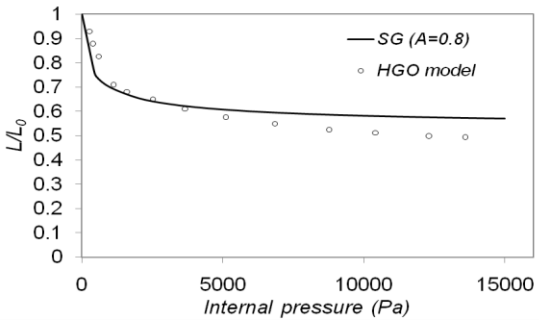

Figure 6.7. Comparison of longitudinal deformation as a function of pressure.

6.4.2. The Effect of the Crimping Fibers on the Deformation of the Artery

In order to observe the effect of the undulated fibers in the reference configuration, the static response of the artery with respect to internal pressure (0–20kPa) is calculated for different values of the crimping parameter A from 0 to 1.0. Again, A≠0 means that the fibers are undulated in the undeformed state and there is no fiber tension until the fibers are straightened. Figure 6.8 describes the relationship between the initial fiber angle and the straightened fiber length L_f with respect to the crimping parameter A. The length L_f increases nonlinearly with A due to the sinusoidal function in Equation (6.2) (the fiber crimping). Figure 6.9 shows the effect of the crimping fibers on the deformation of the artery with respect to the internal pressure. The initial fiber angle α is 49.98 º and the fibers have the same extended fiber length in each simulation. Since there is no fiber tension until the fiber is straightened, larger deformations in the radial direction are observed than the model not including the crimping fiber (A=0). The response is nonlinear due to the crimping shape of the fiber.

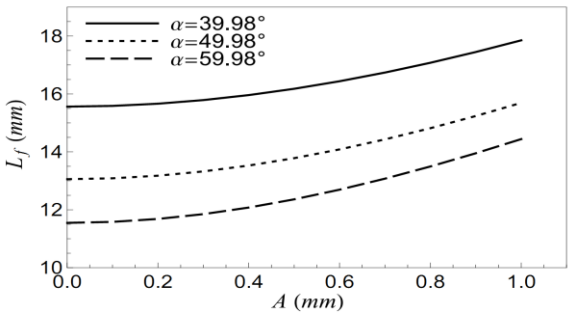

Figure 6.8. Relationship between fiber undulation and straightened fiber length.

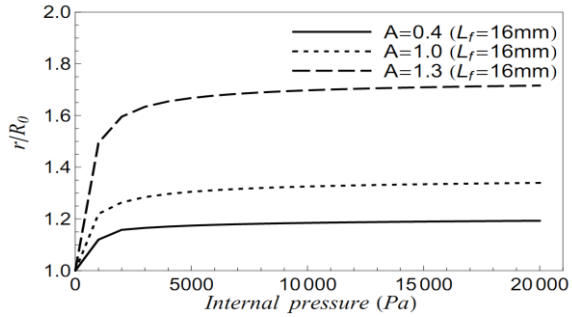

Figure 6.9. The effect of crimping on the deformation response.

6.4.3. Static Deformation of the Artery

In this subsection, the static response of an arterial segment is obtained for a physiological pressure range of 0–20*kPa* using the structural model outlined in Section 6.3. Since the crimping parameter A is given as 0.8, the straightened fiber lengths, L_f, are given as 17.07, 14.81 and 13.49*mm* for 39.98°, 49.98° and 59.98°, respectively. The boundary conditions for the numerical results are as follows: both circular ends of the artery are fixed, the longitudinal stretch ratio L/L_0 is constant and of unit value and the radial stretch ratio λ_2 is of unit value at both ends of the tube. Figure 6.10 and Figure 6.11 show the radial and thickness deformations of the artery for 3 different initial fiber angles. The deformation response is nonlinear and the results show that the nonlinearity is shifted to a higher pressure range when the collagen fiber angle increases. This is because a larger collagen fiber angle provides less constraint on the radial expansion in comparison to smaller fiber angles. Note that the radius of the artery reaches maximum values of 5.66 to 8.00*mm*. Figure 6.10 shows that a smaller fiber angle induces a higher radial constraint as evidenced by the early transition to the plateau region (points 1, 2 and 3 in Figure 6.10).

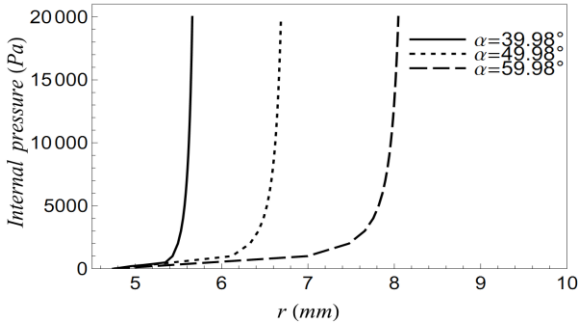

Figure 6.10. Radial deformation as a function of pressure for 3 different fiber angles.

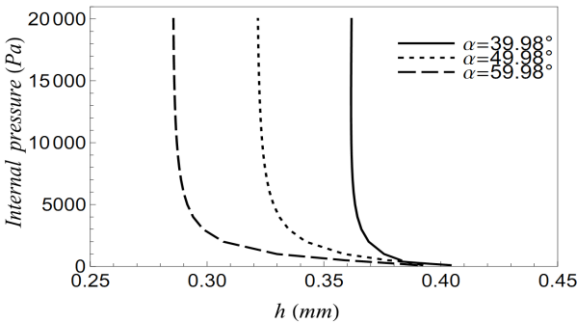

Figure 6.11.Thickness deformation as a function of pressure for 3 different fiber angles.

Figure 6.12 and Figure 6.13 show the variation of the meridional and thickness stretch ratios λ_2 and λ_3 of the arterial membrane along the z axis. In Figure 6.12, λ_2 progressively decreases at points away from the boundary. Conversely, for the thickness stretch in Figure 6.13, λ_3 increases most at points farther away from the middle of arterial wall ($z = 0mm$).

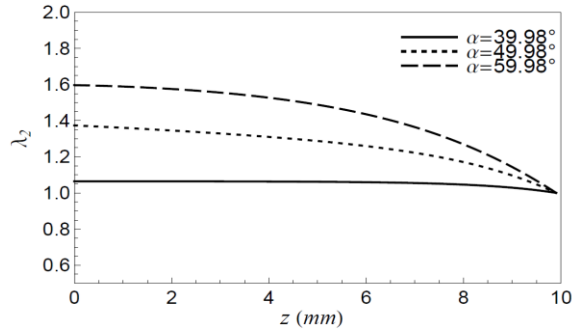

Figure 6.12. Latitudinal stretch ratio as a function of z axis.

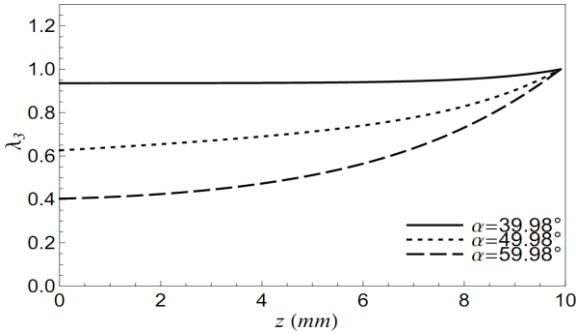

Figure 6.13. Thickness stretch ratio as a function of z axis.

6.4.4. Static and Dynamic Deformation of the Soft DE Sensor and Artery

The static and dynamic electromechanical response of a tubular DE sensor is obtained for a pressure range of 0–20kPa. The initial dimensions of the DE sensor are given in Table 6.3.

Table 6.3. The initial dimensions of a tubular silicone DE sensor (silicone material).

	Rs_0 (mm)	t_0 (mm)	$2L_0$ (mm)	ε_r
Silicone DE sensor	4.525	0.10	20	2.7

Figure 6.14 shows the predicted sensor output for a silicone DE sensor in response to the deformation of the artery. The model procedure is as follows. For a given pressure input, the deformation of the artery is calculated. The calculated deformation profile is used as the mechanical input of the sensor and the sensor output is calculated using Equation (6.23). The relationship between capacitance and pressure is nonlinear. This nonlinearity is shifted to a higher pressure range when the fiber angle increases. The nonlinearity arises from the nonlinear relationship between pressure and deformation of the arterial wall. The observed plateau region in the curve is due to constrained motion as opposed to sensor insensitivity. The capacitance sensitivity for each fiber angle is calculated by Equation (6.25) and is shown in Table 6.4. The results in Table 6.4 imply that the sensitivity is a function of the fiber angle. This is somewhat misleading. The sensitivity actually varies with the stretch and since the fiber angle affects the allowable stretch, different fiber angles yield different apparent sensitivity values.

$$\text{Sensitivity} = \frac{C_n - C_{n-1}}{r_n - r_{n-1}} \quad (pF/mm), \quad C_n = \text{capacitance at } r = r_n. \tag{6.25}$$

Table 6.4. Sensitivity of tubular silicone sensor for each fiber angle.

Fiber angle (α)	39.98 º	49.98 º	59.98 º
Sensitivity (*pF/mm*)	14.09	50.87	61.09

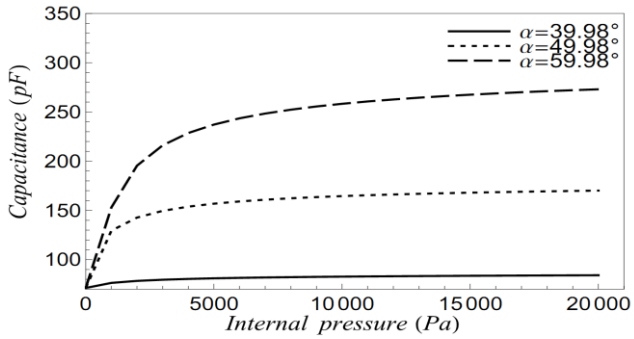

Figure 6.14. Predicted sensor output (capacitance) versus pressure.

Generally, the heart beat rate of infants is 120 beats per minute (around 2*Hz*) and for a person over age 18 it is about 70 beats per minute (around 1*Hz*). So, 1 and 2*Hz* are reasonable choices for the frequencies. Figures 6.15–6.18 show the response of the tubular silicone sensor while a sinusoidal pressure is applied at 1–2*Hz*. Specifically in Figures 6.15–6.18, there is no delay between the input and output signal since damping is not considered in this model. The response of the artery is identical to the static response in Figure 6.10 and Figure 6.14 (α=49.98°) for this low frequency range. Similar to the static response, there is a nonlinear relationship between pressure and radial deformation as shown in Figure 6.15 and Figure 6.17. However, note that the electromechanical response and the sensor output have a linear correlation as shown in Figure 6.16 and Figure 6.18. The non-sinusoidal output or nonlinearity is an innate characteristic of the deformation of the artery wall, but is not a characteristic of the electromechanical response of the sensor.

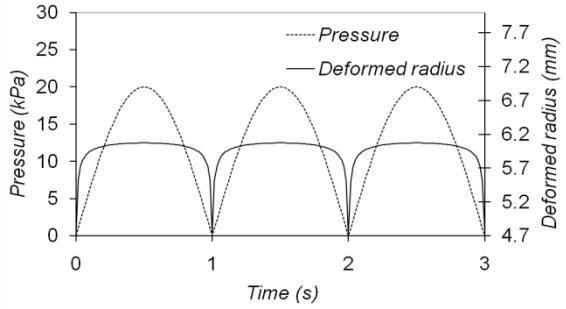

Figure 6.15. The mechanical response of the artery-sensor at 1 *Hz*.

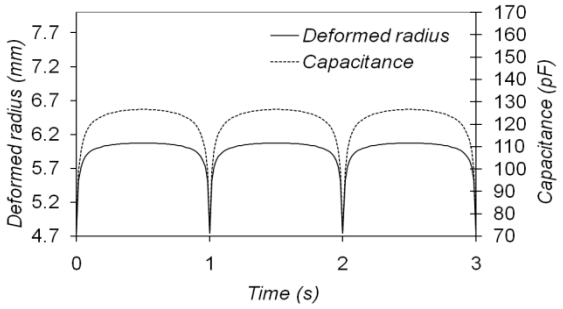

Figure 6.16. The electromechanical response of the artery-sensor at 1 *Hz*.

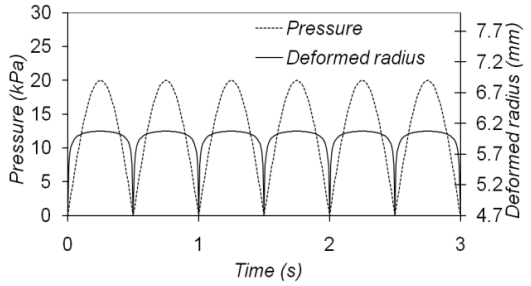

Figure 6.17. The mechanical response of the artery-sensor at 2*Hz*.

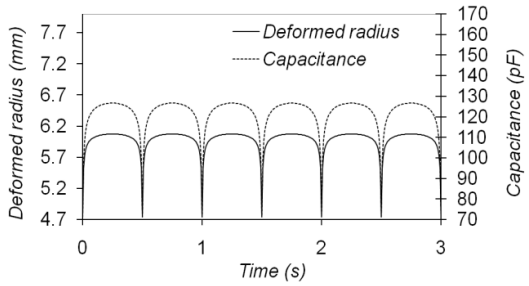

Figure 6.18. The electromechanical response of the artery-sensor at 2*Hz*.

These results show that the strain sensor would be insensitive above $13kPa$ since the artery no longer deforms appreciably. Since the initial dimensions of the sensor are restricted by the dimensions of the arterial wall, sensor sensitivity could only be reasonably increased by say increasing the relative permittivity. The effects of a sensor's permittivity on the sensitivity with respect to initial thickness variation of the sensor are shown in Figure 6.19. For a thickness of $0.01mm$ a higher sensitivity is attained. The sensitivities (Figure 6.19, Figure 6.20 and Table 6.5) are calculated by using Equation (6.26).

$$\begin{aligned} &\text{Sensitivity} = \frac{C_n - C_{n-1}}{P_n - P_{n-1}} \quad (pF/kPa),. \\ &P_n = n\,(kPa),\ C_n = \text{Capacitance at } P_n,\ n = 2,3,\ldots,20. \end{aligned} \tag{6.26}$$

It is non-trivial to increase material permittivity since increased permittivity is often accompanied by an increase in stiffness which would be counter productive for developing a soft sensor. Ha *et al.* developed a hybrid dielectric elastomer based on interpenetrating polymer networks with a dielectric constant of Adding a ceramic inclusion with a higher relative permittivity such as TiO_2 (ε_r=114) has been used to increase the permittivity of silicone [32, 33]. The study shows that a silicone matrix with TiO_2 powder has a lower elastic modulus (which is unusual) and a higher relative permittivity (ε_r=8.0) [32]. Figure 6.20 illustrates the enhanced sensing response of the artery-sensor with respect to the permittivity. The sensor with a higher permittivity (ε_r=30.0) produces higher sensitivity as shown in Figure 6.20 and Table 6.5. It is concluded that higher sensitivity to pressure input (physiological pressure range: 16/10kPa) can be obtained by fabricating thinner sensors or adding an inclusions to increase the permittivity.

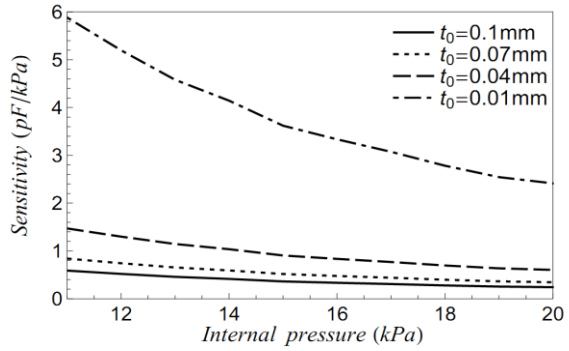

Figure 6.19. The effect of initial thickness on the sensor sensitivity (ε_r=3.0).

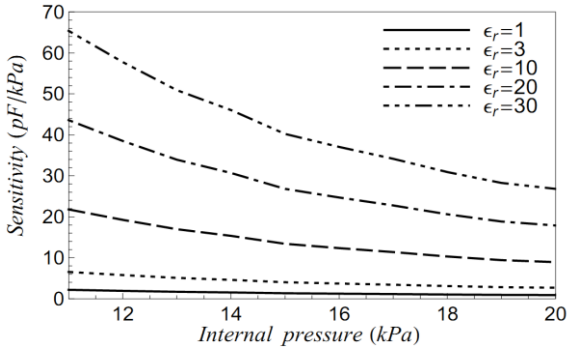

Figure 6.20. Static sensing response of the artery-sensor with respect to permittivity (at t_0=0.01*mm*).

Table 6.5. Sensor sensitivity with respect to permittivity (ε_r) at h_0=0.01*mm*.

Pressure range (*kPa*)	Sensor sensitivity (*pF/kPa*)				
	ε_r=1.0	ε_r=3.0	ε_r=10.0	ε_r=20.0	ε_r=30.0
10–13	1.92	5.77	19.25	38.50	57.75
13–15	1.53	4.6	15.34	30.69	46.04
15–17	1.23	3.70	12.35	24.70	37.05
17–18	1.03	3.09	10.30	20.61	30.92
18–20	0.94	2.82	9.42	18.84	28.26

6.5. Conclusion

In this paper, a numerical model for the arterial wall placed in contact with a tubular DE sensor is derived using large deformation membrane theory and electrostatics. Specifically, a model for the arterial wall with an integrated tubular DE sensor is formulated. Principally, it is assumed that the arterial wall consists of only one layer (adventitia) and the tubular DE sensor does not obstruct the deformation behavior of the arterial wall. The arterial wall in the model is not the full multi-layered structure. Furthermore, membrane theory has been used to model the behavior instead of a full three dimensional approach. For the constitutive relationship of the arterial wall, a *Neo*-Hookean model is employed to describe the non-collagen fiber part of the artery, and the collagen fiber part of the arterial wall is considered structurally. The undulated fibers in the

model are modeled using as a simple sinusoidal waveform. According to the results in Section 6.4.2, the crimped fibers can have a significant effect on the mechanical response of the arterial wall. For the static response, the constitutive model is integrated into the boundary value problem so that the numerical deformation response with respect to a physiological pressure input (0–20kPa) can be obtained. For the dynamic response, only inertial effects in the radial direction are considered. The resulting initial-boundary value problem is solved numerically for physiologically valid frequencies (1–2Hz). The dynamic model is very simple at this point and does not encompass known biological phenomena related to viscoelastic effects.

For the static response of the artery and tubular DE sensor, it is observed that the relationship between pressure and capacitance is nonlinear due to the collagen fibers. Higher collagen fiber angles increase the capacitance sensitivity due to a decreasing radial constraint, which lead to larger deformations for a given input pressure (Table 6.4). For the dynamic response of the artery-sensor, similar to the static response, a nonlinear relationship between pressure and radial deformation is observed for the frequencies considered. Since the nonlinearity is inherent to the arterial wall, specifically the collagen fibers, a linear electromechanical response between radial deformation and capacitance change is observed for all frequencies. The nonlinearity leads to insensitivity of the sensor above 13kPa. However, higher sensitivity can be achieved by fabricating thinner sensors and or tailoring the polymer to attain higher permittivity, though there is the trade-off of increasing sensor modulus.

6.6. References

1. Pei, Q., et al., *Multiple-degrees-of-freedom electroelastomer roll actuators.* Smart Materials and Structures, 2004: p. 86-92.

2. Rosenthal, M., et al. *Applications of dielectric elastomer EPAM sensors*. in *Electroactive Polymer Actuators and Devices (EAPAD) 2007, 19 March 2007*. 2007. USA: SPIE - The International Society for Optical Engineering.
3. Lanir, Y., *Structure-strength relations in mammalian tendon.* Biophysical Journal, 1978: p. 541-54.
4. Comninou, M. and I.V. Yannas, *Dependence of stress strain nonlinearity of connective tissues on the geometry of collagen fibers.* Journal of Biomechanics, 1976: p. 427-433.
5. Lanir, Y., *A structural theory for the homogeneous biaxial stress-strain relationships in flat collagenous tissues.* Journal of Biomechanics, 1979: p. 423-36.
6. Lanir, Y., *Constitutive equations for fibrous connective tissues.* Journal of Biomechanics, 1983: p. 1-12.
7. Freed, A.D. and T.C. Doehring, *Elastic model for crimped collagen fibrils.* Journal of Biomechanical Engineering, 2005: p. 587-593.
8. Grytz, R. and G. Meschke, *Constitutive modeling of crimped collagen fibrils in soft tissues.* Journal of the Mechanical Behavior of Biomedical Materials, 2009: p. 522-533.
9. Adkins, J.E. and R.S. Rivlin, *Large elastic deformations of isotropic materials -- IX. Deformation of thin shells.* Philosophical Transactions, 1952.
10. Adkins, J.E. and R.S. Rivlin, *Elastic Deformations of Isotropic Materials X. Reinforced by Inextensible Cords.* Philosophical Transactions of the Royal Society of London. Series A, 1955: p. 201-223.
11. Green, A.E. and J.E. Adkins, *Large Elastic Deformation*. 1970, London: Oxford University Press.
12. Adkins, J.E. and R.S. Rivlin, *Large elastic deformations of isotropic materials X. Reinforced by in extensible cords.* Royal Society of London -- Philosophical Transactions Series A, 1955.
13. Kydoniefs, A.D., *Finite Axisymmetric Deformations of an Initially Cylindrical Elastic Membrane Enclosing a Rigid Body,.* Quarterly Journal of Mechanics and Applied Mathematics, 1968: p. 319-331.
14. Kydoniefs, A.D., *Finite Axisymmetric Deformations of an Initially Cylindrical Membrane Reinforced with Inextensible Cords.* Quarterly Journal of Mechanics and Applied Mathematics, 1969: p. 481-488.
15. Kydoniefs, A.D., *FINITE AXISYMMETRIC DEFORMATIONS OF INITIALLY CYLINDRICAL REINFORCED MEMBRANES.* Rubber Chemistry and Technology, 1972: p. 1677-1683.
16. Matsikoudi-Iliopoulou, M., *Finite axisymmetric deformations with torsion of an initially cylindrical membrane reinforced with one family inextensible cords.* International Journal of Engineering Science, 1987: p. 673-80.
17. Holzapfel, G.A., T.C. Gasser, and R.W. Ogden, *A new constitutive framework for arterial wall mechanics and a comparative study of material models.* Journal of Elasticity, 2000: p. 1-48.
18. Holzapfel, G.A., et al., *A new axisymmetrical membrane element for anisotropic, finite strain analysis of arteries.* Communications in Numerical Methods in Engineering, 1996: p. 507-17.
19. Goulbourne, N., E. Mockensturm, and M. Frecker, *A nonlinear model for dielectric elastomer membranes.* Journal of Applied Mechanics, Transactions ASME, 2005: p. 899-906.

20. Son, S. and N.C. Goulbourne, *Finite Deformations of Tubular Dielectric Elastomer Sensors.* Journal of Intelligent Material Systems and Structures, 2009: p. 2187-2199.
21. Kornbluh, R., et al., *Ultrahigh strain response of field-actuated elastomeric polymers.* Proceedings of SPIE - The International Society for Optical Engineering, 2000: p. 51-64.
22. Pelrine, R., et al., *High-field deformation of elastomeric dielectrics for actuators.* Materials Science and Engineering C, 2000: p. 89-100.
23. Pelrine, R., R. Kornbluh, and G. Kofod, *High-strain actuator materials based on dielectric elastomers.* Advanced Materials, 2000: p. 1223-1225.
24. Gasser, T.C., R.W. Ogden, and G.A. Holzapfel, *Hyperelastic modelling of arterial layers with distributed collagen fibre orientations.* Journal of the Royal Society Interface, 2006: p. 15-35.
25. Holzapfel, G.A. and T.C. Gasser, *A viscoelastic model for fiber-reinforced composites at finite strains: Continuum basis, computational aspects and applications.* Computer Methods in Applied Mechanics and Engineering, 2001: p. 4379-4403.
26. Elbischger, P.J., et al., *Computer vision*
analysis of collagen fiber bundles in the adventitia of human blood vessels. Studies in health technology and informatics, 2005: p. 97-129.
27. Fung, Y.C., K. Fronek, and P. Patitucci, *Pseudoelasticity of arteries and the choice of its mathematical expression.* American Journal of Physiology - Heart and Circulatory Physiology, 1979: p. H620-H631.
28. Chuong, C.J. and Y.C. Fung, *Three-Dimensional Stress Distribution in Arteries.* J. Biomech. Eng, 1983: p. 268-274.
29. Seyul, S. and N.C. Goulbourne, *Dynamic response of tubular dielectric elastomer transducers.* International Journal of Solids and Structures, 2010: p. 2672-9.
30. Schulze-Bauer, C.A.J., C. Morth, and G.A. Holzapfel, *Passive biaxial mechanical response of aged human iliac arteries.* Journal of Biomechanical Engineering, 2003: p. 395-406.
31. Holzapfel, G.A., et al., *Determination of layer-specific mechanical properties of human coronary arteries with nonatherosclerotic intimal thickening and related constitutive modeling.* Am J Physiol Heart Circ Physiol, 2005: p. H2048-2058.
32. Carpi, F. and D. De Rossi, *Improvement of electromechanical actuating performances of a silicone dielectric elastomer by dispersion of titanium dioxide powder.* IEEE Transactions on Dielectrics and Electrical Insulation, 2005: p. 835-843.
33. Gallone, G., et al., *Dielectric constant enhancement in a silicone elastomer filled with lead magnesium niobate-lead titanate.* Materials Science and Engineering C, 2007: p. 110-116.

Chapter 7. Implementation of an Electro-Elastic Material into a Finite Element Method Tool (ABAQUS)

This chapter is motivated by the difficulty of solving problems involving complicated (asymmetric) configurations and complex boundary and initial conditions by utilizing numerical and analytical methods. The difficulties can be overcome by using a finite element method tool (ABAQUS 6.9-1). Constitutive formulation for isotropic and anisotropic electro-elastic materials is not built into ABAQUS/CAE. Implementation of the formulation into a user subroutine (UMAT: User subroutine to define a material's mechanical behavior) is required to use ABAQUS. In this chapter, the procedure of embedding the constitutive formulation for the isotropic and anisotropic electro-elastic material into a UMAT is presented and the applicability of ABAQUS to the electromechanical coupling problem is described in two different examples.

Since incompressible materials experience a volumetric locking when ABAQUS is employed and volumetric locking causes numerical instabilities, a mathematical treatment is required for preventing the volumetric locking during simulation. For overcoming the volumetric locking, the constitutive formulations for the electro-elastic materials in Chapter 2 are reformulated by considering a multiplicative decomposition of the deformation into purely isochoric and purely volumetric contributions. Then, the decoupled formulation is implemented into a UMAT in ABAQUS. The multiplicative decomposition was introduced at the first time by Flory [1]. Flory assumed that the deformation gradient is expressed as the product of two deformations, one purely volumetric ($\boldsymbol{F_V}$) and the other isochoric ($\overline{\boldsymbol{F}}$)

$$\boldsymbol{F} = \boldsymbol{F}_V \overline{\boldsymbol{F}},\ \boldsymbol{F}_V = (V/V_0)^{1/3} = J^{1/3},\ \overline{\boldsymbol{F}} = J^{-1/3}\boldsymbol{F}, \tag{7.1}$$

where V_0 is the volume in the reference state. The determinants of the isochoric and volumetric deformation gradients are,

$$\det[\overline{\boldsymbol{F}}] = 1,\ \det[\boldsymbol{F}_V] = J. \tag{7.2}$$

Based on the multiplicative decomposition in Flory [1], Ogden [2, 3], Simo and Taylor [4] and Weiss and Maker [5] presented more detailed decompositions of the constitutive laws for isotropic and anisotropic materials. For nearly incompressible materials, Ogden decomposed the deformation into isochoric and volumetric parts following Flory's approach and expanded the strain energy function as a power series in the volumetric strain ε

$$W(\overline{\boldsymbol{F}}, J) = W(\overline{\boldsymbol{F}}, 1) + \varepsilon \frac{\partial W(\overline{\boldsymbol{F}}, 1)}{\partial J} + \frac{1}{2}\varepsilon^2 \frac{\partial^2 W(\overline{\boldsymbol{F}}, 1)}{\partial J^2}. \tag{7.3}$$

Then, in order to investigate the volume change (ε) during the deformation, he applied the decomposition to a simple tension and combined extension and torsion of a circular cylinder [2, 3]. Simo and Talyor developed a closed form expression for the tangent modulus of a nearly incompressible isotropic material by using a multiplicative decomposition of the deformation gradient and considered the variational formulation of several boundary value problems (simple tension, pure shear and equibiaxial extension) in a form suitable for numerical implementation (using a nonlinear finite element analysis program: FEAP) of nearly incompressible materials [4]. Weiss *et al.* [5] also presented the multiplicative decomposition of the constitutive laws for a transversely isotropic material and demonstrated the accuracy and efficiency of the decomposed formulation for fully incompressible transversely isotropic hyperelasticity with several examples (uniaxial, strip biaxial and equibiaxial extension). Their finite element solutions showed excellent agreement with theoretical solutions [5]. In order to decouple the

constitutive formulation of the isotropic and anisotropic electro-elastic materials as considered in this research, the theoretical approaches of Flory [1] and Weiss *et al.* [5] are adopted.

A previous implementation of a dielectric elastomer (DE) into a user subroutine was presented by Zhao and Suo [6], Wissler and Mazza [7, 8] and O'Brien [9]. Zhao and Suo defined the total Cauchy stress as the elastic stress plus the electrostatic stress and implemented the constitutive law for an isotropic DE into a UMAT in ABAQUS [6]. According to their approach, the tangent modulus for the constitutive law is formulated using a strain energy function (*Neo*-Hookean model), not including the electric energy function. However, a closed form of the tangent modulus is not obligatory because it is used for an iterative operator in a UMAT [10]. The tangent modulus in the UMAT is calculated numerically with respect to the deformation, and then the Cauchy stress is updated with given deformation gradients [6]. The computational results for several simple configurations such as rectangular and circular actuators undergoing homogeneous deformations were compared with analytical solutions [6]. Wissler and Mazza's approach [7, 8] for dealing with the electromechanical coupling is to consider the electrostatic pressure as a negative Cauchy stress in the thickness direction. The prestrained circular DE actuator was investigated using ABAQUS. They adopted three strain energy functions (Yeoh [11], Ogden [12] and Mooney-Rivlin [13] hyperelastic models) and the numerical result was compared with their analytical model. The electrostatic pressure is implemented in a user subroutine (UVAR in ABAQUS: An array containing the user-defined output variables) [7, 8]. This model is an oversimplification and approximation of the theoretical stress, which has been rigorously presented and derived in proper form in Goulbourne [14], Suo [15] and McMeeking [16]. O'Brien and McKay considered the total free energy function for an electro-elastic material as a combination of the elastic strain energy and electrostatic energy, and this was

embedded into ABAQUS using a user supplied routine (UHYPER: User subroutine to define a hyperelastic material) [9]. Their approach was employed for simulating dielectric elastomer minimum energy structures (DEMES) which consist of a prestrained DE adhered to a thin and flexible film. Their model predicted well the equilibrium state, free displacement and blocked force of DEMES. This approach is limited to the quasi-static and isotropic case because UHYPER can handle only isotropic material and requires that the derivatives of the free energy density function should be defined with respect to the strain invariants. In the present research, the approach is most consistent with Zhao and Suo [6] for implementing electro-elastic materials. In comparison with the previous work in [6-9, 17], the UMAT developed in this research is not limited to isotropic materials with homogeneous deformation and is here extended to the anisotropic electro-elastic materials with inhomogeneous deformation.

In Section 7.1, the physical meaning and an example of volumetric locking is presented. In Section 7.2, the decoupling of the invariants and the new constitutive formulation in Chapter 2 is implemented by using multiplicative decomposition. An objective rate of the stress tensor for describing the material rotation in the UMAT is presented in Section 7.3. The procedure for updating the solution for the each increment in ABAQUS by using the Newton-Raphson method is described in Section 7.4. The numerical stability of the electro-elastic material when the finite element modeling is employed is discussed in Section 7.5 using the polyconvexity condition in Chapter 3. Two numerical examples are simulated using ABAQUS with the new UMAT for large deformations of isotropic and anisotropic electro-elastic materials in Section 7.6.

7.1. Volumetric Locking

Volumetric locking in fluid and solid mechanics is an undesirable consequence of a given numerical technique which produces erroneous numerical solutions. The locking is caused by the fact that there are too many incompressibility constraints imposed on a discretized solution relative to the number of degrees of freedom. Mathematically, as Poisson's ratio ν approaches 0.5 ($\nu \rightarrow 0.5$), the volumetric locking becomes significant because the material becomes incompressible. The bulk modulus κ is given by

$$\kappa = \frac{\mathsf{E}}{3-6\nu}, \tag{7.4}$$

where E is the Young's Modulus.

For $\nu = 0$, there is no volumetric locking as $\kappa = \mathsf{E}/3$. However, the locking becomes very noticeable as $\nu \rightarrow 0.5$ because in this limit

$$\kappa = \lim_{\nu \rightarrow 0.5} \frac{\mathsf{E}}{3-6\nu} = \infty. \tag{7.5}$$

An infinite bulk modulus implies that the behavior of the material is incompressible.

In order to further illustrate the concept of volumetric locking, a simple numerical example is presented. Let's consider an elastic rectangular block under uniaxial force (force control). The material properties and initial dimensions of the material are given in Table 7.1. In this numerical example, the uniaxial displacement of the material in the X_1 direction (X in ABAQUS) is observed for investigating the volumetric locking as ν approaches to 0.5.

Table 7.1. Material properties and initial dimensions of the elastic rectangular block.

E	ν	Length	width	Thickness
10 *kPa*	0.1–0.5	200 *mm*	20 *mm*	20 *mm*

Figure 7.1 depicts the undeformed and deformed configurations of the elastic block in ABAQUS/CAE. The boundary condition is one fixed end and uniaxial force (1 *N*) at free end. 8

node linear elements (C3D8 and C3D8R) are employed for the mesh type. The difference between C3D8 and C3D8R is the integration scheme in ABAQUS/CAE. The elements C3D8 and C3D8R employ the full integration and the reduced integration, respectively. The reduced integration is the simplest way to void the volumetric locking. Since the full integration cannot make the strain field volume preserving at all the integration points in element, the reduced integration is able to reduce the number of integration points so that the constraint can be met.

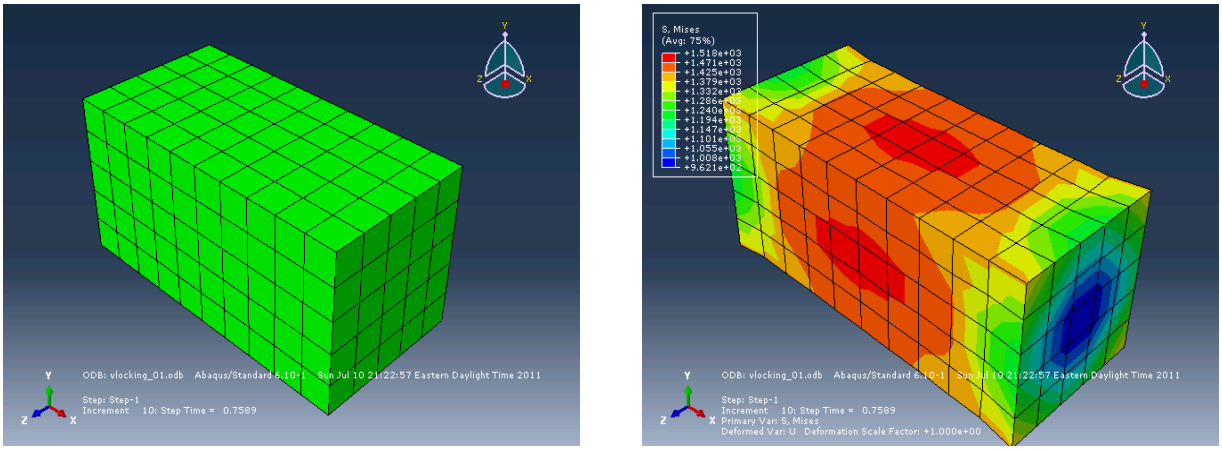

Figure 7.1. Undeformed (Left) and deformed (Right) configuration of the elastic block under uniaxial force 1 *N* at the free end (X direction).

Figure 7.2 shows the displacement of the elastic block at the free end with respect to uniaxial force 1 *N* simulated by using two different element types C3D8 and C3D8R. Since Young's modulus and external force are prescribed, the strain (or displacement in the X_1 direction) should be consistent along with different Poisson's ratio (ν = 0.1–0.5). As ν approaches 0.5 for C3D8, the finite element solution gradually underestimates the displacements, which implies significant volumetric locking. This result indicates that the solution with respect to the different Poisson's ratios have not converged due to the volumetric locking.

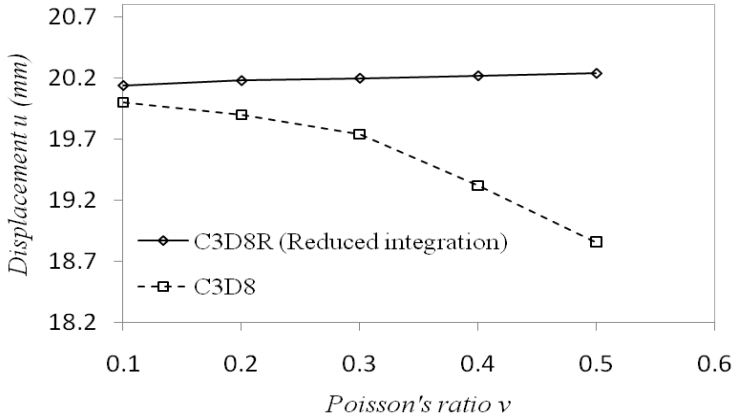

Figure 7.2. Effect of Poisson ratio on the maximum displacement of the elastic block with respect to uniaxial force 1*N* (Volumetric locking effect).

7.2. Multiplicative Decomposition of the Constitutive Formulation

In order to prevent volumetric locking, the incompressibility constraint of a material is released by treating the material as nearly incompressible. For a nearly incompressible material, the constitutive relations are decoupled into isochoric and volumetric parts. In Section 7.2.1, the Cauchy-Green tensors and invariants are decomposed by using multiplicative decomposition following Flory's approach [1]. Additionally in Section 7.2.1, the physical conditions for the decoupled free energy function are presented. In Sections 7.2.2 and 7.2.3, the total Cauchy stress and tangent modulus for the anisotropic electro-elastic materials from Chapter 2 are decoupled.

7.2.1. Invariants and Free Energy Function for Electro-elastic Materials: Nearly Incompressible Material

The deformation gradient $\boldsymbol{F}$ can be expressed as the product of two deformation gradients, one purely volumetric $(\boldsymbol{F}_V)$ and the other isochoric $(\overline{\boldsymbol{F}})$ [1, 2, 4, 5]:

$$\boldsymbol{F} = \boldsymbol{F}_V \overline{\boldsymbol{F}},\ \boldsymbol{F}_V = (V/V_0)^{1/3} = J^{1/3},\ \overline{\boldsymbol{F}} = J^{-1/3}\boldsymbol{F}, \tag{7.6}$$

where V_0 is the volume in the reference state. The determinants of the isochoric and volumetric deformation gradients are,

$$\det[\overline{\boldsymbol{F}}] = 1,\ \det[\boldsymbol{F}_V] = J. \tag{7.7}$$

The isochoric left and right Cauchy-Green tensors can be written in terms of the deformation gradient $\overline{\boldsymbol{F}}$ and $\boldsymbol{F}$,

$$\begin{aligned} \overline{\boldsymbol{B}} &= \overline{\boldsymbol{F}}\,\overline{\boldsymbol{F}}^T = J^{-2/3}\boldsymbol{F}\boldsymbol{F}^T = J^{-2/3}\boldsymbol{B}, \\ \overline{\boldsymbol{C}} &= \overline{\boldsymbol{F}}^T\overline{\boldsymbol{F}} = J^{-2/3}\boldsymbol{F}^T\boldsymbol{F} = J^{-2/3}\boldsymbol{C}. \end{aligned} \tag{7.8}$$

Additionally, the invariants for the incompressible material introduced in Chapter 6 need to be modified using the decompositions in Equations (7.6)–(7.8),

$$\overline{I}_1 = \mathrm{tr}[\overline{\boldsymbol{C}}] = J^{-2/3}I_1,\ I_2 = \mathrm{tr}[\mathrm{cof}[\overline{\boldsymbol{C}}]] = J^{-2/3}I_2,\ \overline{I}_3 = \det[\overline{\boldsymbol{C}}] = 1. \tag{7.9}$$

The rest of the invariants are also modified in a similar manner:

$$\begin{aligned} &\overline{I}_4 = J^{-2/3}I_4,\ \overline{I}_5 = J^{-4/3}I_5,\ \overline{I}_6 = J^{-2/3}I_6,\ \overline{I}_7 = J^{-4/3}I_7,\ \overline{I}_8 = J^{-2/3}I_8, \\ &\overline{I}_9 = J^{-4/3}I_9, \overline{I}_{10} = I_{10},\ \overline{I}_{11} = J^{2/3}I_{11},\ \overline{I}_{12} = J^{4/3}I_{12},\ \overline{I}_{13} = I_{13},\ \overline{I}_{14} = J^{-2/3}I_{14}, \\ &\overline{I}_{15} = I_{15},\ \overline{I}_{16} = J^{-2/3}I_{16}, \overline{I}_{17} = I_{17},\ \overline{I}_{18} = J^{-2/3}I_{18},\ \overline{I}_{19} = J^{-4/3}I_{19}. \end{aligned} \tag{7.10}$$

7.2.2. Decoupled Total Cauchy Stress

The free energy function for the nearly incompressible material is decoupled into

$$
\begin{aligned}
&W = \overline{W} + U(J), \\
&\overline{W} = \overline{W}(\bar{I}_1, \bar{I}_2, \bar{I}_4, \bar{I}_6, \bar{I}_8, \bar{I}_{11}, \bar{I}_{14}, \bar{I}_{16}, \bar{I}_{18}),
\end{aligned} \tag{7.11}
$$

where $\overline{W}$ is the isochoric part, $U(J)$ is the volumetric part and the volumetric function is given in [18, 19],

$$
U(J) = \frac{\kappa}{2}(J-1)^2, \tag{7.12}
$$

which is just one choice of the volumetric function.

The total Cauchy stress is

$$
\begin{aligned}
&\boldsymbol{\sigma} = \frac{1}{J}\boldsymbol{F}\boldsymbol{S}\boldsymbol{F}^T = \frac{2}{J}\boldsymbol{F}\left(\frac{\partial \overline{W}}{\partial \boldsymbol{C}} + \frac{\partial U(J)}{\partial \boldsymbol{C}}\right)\boldsymbol{F}^T = \frac{1}{J}\boldsymbol{F}(\bar{\boldsymbol{S}} + \boldsymbol{S}_{\boldsymbol{V}})\boldsymbol{F}^T, \\
&\boldsymbol{\sigma} = \bar{\boldsymbol{\sigma}} + \boldsymbol{\sigma}_{\boldsymbol{V}},
\end{aligned} \tag{7.13}
$$

where $\boldsymbol{S} = \bar{\boldsymbol{S}} + \boldsymbol{S}_{\boldsymbol{V}}$ is the 2nd Piola-Kirchhoff stress.

$\boldsymbol{S}_{\boldsymbol{V}}$ in Equation (7.13) becomes

$$
\boldsymbol{S}_{\boldsymbol{V}} = 2\frac{\partial U(J)}{\partial \boldsymbol{C}} = 2\frac{\partial}{\partial \boldsymbol{C}}\left(\frac{\kappa}{2}(J-1)^2\right) = 2\kappa(J-1)\frac{\partial J}{\partial \boldsymbol{C}} = \kappa(J-1)J\boldsymbol{C}^{-1}. \tag{7.14}
$$

The derivative of the isochoric free energy function with respect to $\boldsymbol{C}$ can be written as

$$
\begin{aligned}
&\frac{\partial \overline{W}}{\partial \boldsymbol{C}} = \frac{\partial \bar{\boldsymbol{C}}}{\partial \boldsymbol{C}} : \frac{\partial \overline{W}}{\partial \bar{\boldsymbol{C}}}, \ \frac{\partial}{\partial \boldsymbol{C}}(J^{-2/3}) = -\frac{1}{3}J^{-4/3}\bar{\boldsymbol{C}}^{-1}, \\
&\frac{\partial \bar{\boldsymbol{C}}}{\partial \boldsymbol{C}} = \frac{\partial}{\partial \boldsymbol{C}}(J^{-2/3}\boldsymbol{C}) = \boldsymbol{C}\frac{\partial}{\partial \boldsymbol{C}}(J^{-2/3}) + J^{-2/3}\frac{\partial \boldsymbol{C}}{\partial \boldsymbol{C}} = J^{-2/3}\left(\boldsymbol{I} - \frac{1}{3}\boldsymbol{C}\otimes\boldsymbol{C}^{-1}\right), \\
&\frac{\partial \overline{W}}{\partial \bar{\boldsymbol{C}}} = \sum_{i=1}^{18}\frac{\partial \overline{W}}{\partial \bar{I}_i}\frac{\partial \bar{I}_i}{\partial \bar{\boldsymbol{C}}}, \ (i = 1,2,3,4,6,8,11,14,16,18) \\
&\frac{\partial \overline{W}}{\partial \bar{\boldsymbol{C}}} = \overline{W}_1\boldsymbol{1} + \overline{W}_2(I_1\boldsymbol{1} - \bar{\boldsymbol{C}}) + \overline{W}_4\boldsymbol{a}\otimes\boldsymbol{a} + \overline{W}_6\boldsymbol{b}\otimes\boldsymbol{b} + \overline{W}_8\boldsymbol{a}\otimes\boldsymbol{b} - \overline{W}_{11}\bar{\boldsymbol{C}}^{-2}(\boldsymbol{E}\otimes\boldsymbol{E}) \\
&+ \overline{W}_{14}\boldsymbol{a}\otimes\boldsymbol{E} + \overline{W}_{16}\boldsymbol{b}\otimes\boldsymbol{E} + \overline{W}_{18}\boldsymbol{d}\otimes\boldsymbol{E}, \\
&\boldsymbol{d} = \boldsymbol{a}\times\boldsymbol{b}
\end{aligned} \tag{7.15}
$$

where $\boldsymbol{1}$ and $\boldsymbol{I}$ represent the 2nd and 4th order identity tensors, $\boldsymbol{E}$ is the nominal electric field and (:) is the double dot product, which are defined as

$$
\begin{aligned}
&I_{ijkl} = \frac{1}{2}(\delta_{ik}\delta_{jl} + \delta_{il}\delta_{jk}),\\
&\boldsymbol{A}:\boldsymbol{B} = \sum_{i=1}^{3}\sum_{j=1}^{3} A_{ij}B_{ji.}
\end{aligned}
\tag{7.16}
$$

By using Equation (7.15), $\overline{\boldsymbol{S}}$ becomes

$$
\begin{aligned}
&\overline{\boldsymbol{S}} = 2\frac{\partial \overline{\boldsymbol{C}}}{\partial \boldsymbol{C}} : \frac{\partial \overline{W}}{\partial \overline{\boldsymbol{C}}},\\
&\overline{\boldsymbol{S}} = 2J^{-2/3}(\boldsymbol{I} - \frac{1}{3}\overline{\boldsymbol{C}} \otimes \overline{\boldsymbol{C}}^{-1}) : \{\overline{W}_1\boldsymbol{1} + \overline{W}_2(I_1\boldsymbol{1} - \overline{\boldsymbol{C}}) + \overline{W}_4\boldsymbol{a}\otimes\boldsymbol{a} + \overline{W}_6\boldsymbol{b}\otimes\boldsymbol{b} + \overline{W}_8\boldsymbol{a}\otimes\boldsymbol{b}\\
&-\overline{W}_{11}\overline{\boldsymbol{C}}^{-2}(\boldsymbol{E}\otimes\boldsymbol{E}) + \overline{W}_{14}\boldsymbol{a}\otimes\boldsymbol{E} + \overline{W}_{16}\boldsymbol{b}\otimes\boldsymbol{E} + \overline{W}_{18}\boldsymbol{d}\otimes\boldsymbol{E}\}.
\end{aligned}
\tag{7.17}
$$

Therefore, the total stress is obtained by inserting Equations (7.14)and (7.17) into (7.13),

$$
\begin{aligned}
&\boldsymbol{\sigma} = \frac{2}{J}[\{\overline{W}_1\overline{\boldsymbol{B}} + \overline{W}_2(\overline{I}_1\overline{\boldsymbol{B}} - \overline{\boldsymbol{B}}^2) + \overline{W}_4(\overline{\boldsymbol{F}}\boldsymbol{a}\otimes\overline{\boldsymbol{F}}\boldsymbol{a}) + \overline{W}_6(\overline{\boldsymbol{F}}\boldsymbol{b}\otimes\overline{\boldsymbol{F}}\boldsymbol{b}) + \overline{W}_8(\overline{\boldsymbol{F}}\boldsymbol{a}\otimes\overline{\boldsymbol{F}}\boldsymbol{b})\\
&-\overline{W}_{11}(\boldsymbol{e}\otimes\boldsymbol{e}) + \overline{W}_{14}(\overline{\boldsymbol{F}}\boldsymbol{a}\otimes\overline{\boldsymbol{B}}\boldsymbol{e}) + \overline{W}_{16}(\overline{\boldsymbol{F}}\boldsymbol{b}\otimes\overline{\boldsymbol{B}}\boldsymbol{e}) + \overline{W}_{18}(\overline{\boldsymbol{F}}\boldsymbol{d}\otimes\overline{\boldsymbol{B}}\boldsymbol{e}\} - \frac{1}{3}\{\overline{W}_1\overline{I}_1 + 2\overline{W}_2\overline{I}_2\\
&+\overline{W}_4\overline{I}_4 + \overline{W}_6\overline{I}_6 + \overline{W}_8\overline{I}_8 - \overline{W}_{11}\overline{I}_{11} + \overline{W}_{14}\overline{I}_{14} + \overline{W}_{16}\overline{I}_{16} + \overline{W}_{18}\overline{I}_{18}\}] + \kappa J(J-1)\boldsymbol{1},
\end{aligned}
\tag{7.18}
$$

where $\boldsymbol{e}$ is the true electric field.

Doll and Schweizerhof summarized the required physical conditions for several volumetric functions given in the literature [20]. In the reference state, free energy is zero:

$$
\begin{aligned}
&\overline{W}(\overline{I}_1, \overline{I}_2, ...) = 0,\ U(J=1) = 0,\\
&U(J)\big|_{J=1} = \frac{\kappa}{2}(J-1)^2\Big|_{J=1} = 0.
\end{aligned}
\tag{7.19}
$$

If it is assumed that there is no residual stress in the reference state, then

$$
\begin{aligned}
&p = \frac{\partial U(J)}{\partial J},\\
&\frac{\partial U(J)}{\partial J}\Big|_{J=1} = \kappa(J-1)\big|_{J=1} = 0,
\end{aligned}
\tag{7.20}
$$

where $p = \partial U(J)/\partial J$ represents the hydrostatic pressure.

During the deformation, the free energy is greater than zero:

$$\overline{W}(\bar{I}_1, \bar{I}_2, \bar{I}_3, \ldots) > 0, \; U(J) > 0. \tag{7.21}$$

For the nearly incompressible material, the bulk modulus is defined as

$$\left. \frac{\partial^2 U(J)}{\partial J^2} \right|_{J \to 1} = \kappa \tag{7.22}$$

With respect to the requirement of polyconvexity of the free energy function [21], the volumetric part has to satisfy the convexity condition,

$$\begin{aligned} &\frac{\partial^2 U(J)}{\partial J^2} \geq 0, \\ &\frac{\partial^2}{\partial J^2}\left(\frac{\kappa}{2}(J-1)^2 \right) = \kappa \geq 0. \end{aligned} \tag{7.23}$$

7.2.3. Decoupled Tangent Modulus

For nearly incompressible materials, the tangent modulus is also decoupled by using the multiplicative decomposition in Section 7.2.1. First, the 2nd Piola-Kirchhoff stress $\boldsymbol{S}$ in Equation (7.13) can be rewritten as

$$\boldsymbol{S} = 2\left(\frac{\partial U(J)}{\partial J}\frac{\partial J}{\partial \boldsymbol{C}} + \frac{\partial \overline{W}}{\partial \overline{\boldsymbol{C}}}\frac{\partial \overline{\boldsymbol{C}}}{\partial \boldsymbol{C}} \right). \tag{7.24}$$

The tangent modulus is defined as

$$\boldsymbol{\mathcal{C}} = 4\frac{\partial^2 W}{\partial \boldsymbol{C} \partial \boldsymbol{C}} = 2\frac{\partial \boldsymbol{S}}{\partial \boldsymbol{C}}. \tag{7.25}$$

The tangent modulus can be obtained by using Equations (7.14), (7.15) and (7.24) in Equation (2.25):

$$
\begin{aligned}
\boldsymbol{\mathcal{C}} &= 2\frac{\partial}{\partial \boldsymbol{C}}\left[pJ\boldsymbol{C}^{-1} + 2J^{-2/3}\frac{\partial \overline{W}}{\partial \overline{\boldsymbol{C}}}\left(\boldsymbol{I} - \frac{1}{3}\overline{\boldsymbol{C}}\otimes\overline{\boldsymbol{C}}^{-1}\right)\right], \\
&= pJ(\boldsymbol{C}^{-1}\otimes\boldsymbol{C}^{-1} + 2\frac{\partial \boldsymbol{C}^{-1}}{\partial \boldsymbol{C}}) + \left\{4\frac{\partial \overline{W}}{\partial \overline{\boldsymbol{C}}}\frac{\partial}{\partial \boldsymbol{C}}(J^{-2/3}) + 4J^{-2/3}\frac{\partial}{\partial \boldsymbol{C}}\left(\frac{\partial \overline{W}}{\partial \overline{\boldsymbol{C}}}\right)\right\}\left(\boldsymbol{I} - \frac{1}{3}\overline{\boldsymbol{C}}\otimes\overline{\boldsymbol{C}}^{-1}\right) \\
&+ 4J^{-2/3}\frac{\partial \overline{W}}{\partial \overline{\boldsymbol{C}}}\frac{\partial}{\partial \boldsymbol{C}}\left(\boldsymbol{I} - \frac{1}{3}\overline{\boldsymbol{C}}\otimes\overline{\boldsymbol{C}}^{-1}\right),
\end{aligned}
\tag{7.26}
$$

where

$$
\begin{aligned}
&\frac{\partial}{\partial \boldsymbol{C}}\left(\frac{\partial \overline{W}}{\partial \overline{\boldsymbol{C}}}\right) = \frac{\partial \overline{\boldsymbol{C}}}{\partial \boldsymbol{C}} : \frac{\partial}{\partial \overline{\boldsymbol{C}}}\left(\frac{\partial \overline{W}}{\partial \overline{\boldsymbol{C}}}\right) = J^{-2/3}(\boldsymbol{I} - \frac{1}{3}\boldsymbol{C}\otimes\boldsymbol{C}^{-1}) : \frac{\partial^2 \overline{W}}{\partial \overline{\boldsymbol{C}}^2}, \\
&\frac{\partial}{\partial \boldsymbol{C}}\left(\boldsymbol{I} - \frac{1}{3}\boldsymbol{C}\otimes\boldsymbol{C}^{-1}\right) = \frac{\partial \overline{\boldsymbol{C}}}{\partial \boldsymbol{C}} : \frac{\partial}{\partial \overline{\boldsymbol{C}}}\left(\boldsymbol{I} - \frac{1}{3}\boldsymbol{C}\otimes\boldsymbol{C}^{-1}\right) = -\frac{J^{-2/3}}{3}\left(\frac{\partial \overline{\boldsymbol{C}}}{\partial \overline{\boldsymbol{C}}}\otimes\overline{\boldsymbol{C}}^{-1} + \overline{\boldsymbol{C}}\otimes\frac{\partial \overline{\boldsymbol{C}}^{-1}}{\partial \overline{\boldsymbol{C}}}\right).
\end{aligned}
\tag{7.27}
$$

Simplifying the full expression for the tangent modulus yields

$$
\begin{aligned}
\boldsymbol{\mathcal{C}} &= -\frac{4}{3}J^{-4/3}\left(\frac{\partial \overline{W}}{\partial \overline{\boldsymbol{C}}}\otimes\overline{\boldsymbol{C}}^{-1} + \overline{\boldsymbol{C}}^{-1}\otimes\frac{\partial \overline{W}}{\partial \overline{\boldsymbol{C}}}\right) - \frac{4}{3}J^{-4/3}\left(\frac{\partial \overline{W}}{\partial \overline{\boldsymbol{C}}} : \overline{\boldsymbol{C}}\right)\left(\frac{\partial \overline{\boldsymbol{C}}^{-1}}{\partial \overline{\boldsymbol{C}}} - \frac{1}{3}\overline{\boldsymbol{C}}^{-1}\otimes\overline{\boldsymbol{C}}^{-1}\right) \\
&+ 4J^{-4/3}\frac{\partial^2 \overline{W}}{\partial \overline{\boldsymbol{C}}^2} - \frac{4}{3}J^{-4/3}\left\{\left(\frac{\partial^2 \overline{W}}{\partial \overline{\boldsymbol{C}}^2} : \overline{\boldsymbol{C}}\right)\otimes\overline{\boldsymbol{C}}^{-1} - \overline{\boldsymbol{C}}^{-1}\otimes\left(\frac{\partial^2 \overline{W}}{\partial \overline{\boldsymbol{C}}^2} : \overline{\boldsymbol{C}}\right)\right\} \\
&+ \frac{4}{9}J^{-4/3}\left(\overline{\boldsymbol{C}} : \frac{\partial^2 \overline{W}}{\partial \overline{\boldsymbol{C}}^2} : \overline{\boldsymbol{C}}\right)\overline{\boldsymbol{C}}^{-1}\otimes\overline{\boldsymbol{C}}^{-1} + pJ(\boldsymbol{C}^{-1}\otimes\boldsymbol{C}^{-1} + 2\frac{\partial \boldsymbol{C}^{-1}}{\partial \boldsymbol{C}}).
\end{aligned}
\tag{7.28}
$$

By using the push-forward operator,

$$
\begin{aligned}
\boldsymbol{c} &= \frac{1}{J}\boldsymbol{F}\boldsymbol{F}\boldsymbol{\mathcal{C}}\boldsymbol{F}^T\boldsymbol{F}^T \\
\boldsymbol{c} &= -\frac{4}{3J}\overline{\boldsymbol{F}}\left(\frac{\partial \overline{W}}{\partial \overline{\boldsymbol{C}}}\otimes\boldsymbol{1} + \boldsymbol{1}\otimes\frac{\partial \overline{W}}{\partial \overline{\boldsymbol{C}}}\right)\overline{\boldsymbol{F}}^T - \frac{4}{3J}\left(\frac{\partial \overline{W}}{\partial \overline{\boldsymbol{C}}} : \overline{\boldsymbol{C}}\right)\left\{\boldsymbol{I} - \frac{1}{3}(\boldsymbol{1}\otimes\boldsymbol{1})\right\} \\
&+ \frac{4}{J}\overline{\boldsymbol{F}}\overline{\boldsymbol{F}}\frac{\partial^2 \overline{W}}{\partial \overline{\boldsymbol{C}}^2}\overline{\boldsymbol{F}}^T\overline{\boldsymbol{F}}^T - \frac{4}{3J}\overline{\boldsymbol{F}}\left\{\left(\frac{\partial^2 \overline{W}}{\partial \overline{\boldsymbol{C}}^2} : \overline{\boldsymbol{C}}\right)\otimes\boldsymbol{1} + \boldsymbol{1}\otimes\left(\frac{\partial^2 \overline{W}}{\partial \overline{\boldsymbol{C}}^2} : \overline{\boldsymbol{C}}\right)\right\}\overline{\boldsymbol{F}}^T \\
&+ \frac{4}{9J}\left(\overline{\boldsymbol{C}} : \frac{\partial^2 \overline{W}}{\partial \overline{\boldsymbol{C}}^2} : \overline{\boldsymbol{C}}\right)\boldsymbol{1}\otimes\boldsymbol{1} + pJ(\boldsymbol{1}\otimes\boldsymbol{1} - 2\boldsymbol{I}),
\end{aligned}
\tag{7.29}
$$

where

$$\frac{\partial^2 \overline{W}}{\partial \overline{\boldsymbol{C}}^2} = \boldsymbol{1} \otimes \frac{\partial \overline{W}_1}{\partial \overline{\boldsymbol{C}}} + \boldsymbol{1} \otimes \overline{W}_2 \frac{\partial I_2}{\partial \overline{\boldsymbol{C}}} + \boldsymbol{1} \otimes \bar{I}_1 \frac{\partial \overline{W}_2}{\partial \overline{\boldsymbol{C}}} - \overline{\boldsymbol{C}} \otimes \frac{\partial \overline{W}_2}{\partial \overline{\boldsymbol{C}}} - \overline{W}_2 \frac{\partial \overline{\boldsymbol{C}}}{\partial \overline{\boldsymbol{C}}} - \bar{I}_1 \overline{\boldsymbol{C}} \otimes \frac{\partial \overline{\boldsymbol{C}}}{\partial \overline{\boldsymbol{C}}}$$
$$+ \boldsymbol{a} \otimes \boldsymbol{a} \otimes \frac{\partial \overline{W}_4}{\partial \overline{\boldsymbol{C}}} + \boldsymbol{b} \otimes \boldsymbol{b} \otimes \frac{\partial \overline{W}_6}{\partial \overline{\boldsymbol{C}}} + \boldsymbol{a} \otimes \boldsymbol{b} \otimes \frac{\partial \overline{W}_8}{\partial \overline{\boldsymbol{C}}} - \frac{\partial \overline{W}_{11}}{\partial \overline{\boldsymbol{C}}} \otimes \overline{\boldsymbol{C}}^{-2} (\boldsymbol{E} \otimes \boldsymbol{E})$$
$$+ 2\overline{W}_{11} \overline{\boldsymbol{C}}^{-3} (\boldsymbol{E} \otimes \boldsymbol{E}) \otimes \frac{\partial \overline{\boldsymbol{C}}^{-1}}{\partial \overline{\boldsymbol{C}}} + \boldsymbol{a} \otimes \boldsymbol{E} \otimes \frac{\partial \overline{W}_{14}}{\partial \overline{\boldsymbol{C}}} + \boldsymbol{b} \otimes \boldsymbol{E} \otimes \frac{\partial \overline{W}_{16}}{\partial \overline{\boldsymbol{C}}} + \boldsymbol{d} \otimes \boldsymbol{E} \otimes \frac{\partial \overline{W}_{18}}{\partial \overline{\boldsymbol{C}}}, \tag{7.30}$$
$$\frac{\partial \overline{W}_i}{\partial \overline{\boldsymbol{C}}} = \sum_{j=1}^{18} \frac{\partial \overline{W}_i}{\partial \bar{I}_j} \frac{\partial \bar{I}_j}{\partial \overline{\boldsymbol{C}}}, (i, j = 1,2,3,4,6,8,11,14,16 \text{ and } 18),$$
$$= \overline{W}_{i1} \boldsymbol{1} + \overline{W}_{i2} (\bar{I}_1 \boldsymbol{1} - \overline{\boldsymbol{C}}) + \overline{W}_{i4} \boldsymbol{a} \otimes \boldsymbol{b} + \overline{W}_{i6} \boldsymbol{b} \otimes \boldsymbol{b} + \overline{W}_{i8} \boldsymbol{a} \otimes \boldsymbol{b} - \overline{W}_{i11} \overline{\boldsymbol{C}}^{-2} (\boldsymbol{E} \otimes \boldsymbol{E})$$
$$+ \overline{W}_{i14} \boldsymbol{a} \otimes \boldsymbol{E} + \overline{W}_{i16} \boldsymbol{b} \otimes \boldsymbol{E} + \overline{W}_{i18} \boldsymbol{d} \otimes \boldsymbol{E}.$$

The decoupled constitutive formulations in Equations (7.6), (7.8), (7.18) and (7.29) are implemented in ABAQUS using a user defined UMAT. The UMAT code is given Appendix D. Specific examples of the decoupled constitutive formulation for isotropic and anisotropic electro-elastic materials are presented with numerical examples in Section 7.6.

7.3. Objective Rate of the Tangent Modulus

According to Belytschko *et al.* [22], in order to account for material rotation, an objective rate of the stress tensor is required for the finite element program. In detail, since the stress is a material quantity, the objectivity is automatically satisfied,

$$\boldsymbol{\sigma} = \boldsymbol{R} \cdot \boldsymbol{\sigma} \cdot \boldsymbol{R}^T, \ \boldsymbol{R} \cdot \boldsymbol{R}^T = 1, \tag{7.31}$$

where the rotational tensor $\boldsymbol{R}$ is orthogonal. However, the first derivative of the stress $\boldsymbol{\sigma}$ with respect to time t (stress rate) is not objective because

$$\dot{\boldsymbol{\sigma}} = \frac{d\boldsymbol{\sigma}}{dt} = \frac{d(\boldsymbol{R} \cdot \boldsymbol{\sigma} \cdot \boldsymbol{R}^T)}{dt} = \dot{\boldsymbol{R}} \cdot \boldsymbol{\sigma} \cdot \boldsymbol{R}^T + \boldsymbol{R} \cdot \dot{\boldsymbol{\sigma}} \cdot \boldsymbol{R}^T + \boldsymbol{R} \cdot \boldsymbol{\sigma} \cdot \dot{\boldsymbol{R}}^T, \ \frac{d\boldsymbol{\sigma}}{dt} \neq \boldsymbol{R} \cdot \frac{d\boldsymbol{\sigma}}{dt} \cdot \boldsymbol{R}^T. \tag{7.32}$$

Therefore, in order to account for the rotation $\boldsymbol{R}$ during the deformation and keeping the objectivity, an objective rate of the stress tensor needs to be employed.

In ABAQUS/CAE, the material is considered as being in a fixed global coordinate system. However, since incremental rotations are passed in to the user subroutine (UMAT) at the beginning of each increment, the material is taken to lie in a corotational coordinate system. In ABAQUS/CAE, the Jaumann rate is adopted as a corotational rate (objective rate of the stress tensor), where the material coordinates rotate with deformation.

The Lie derivative of the Kirchhoff stress $\boldsymbol{L_v\tau}$ can be written as

$$\begin{aligned}\boldsymbol{L_v\tau} &= \boldsymbol{F}\cdot\left[\frac{d(\boldsymbol{F}^{-1}\cdot\boldsymbol{\tau}\cdot\boldsymbol{F}^{-T})}{dt}\right]\cdot\boldsymbol{F}^{T} = \boldsymbol{F}\cdot(\dot{\boldsymbol{F}}^{-1}\cdot\boldsymbol{\tau}\cdot\boldsymbol{F}^{-T})\cdot\boldsymbol{F}^{T} + \boldsymbol{F}\cdot(\boldsymbol{F}^{-1}\cdot\dot{\boldsymbol{\tau}}\cdot\boldsymbol{F}^{-T})\cdot\boldsymbol{F}^{T} \\ &+ \boldsymbol{F}\cdot(\boldsymbol{F}^{-1}\cdot\boldsymbol{\tau}\cdot\dot{\boldsymbol{F}}^{-T})\cdot\boldsymbol{F}^{T} = -\boldsymbol{L}\cdot\boldsymbol{\tau} + \dot{\boldsymbol{\tau}} - \boldsymbol{\tau}\cdot\boldsymbol{L}^{T},\ \frac{d\boldsymbol{\tau}}{dt} - \boldsymbol{L}\cdot\boldsymbol{\tau} - \boldsymbol{\tau}\cdot\boldsymbol{L}^{T} = J\boldsymbol{c}:\boldsymbol{D},\end{aligned} \tag{7.33}$$

where $\boldsymbol{\tau} = J\boldsymbol{\sigma}$ and $\boldsymbol{L}$ is the velocity gradient and $\boldsymbol{D}$ is the rate of deformation,

$$\boldsymbol{L} = \frac{\partial \boldsymbol{v}}{\partial x},\ \boldsymbol{D} = \frac{1}{2}(\boldsymbol{L} + \boldsymbol{L}^{T}). \tag{7.34}$$

The Jaumann rate in ABAQUS/CAE is defined as

$$\begin{aligned}\boldsymbol{\tau}^{\nabla} &= \frac{d\boldsymbol{\tau}}{dt} - \boldsymbol{W\tau} - \boldsymbol{\tau W}^{T} = \boldsymbol{C}^{\nabla}:\boldsymbol{D}, \\ \frac{d\boldsymbol{\tau}}{dt} &= \boldsymbol{C}^{\nabla}:\boldsymbol{D} + \boldsymbol{W\tau} + \boldsymbol{\tau W}^{T},\end{aligned} \tag{7.35}$$

where $\boldsymbol{C}^{\nabla}$ is the Jaumann tangent modulus and $\boldsymbol{W}$ is the spin tensor,

$$\boldsymbol{W} = \frac{1}{2}(\boldsymbol{L} - \boldsymbol{L}^{T}). \tag{7.36}$$

By inserting the time derivative of $\boldsymbol{\tau}$ in Equation (7.35) into Equation (7.33), the following relation is obtained

$$J\boldsymbol{c}:\boldsymbol{D}=\boldsymbol{C}^{\nabla}:\boldsymbol{D}-(\boldsymbol{L}-\boldsymbol{W})\boldsymbol{\tau}-\boldsymbol{\tau}(\boldsymbol{L}-\boldsymbol{W})^{T}=\boldsymbol{C}^{\nabla}:\boldsymbol{D}-\boldsymbol{D}\boldsymbol{\tau}-\boldsymbol{\tau}\boldsymbol{D}^{T}, \tag{7.37}$$

The Jaumann tangent modulus is

$$\begin{aligned}&\boldsymbol{C}^{\nabla}:\boldsymbol{D}=J\boldsymbol{c}:\boldsymbol{D}+J\boldsymbol{D}\boldsymbol{\sigma}+J\boldsymbol{\sigma}\boldsymbol{D}^{T}=J(\boldsymbol{c}:\boldsymbol{D}+\boldsymbol{c}':\boldsymbol{D}),\\&\boldsymbol{C}^{\nabla}=J(\boldsymbol{c}+\boldsymbol{c}').\end{aligned} \tag{7.38}$$

where

$$\boldsymbol{c}':\boldsymbol{D}=\boldsymbol{D}\boldsymbol{\sigma}+\boldsymbol{\sigma}\boldsymbol{D}^{T}. \tag{7.39}$$

The tangent modulus for ABAQUS is obtained,

$$\boldsymbol{c}^{ABAQUS}=\frac{1}{J}\boldsymbol{C}^{\nabla}=(\boldsymbol{c}+\boldsymbol{c}'). \tag{7.40}$$

In index notation, the tangent modulus (for ABAQUS) is

$$c_{ijkl}^{ABAQUS}=\boldsymbol{c}_{ijkl}+\boldsymbol{c}'_{ijkl}, \tag{7.41}$$

where

$$c'_{ijkl}=\frac{1}{2}(\delta_{ik}\sigma_{jl}+\delta_{il}\sigma_{jk}+\delta_{jk}\sigma_{il}+\delta_{jl}\sigma_{ik}). \tag{7.42}$$

The user subroutine (UMAT) developed in this dissertation includes the constitutive formulations which are the total stress and tangent modulus in Sections 7.2.2, 7.2.3 and 7.3. The ser subroutines (UMAT: E_MRmodel.f and E_Anisomodel.f) for isotropic and anisotropic electro-elastic materials are given in Appendix D.

7.4. Implementation of the Finite Element Method

In this section, the procedure to solve a nonlinear electro-elastic problem in ABAQUS is outlined. The general equilibrium equation for the finite element mesh is

$$\Pi^i(u^i) = 0, \tag{7.43}$$

where Π^i is the force conjugate to node number *i*, u^i is the nodal displacement at node number *i*, ($i = 1, 2, \ldots, N$), respectively and *N* is the number of nodes in the mesh.

The first solution u^i is guessed and inserted into Equation (7.43). If the equilibrium equation is not satisfied with the first guess u^i, the solution is improved by adding a small correction du^i. This procedure is repeated until the equilibrium equation is approximately satisfied within a sufficient degree of accuracy, which is defined by user or ABAQUS/CAE.

By inserting the updated solution u^i+du^i, the equilibrium equation becomes,

$$\Pi(u^i + du^i) = 0. \tag{7.44}$$

Equation (7.44) is modified by using a Taylor expansion

$$\Pi(u^i) + \left.\frac{d\Pi(u)}{du}\right|_{u=u^i} du^i = 0, \tag{7.45}$$

where $\left.\frac{d\Pi(u)}{du}\right|_{u=u^i}$ is the stiffness matrix, which is a function of the tangent modulus. Since Equation (7.45) can be solved for du^i, the guessed u^i can be corrected. The next solution is obtained by using the Newton-Raphson method [23]. Let u^i be a good guess for u^{i+1},

$$u^{i+1} = u^i + du^i. \tag{7.46}$$

By rearranging Equation (7.45), du^i is obtained as

$$du^i = -\Pi(u^i)\left(\left.\frac{d\Pi(u)}{du}\right|_{u=u^i}\right)^{-1}. \tag{7.47}$$

The next guess u^{i+1} is obtained by inserting Equation (7.47) into Equation (7.46),

$$u^{i+1} = u^i - \Pi(u^i)\left(\frac{d\Pi(u)}{du}\bigg|_{u=u^i} \right)^{-1} \tag{7.48}$$

The convergence rate of the solution u^{i+1} is significantly dependent on the tangent modulus. The tangent modulus serves as an iterative operator for the next solution. Even though an exact closed –form solution for the tangent modulus gives the most rapid convergence, the exact tangent modulus is not mandatory to achieve correct solutions [10].

Based on Equations (7.43)–(7.48), the solution procedure in UMAT of ABAQUS can be summarized:

(i). The displacement field is specified as u^i and the deformation gradient $\overline{\boldsymbol{F}}$, the left and right Cauch-Green tensors $\overline{\boldsymbol{B}}$ and $\overline{\boldsymbol{C}}$ are calculated by using u^i.

(ii). Given the deformation gradient, the left and right Cauchy-Green tensors, the Kirchhoff stress ($J\boldsymbol{\sigma}$), Cauchy stress ($\boldsymbol{\sigma}$) and tangent modulus ($\mathbb{c}$) are calculated using Equations (7.18), (7.29) and (7.41).

(iii). The values from 1 and 2 are substituted into the equilibrium equation in Equation (7.43). If the equilibrium equation is not satisfied with the first guess u^i, u^i is corrected to bring it closer to the proper solution by setting $u^i + du^i$.

(iv). The procedures (i), (ii) and (iii) are repeated until the equilibrium equation is satisfied.

7.5. Numerical Stability of Electro-elastic Constitutive Model in ABAQUS

In this section, the numerical stability of the constitutive model for the electro-elastic material is investigated using the polyconvexity condition which is introduced in the Chapter 3. In ABAQUS, the Newton-Raphson method is generally employed to update the solution for each

node u^i. The material stiffness matrix $\left.\frac{d\Pi(u)}{du}\right|_{u=u^i}$ is used for iteration operator in the Newton-Raphson method. The material stiffness matrix is a function of the tangent modulus $\boldsymbol{C}$. According to Chapter 3, the electromechanical stability of the electro-elastic material is satisfied if W is polyconvex with respect to the independent variables ($\boldsymbol{F}$, cof[$\boldsymbol{F}$], det[$\boldsymbol{F}$] and $\boldsymbol{E}$). That is to say, if $\boldsymbol{C}$ is positive definite ($\boldsymbol{C}$ is the second derivative of W with respect to $\boldsymbol{C}$), the numerical solution of the equilibrium equations will be stable electromechanically. Thus, by requiring the polyconvexity condition of W, the numerical solutions for the electro-elastic material becomes stable. The polyconvexity condition from the Chapter 3 is written in the form

$$W(\boldsymbol{F},\boldsymbol{E}) = g(\boldsymbol{F},\mathrm{cof}[\boldsymbol{F}],\det[\boldsymbol{F}],\boldsymbol{E}), \tag{7.49}$$

with g convex for each independent variable $\boldsymbol{F}$, cof[$\boldsymbol{F}$], det[$\boldsymbol{F}$] and $\boldsymbol{E}$.

The numerical stability of the examples in Section 7.6 is investigated by using the polyconvexity condition in Equation (3.23).

7.6. Numerical Examples

In this section, two numerical examples for an isotropic electro-elastic material and an anisotropic electro-elastic material in ABAQUS are presented to show the capability of the user subroutine (UMAT). In Section 7.6.1, the decoupled constitutive formulation for an isotropic electro-elastic material is derived and a numerical example (equibiaxial extension of an isotropic dielectric elastomer (DE)) is simulated to validate the UMAT developed in this research. For showing the applicability of the UMAT, a more complicated example employing an anisotropic DE is presented in Section 7.6.2.

7.6.1. Equibiaxial Extension of Isotropic Electro-elastic Materials: Dielectric Elastomer

The finite element simulation for simple equibiaxial extension is compared with the analytical solution using the constitutive law presented in Chapter 2. Let's consider an isotropic electro-elastic material specifically a DE (see Figure 7.3). An electric field is applied in the X_3 direction. The initial dimensions for the simulation are given as $L_1 = L_2 = 200$ mm and $h_0 = 0.5$ *mm*.

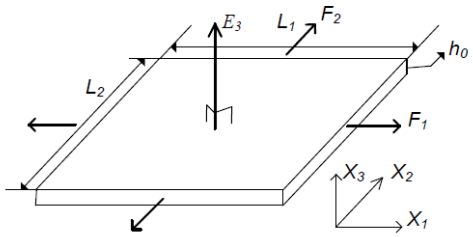

Figure 7.3. Equibiaxial extension of an isotropic dielectric elastomer membrane with nominal electric field E_3 in the reference state.

The free energy function is assumed to be invariant-based, where for a DE the following formulation is used

$$\begin{aligned} W &= \overline{W}(\bar{I}_1, \bar{I}_2, \bar{I}_{11}) + U(J), \\ \overline{W} &= \overline{W}_{elastic} + \overline{W}_{electric}, \end{aligned} \tag{7.50}$$

where the volumetric function $U(J)$ is given in Equation (7.12). A Mooney-Rivlin model is adopted for the elastic part,

$$\overline{W}_{elastic} = C_1(\bar{I}_1 - 3) + C_2(\bar{I}_2 - 3), \tag{7.51}$$

where C_1 and C_2 are material constants for the Mooney-Rivlin model ($C_1 = 16$ *kPa*, $C_2 = 7.3$ *kPa* for 3M VHB 4905 [24, 25]). For small to medium stretch (< 2.0), this is a reasonable assumption [24, 26].

The electrostatic energy function is given as

$$\overline{W}_{electric} = J\varepsilon_0\varepsilon_r \frac{\boldsymbol{E}\cdot\overline{\boldsymbol{C}}^{-1}\cdot\boldsymbol{E}}{2} = J\varepsilon_0\varepsilon_r \frac{\bar{I}_{11}}{2}, \tag{7.52}$$

where ε_0 = 8.85×10^{-12} F/m and ε_r = 4.7 for VHB 4905 represent the vacuum and relative permittivity.

By inserting the free energy function into Equation (7.18), the total Cauchy stress is

$$\begin{aligned}\boldsymbol{\sigma} = &\frac{2}{J}[\{\overline{W}_1\overline{\boldsymbol{B}} + \overline{W}_2(\bar{I}_1\overline{\boldsymbol{B}} - \overline{\boldsymbol{B}}^2) - \overline{W}_{11}(\boldsymbol{e}\otimes\boldsymbol{e})\} - \frac{1}{3}(\overline{W}_1\bar{I}_1 + 2\overline{W}_2\bar{I}_2 - \overline{W}_{11}\bar{I}_{11})] \\ &+ KJ(J-1)\boldsymbol{1}.\end{aligned} \tag{7.53}$$

The total Cauchy stress is written in index notation as

$$\begin{aligned}\sigma_{ij} = &\frac{2}{J}[\{C_1\overline{B}_{ij} + C_2(\bar{I}_1\overline{B}_{ij} - \overline{B}^2_{ij}) + \frac{J\varepsilon_0\varepsilon_r}{2}e_ie_j\} - \frac{1}{3}(\overline{W}_1\bar{I}_1 + 2\overline{W}_2\bar{I}_2 - \overline{W}_{11}\bar{I}_{11})\delta_{ij}] \\ &+ KJ(J-1)\delta_{ij},\ (i,j=1,2,3).\end{aligned} \tag{7.54}$$

The tangent modulus for the isotropic electro-elastic material is given as

$$\begin{aligned}\mathfrak{c} = &-\frac{4}{3J}\overline{F}[\{\overline{W}_1\overline{\boldsymbol{B}} + \overline{W}_2(\bar{I}_1\overline{\boldsymbol{B}} - \overline{\boldsymbol{B}}^2) - \overline{W}_{11}(\boldsymbol{e}\otimes\boldsymbol{e})\}\otimes\boldsymbol{1} + \boldsymbol{1}\otimes\{\overline{W}_1\overline{\boldsymbol{B}} + \overline{W}_2(\bar{I}_1\overline{\boldsymbol{B}} - \overline{\boldsymbol{B}}^2) \\ &- \overline{W}_{11}(\boldsymbol{e}\otimes\boldsymbol{e})\}] - \frac{4}{3J}\{\overline{W}_1\bar{I}_1 + 2\overline{W}_2\bar{I}_1 - \overline{W}_{11}(\boldsymbol{e}\cdot\boldsymbol{e})\}\left\{\boldsymbol{I} - \frac{1}{3}(\boldsymbol{1}\otimes\boldsymbol{1})\right\} \\ &+ \frac{4}{J}\{\overline{W}_2\overline{\boldsymbol{B}}\otimes\overline{\boldsymbol{B}} - \overline{W}_2\overline{\boldsymbol{B}}^2 + 2\overline{W}_{11}(\boldsymbol{e}\otimes\boldsymbol{e})\} - \frac{4}{3J}[\{\overline{W}_2\bar{I}_2\overline{\boldsymbol{B}} + \overline{W}_2\overline{\boldsymbol{B}}^2 \\ &+ 2\overline{W}_{11}\overline{\boldsymbol{B}}^{-1}(\boldsymbol{e}\cdot\boldsymbol{e})\}\otimes\boldsymbol{1} + \boldsymbol{1}\otimes\{\overline{W}_2\bar{I}_2\overline{\boldsymbol{B}} + \overline{W}_2\overline{\boldsymbol{B}}^2 + 2\overline{W}_{11}\overline{\boldsymbol{B}}^{-1}(\boldsymbol{e}\cdot\boldsymbol{e})\}] \\ &+ \frac{4}{9J}\{\overline{W}_2\bar{I}_1^2 + \overline{W}_2(\bar{I}_1^2 - 2\bar{I}_2)\overline{\boldsymbol{C}} + 2\overline{W}_{11}\bar{I}_{11}\}\boldsymbol{1}\otimes\boldsymbol{1} + pJ(\boldsymbol{1}\otimes\boldsymbol{1} - 2\boldsymbol{I}).\end{aligned} \tag{7.55}$$

In index notation, it is written as

$$
\begin{aligned}
c_{ijkl} = & -\frac{4}{3J}\overline{F}[\{C_1\overline{B}_{ij} + C_2(\bar{I}_1\overline{B}_{ij} - \overline{B}^2_{ij}) + \frac{J\varepsilon_0\varepsilon_r}{2}(e_i e_j)\}\delta_{kl} + \delta_{ij}\{C_1\overline{B}_{kl} + C_2(\bar{I}_1\overline{B}_{kl} \\
& - \overline{B}^2_{kl}) + \frac{J\varepsilon_0\varepsilon_r}{2}(e_k e_l)\}] - \frac{4}{3J}\{C_1\bar{I}_1 + 2C_2\bar{I}_1 + \frac{J\varepsilon_0\varepsilon_r}{2}(e\cdot e)\}\left\{I_{ijkl} - \frac{1}{3}(\delta_{ij}\delta_{kl})\right\} \\
& + \frac{4}{J}\{C_2\overline{B}_{ij}\overline{B}_{kl} - C_2\overline{B}^2_{ij}\delta_{kl} - J\varepsilon_0\varepsilon_r(e_i e_j)\delta_{kl}\} - \frac{4}{3J}[\{C_2\bar{I}_2\overline{B}_{ij} + C_2\overline{B}^2_{ij} \\
& - J\varepsilon_0\varepsilon_r\bar{I}_{11}\overline{B}^{-1}_{ij}\}\delta_{kl} + \delta_{ij}\{C_2\bar{I}_2\overline{B}_{kl} + C_2\overline{B}^2_{kl} - J\varepsilon_0\varepsilon_r\bar{I}_{11}\overline{B}^{-1}_{kl}\}] \\
& + \frac{4}{9J}\{C_2\bar{I}^2_1 + C_2(\bar{I}^2_1 - 2\bar{I}_2)\overline{C} - J\varepsilon_0\varepsilon_r\bar{I}_{11}\}\delta_{ij}\delta_{kl} + pJ(\delta_{ij}\delta_{kl} - 2I_{ijkl}),\ (i,j,k,l = 1,2,3).
\end{aligned}
\tag{7.56}
$$

Now, Equations (7.54) and (7.56) are implemented into the UMAT (ABAQUS). Details of the UMAT are given in Appendix D.

The numerical stability of the isotropic DE with respect to the independent variables (F_{11} and E_3) is investigated using the polyconvexity condition in Equation (3.23) and the results in the Chapter 3 (det[$\boldsymbol{F}$] is not independent variable because det[$\boldsymbol{F}$] is treated as a constant for nearly incompressible material (det[$\boldsymbol{F}$] ≈ 1.0 in ABAQUS)). The numerical stability under equibiaxial extension is expressed as the applicable electric field range

$$
\begin{aligned}
\left|E_3\right| &\le \sqrt{\frac{(5+\overline{F}^6_{11}) + 3F^2_{11}(1+\overline{F}^6_{11})R_2}{5\overline{F}^8_{11}R_{11}}}, \\
R_2 &= \frac{\overline{W}_2}{\overline{W}_1} = \frac{C_2}{C_1},\ R_{11} = \frac{\overline{W}_{11}}{\overline{W}_1} = \frac{\varepsilon_0\varepsilon_r}{C_1},
\end{aligned}
\tag{7.57}
$$

where R_2 = 0.456 and $R_{11} = 2.6\times10^{-15}$ for VHB 4905.

Figure 3.4. shows the numerical stability region of the isotropic DE with respect to the deformation gradient F_{11}. The curve represents the upper boundary of the electric field for keeping the numerical stability and the area under the curve represents the stable region during the deformation.

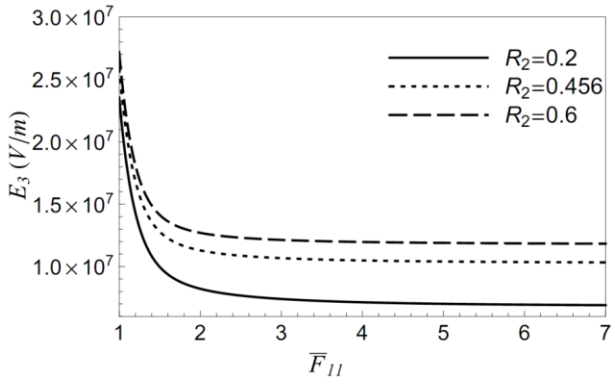

Figure 7.4. Electromechanical stability of isotropic dielectric elastomer, C_1 = 16 *kPa*, R_2 = 0.2–0.6 and R_{11} = 2.6×10^{-15} (VHB 4905, R_2=0.456).

In ABAQUS/Standard, a 3D element (C3D8: 8 node linear brick) is employed for the equibiaxial extension of the isotropic DE with prestretch (3.0) in Figure 7.3. C3D8 is one of continuum elements in ABAQUS. The continuum element is the standard volume elements in ABAQUS and is composed of a single homogeneous material, but cannot include structural elements such as beams, shells, membranes, and trusses. Figure 7.5 shows the electromechanical response of the isotropic DE under the equibiaxial extension with respect to the applied voltage. As expected, Figure 7.5 shows that the membrane becomes increasingly compliant with higher input voltage. The numerical result from ABAQUS with the UMAT is identical to the analytical solution in Figure 7.5. The analytical solution is based on the approaches in Son and Goulbourne [27, 28]. For the analytical solution, since the isotropic DE was assumed to be membrane, only the stress in the principal direction was considered [27, 28]. For the finite element modeling, 3D continuum element was employed and any assumption was not included.

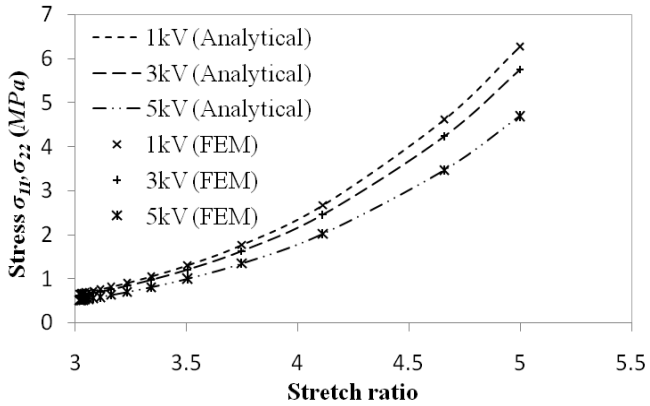

Figure 7.5. Electromechanical response of the prestretched isotropic dielectric elastomer with respect to the applied voltage (1–5 *kV*).

In this section, the finite element modeling result for the electromechanical response of an isotropic electro-elastic membrane was compared to the analytical solution. The result in validates the UMAT of the electro-elastic material. In the next section, a problem with a more complicated configuration is considered to show the ability of the UMAT for electro-elastic materials.

7.6.2. M-framed Anisotropic Electro-Elastic Material with Electri al and Mechanical stimulus

In this section, a more complex problem employing an anisotropic electro-elastic material (specifically anisotropic DE) is presented. Example in Figure 7.6 is inspired from batwing surface, which is scaled from real batwing structure [26]. In Figure 7.6, consider an anisotropic DE with static or dynamic pressure P on the X_1-X_2 plane, an nominal electric field E_3 given in the X_3 direction and uniaxial stretch at the right boundary. The anisotropic DE consists of an isotropic DE and two families of electro-passive fibers characterized by the reference angles a and β (see Figure 7.6). The families of the electro-passive fibers are described using local

directional vectors ***a*** and ***b***, which have been introduced in Chapter 2. The initial dimensions of the anisotropic DE are given in Figure 7.6.

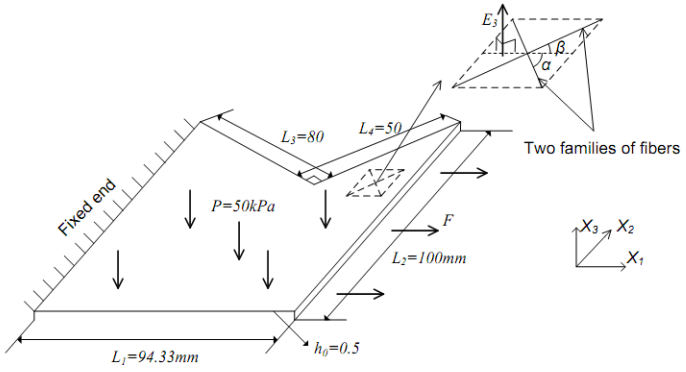

Figure 7.6. Schematic of the M-framed anisotropic dielectric elastomer with the pressure profile, applied electric field and uniaxial stretch in the reference state.

Since the fibers are not electro-active, there is no coupling between the fibers and the electric field. The free energy is a function of the invariants in terms of the deformation gradient, the electro-passive directional vectors and the electric field,

$$\begin{aligned} &\overline{W} = \overline{W}(\bar{I}_1, \bar{I}_4, \bar{I}_6, \bar{I}_{11}), \\ &\overline{W} = \overline{W}_{elastic} + \overline{W}_{electric} + U(J), \\ &\overline{W}_{elastic} = \overline{W}_{iso} + \overline{W}_{aniso}. \end{aligned} \tag{7.58}$$

$\overline{W}_{electric}$ is given in Equation (7.52) and *Neo*-Hookean ($\overline{W}_{NH}$) and GOH models ($\overline{W}_{GOH}$: Gasser-Ogden-Holzapfel model [29]) are adopted for the isotropic ($\overline{W}_{iso}$) and anisotropic ($\overline{W}_{aniso}$) strain energy functions, respectively:

$$\begin{aligned} &\overline{W}(\bar{I}_1) = \overline{W}_{iso} = \overline{W}_{NH} = C_1(\bar{I}_1 - 3), \\ &\overline{W}(\bar{I}_1, \bar{I}_4, \bar{I}_6) = \overline{W}_{aniso} = \overline{W}_{GOH} = \frac{1}{2}\left\{ \begin{aligned} &\frac{k_{11}}{k_{21}}[\exp[k_{21}\{\bar{I}_1 + (1-3\kappa_1)\bar{I}_4 - 1\}^2] - 1] \\ &+ \frac{k_{12}}{k_{22}}[\exp[k_{22}\{\bar{I}_1 + (1-3\kappa_2)\bar{I}_6 - 1\}^2] - 1] \end{aligned} \right\}, \end{aligned} \tag{7.59}$$

where k_{1i} is a material parameter, k_{2i} is a dimensionless material parameter which will affect the shape of the stress-strain curve, and κ_i represents the distribution of two families of fibers about a

dominant fiber angle (i = 1 and 2). The distribution accounts for variations from the otherwise dominant fiber angles α and β. (The distribution of the fiber angle was described in Son and Goulbourne [28].)

By inserting the free energy function into Equation (7.18), the total stress becomes

$$\begin{aligned}\boldsymbol{\sigma} &= \frac{2}{J}[\{\overline{W}_1\overline{\boldsymbol{B}} + \overline{W}_2(\overline{I}_1\overline{\boldsymbol{B}} - \overline{\boldsymbol{B}}^2) + \overline{W}_4(\overline{\boldsymbol{F}}\boldsymbol{a}\otimes\overline{\boldsymbol{F}}\boldsymbol{a}) + \overline{W}_6(\overline{\boldsymbol{F}}\boldsymbol{b}\otimes\overline{\boldsymbol{F}}\boldsymbol{b}) - \overline{W}_{11}(\boldsymbol{e}\otimes\boldsymbol{e})\} \\ &- \frac{1}{3}(\overline{W}_1\overline{I}_1 + 2\overline{W}_2\overline{I}_2 + \overline{W}_4\overline{I}_4 + \overline{W}_6\overline{I}_6 - \overline{W}_{11}\overline{I}_{11})] + KJ(J-1)\boldsymbol{1}.\end{aligned} \tag{7.60}$$

With index notation, Equation (7.60) is written as

$$\begin{aligned}\sigma_{ij} &= \frac{2}{J}[\{\overline{W}_1\overline{B}_{ij} + \overline{W}_4(\overline{F}_{im}a_m\overline{F}_{jn}a_n) + \overline{W}_6(\overline{F}_{im}b_m\overline{F}_{jn}b_n) - \overline{W}_{11}e_ie_j\} \\ &- \frac{1}{3}(\overline{W}_1\overline{I}_1 + 2\overline{W}_2\overline{I}_2 + + \overline{W}_4\overline{I}_4 + \overline{W}_6\overline{I}_6 - \overline{W}_{11}\overline{I}_{11})\delta_{ij}] + KJ(J-1)\delta_{ij},\ (i,j,m,n = 1,2,3).\end{aligned} \tag{7.61}$$

The tangent modulus for the strain energy function is given as

$$\begin{aligned}\boldsymbol{c} &= -\frac{4}{3J}[\{\overline{W}_1\overline{\boldsymbol{B}} + \overline{W}_4\overline{\boldsymbol{F}}\boldsymbol{a}\otimes\overline{\boldsymbol{F}}\boldsymbol{a} + \overline{W}_6\overline{\boldsymbol{F}}\boldsymbol{b}\otimes\overline{\boldsymbol{F}}\boldsymbol{b} - \overline{W}_{11}(\boldsymbol{e}\otimes\boldsymbol{e})\}\otimes\boldsymbol{1} + \boldsymbol{1}\otimes\{\overline{W}_1\overline{\boldsymbol{B}} \\ &+ \overline{W}_4\overline{\boldsymbol{F}}\boldsymbol{a}\otimes\overline{\boldsymbol{F}}\boldsymbol{a} + \overline{W}_6\overline{\boldsymbol{F}}\boldsymbol{b}\otimes\overline{\boldsymbol{F}}\boldsymbol{b} + \overline{W}_2(\overline{I}_1\overline{\boldsymbol{B}} - \overline{\boldsymbol{B}}^2) - \overline{W}_{11}(\boldsymbol{e}\otimes\boldsymbol{e})\}] - \frac{4}{3J}\{\overline{W}_1\overline{I}_1 + \overline{W}_4\overline{I}_4 \\ &+ \overline{W}_6\overline{I}_6 - \overline{W}_{11}\overline{I}_{11}\}\left\{I - \frac{1}{3}(1\otimes 1)\right\} + \frac{4}{J}\{\overline{W}_1\overline{\boldsymbol{B}}\otimes\overline{\boldsymbol{B}} + \overline{W}_{14}(\overline{\boldsymbol{B}}\otimes\overline{\boldsymbol{F}}\boldsymbol{a}\otimes\overline{\boldsymbol{F}}\boldsymbol{a} \\ &+ \overline{\boldsymbol{F}}\boldsymbol{a}\otimes\overline{\boldsymbol{F}}\boldsymbol{a}\otimes\overline{\boldsymbol{B}}) + \overline{W}_{16}(\overline{\boldsymbol{B}}\otimes\overline{\boldsymbol{F}}\boldsymbol{b}\otimes\overline{\boldsymbol{F}}\boldsymbol{b} + \overline{\boldsymbol{F}}\boldsymbol{b}\otimes\overline{\boldsymbol{F}}\boldsymbol{b}\otimes\overline{\boldsymbol{B}}) + \overline{W}_{44}(\overline{\boldsymbol{F}}\boldsymbol{a}\otimes\overline{\boldsymbol{F}}\boldsymbol{a}\otimes\overline{\boldsymbol{F}}\boldsymbol{a}\otimes\overline{\boldsymbol{F}}\boldsymbol{a}) \\ &+ \overline{W}_{66}(\overline{\boldsymbol{F}}\boldsymbol{b}\otimes\overline{\boldsymbol{F}}\boldsymbol{b}\otimes\overline{\boldsymbol{F}}\boldsymbol{b}\otimes\overline{\boldsymbol{F}}\boldsymbol{b}) + 2\overline{W}_{11}(\boldsymbol{e}\otimes\boldsymbol{e})\} - \frac{4}{3J}[\{\overline{W}_{11}\overline{I}_1\overline{\boldsymbol{B}} + \overline{W}_{14}\overline{I}_4\overline{\boldsymbol{B}} + \overline{W}_{16}\overline{I}_6\overline{\boldsymbol{B}} \\ &+ (\overline{W}_{14}\overline{I}_4 + \overline{W}_{44}\overline{I}_4)\overline{\boldsymbol{F}}\boldsymbol{a}\otimes\overline{\boldsymbol{F}}\boldsymbol{a} + (\overline{W}_{16}\overline{I}_6 + \overline{W}_{66}\overline{I}_6)\overline{\boldsymbol{F}}\boldsymbol{b}\otimes\overline{\boldsymbol{F}}\boldsymbol{b} + 2\overline{W}_{11}\overline{I}_{11}\overline{\boldsymbol{B}}^{-1}\}\otimes\boldsymbol{1} \\ &+ \boldsymbol{1}\otimes\{\overline{W}_{11}\overline{I}_1\overline{\boldsymbol{B}} + \overline{W}_{14}\overline{I}_4\overline{\boldsymbol{B}} + \overline{W}_{16}\overline{I}_6\overline{\boldsymbol{B}} + (\overline{W}_{14}\overline{I}_4 + \overline{W}_{44}\overline{I}_4)\overline{\boldsymbol{F}}\boldsymbol{a}\otimes\overline{\boldsymbol{F}}\boldsymbol{a} + (\overline{W}_{16}\overline{I}_6 \\ &+ \overline{W}_{66}\overline{I}_6)\overline{\boldsymbol{F}}\boldsymbol{b}\otimes\overline{\boldsymbol{F}}\boldsymbol{b} + 2\overline{W}_{11}\overline{I}_{11}\overline{\boldsymbol{B}}^{-1}\}] + \frac{4}{9J}\{\overline{W}_{11}\overline{I}_1^2 + 2\overline{W}_{14}\overline{I}_1\overline{I}_4 + \overline{W}_{44}\overline{I}_4^2 \\ &+ 2\overline{W}_{11}\overline{I}_{11}\}\boldsymbol{1}\otimes\boldsymbol{1} + pJ(\boldsymbol{1}\otimes\boldsymbol{1} - 2\boldsymbol{I}).\end{aligned} \tag{7.62}$$

With index notation, Equation (7.62) is rewritten as

$$
\begin{aligned}
c_{ijkl} &= -\frac{4}{3J}[\{\overline{W}_1\overline{B}_{ij} + \overline{W}_4\overline{F}_{im}a_m\overline{F}_{jn}a_n + \overline{W}_6\overline{F}_{im}b_m\overline{F}_{jn}b_n - \overline{W}_{11}(e_ie_j)\}\delta_{kl} \\
&+ \delta_{ij}\{\overline{W}_1\overline{B}_{kl} + \overline{W}_4\overline{F}_{kn}a_n\overline{F}_{lm}a_m + \overline{W}_6\overline{F}_{kn}b_n\overline{F}_{lm}b_m - \overline{W}_{11}(e_ke_l)\}] - \frac{4}{3J}\{\overline{W}_1\overline{I}_1 \\
&+ \overline{W}_4\overline{I}_4 + \overline{W}_6\overline{I}_6 - \overline{W}_{11}\overline{I}_{11}\}\left\{I_{ijkl} - \frac{1}{3}(\delta_{ij}\delta_{kl})\right\} + \frac{4}{J}\{\overline{W}_1\overline{B}_{ij}\overline{B}_{kl} + \overline{W}_{14}(\overline{B}_{ij}\overline{F}_{kn}a_n\overline{F}_{lm}a_m \\
&+ \overline{F}_{in}a_n\overline{F}_{jm}a_m\overline{B}_{kl}) + \overline{W}_{16}(\overline{B}_{ij}\overline{F}_{kn}b_n\overline{F}_{lm}b_m + \overline{F}_{in}b_n\overline{F}_{jm}b_m\overline{B}_{kl}) \\
&+ \overline{W}_{44}(\overline{F}_{in}a_n\overline{F}_{jm}a_m\overline{F}_{kp}a_p\overline{F}_{lq}a_q) + \overline{W}_{66}(\overline{F}_{in}b_n\overline{F}_{jm}b_m\overline{F}_{kp}b_p\overline{F}_{lq}b_q) + 2\overline{W}_{11}(e_ie_j\delta_{kl})\} \\
&- \frac{4}{3J}[\{(\overline{W}_{11}\overline{I}_1 + \overline{W}_{14}\overline{I}_4 + \overline{W}_{16}\overline{I}_6)\overline{B}_{ij} + (\overline{W}_{14}\overline{I}_4 + \overline{W}_{44}\overline{I}_4)\overline{F}_{in}a_n\overline{F}_{jm}a_m + (\overline{W}_{16}\overline{I}_6 \\
&+ \overline{W}_{66}\overline{I}_6)\overline{F}_{in}b_n\overline{F}_{jm}b_m + 2\overline{W}_{11}\overline{I}_{11}\overline{B}_{ij}^{-1}\}\delta_{kl} + \delta_{ij}\{(\overline{W}_{11}\overline{I}_1 + \overline{W}_{14}\overline{I}_4 + \overline{W}_{16}\overline{I}_6)\overline{B}_{kl} \\
&+ (\overline{W}_{14}\overline{I}_4 + \overline{W}_{44}\overline{I}_4)\overline{F}_{kp}a_p\overline{F}_{lq}a_q + (\overline{W}_{16}\overline{I}_6 + \overline{W}_{66}\overline{I}_6)\overline{F}_{kp}b_p\overline{F}_{lq}b_q + 2\overline{W}_{11}\overline{I}_{11}\overline{B}_{kl}^{-1}\}] \\
&+ \frac{4}{9J}\{\overline{W}_{11}\overline{I}_1^2 + 2\overline{W}_{14}\overline{I}_1\overline{I}_4 + \overline{W}_{44}\overline{I}_4^2 + 2\overline{W}_{11}\overline{I}_{11}\}\delta_{ij}\delta_{kl} + pJ(\delta_{ij}\delta_{kl} - 2I_{ijkl}), \\
&(i, j, k, l, m, n, p, q = 1,2,3).
\end{aligned}
\tag{7.63}
$$

Now, Equation (7.61) and (7.63) are employed in the newly developed UMAT (ABAQUS). Details of the UMAT are given in Appendix D.

The numerical stability of the anisotropic DE with respect to the independent variables (F_{11} and E_3) is investigated using the polyconvexity condition in Equation (3.23) and the results in the Chapter 3. The numerical stability under equibiaxial extension is expressed as the applicable electric field range from Chapter 3,

$$
\begin{aligned}
&\left|E_3\right| \le \sqrt{\frac{(10\overline{W}_4 + 10\overline{W}_6)}{100\overline{F}_{11}^8 R_{11}}}, \\
&\overline{W}_4 = 1 + 2\kappa_1 R_4\{\overline{I}_1 + (1-3\kappa_1)\overline{I}_4 - 1\}\left(\exp[k_{21}\{\overline{I}_1 + (1-3\kappa_1)\overline{I}_4 - 1\}^2] - 1\right), \\
&\overline{W}_6 = 1 + 2\kappa_2 R_6\{\overline{I}_1 + (1-3\kappa_1)\overline{I}_6 - 1\}\left(\exp[k_{22}\{\overline{I}_1 + (1-3\kappa_2)\overline{I}_6 - 1\}^2] - 1\right), \\
&R_4 = \frac{k_{11}}{C_1} = R_6 = \frac{k_{12}}{C_1},\ R_{11} = \frac{\overline{W}_{11}}{\overline{W}_1} = \frac{\varepsilon_0\varepsilon_r}{C_1},
\end{aligned}
\tag{7.64}
$$

where the nominal electric field E_3 is written in terms of voltage input in the X_3 direction (Z in ABAQUS)

$$
V_3 = h_0 E_3. \tag{7.65}
$$

Figure 7.7 shows the numerical stability region of the anisotropic DE under equibiaxial extension. Each curve represents the upper boundary of the stable region during the deformation with different stiffness of fibers. Differently from the stability of the isotropic DE, the stability region becomes larger after stretch ratio 1.6–1.8. This is due to that the fiber stress increases exponentially from the anisotropic strain energy function W_{GOH} in Equation (7.59). Even though the fiber stiffness is smaller than the stiffness of the isotropic matrix ($R_4 < 1.0$), the stability region becomes larger after stretch ratio 1.8 because of the exponential form of the fiber strain energy function in Equation (7.59). This result implies that the numerical stability of the anisotropic DE can be controllable by tuning the properties of the fibers.

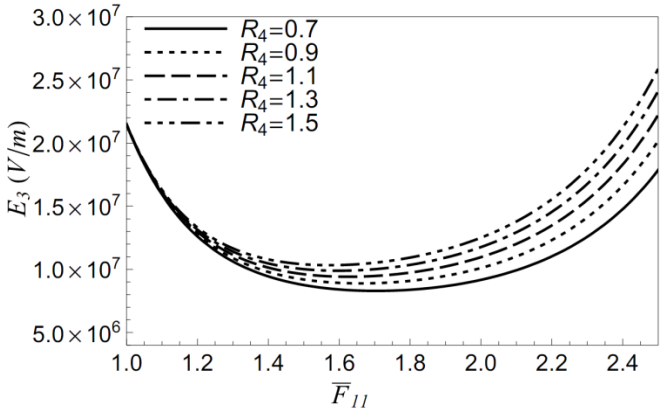

Figure 7.7. Electromechanical stability of anisotropic material with two families of electro-passive fibers, C_1 = 100 *kPa*, $k_{11} = k_{12}$ = 150 *kPa*, $k_{21} = k_{22}$ = 0.2, $\kappa_1 = \kappa_2$=0.1, α = 10°, ε_r = 4.7, $R_{11} = 2.6\times10^{-15}$ and R_4=0.7–1.5.

The finite element model for Figure 7.6 consists of 3 dimensional element in Figure 7.8 (C3D8). The material consists of isotropic matrix and two families of the electro-passive fibers in Figure 7.8. The local orientations of two families of fibers are prescribed in the UMAT and ABAQUS input file. Specifically, when the free energy function is invariant-based, the local directions of each family of fibers must be defined by a user. Note that if no local directions are specified in

the ABAQUS input file, ABAQUS assumes that the families of fibers are aligned initially with the axes of the local system. In order to define *N* local directions of the fibers, "ORIENTATION, LOCAL DIRECTIONS=*N*" is included in the ABAQUS input file. The detailed input file for the anisotropic electro-elastic membrane is presented in Appendix E. The kinematic boundary consists of two rigid frames. The elements on the top edge of the material are assigned rigid and act like a rigid frame on the material. The other boundary conditions are prescribed in the finite element model as pinned at left boundary and specified displacement (10 *mm*) on right boundary. The static and dynamic pressure is applied on the surface of the material. As expected, stress concentrations occur at the boundaries and the joint in Figure 7.8.

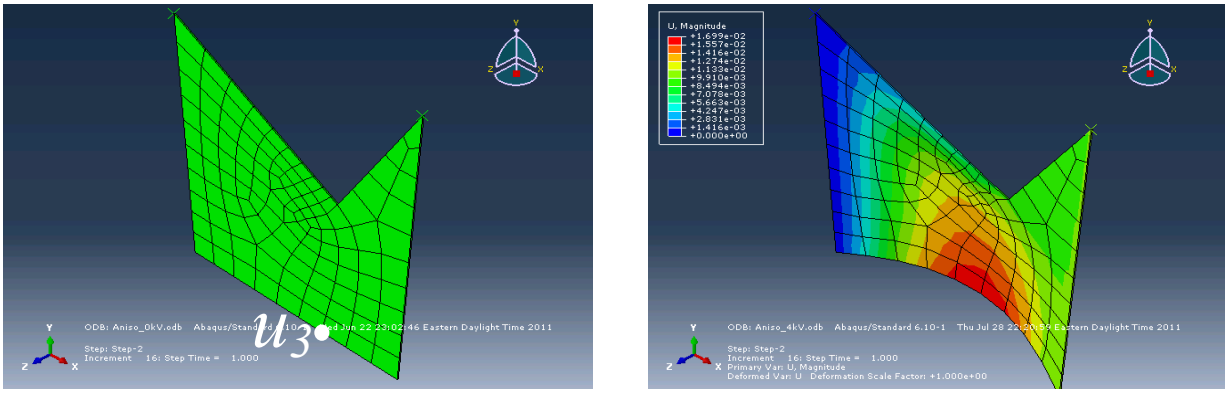

Figure 7.8. The ABAQUS/CAE simulation results of M-framed anisotropic material in the undeformed (Left) and deformed (Right) shape by stretch at the right boundary and static pressure on the X-Y plane.

Figures 7.9–7.11 shows the electromechanical response of the anisotropic DE with respect to the uniaxial stretch in the X_1 direction, the static pressure (P = 0–50 *kPa*) on the X_1-X_2 plane and voltage input in the X_3 direction (In ABAQUS, X_1, X_2 and X_3 in Figure 7.6 are X, Y and Z, respectively). The material properties for Figures 7.8–7.11 are given in Table 7.2, which are prescribed arbitrarily.

Table 7.2. Material properties of the anisotropic dielectric elastomer in Figures 7.8–7.11.

C_1	$k_{11} = k_{12}$	$k_{21} = k_{22}$	$\kappa_1 = \kappa_2$	α ($\beta = -\alpha$)	ε_r
100 *kPa*	150 *kPa*	0.2	0.1	10°	4.7

Figure 7.9 shows the deformation of the anisotropic dielectric elastomer with respect to the static pressure with 4 *kV*. The color variation describes the primary displacement with respect to the external force (the displacement and the static pressure). The red and blue regions represent the maximum and minimum displacements, respectively. Figure 7.10 describes the transverse displacement (u_3 in Figure 7.8) in the Z direction with respect to the static pressure (P = 0–50 *kPa*). As expected, a higher voltage input leads to the larger transverse displacement with respect to the static pressure P. Figure 7.11 shows the fiber angles α (at u_3 in Figure 7.8) at the deformation state with respect to the displacement (10 *mm* in the X direction) and the static pressure (P = 0–50 *kPa*) under 4 *kV*.

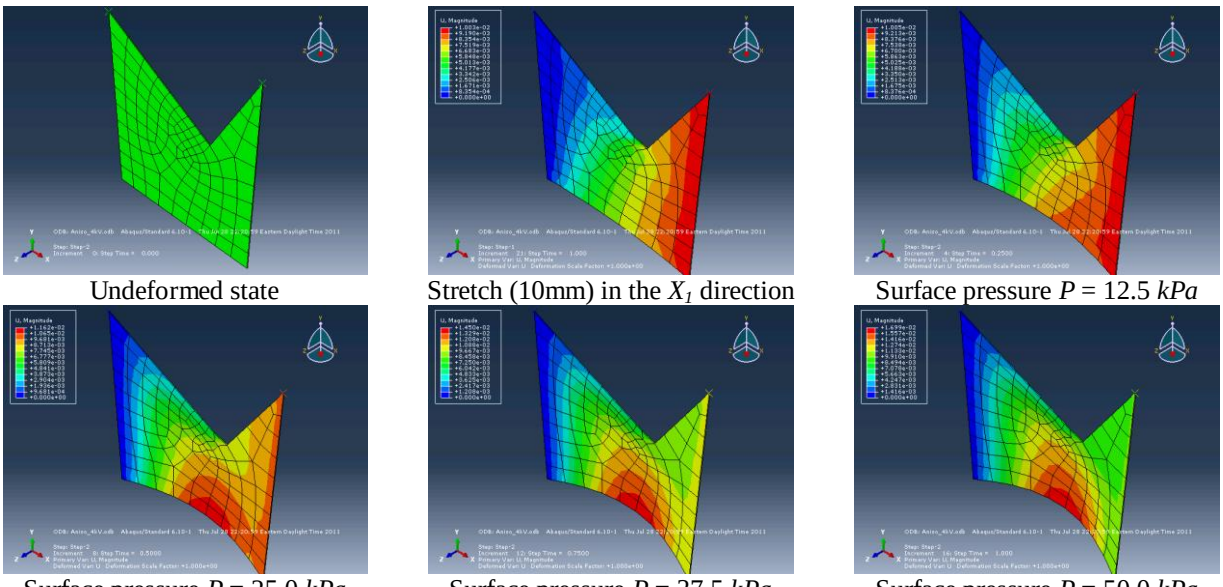

Undeformed state | Stretch (10mm) in the X_1 direction | Surface pressure P = 12.5 *kPa*

Surface pressure P = 25.0 *kPa* | Surface pressure P = 37.5 *kPa* | Surface pressure P = 50.0 *kPa*

Figure 7.9. Static deformation of the anisotropic dielectric elastomer with respect to the static pressure (50 *kPa*) and voltage input (4 *kV*) in ABAQUS/CAE

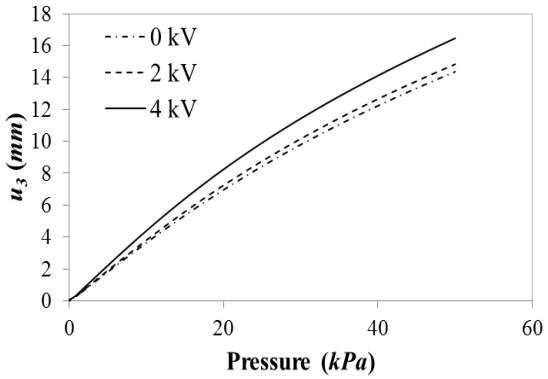

Figure 7.10. The transverse displacement u_3 of the anisotropic dielectric elastomer in the Z direction with respect to static pressure and voltage input.

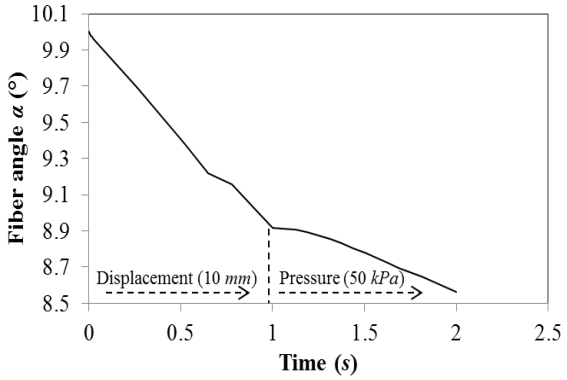

Figure 7.11. The fiber angle α in the deformed state of the anisotropic dielectric elastomers with respect to the displacement and static pressure at 4 *kV*.

For the dynamic response of the M-shaped anisotropic DE, the dynamic pressure is given as a function of time

$$P\ (kPa) = \left|50\sin(2\pi\ f\ t)\right|, \tag{7.66}$$

where f is the frequency (Hz) of the pressure and t is the time domain, $0 \le t \le 1/2f$ (sec) for Figures 7.12–7.14 and $0 \le t \le 2/f$ (s) for Figure 7.15. The material properties are given in Table 7.3, which are prescribed arbitrarily.

Table 7.3. Material properties of the anisotropic dielectric elastomer in Figures 7.12–7.15.

ρ (density)	C_1	$k_{11} = k_{12}$	$k_{21} = k_{22}$	$\kappa_1 = \kappa_2$	α, ($\beta = -\alpha$)	ε_r
1000 kg/m^3	100 *kPa*	150 *kPa*	0.2	0.1	10°	4.7

Figure 7.12 shows the dynamic deformation of the anisotropic dielectric elastomer with respect to the dynamic pressure in Equation (7.66) with 0.5 *Hz*. After one cycle of a sinusoidal pressure (P_{max} = 50 *kPa*), the pressure is kept as zero until 2 *s*.

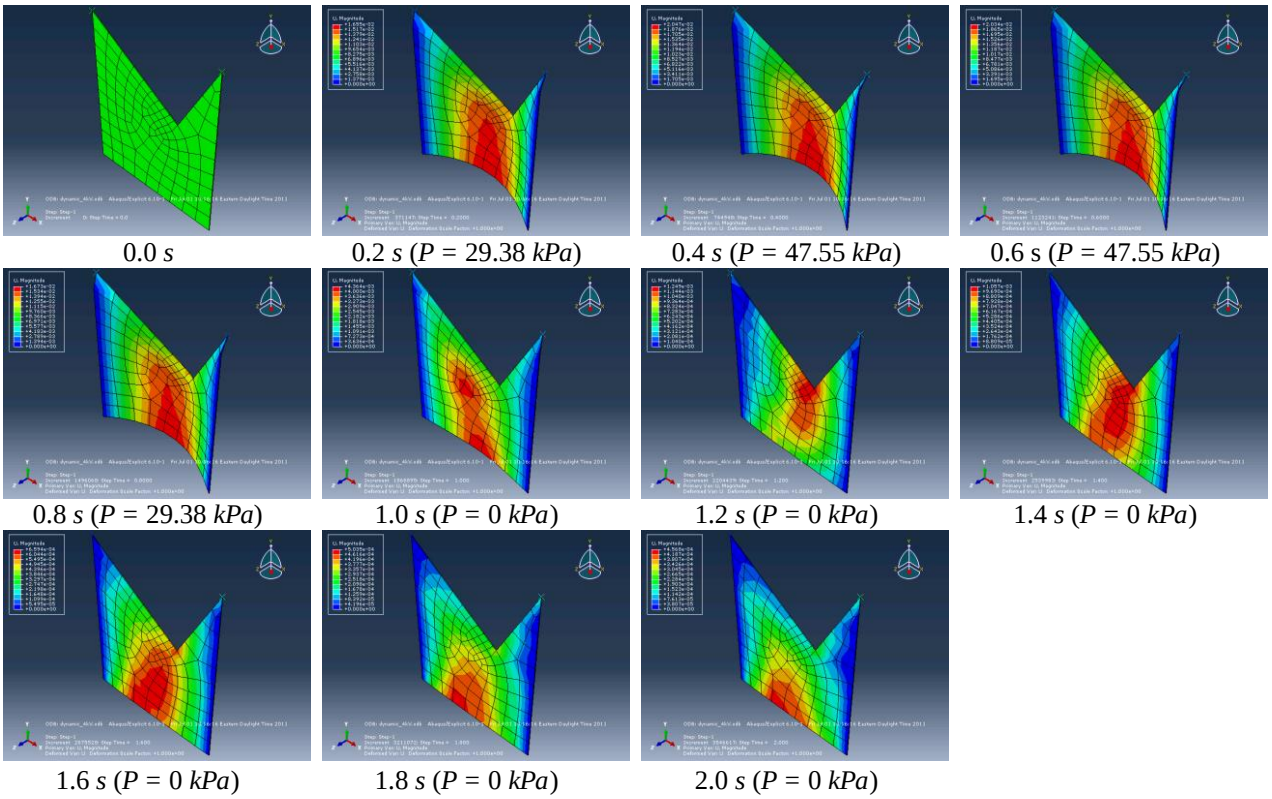

7.12. Dynamic deformation of the anisotropic dielectric elastomer with respect to the dynamic pressure in Equation (7.66) with 0.5 *Hz and* 4 *kV* in ABAQUS/CAE.

Similarly to the static response in Figure 7.10, larger transverse displacement u_3 proportional to the voltage input (0–4.0 *kV*) is obtained under the dynamic pressure in Equation (7.66) with f = 0.5 *Hz* in Figure 7.13. Figure 7.14 shows the transverse displacement with respect to different frequencies (f = 0.5–4.0 *Hz*) at 4 *kV*. The maximum displacement ($u_3 \approx 18$ *mm*) is almost constant with respect to the frequencies (0.5–4.0 *Hz*). Figure 7.15 shows the displacement u_3 and the dynamic pressure P (f = 0.5 *Hz*) with respect to time at voltage input 4 *kV*. The displacement shows linear response with respect to the sinusoidal pressure input and there is no delay between the pressure input and the displacement. This is due to that the material damping is not included in the UMAT of ABAQUS. In order to describe the material damping, the constitutive law for the electro-viscoelastic material needs to be formulated in the UMAT.

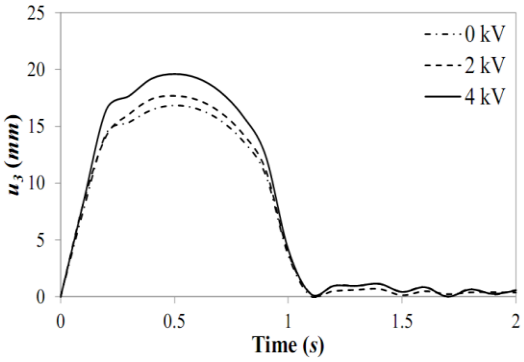

Figure 7.13. The transverse displacement u_3 of the anisotropic electro-elastic material in the *Z* direction with respect to applied dynamic pressure and voltage input at 0.5 *Hz*.

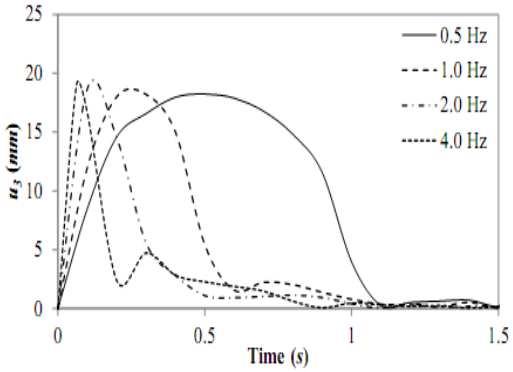

Figure 7.14. The transverse displacement u_3 of the anisotropic electro-elastic membrane in the *Z* direction with respect to frequencies (0.5–4 *Hz*) at 4 *kV*.

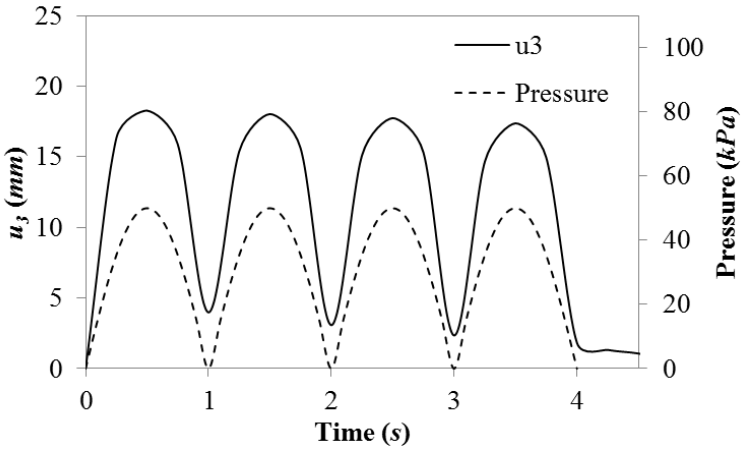

Figure 7.15. The transverse displacement u_3 of the anisotropic DE and dynamic pressure (f = 0.5 *Hz*) with respect to time at 4 *kV* ($0 \leq t \leq 4.0$ *s* for the dynamic pressure).

7.7. Summary

In order to prevent volumetric locking during the ABAQUS simulation, a multiplicative decomposition of the constitutive formulation for isotropic and anisotropic electro-elastic materials is employed using Flory's approach [1]. From the multiplicative decomposition, a closed form solution for the tangent modulus of isotropic and anisotropic electro-elastic materials is introduced for the first time. Through the decoupling of the constitutive equation, several UMATs for electro-elastic materials are developed. The FEM model facilitates simulating

complex electromechanical coupling problems. To validate the UMAT, equi-biaxial extension of isotropic electro-elastic material was presented. The computational result matches well with the analytical solution. A more complex problem considering an anisotropic dielectric elastomer subject to static and dynamic mechanical loads and asymmetric boundary conditions was solved to highlight the advantage of having a FEM solver. The UMATs for anisotropic electro-elastic materials can be used to solve a range of problems with arbitrary boundary conditions and applied loadings.

7.8. Reference

1. Flory, P., J, *Thermodynamic relations for highly elastic materials.* Transactions of the Faraday Society, 1961: p. 829-838.
2. Ogden, R.W., *Nearly isochoric elastic deformations: Application to rubberlike solids.* Journal of the Mechanics and Physics of Solids, 1978: p. 37-57.
3. Ogden, R.W., *Volume changes associated with the deformation of rubber-like solids.* Journal of the Mechanics and Physics of Solids, 1976: p. 323-38.
4. Simo, J.C. and R.L. Taylor, *Quasi-incompressible finite elasticity in principal stretches. Continuum basis and numerical algorithms.* Computer Methods in Applied Mechanics and Engineering, 1991: p. 273-310.
5. Weiss, J.A., B.N. Maker, and S. Govindjee, *Finite element implementation of incompressible, transversely isotropic hyperelasticity.* Computer Methods in Applied Mechanics and Engineering, 1996: p. 107-28.
6. Xuanhe, Z. and S. Zhigang, *Method to analyze programmable deformation of dielectric elastomer layers.* Applied Physics Letters, 2008: p. 251902 (3 pp.).
7. Wissler, M. and E. Mazza, *Modeling and simulation of dielectric elastomer actuators.* Smart Materials and Structures, 2005: p. 1396-1402.
8. Wissler, M. and E. Mazza, *Modeling of a pre-strained circular actuator made of dielectric elastomers.* Sensors and Actuators A (Physical), 2005: p. 184-92.
9. O'Brien, B., et al., *Finite element modelling of dielectric elastomer minimum energy structures.* Applied Physics A: Materials Science & Processing, 2009: p. 507-14.
10. Wei, S., E.L. Chaikof, and M.E. Levenston, *Numerical approximation of tangent moduli for finite element implementations of nonlinear hyperelastic material models.* Journal of Biomechanical Engineering, 2008: p. 061003 (7 pp.).
11. Yeoh, O.H., *Some forms of the strain energy function for rubber.* Rubber Chemistry and Technology, 1993: p. 754-771.
12. Ogden, R.W., *Large Deformation Isotropic Elasticity - On the Correlation of Theory and Experiment for Incompressible Rubberlike Solids.* Philosophical Transactions of the Royal Society of London. Series A, 1972: p. 398-416.

13. Mooney, M., *Theory of large elastic deformation.* Journal of Applied Physics, 1940: p. 582-592.
14. Goulbourne, N., E. Mockensturm, and M. Frecker, *A nonlinear model for dielectric elastomer membranes.* Journal of Applied Mechanics, Transactions ASME, 2005: p. 899-906.
15. Zhigang, S., Z. Xuanhe, and W.H. Greene, *A nonlinear field theory of deformable dielectrics.* Journal of the Mechanics and Physics of Solids, 2008: p. 467-86.
16. McMeeking, R.M. and C.M. Landis, *Electrostatic forces and stored energy for deformable dielectric materials.* Transactions of the ASME. Journal of Applied Mechanics, 2005: p. 581-90.
17. Xuanhe, Z., H. Wei, and S. Zhigang, *Electromechanical hysteresis and coexistent states in dielectric elastomers.* Physical Review B (Condensed Matter and Materials Physics), 2007: p. 134113-1.
18. Sussman, T. and K.J. Bathe. *A finite element formulation for nonlinear incompressible elastic and inelastic analysis*. in *6th ADINA Conference on Nonlinear Finite Element Analysis and ADINA, 10-12 June 1987*. 1987. UK.
19. Simo, J.C., *A framework for finite strain elastoplasticity based on maximum plastic dissipation and the multiplicative decomposition. I. Continuum formulation.* Computer Methods in Applied Mechanics and Engineering, 1988: p. 199-219.
20. Doll, S. and K. Schweizerhof, *On the development of volumetric strain energy functions.* Transactions of the ASME. Journal of Applied Mechanics, 2000: p. 17-21.
21. Hartmann, S. and P. Neff, *Polyconvexity of generalized polynomial-type hyperelastic strain energy functions for near-incompressibility*. International Journal of Solids and Structures, 2003: p. 2767-2791.
22. Belytschko, T., W.K. Liu, and B. Moran, *Nonlinear finite elements for continua and structures*. 2000, Chichester: Wiley.
23. Abramowitz, M. and I.A. Stegun, *Handbook of Mathematical Functions with Formulas, Graphs, and Mathematical Tables*. 1972, New York: Dover.
24. Seyul, S. and N.C. Goulbourne, *Finite Deformations of Tubular Dielectric Elastomer Sensors.* Journal of Intelligent Material Systems and Structures, 2009: p. 2187-99.
25. Son, S. and N.C. Goulbourne, *Dynamic response of tubular dielectric elastomer transducers.* International Journal of Solids and Structures, 2010: p. 2672-2679.
26. Son, S. and N.C. Goulbourne. *Large deformations of reconfigurable active membranes: A finite element model*. in *Electroactive Polymer Actuators and Devices (EAPAD) 2010, March 8, 2010 - March 11, 2010*. 2010. San Diego, CA, United states: SPIE.
27. Son, S. and N.C. Goulbourne, *Finite Deformations of Tubular Dielectric Elastomer Sensors.* Journal of Intelligent Material Systems and Structures, 2009: p. 2187-2199.
28. Son, S. and N.C. Goulbourne, *Anisotropic Bistable Electroactive Polymers: Large Strain Actuation of Shape Memory Polymers.* ASME Conference Proceedings, 2010: p. 343-350.
29. Gasser, T.C., R.W. Ogden, and G.A. Holzapfel, *Hyperelastic modelling of arterial layers with distributed collagen fibre orientations.* Journal of the Royal Society Interface, 2006: p. 15-35.

Chapter 8. Conclusions and Summary

In this section, the main contributions of this research are presented.

The objectives of this research are four fold: (1) The derivation of a general constitutive law for electro-elastic materials within a continuum mechanics framework, (2) Examining polyconvexity conditions of a general invariant-based electro-elastic free energy function for anisotropic electro-elastic materials, (3) The investigation of the sensing and actuation response of tubular dielectric elastomer (DE) transducers along with their applications, and (4) Implementation of the constitutive model for electro-elastic materials into a user subroutine (UMAT) in ABAQUS.

8.1. General Constitutive Formulation for Anisotropic Electro-Elastic Materials

A class of anisotropic electro-elastic materials is considered that consists of an isotropic matrix embedded with two families of electro-active or passive fibers (or particles). Invariant-based free energy formulations are derived to investigate the coupling between the fibers and the applied electric field. The fibers and particles are represented by a unit directional vector in the free energy function.

Coupling between the electro-active directional vectors and the electric field is scrutinized with respect to the orientations of the vectors and the polarity and magnitude of the applied electric field. Two simple boundary value problems (equibiaxial extension and simple shear) are used to determine the conditions that yield local maxima and minima. The results indicate that the magnitude and orientation of the coupling is significantly dependent on the orientations of the directional vectors and the polarity and magnitude of the electric field.

Through the invariant approach, the electromechanical couplings of the anisotropic electro-elastic continuum are included directly in the constitutive formulation as invariants, which are combinations of deformation gradient tensor, nominal electric field and directional vectors. Several combinations between the symmetric tensor and vectors produce the invariants to illustrate the electromechanical couplings. The advantage of this approach is that the electromechanical couplings can be introduced conveniently into the constitutive formulations by using the invariants. However, main issue of this approach is the selection of realistic forms of energy function to model the response of large deformation of the electro-elastic materials. For the proper models, several perspectives are needed. These include the evaluation of stability inequalities (polyconvexity condition in Chapter 3) and mathematical aspects concerned with material properties from comprehensive sets of experimental data which assess the dependence of the mechanical and the electromechanical response on the deformation, electric field and directions for specific fiber families.

8.2. Electromechanical Stability of Isotropic and Anisotropic Electro-Elastic Materials

The electromechanical stability of an electro-elastic material under specific boundary conditions was examined using the convexity and polyconvexity conditions. Specifically, the convexity of the invariants for the electro-active directional vectors and the applied nominal electric field and polyconvexity of the invariant-based electro-elastic free energy function with respect to the independent variables (the deformation gradient and the applied nominal electric field) under equibiaxial extension was investigated. Strict polyconvexity condition requires that the subgroups of a free energy function W are convex with respect to the independent variables then

W is polyconvex. General polyconvexity condition requires that the W is polyconvex if W is convex with respect to the independent variables. For convexity of the invariants, the results show that the invariants (I_{11}, I_{12}, I_{14}, I_{16}, I_{17}, I_{18} and I_{19}) under equibiaxial extension are not convex with respect to the independent variables F_{11} and E_3. This result implies that an invariant-based free energy function for an electro-elastic material which is a linear combination of the invariants ($W = W_1(I_1)+W_2(I_2)+,\ldots,+W_{19}(I_{19})$) will not satisfy the strict polyconvexity condition. An explicit condition required for polyconvexity of the electro-elastic free energy function was obtained by using the general polyconvexity condition and solving for the nominal electric field. By the polyconvexity condition, it is shown that the free energy for the electro-elastic material is non-polyconvex because of the non-convex invariants, leading to the wrinkling and the electric breakdown. The explicit polyconvexity condition for the electro-elastic material informs us the electromechanical stable region to prevent the instabilities during the deformation. The polyconvexity condition is helpful to build a stable electro-elastic free energy function. Specifically within the explicit polyconvexity condition, the constitutive formulation for the electro-elastic material can be derived using the continuum mechanics framework and invariants. Additionally, the condition is useful to keep the numerical stability of the electro-elastic material in finite element model tool (ABAQUS) which was shown as the applicable electric field in Chapter 7 (see Figures 7.4 and 7.7).

Specifically for an isotropic electro-elastic material, the polyconvexity condition implies that the range of the applicable electric field for maintaining polyconvexity is significantly dependent on the ratio between the mechanical and electric material parameters ($R_{11} = W_{11}/W_1$). For an anisotropic electro-elastic material, the polyconvexity condition can be controlled by adjusting the orientation of the electro-active and/or passive directional vectors. That is to say, the

electromechanical stability for electro-elastic materials is governed by the orientation of the fibers and/or particles.

8.3. Electromechanical Response of the Tubular DE Transducers

In Chapters 4, 5 and 6, theoretical modeling and experimentation on the electromechanical actuation and sensing response of tubular DE transducers and DE were described. Two DE integrated systems were considered involving a fiber-reinforced pneumatic actuator and an arterial wall segment. In both systems, the DE was used as a sensor. The fiber-reinforced pneumatic actuator and arterial wall were modeled as fiber-reinforced axisymmetric tubular membranes with two families of fibers. In both cases, it was assumed that the DE sensor undergoes the same motion as the host and that the DE sensor is structurally negligible. Under this assumption, the sensor output (capacitance) was then calculated by using electrostatics and a measure of the known mechanical strain of the host system. In detail of the DE integrated systems, since there is no electromechanical coupling, the invariants for the deformation gradient tensor in Chapter 2 were employed to illustrate the constitutive formulation of the isotropic membrane. Under the fiber inextensibility assumption, the fibers were considered as structural components and the fiber stress was added to the constitutive formulation instead of using the invariants for the families of fibers in Chapter 2. It was shown in Chapter 6 (see Figures 6.6 and 6.7) that the structural approach for the families of the fibers are equivalent to the continuum mechanics approach with the invariants in Chapter 2. However, the invariant formulation has the advantage to describe the electromechanical couplings between the electro-active fibers and the electric field without any difficulties.

The DE sensor integrated pneumatic actuator in Chapters 4, 5 and the arterial wall in-situ DE sensor in Chapter 6 both produce a nonlinear response with respect to the input pressure, which is due to the constraint of the fibers. That is to say, the nonlinear sensing response is not due to an inherent property of the DE, but a characteristic of the fiber-reinforced host system for the range of strains considered. This nonlinearity reduces the sensor's sensitivity. However, higher sensitivity can be achieved by fabricating thinner sensors and adding metallic filler, which has a higher permittivity value such as titanium dioxide powder (ε_r = 86 – 173). In terms of the actuation of the DE, enhancing the sensitivity with metallic filler additive is not recommended because the metallic filler leads to the electric breakdown and decreases the electromechanical actuation due to the higher stiffness. This is already described as the explicit polyconvexity condition of the isotropic DE in Chapter 3 (see Figure 3.4). According to Chapter 3, the higher permittivity causes the electromechanical instability of the isotropic DE.

Analysis of the static and dynamic sensing characteristics of the DE transducers shows that silicone based DE sensors has a good quasi-static and dynamic sensing response at higher frequencies up to 5.0 *Hz*, whereas polyacrylate (VHB 4905) shows a poor dynamic response after 2.0 *Hz* due to material viscoelasticity and apparent time required for charging/discharging the sensor. The DE sensor model correlates well with the experimental results, thus the model is a good tool for predicting large strain DE sensing behavior.

8.4. Implementation of Electro-Elastic Materials into ABAQUS

In Chapters 4, 5 and 6, the electromechanical response of isotropic electrostatic-elastic materials (dielectric elastomers: DEs) in an axisymmetric configuration was studied using a numerical method. Computational methods are required to solve more complex problems such as those

involving: complex 3D-geometric shapes, viscoelastic material behavior, anisotropic, complicated loading and/or boundary conditions (asymmetries for example). One solver, ABAQUS, offers powerful and complete solutions for both routine and sophisticated engineering problems covering a vast spectrum of applications in various fields. ABAQUS also provides the expandability and flexibility of the code with user subroutines, in which one can define almost arbitrary user materials. By using these capabilities, the electromechanical response of isotropic or anisotropic electro-elastic materials can be solved. Since electro-elastic materials are not built into the material library of ABAQUS/CAE, UMATs for electro-elastic materials were developed in this dissertation. Two different examples were presented to show the capability of the UMATs developed in this research. In order to validate the UMATs, results for equibiaxial extension of an isotropic electro-elastic material were presented. The numerical results from ABAQUS were shown to match well with the analytical solution. A more challenging problem involving an anisotropic electro-elastic material was presented to illustrate the advantage of using an FEM solver. Electromechanical response of the anisotropic electro-elastic material under asymmetric boundary conditions with uniform electric field and static/dynamic pressure is simulated using the developed UMAT in ABAQUS. Clearly, this example shows the applicability of the UMAT developed in this research to the various situations for the electro-elastic materials without establishing the constitutive formulation from scratch. Additionally, anyone who is not familiar with the electro-elastic material can simulate the electromechanical deformation of the electro-elastic material using the UMATs developed in this research with a simple instruction for the UMAT and ABAQUS/CAE. These are powerful advantages of the FEM solver over any other numerical methods.

8.5. Contributions

In this section, the main contributions of this research are presented.

1. Previously, the invariant-based constitutive formulations for the isotropic electro-elastic materials and the transversely isotropic electro-elastic materials have been developed by Dorfmann and Ogden [1, 2], Rajagopal and Wineman [3] and Bustamante [4]. In this dissertation, a full set of generalized constitutive relationships for the anisotropic electro-elastic materials with two families of the electro-active fibers (or particles) were derived for the first time. For the electromechanical constitutive formulation, invariants for the coupling between two electro-active directional vectors and the electric field were introduced. The advantage of the proposed constitutive formulation is that various electromechanical couplings can be illustrated easily by choosing invariants for the deformation gradient tensor, the electro-active directional vectors, and the electric field.

2. The polyconvexity of the invariant-based strain energy for the isotropic and the anisotropic materials was explored by [5], Steigmann [6], and Schrőder and Neff [7, 8]. The electromechanical stability of the isotropic dielectric elastomer was examined using convexity condition in the work of Zhao and Suo [9-11]. In this dissertation, convexity of the coupling invariants between the electro-active directional vectors and the applied electric field was examined. The electromechanical stability of the general electro-elastic material including isotropic and anisotropic dielectric elastomer is investigated using the polyconvexity condition for the first time. It was shown that the electromechanical stability can be controlled by tuning the material properties and the orientation of the directional vectors. The polyconvexity condition (which is expressed as the applicable electric field range) is useful to build a

polyconvex free energy function and prevent the instabilities (wrinkling and electric breakdown) and the numerical instability in FEM solver (ABAQUS) for the electro-elastic materials.

3. Theoretical modeling of the sensing response of DE transducers was developed using large deformation membrane theory and electrostatics. The numerical model's good correlation with experimental results confirms that it is a good tool for predicting the DE sensor response. The dynamic and static sensing ability of the DEs (silicone and polyacrylate (VHB 4905)) was examined experimentally by varying the magnitude and frequency of the applied internal pressure.

4. A previous implementation of an isotropic DE into a user subroutine was presented by Zhao and Suo [10], Wissler and Mazza [12, 13] and O'Brien [14]. Based on the invariant-based constitutive formulations for the electro-elastic material, UMAT for the electro-elastic materials including the isotropic and anisotropic DEs were developed in this dissertation for the first time. The applicability of the UMAT is shown by simulating a complicated electromechanical coupling problem in ABAQUS/CAE; the electromechanical response of the anisotropic electro-elastic material under asymmetric boundary conditions with uniform electric field and static/dynamic pressure.

8.6. Future Work

1. Implementation of the model for an anisotropic electro-elastic material with electro-active directional vectors into the UMAT should be developed.

- Similar to the example of an anisotropic electro-elastic material with two families of electro-passive fibers in Chapter 7, an anisotropic electro-elastic material with electro-active fibers and particles can be simulated by developing a UMAT. The coupling effects between the electro-

active fibers and particles and the applied electric field could be visualized in the finite element modeling tool (ABAQUS).

2. Implementation of a closed form of the tangent modulus for electro-elastic materials can be developed to achieve a faster convergence rate of the solution than that of the approximated tangent modulus.

- It was mentioned in Chapter 7 that the convergence rate of the solution in the finite element model is significantly dependent on the tangent modulus which serves as an iterative operator for the solution. More complicated initial and boundary condition causes a slower convergence rate of the solution in the finite element model. In order to improve the convergence rate, possible methods are to simplify the problem (initial and boundary conditions, mesh size and geometry) and to use the closed form of the tangent modulus. Since simplifying the problem is fundamentally limited with respect to achieving an accurate solution, utilization of the closed form of the tangent modulus is optimal way. The convergence rate of the solution with the approximate and closed form tangent moduli for an electro-elastic material could then be compared for relevant examples.

8.7. References

1. Dorfmann, A. and R.W. Ogden, *Nonlinear electroelasticity.* Acta Mechanica, 2005: p. 167-83.
2. Dorfmann, A. and R.W. Ogden, *Nonlinear electroelastic deformations.* Journal of Elasticity, 2006: p. 99-127.
3. Rajagopal, K.R. and A. Wineman, *A constitutive equation for non-linear electro-active solids.* Acta Mechanica, 1999: p. 219-28.
4. Bustamante, R., A. Dorfmann, and R.W. Ogden, *Nonlinear electroelastostatics: A variational framework.* Zeitschrift fur Angewandte Mathematik und Physik, 2009: p. 154-177.
5. Raoult, A., *Non-polyconvexity of the stored energy function of a Saint Venant-Kirchhoff material.* Applications of Mathematics, 1986: p. 417-419.

6. Steigmann, D.J., *On Isotropic, Frame-Invariant, Polyconvex Strain-Energy Functions.* The Quarterly Journal of Mechanics and Applied Mathematics, 2003: p. 483-491.
7. Schröder, J., *Anisotropie polyconvex energies*, in *Poly-, Quasi- and Rank-One Convexity in Applied Mechanics*, J. Schröder and P. Neff, Editors. 2010, Springer Vienna. p. 53-105.
8. Schroder, J. and P. Neff, *Invariant formulation of hyperelastic transverse isotropy based on polyconvex free energy functions.* International Journal of Solids and Structures, 2003: p. 401-45.
9. Xuanhe, Z., H. Wei, and S. Zhigang, *Electromechanical hysteresis and coexistent states in dielectric elastomers.* Physical Review B (Condensed Matter and Materials Physics), 2007: p. 134113-1.
10. Xuanhe, Z. and S. Zhigang, *Method to analyze programmable deformation of dielectric elastomer layers.* Applied Physics Letters, 2008: p. 251902 (3 pp.).
11. Xuanhe, Z. and S. Zhigang, *Method to analyze electromechanical stability of dielectric elastomers.* Applied Physics Letters, 2007: p. 061921-1.
12. Wissler, M. and E. Mazza, *Modeling and simulation of dielectric elastomer actuators.* Smart Materials and Structures, 2005: p. 1396-1402.
13. Wissler, M. and E. Mazza, *Modeling of a pre-strained circular actuator made of dielectric elastomers.* Sensors and Actuators A (Physical), 2005: p. 184-92.
14. O'Brien, B., et al., *Finite element modelling of dielectric elastomer minimum energy structures.* Applied Physics A: Materials Science & Processing, 2009: p. 507-14.

Appendix A. Mathematica Codes

1. Static response of a fiber reinforced tubular membrane

```
ClearAll[T1, T2]
Off[General::spell1]
SetAttributes[{h0, C1, C2, R, ρ,L0,τ,△,α}, Constant];
W=C1  (1/α1*(λ1^α1+λ2^α1+λ3^α1-3)+β2*1/α2*(λ1^α2+λ2^α2+λ3^α2-3)+β3*  1/α3*(λ1^α3+λ2^α3+λ3^α3-
3));
t1=4 h0 λ3 (λ1^2-λ3^2) (D[W,I1]+λ2^2 D[W,I2]);
t2=4 h0 λ3 (λ2^2-λ3^2) (D[W,I1]+λ1^2 D[W,I2]);
tf1=2*τ*(λ1/(λ2*△)* (Cos[α])^2);
tf2=2*τ*((λ2*(Sin[α])^2)/(λ1*△));
T1=t1+tf1;
T2=t2+tf2;
K11=-(R/λ1) Dt[1/λ1 Dt[λ2,η],η]/(1-(R/λ1 Dt[λ2,η])^2)^(1/2);
K22=1/(R λ2) (1-(R/λ1 Dt[λ2,η])^2)^(1/2);
λ3=1/(λ1 λ2);
u1=35480.47;u2=100810.93;u3=-100810.93;α1=2.505;α2=-0.5729;α3=-0.5729;C1=u1;β2=u2/u1;β3=u3/u1;
h0=2.4*10^-3;R=8.7*10^-3;L0=0.5*264.0*10^-3;
 NN=500 ;△=1.5*10^-3;α=17.688*(2 Pi)/360;
h=L0/NN;P=500000.0;(*P=(2*6894.757*Sin[(j+2)/8]);*)
lamda11=((1-λ2^2 Sin[α]^2)/Cos[α]^2)^(1/2);
dlamda2=-(λ1/R) (1-K2^2 λ2 R^2)^(1/2);
dK2=1/λ2 (K1-K2) dlamda2;
dT1=1/λ2 (T2-T1) dlamda2;
so1=Flatten[Solve[Dt[T1,η]==DT1,Dt[λ1,η]],1];
dlamda1=Dt[lamda11,η]/.{Dt[λ2,η]→dlamda2,DT1→dT1};
dT2=Dt[T2,η]/.{Dt[λ2,η]→dlamda2,Dt[λ1,η]→dlamda1};
dK1=-(1/T1) (K1 dT1+K2 dT2+T2 dK2);
ddlamda2=-K1 K2 λ1^2 λ2;
ddK2=1/λ2 (K1-K2)ddlamda2;
ddT1=1/λ2 (T2-T1) ddlamda2;
ddlamda1=Dt[Dt[lamda11,η],η]/.{Dt[λ2,η]→0,Dt[λ1,η]→0,Dt[λ2,{η,2}]→ddlamda2,Dt[DT1,η]→ddT1};
ddT2=Dt[Dt[T2,η],η]/.{Dt[λ1,η]→0,Dt[λ2,η]→0,Dt[λ1,{η,2}]→ddlamda1,Dt[λ2,{η,2}]→ddlamda2};
ddK1=-(1/T1) (K1 ddT1+K2 ddT2+T2 ddK2);
 (*F=0;jj=-1;tau=0.0436;*)
SetDirectory["F:\\Simulation results\\Dynamic response\\Fiber reinforced tubular membrane\\Pressure"];
λ2t=Table[0,{i,1,NN}];
λ1t=Table[0,{i,1,NN}];
KK1=Table[0,{i,1,NN}];
KK2=Table[0,{i,1,NN}];
TT1=Table[0,{i,1,NN}];
TT2=Table[0,{i,1,NN}];
FRKmethod[x_,y_,z_]:=Module[{F=x,jj=y,tau=z},
  ClearAll[T10,K20,so2,λ10,T20,K10];
  λ100==((1-λ200^2 Sin[α]^2)/Cos[α]^2)^(1/2);
  sol=Solve[T1==F/(2 Pi λ200 R)+(P λ200 R)/2 /.j→jj/.{λ2->λ200,λ1->λ100,τ→tau},λ200];
  sol1=Table[λ200/.sol[[i]],{i,1,Length[sol]}];
  λ20t=Catch[Do[If[Im[sol1[[i]]]==0&&Re[sol1[[i]]]>1,Throw[sol1[[i]]]],{i,1,Length[sol1]}]];
  K20t=1/(λ20t R);
  T10t=F/(2 Pi λ20t R)+(P λ20t R)/2 /.{j→jj,τ→tau};
  so2=Solve[T1==T10t/.{λ2->λ20t,τ→tau},λ1];
  λ10t=λ1/.so2[[1]];
  T20t=T2/.{λ2->λ20t,λ1->λ10t,τ→tau};
```

```
 K10t=1/T10t (P-K20t T20t)/.{j→jj,τ→tau};
 dn=h;
 λ20=λ20t+0.5 ddlamda2*dn^2/.{K1→K10t,K2→K20t,λ2->λ20t,λ1->λ10t,τ→tau};
 λ10=λ10t+0.5 ddlamda1*dn^2/.{K1→K10t,K2→K20t,λ2->λ20t,λ1->λ10t,τ→tau};
 K20=K20t+0.5 ddK2*dn^2/.{K1→K10t,K2→K20t,λ2->λ20t,λ1->λ10t,τ→tau};
 K10=K10t+0.5 ddK1*dn^2/.{K1→K10t,K2→K20t,λ2->λ20t,λ1->λ10t,τ→tau};
 T20=T20t+0.5 ddT2*dn^2/.{K1→K10t,K2→K20t,λ2->λ20t,λ1->λ10t,τ→tau};
 T10=T10t+0.5 ddT1*dn^2/.{K1→K10t,K2→K20t,λ2->λ20t,λ1->λ10t,τ→tau};
 λ2t[[1]]=λ20;
 λ1t[[1]]=λ10;
 KK1[[1]]=K10;
 KK2[[1]]=K20;
 TT1[[1]]=T10;
 TT2[[1]]=T20;
 For[i=0,i<NN-1,
  λ2t[[i+1]]=λ2t[[i]]+dlamda2*dn/.{K1→KK1[[i]],K2→KK2[[i]],λ2->λ2t[[i]],λ1->λ1t[[i]],τ→tau};
  λ1t[[i+1]]=λ1t[[i]]+dlamda1*dn/.{K1→KK1[[i]],K2→KK2[[i]],λ2->λ2t[[i]],λ1->λ1t[[i]],τ→tau};
  KK2[[i+1]]=KK2[[i]]+dK2*dn/.{K1→KK1[[i]],K2→KK2[[i]],λ2->λ2t[[i]],λ1->λ1t[[i]],τ→tau};
  KK1[[i+1]]=KK1[[i]]+dK1*dn/.{K1→KK1[[i]],K2→KK2[[i]],λ2->λ2t[[i]],λ1->λ1t[[i]],τ→tau};
  TT1[[i+1]]=TT1[[i]]+dT1*dn/.{K1→KK1[[i]],K2→KK2[[i]],λ2->λ2t[[i]],λ1->λ1t[[i]],τ→tau};
  TT2[[i+1]]=TT2[[i]]+dT2*dn/.{K1→KK1[[i]],K2→KK2[[i]],λ2->λ2t[[i]],λ1->λ1t[[i]],τ→tau},i++];
 Print["Pressure:",P/6894.757/.j→jj,"PSI"];
 Print["λ2(L0):",λ2t[[Length[λ2t]]]];
 Print["λ2(0):",λ2t[[1]]];
 Print["λ1(0):",λ1t[[1]]];
 Print["K1(0):",KK1[[1]]];
 Print["K2(0):",KK2[[1]]];]
Int=(λ1^2-R^2 (dlamda2)^2)^(1/2);
Int1=Table[Int/.{λ1->λ1t[[ii]],λ2->λ2t[[ii]],K2→KK2[[ii]]},{ii,1,Length[λ2t]}];
Int2=Table[h/2 (Int1[[ii]]+Int1[[ii+1]]),{ii,1,Length[Int1]-1}];
L=Sum[Int2[[ii]],{ii,1,Length[Int2]}]*10^3;
Stretch=L*10^-3/L0
Print["L:",L,"mm"]
```

2. Dynamic response of a tubular membrane

```
ClearAll[T1, T2]
Off[General::spell1]
SetAttributes[{h0, C1, C2,Γ,R,ρ,L0}, Constant];
W=C1 (I1-3)+C2 (I2-3);

t1=4 h0 λ3 (λ1^2-λ3^2) (D[W,I1]+λ2^2 D[W,I2]);
t2=4 h0 λ3 (λ2^2-λ3^2) (D[W,I1]+λ1^2 D[W,I2]);
T1=t1/(4 h0 C1);
T2=t2/(4 h0 C1);
λ3=1/(λ1 λ2);
K11=-((1/λ1 Dt[1/λ1 Dt[r,η],η])/(1- Dt[r,ξ]^2)^(1/2)) /.Dt[r,ξ]->1/λ1 Dt[r,η]/.r→R λ2;
K22=1/r (1- Dt[r,ξ]^2)^(1/2))/.Dt[r,ξ]->1/λ1 Dt[r,η]/.r→R λ2;
SolDlamda2=Solve[K22==K2, Dt[λ2,η]];
dlamda2=Dt[λ2,η]/.SolDlamda2[[1]];
eqnDK2=Dt[K2 r,ξ]==K1 Dt[r,ξ]/.{Dt[r,ξ]->1/λ1 Dt[r,η],Dt[K2,ξ]->1/λ1 Dt[K2,η]};
SolDK2=Solve[eqnDK2,Dt[K2,η]];
dK2=Dt[K2,η]/.SolDK2[[1]]/.r→R λ2;
eqnDT1=Dt[TT1 r,ξ]==TT2 Dt[r,ξ]/.Dt[r,ξ]->1/λ1 Dt[r,η]/.Dt[TT1,ξ]->1/λ1 Dt[TT1,η]/.r→R λ2;
```

```
SolDT1=Solve[eqnDT1,Dt[TT1,η]];
dT1=Dt[TT1,η]/.SolDT1[[1]]/.{TT1→T1,TT2→T2};
SolDlamda1=Solve[Dt[TT1,η]==Dt[T1,η],Dt[λ1,η]]/.Dt[TT1,η]→dT1;
dlamda1=Dt[λ1,η]/.SolDlamda1[[1]];
dT2=Dt[T2,η];
SolDK1=Solve[Dt[K1 T1,η]+Dt[K2 T2,η]==0,Dt[K1,η]];
dK1=Dt[K1,η]/.SolDK1[[1]];
Solddlamda2=Solve[K1*K2==K11*K22,Dt[λ2,{η,2}]];
ddlamda2=Dt[λ2,{η,2}]/.Solddlamda2[[1]]/.{Dt[λ1,η]→0,Dt[λ2,η]→0};
ddK2=Dt[dK2,η]/.{Dt[λ1,η]→0,Dt[λ2,η]→0};
ddT1=Dt[dT1,η]/.{Dt[λ1,η]→0,Dt[λ2,η]→0};
ddlamda1=Dt[dlamda1,η]/.{Dt[λ1,η]→0,Dt[λ2,η]→0};
ddT2=Dt[dT2,η]/.{Dt[λ1,η]→0,Dt[λ2,η]→0};
ddK1=Dt[dK1,η]/.{Dt[λ1,η]→0,Dt[λ2,η]→0};
C1=16000;C2=7300;h0=0.50*10^-3;R=9.56*10^-3;L0=20*10^-3;P=2000; rho=960.0;
NN=300;
h=L0/NN;
dK2=dK2/.Dt[λ2,η]->dlamda2;
dT1=dT1/.Dt[λ2,η]->dlamda2;
dlamda1=dlamda1/.{Dt[λ1,η]->dlamda1,Dt[λ2,η]->dlamda2};
dT2=dT2/.{Dt[λ1,η]->dlamda1,Dt[λ2,η]->dlamda2};
dK1=dK1/.{Dt[λ1,η]->dlamda1,Dt[λ2,η]->dlamda2,Dt[K2,η]→dK2};
ddK2=ddK2/.Dt[λ2,{η,2}]→ddlamda2;
ddT1=ddT1/.Dt[λ2,{η,2}]→ddlamda2;
ddlamda1=ddlamda1/.Dt[λ2,{η,2}]→ddlamda2;
ddT2=ddT2/.Dt[λ2,{η,2}]→ddlamda2;
ddK1=ddK1/.Dt[λ2,{η,2}]→ddlamda2;
λ3t=Table[0,{i,1,NN}];
λ2t=Table[0,{i,1,NN}];
λ1t=Table[0,{i,1,NN}];
KK1=Table[0,{i,1,NN}];
KK2=Table[0,{i,1,NN}];
TT1=Table[0,{i,1,NN}];
TT2=Table[0,{i,1,NN}];
SonnyMethod[x_,y_,z_]:=Module[{F=x,jj=y,λ20t=z},
 ClearAll[λ10,λ20,T10,T20,K10,K20,so2,dn];
 T10=F/(2 Pi λ20t R (4 h0 C1))+(P λ20t R)/(2 (4 h0 C1))/.j→jj;
 K20t=1/(λ20t R);
 so2=Solve[T1==T10/.λ2->λ20t,λ1];
 λ10t=λ1/.so2[[4]];
 T20=T2/.{λ2->λ20t,λ1->λ10t};
 K10t=1/T10 (P/(4 h0 C1)-K20t T20)/.j→jj;
 T10t=T10;
 T20t=T20;
 ClearAll[T10,T20];
 dn=h;
 λ20=λ20t+0.5 ddlamda2*dn^2/.{K1→K10t,K2→K20t,λ2->λ20t,λ1->λ10t};
 λ10=λ10t+0.5 ddlamda1*dn^2/.{K1→K10t,K2→K20t,λ2->λ20t,λ1->λ10t};
 K20=K20t+0.5 ddK2*dn^2/.{K1→K10t,K2→K20t,λ2->λ20t,λ1->λ10t};
 K10=K10t+0.5 ddK1*dn^2/.{K1→K10t,K2→K20t,λ2->λ20t,λ1->λ10t};
 T10=T10t+0.5 ddT1*dn^2/.{K1→K10t,K2→K20t,λ2->λ20t,λ1->λ10t};
 T20=T20t+0.5 ddT2*dn^2/.{K1→K10t,K2→K20t,λ2->λ20t,λ1->λ10t};
 λ3t[[1]]=1/(λ20*λ10);
 λ2t[[1]]=λ20;
 λ1t[[1]]=λ10;
```

```
 KK1[[1]]=K10;
 KK2[[1]]=K20;
 TT1[[1]]=T10;
 TT2[[1]]=T20;
 For[i=0,i<NN-1,
  λ2t[[i+1]]=λ2t[[i]]+dlamda2*dn/.{K1→KK1[[i]],K2→KK2[[i]],λ2->λ2t[[i]],λ1->λ1t[[i]]};
  λ1t[[i+1]]=λ1t[[i]]+dlamda1*dn/.{K1→KK1[[i]],K2→KK2[[i]],λ2->λ2t[[i]],λ1->λ1t[[i]]};
  λ3t[[i+1]]=1/(λ1t[[i]]*λ2t[[i]]);
  KK2[[i+1]]=KK2[[i]]+dK2*dn/.{K1→KK1[[i]],K2→KK2[[i]],λ2->λ2t[[i]],λ1->λ1t[[i]]};
  KK1[[i+1]]=KK1[[i]]+dK1*dn/.{K1→KK1[[i]],K2→KK2[[i]],λ2->λ2t[[i]],λ1->λ1t[[i]]};
  TT1[[i+1]]=TT1[[i]]+dT1*dn/.{K1→KK1[[i]],K2→KK2[[i]],λ2->λ2t[[i]],λ1->λ1t[[i]]};
  TT2[[i+1]]=TT2[[i]]+dT2*dn/.{K1→KK1[[i]],K2→KK2[[i]],λ2->λ2t[[i]],λ1->λ1t[[i]]},i++];
 Int=(λ1^2-R^2 (dlamda2)^2)^(1/2);
 Int1=Table[Int/.{λ1->λ1t[[ii]],λ2->λ2t[[ii]],K2→KK2[[ii]]},{ii,1,Length[λ2t]}];
 Int2=Table[h/2 (Int1[[ii]]+Int1[[ii+1]]),{ii,1,Length[Int1]-1}];
 L=Sum[Int2[[ii]],{ii,1,Length[Int2]}]*10^3;
 (*Print["L:",L,"mm"]
 Print["R:",λ2t[[1]]*R*10^3,"mm"]*)
 λ2t[[NN]]
 ]
x=1.138145;
sol=SonnyMethod[0,0,x]
Print["Error: ",Abs[(sol-1)*100],"%"]
(*nn=2;
initial=λ2t[[Length[λ2t]]];
statlamda2=Table[0,{i,1,nn}];
statlamda2[[1]]=initial;
Clear[ii]
For[ii=1,ii<nn/2+1,
x1=Catch[Do[If[Abs[RKmethod[0,ii-2,j1]-1]*100<3,Throw[j1]],{j1,initial,initial+0.2,0.00001}]];
Clear[initial];
initial=x1+0.1;
statlamda2[[ii]]=x1;
Print[x1],
ii++];*)
f=10.0;
T=1/f;
Clear[i,nPDE1,nPDE2,P]
MM1=10^4;
P=2000+500.0*If[MM1/(2f)<j&&j<2*MM1/(2f),1,0];(*1500.0*If[MM1/(2f)<j&&j<2*MM1/(2f),1,0];*)
(*1000.0*If[0<j&&j<MM1/(2f),1,0];*)(*Abs[(1000.0*Sin[2π f j/MM1 ])]*)
nPDE1=R λ2 Dt[T1,η]+R T1 Dt[λ2,η]==T2 R Dt[λ2,η];
p=P/(4 h0 C1);
nPDE2=p-K11 T1-K22 T2==(2 ρ λ3 h0)/(4 h0 C1) Dt[r,{t,2}]/.r→R λ2;
Clear[i,λ1,λ2,K1,K2,IC2,IC21]
Table[λ2[i-1,0]=λ2t[[i]],{i,1,NN}];
Table[λ1[i-1,0]=λ1t[[i]],{i,1,NN}];
Table[K2[i-1,0]=KK2[[i]],{i,1,NN}];
Table[K1[i-1,0]=KK1[[i]],{i,1,NN}];
Table[λ2[i-1,1]=λ2t[[i]],{i,1,NN}];
Table[λ1[i-1,1]=λ1t[[i]],{i,1,NN}];
Table[K2[i-1,1]=KK2[[i]],{i,1,NN}];
Table[K1[i-1,1]=KK1[[i]],{i,1,NN}];
Table[λ1[-1,j]=λ1[1,j],{i,0,NN}];
Table[λ2[-1,j]=λ2[1,j],{i,0,NN}];
```

```
nPDE22=nPDE2/.{K1→K11,K2→K22}/.{Dt[λ2,{t,2}]->(λ2[i,j+1]-2 λ2[i,j]+λ2[i,j-1])/k^2,Dt[λ1,η]->(λ1[i+1,j]-
λ1[i-1,j])/(2 h)
   ,Dt[λ2,η]->(λ2[i+1,j]-λ2[i-1,j])/(2 h),Dt[λ2,{η,2}]->(λ2[i+1,j]-2 λ2[i,j]+λ2[i-1,j])/h^2,λ1->λ1[i,j],λ2->λ2[i,j]};
Sollamda2time=Solve[nPDE22,λ2[i,1+j]];
ClearAll[lamda1,lamda2,pp]
lamda1=Table[0,{i,1,2*MM1/(2f)},{j,1,NN}];
lamda2=Table[0,{i,1,2*MM1/(2f)},{j,1,NN}];
pp=Table[0,{i,1,2*MM1/(2f)}];
time=Table[0,{i,1,2*MM1/(2f)}];
lamda1[[1]]=λ1t;
lamda2[[1]]=λ2t;
pp[[1]]=P/.j→0;
SonnyMethod1[x_,y_]:=Module[{jj=x,M1=y},
 ClearAll[MM,k,Sollamda2];
 MM=M1;
 k=T/MM;
 λ2[-1,jj]=λ2[1,jj];(*Boundary condition at 0*)
 λ1[-1,jj]=λ1[1,jj];
 Sollamda2=Table[λ2[i,1+j]/.Sollamda2time[[1]]/.{i→ii,j→jj},{ii,0,NN-1}];
 Table[λ2[i-1,jj+1]=Sollamda2[[i]],{i,1,NN-1}];
 λ2[NN-1,jj+1]=λ2t[[NN]];(*Boundary condition at L0*)
 pp[[jj+1]]=P/.j→jj;
 time[[jj+1]]=k jj;
 lamda2[[jj+1]]=Table[λ2[i,jj+1],{i,0,NN-1}];
 T10=(P λ2[0,j+1] R)/(2 (4 h0 C1))/.j→jj;
 SolBC3=Solve[T1==T10/.λ2->λ2[0,jj+1],λ1];
 so=Table[λ1/.SolBC3[[i]],{i,1,Length[SolBC3]}];
 For[i=0,i<Length[SolBC3],If[Im[so[[i]]]==0&&Re[so[[i]]]>1,λ10=so[[i]]],i++];
 Clear[i];
 λ1[0,jj+1]=λ10;
 λ2[-1,jj+1]=λ2[1,jj+1];(*Boundary condition at 0*)
 λ1[-1,jj+1]=λ1[1,jj+1];
 λ1[1,jj+1]=λ1[0,jj+1];
 Sollamda1time=Solve[nPDE1/.{Dt[λ1,η]->(λ1[i+1,j]-λ1[i-1,j])/(2h),Dt[λ2,η]->(λ2[i+1,j]-λ2[i-1,j])/(2h),λ1-
>λ1[i,j],λ2->λ2[i,j]},λ1[i+1,j]];
 Sollamda1=Table[λ1[i+1,j]/.Sollamda1time[[1]]/.{i→ii,j→jj},{ii,1,NN-1}];
 Table[λ1[i+1,jj+1]=Sollamda1[[i]],{i,1,NN-2}];
 lamda1[[jj+1]]=Table[λ1[i,jj+1],{i,0,NN-1}];
```

3. Static and dynamic response of arterial wall with crimped collagen fiber

```
ClearAll[T1, T2]
Off[General::spell1]
SetAttributes[{h0, C1, C2, R, ρ,L0,τ,Δ,α}, Constant];
W=C1/2 (I1-3);
t1=4 h0 λ3 (λ1^2-λ3^2) (D[W,I1]+λ2^2 D[W,I2]);
t2=4 h0 λ3 (λ2^2-λ3^2) (D[W,I1]+λ1^2 D[W,I2]);
tf1=2*Tf*(λ1/λ2* (Cos[α])^2);
tf2=2*Tf*((λ2*(Sin[α])^2)/λ1);
Tf=(4 Exp[k2(-1+λ1^2 Cos[α]^2+λ2^2 Sin[α]^2)^2] h0 k1 (-1+λ1^2 Cos[α]^2+λ2^2 Sin[α]^2))/( λ1^2 Cos[α]^2+λ2^2
Sin[α]^2)^(1/2);
T1=t1+tf1;
T2=t2+tf2;
K11=-(R/λ1) Dt[1/λ1 Dt[λ2,η],η]/(1-(R/λ1 Dt[λ2,η])^2)^(1/2);
K22=1/(R λ2) (1-(R/λ1 Dt[λ2,η])^2)^(1/2);
```

```
λ3=1/(λ1 λ2);
C1=7.64*10^3;h0=0.5*0.43*10^-3;R=4.745*10^-3;L0=10*10^-3;k1=996*10^3;k2=524.6;
 NN=100 ;∆=1.0*10^-3;α=(90-39.98)*(2 Pi)/360;∈0=8.8542*10^-12;∈r=2.7;
h=L0/NN;P=1000.0*j;(*P=(2*6894.757*Sin[(j+2)/8]);*)
α=(90-59.98)*(2 Pi)/360;
A=1.3*10^-3;
B=4π Cos[α]/L0;
Lf=8 NIntegrate[1/Cos[ArcTan[A B Cos[B x]]],{x,0,L0/(8 Cos[α])}]
dlamda2=-(λ1/R)(1-K2^2 λ2^2 R^2)^(1/2);
dK2=1/λ2 (K1-K2) dlamda2;
dT1=1/λ2 (T2-T1) dlamda2;
so1=Flatten[Solve[Dt[T1,η]==dT1,Dt[λ1,η]],1];
dlamda1=Dt[λ1,η]/.so1[[1]]/.Dt[λ2,η]→dlamda2;
dT2=Dt[T2,η]/.{Dt[λ2,η]→dlamda2,Dt[λ1,η]→dlamda1};
dK1=-(1/T1) (K1 dT1+K2 dT2+T2 dK2);
ddlamda2=-K1 K2 λ1^2 λ2;
ddK2=1/λ2 (K1-K2)ddlamda2;
ddT1=1/λ2 (T2-T1) ddlamda2;
Dso1=Dt[so1,η]/.{Dt[K2,η]→0,Dt[λ2,η]→0,Dt[λ1,η]→0,Dt[λ2,{η,2}]→ddlamda2,Dt[DT1,η]→ddT1};
ddlamda1=Dt[λ1,{η,2}]/.Dso1[[1]];
ddT2=Dt[Dt[T2,η],η]/.{Dt[λ1,η]→0,Dt[λ2,η]→0,Dt[λ1,{η,2}]→ddlamda1,Dt[λ2,{η,2}]→ddlamda2};
ddK1=-(1/T1) (K1 ddT1+K2 ddT2+T2 ddK2);
(*F=0;jj=-1;tau=0.0436;*)
λ2t=Table[0,{i,1,NN}];
λ1t=Table[0,{i,1,NN}];
KK1=Table[0,{i,1,NN}];
KK2=Table[0,{i,1,NN}];
TT1=Table[0,{i,1,NN}];
TT2=Table[0,{i,1,NN}];
Solutionλ2=Table[{1,0},{i,1,25}];
Solutionλ1=Table[{1,0},{i,1,25}];
Solutionλ3=Table[{1,0},{i,1,25}];
SolutionC=Table[{1,0},{i,1,25}];
SolutionR=Table[{1,0},{i,1,25}];
FRKmethod[y_,z_]:=Module[{jj=y,λ200=z},
 ClearAll[T10,K20,so2,λ10,T20,K10];
 j=jj;
 λ20=λ200;
 so2=FindRoot[T1==F/(2 Pi λ20 R)+(P λ20 R)/2 /.{F→0,λ2->λ20},{λ1,1.0}];
 λ10t=λ1/.so2[[1]];
 λ20t=λ20;
 K20t=1/(λ20t R);
 T10t=F/(2 π λ20t R)+(P λ20t R)/2 /.{F→0};
 T20t=T2/.{λ2->λ20t,λ1->λ10t};
 K10t=1/T10t (P-K20t T20t);
 dn=h;
 λ20=λ20t+0.5 ddlamda2*dn^2/.{K1→K10t,K2→K20t,λ2->λ20t,λ1->λ10t,τ→tau};
 λ10=λ10t+0.5 ddlamda1*dn^2/.{K1→K10t,K2→K20t,λ2->λ20t,λ1->λ10t,τ→tau};
 K20=K20t+0.5 ddK2*dn^2/.{K1→K10t,K2→K20t,λ2->λ20t,λ1->λ10t,τ→tau};
 K10=K10t+0.5 ddK1*dn^2/.{K1→K10t,K2→K20t,λ2->λ20t,λ1->λ10t,τ→tau};
 T20=T20t+0.5 ddT2*dn^2/.{K1→K10t,K2→K20t,λ2->λ20t,λ1->λ10t,τ→tau};
 T10=T10t+0.5 ddT1*dn^2/.{K1→K10t,K2→K20t,λ2->λ20t,λ1->λ10t,τ→tau};
 λ2t[[1]]=λ20;
 λ1t[[1]]=λ10;
 KK1[[1]]=K10;
```

```
 KK2[[1]]=K20;
 TT1[[1]]=T10;
 TT2[[1]]=T20;
 For[i=0,i<NN-1,
  λ2t[[i+1]]=λ2t[[i]]+dlamda2*dn/.{K1→KK1[[i]],K2→KK2[[i]],λ2->λ2t[[i]],λ1->λ1t[[i]],τ→tau};
  λ1t[[i+1]]=λ1t[[i]]+dlamda1*dn/.{K1→KK1[[i]],K2→KK2[[i]],λ2->λ2t[[i]],λ1->λ1t[[i]],τ→tau};
  KK2[[i+1]]=KK2[[i]]+dK2*dn/.{K1→KK1[[i]],K2→KK2[[i]],λ2->λ2t[[i]],λ1->λ1t[[i]],τ→tau};
  KK1[[i+1]]=KK1[[i]]+dK1*dn/.{K1→KK1[[i]],K2→KK2[[i]],λ2->λ2t[[i]],λ1->λ1t[[i]],τ→tau};
  TT1[[i+1]]=TT1[[i]]+dT1*dn/.{K1→KK1[[i]],K2→KK2[[i]],λ2->λ2t[[i]],λ1->λ1t[[i]],τ→tau};
  TT2[[i+1]]=TT2[[i]]+dT2*dn/.{K1→KK1[[i]],K2→KK2[[i]],λ2->λ2t[[i]],λ1->λ1t[[i]],τ→tau},i++];
 Print["K1(0):",KK1[[1]]];
 Print["Pressure:",P,"Pa"];
 Print["λ2(L0):",λ2t[[Length[λ2t]]]];
 h1=0.1*10^-3;
 Solutionλ2[[j+5,1]]=P;
 Solutionλ2[[j+5,2]]=λ2t[[1]]+0.11;
 Solutionλ1[[j+5,1]]=P;
 Solutionλ1[[j+5,2]]=λ1t[[1]];
 Solutionλ3[[j+5,1]]=P;
 Solutionλ3[[j+5,2]]=1/(λ1t[[1]] (λ2t[[1]]+0.11));
 Cap=4*π*∈0*∈r*L0*(Log[(R λ2t[[1]]+h1 (2-λ2t[[1]])) /(R λ2t[[1]]-h1 (2-λ2t[[1]]))])^-1*10^12;
 SolutionC[[j+5,1]]=P;
 SolutionC[[j+5,2]]=Cap;
 SolutionR[[j+5,2]]=P;
 SolutionR[[j+5,1]]=(λ2t[[1]]+0.11)*R*10^3;
 Print["Capacitance:",Cap,"pF"]; ]
```

4. Coupling between directional vectors and the electric field

```
Clear[Evaluate[Context[]<>"*"]]
Off[General::spell1]
SetDirectory["F:\\"];
F=(\[NoBreak]{
    {F11, F12, F13},
    {F21, F22, F23},
    {F31, F32, F33}
   }\[NoBreak]);
F21=F31=F32=F12=F13=F23=0;F33=1/(F11 F22);F22=F11;
(*F11=F22=F33=1;F13=F23=F32=F31=0;F21=0;F12=k1;*)
B=F.Transpose[F];
a={a1,a2,a3};
a1=Cos[γ]Cos[α];a2=Cos[γ]Sin[α];a3=Sin[γ];
b={b1,b2,b3};
b1=Cos[γ]Cos[β];b2=Cos[γ]Sin[β];b3=Sin[γ];
ab=Cross[a,b];
EE={E1,E2,E3};
Enn={En1,En2,En3};
(*E1=E2=0;*)
m=F.a;
BE=B.EE;
A[i_,j_]:=Sum[F[[i,k]]a[[k]]B[[j,l]]EE[[l]],{k,1,3},{l,1,3}]
B1[i_,j_]:=Sum[F[[i,k]]b[[k]]B[[j,l]]EE[[l]],{k,1,3},{l,1,3}]
(*A[i_,j_]:=m[[i]]Sum[B[[j,k]] EE[[k]],{k,1,3}]+Sum[B[[i,k]] EE[[k]],{k,1,3}]m[[j]];*)
fa[x_,y_]:=D[A[x,y]-A[3,3],α];
fr[x_,y_]:=D[A[x,y]-A[3,3],γ];
```

```
fa2[x_,y_]:=D[A[x,y]-A[3,3],{α,2}];
fr2[x_,y_]:=D[A[x,y]-A[3,3],{γ,2}];
far[x_,y_]:=D[D[A[x,y]-A[3,3],α],γ];
fra[x_,y_]:=D[D[A[x,y]-A[3,3],γ],α];
D1[x_,y_]:=fa2[x,y]fr2[x,y]-far[x,y]^2;
Reduce[{fa[1,1]==0,fr[1,1]==0,-(π/2)<=α≤π/2,-(π/2)<=γ<=π/2,F11>1},{α,γ}]
ClearAll[E1,E2,E3,k1]
(*E1=E2=E3;*)
x1=1;y1=1;
Sol1=Reduce[{fa[x1,y1]==0,fr[x1,y1]==0,-(π/2)<=α≤π/2,-(π/2)<=γ<=π/2,E3>0,F11>0,k1>0},{α,γ}]
Solve[Simplify[D[A[x1,y1],α]]==0,α]
E3=1;
ContourPlot[ A[x1,y1]/.k1→π/4,{α,-π/2,π/2},{γ,-π/2,π/2},FrameTicks→{{-Pi/2,0,Pi/2},{-
Pi/2,0,Pi/2}},ClippingStyle→Automatic]
PA[i_,j_]:=Sum[F[[i,k]]a[[k]]F[[j,l]]a[[l]],{k,1,3},{l,1,3}];
PB[i_,j_]:=Sum[F[[i,k]]b[[k]]F[[j,l]]b[[l]],{k,1,3},{l,1,3}];
PAB[i_,j_]:=Sum[F[[i,k]]a[[k]]F[[j,l]]b[[l]],{k,1,3},{l,1,3}];
DSa[x_,y_]:=D[W4 PA[x,y]+W8 PAB[x,y]+W14 A[x,y],α];
DSb[x_,y_]:=D[W4 PA[x,y]+W8 PAB[x,y]+W14 A[x,y],β];
DSr[x_,y_]:=D[W4 PA[x,y]+W8 PAB[x,y]+W14 A[x,y],γ];
DSa2[x_,y_]:=D[W4 PA[x,y]+W8 PAB[x,y]+W14 A[x,y],{α,2}];
DSb2[x_,y_]:=D[W4 PA[x,y]+W8 PAB[x,y]+W14 A[x,y],{β,2}];
DSr2[x_,y_]:=D[W4 PA[x,y]+W8 PAB[x,y]+W14 A[x,y],{γ,2}];
DSar[x_,y_]:=D[D[W4 PA[x,y]+W8 PAB[x,y]+W14 A[x,y],α],γ];
DSab[x_,y_]:=D[D[W4 PA[x,y]+W8 PAB[x,y]+W14 A[x,y],α],β];
DSra[x_,y_]:=D[D[W4 PA[x,y]+W8 PAB[x,y]+W14 A[x,y],γ],α];
DSrb[x_,y_]:=D[D[W4 PA[x,y]+W8 PAB[x,y]+W14 A[x,y],γ],β];
D11[x_,y_]:=DSa2[x,y]DSr2[x,y]-DSar[x,y]^2;
DD1[x_,y_]:=(\[NoBreak]{
   {DSa2[x,y], DSab[x,y], DSar[x,y]},
   {DSab[x,y], DSb2[x,y], DSrb[x,y]},
   {DSar[x,y], DSrb[x,y], DSr2[x,y]}
  }\[NoBreak]);
β=-α;
E1=E2=E3;
x1=1;y1=1;
Sol=Reduce[{DSa[x1,y1]==0,DSr[x1,y1]==0,-(π/2)<=α<=π/2,-(π/2)<γ<π/2,E3>0,F11>0,k1>0},{α,γ}]
mn=F.ab;
β=-α;
AB[i_,j_]:=Sum[F[[i,k]]ab[[k]]B[[j,l]]EE[[l]]+B[[i,k]]EE[[k]]F[[j,l]]ab[[l]],{k,1,3},{l,1,3}]
cfa[x_,y_]:=D[AB[x,y]-AB[3,3],α];
cfb[x_,y_]:=D[AB[x,y]-AB[3,3],β];
cfr[x_,y_]:=D[AB[x,y]-AB[3,3],γ];
cfa2[x_,y_]:=D[AB[x,y]-AB[3,3],{α,2}];
cfb2[x_,y_]:=D[AB[x,y]-AB[3,3],{β,2}];
cfr2[x_,y_]:=D[AB[x,y]-AB[3,3],{γ,2}];
cfar[x_,y_]:=D[D[AB[x,y]-AB[3,3],α],γ];
cfab[x_,y_]:=D[D[AB[x,y]-AB[3,3],α],β];
cfbr[x_,y_]:=D[D[AB[x,y]-AB[3,3],β],γ];
D3[x_,y_]:=(\[NoBreak]{
   {cfa2[x,y], cfab[x,y], cfar[x,y]},
   {cfab[x,y], cfb2[x,y], cfbr[x,y]},
   {cfar[x,y], cfbr[x,y], cfr2[x,y]}
  }\[NoBreak]);
D2[x_,y_]:=(\[NoBreak]{
```

```
    {cfa2[x,y], cfar[x,y]},
    {cfar[x,y], cfr2[x,y]}
   }\[NoBreak]);
ClearAll[E1,E2,E3]
x1=2;y1=2;
(*E1=0;*)
Sol=Solve[{cfa[x1,y1]==0,cfr[x1,y1]==0},{α,γ}];
SolE1=Sol/.E1→0
{cfa2[x1,y1],Det[D2[x1,y1]]}/.E1→0/.{α→-π/4,γ→0}
SolE3=Sol/.E3→0;
{cfa2[x1,y1],Det[D2[x1,y1]]}/.E3→0/.{α→-π/2,γ→-π/4}
E3=0;
x1=1;y1=1;
Sol=Reduce[{cfa[x1,y1]==0,cfr[x1,y1]==0,-(π/2)<=α<=π/2,-(π/2)<γ<π/2,F11>0,k1>0},{α,γ}]
cgoodplot2[Cos[γ] Sin[α] Sin[γ],{α,-π/2,π/2},{γ,-π/2,π/2},{{-Pi/2,0,Pi/2},{-Pi/2,0,Pi/2}},α,γ,"Pastel"]
PAB[i_,j_]:=Sum[F[[i,k]]a[[k]]F[[j,l]]b[[l]],{k,1,3},{l,1,3}];
DSa[x_,y_]:=D[W4 PA[x,y]+W6 PB[x,y]+W8 PAB[x,y]+W14 A[x,y]+W16 B1[x,y]+W18 AB[x,y],α];
DSb[x_,y_]:=D[W4 PA[x,y]+W6 PB[x,y]+W8 PAB[x,y]+W14 A[x,y]+W16 B1[x,y]+W18 AB[x,y],β];
DSr[x_,y_]:=D[W4 PA[x,y]+W6 PB[x,y]+W8 PAB[x,y]+W14 A[x,y]+W16 B1[x,y]+W18 AB[x,y],γ];
DSa2[x_,y_]:=D[W4 PA[x,y]+W6 PB[x,y]+W8 PAB[x,y]+W14 A[x,y]+W16 B1[x,y]+W18 AB[x,y],{α,2}];
DSb2[x_,y_]:=D[W4 PA[x,y]+W6 PB[x,y]+W8 PAB[x,y]+W14 A[x,y]+W16 B1[x,y]+W18 AB[x,y],{β,2}];
DSr2[x_,y_]:=D[W4 PA[x,y]+W6 PB[x,y]+W8 PAB[x,y]+W14 A[x,y]+W16 B1[x,y]+W18 AB[x,y],{γ,2}];
DSar[x_,y_]:=D[D[W4 PA[x,y]+W6 PB[x,y]+W8 PAB[x,y]+W14 A[x,y]+W16 B1[x,y]+W18 AB[x,y],α],γ];
DSab[x_,y_]:=D[D[W4 PA[x,y]+W6 PB[x,y]+W8 PAB[x,y]+W14 A[x,y]+W16 B1[x,y]+W18 AB[x,y],α],β];
DSra[x_,y_]:=D[D[W4 PA[x,y]+W6 PB[x,y]+W8 PAB[x,y]+W14 A[x,y]+W16 B1[x,y]+W18 AB[x,y],γ],α];
DSrb[x_,y_]:=D[D[W4 PA[x,y]+W6 PB[x,y]+W8 PAB[x,y]+W14 A[x,y]+W16 B1[x,y]+W18 AB[x,y],γ],β];
D11[x_,y_]:=DSa2[x,y]DSr2[x,y]-DSar[x,y]^2;
DD1[x_,y_]:=(\[NoBreak]{
    {DSa2[x,y], DSab[x,y], DSar[x,y]},
    {DSab[x,y], DSb2[x,y], DSrb[x,y]},
    {DSar[x,y], DSrb[x,y], DSr2[x,y]}
   }\[NoBreak]);
Solr=Solve[{DSa[1,1]==0,DSb[1,1]==0,DSr[1,1]==0},{α,β,γ}]
ClearAll[E1,E2,E3,F22]
Sola=Solve[{cfa[1,1]}==0,{α,β,γ}]
Solb=Solve[cfb[1,1]==0,{α,β,γ}]
Solr=Solve[cfr[1,1]==0,{α,β,γ}]
```

5. Convexity and Polyconvexity of Invariants and Invariant-based Free Energy Function

```
Clear[Evaluate[Context[]<>"*"]]
Off[General::spell1]
SetDirectory["F:\\"];
<<Combinatorica`
F=(\[NoBreak]{
    {F11, F12, F13},
    {F12, F22, F23},
    {F13, F23, F33}
   }\[NoBreak]);
F=J^(-1/3) F;
F12=F13=F23=0;F22=F11;F33=J/(F11 F22);
C1=Transpose[F].F;
IC1=Inverse[C1];
B1=F.Transpose[F];
J=1;
```

```
I1=Tr[C1];
Ivar={F11};
DI11=IdentityMatrix[Length[Ivar]];
DI1[i_,j_]:=D[D[I1,Ivar[[i]]],Ivar[[j]]];
Table[DI11[[i,j]]=DI1[i,j],{i,1,Length[Ivar]},{j,1,Length[Ivar]}];
Simplify[Det[DI11]]
CofFT=IdentityMatrix[3];
Table[CofFT[[i,j]]=Cofactor[Transpose[F],{i,j}],{i,1,3},{j,1,3}];
CofF=IdentityMatrix[3];
Table[CofF[[i,j]]=Cofactor[F,{i,j}],{i,1,3},{j,1,3}];
CF=(\[NoBreak]{
   {CF11, CF12, CF13},
   {CF12, CF22, CF23},
   {CF13, CF23, CF33}
  }\[NoBreak]);(*cofactor of F*)
CC1=CF.CF;(*Cof[FT].Cof[F]*)
I2=Tr[CC1]
Ivar={CF11,CF22,CF33,CF12,CF13,CF23};
DI21=IdentityMatrix[Length[Ivar]];
DI2[i_,j_]:=D[D[I2,Ivar[[i]]],Ivar[[j]]];
Table[DI21[[i,j]]=DI2[i,j],{i,1,Length[Ivar]},{j,1,Length[Ivar]}];
Det[DI21]
I3=Det[C1];
ClearAll[a1,a2,a3,γ]
a={a1,a2,a3};
a1=Cos[γ]Cos[α];a2=Cos[γ]Sin[α];a3=Sin[γ];
M1=IdentityMatrix[3];
Table[M1[[i,j]]=a[[i]]a[[j]],{i,1,3},{j,1,3}];
I4=a.(C1.a);
Ivar2={F11};
DI4=IdentityMatrix[Length[Ivar2]];
DI41[i_,j_]:=D[D[I4,Ivar2[[i]]],Ivar2[[j]]];
Table[DI4[[i,j]]=DI41[i,j],{i,1,Length[Ivar2]},{j,1,Length[Ivar2]}];
Det[DI4]
I5=a.((C1 C1).a);
Ivar2={F11};
DI5=IdentityMatrix[Length[Ivar2]];
DI51[i_,j_]:=D[D[I5,Ivar2[[i]]],Ivar2[[j]]];
Table[DI5[[i,j]]=DI51[i,j],{i,1,Length[Ivar2]},{j,1,Length[Ivar2]}];
Det[DI5]
b={b1,b2,b3};
b1=Cos[γ]Cos[β];b2=Cos[γ]Sin[β];b3=Sin[γ];
M2=IdentityMatrix[3];
Table[M2[[i,j]]=b[[i]]b[[j]],{i,1,3},{j,1,3}];
I6=b.(C1.b);
Ivar2={F11};
DI6=IdentityMatrix[Length[Ivar2]];
DI61[i_,j_]:=D[D[I6,Ivar2[[i]]],Ivar2[[j]]];
Table[DI6[[i,j]]=DI61[i,j],{i,1,Length[Ivar2]},{j,1,Length[Ivar2]}];
Det[DI6]
I7=b.((C1 C1).b);
Ivar2={F11};
DI7=IdentityMatrix[Length[Ivar2]];
DI71[i_,j_]:=D[D[I7,Ivar2[[i]]],Ivar2[[j]]];
Table[DI7[[i,j]]=DI71[i,j],{i,1,Length[Ivar2]},{j,1,Length[Ivar2]}];
Det[DI7]
```

```
I8=a.(C1.b)
Ivar21={F11};
(*Ivar21={F11,F22};*)
DI8=IdentityMatrix[Length[Ivar21]];
DI81[i_,j_]:=D[D[I8,Ivar21[[i]]],Ivar21[[j]]];
Table[DI8[[i,j]]=DI81[i,j],{i,1,Length[Ivar21]},{j,1,Length[Ivar21]}];
FullSimplify[Det[DI8]]
I9=a.((C1 C1).b)
Ivar21={F11};
(*Ivar21={F11,F22};*)
DI9=IdentityMatrix[Length[Ivar21]];
DI91[i_,j_]:=D[D[I9,Ivar21[[i]]],Ivar21[[j]]];
Table[DI9[[i,j]]=DI91[i,j],{i,1,Length[Ivar21]},{j,1,Length[Ivar21]}];
FullSimplify[Det[DI9]]
ClearAll[En1,En2,En3]
ClearAll[En]
En={En1,En2,En3};
En1=En2=0;
I11=En.(IC1.En)
var={F11,En3};
DI11E[i_,j_]:=D[D[I11,var[[i]]],var[[j]]];
DI111E=IdentityMatrix[Length[var]];
Table[DI111E[[i,j]]=DI11E[i,j],{i,1,Length[var]},{j,1,Length[var]}];
Simplify[Det[DI111E]]
I12=En.((IC1 IC1).En)
var={F11,En3};
DI12E[i_,j_]:=D[D[I12,var[[i]]],var[[j]]];
DI121E=IdentityMatrix[Length[var]];
Table[DI121E[[i,j]]=DI12E[i,j],{i,1,Length[var]},{j,1,Length[var]}];
Simplify[Det[DI121E]]
I13=a.En
var={F11,En3};
DI13[i_,j_]:=D[D[I13,var[[i]]],var[[j]]]
DI131=IdentityMatrix[Length[var]];
Table[DI131[[i,j]]=DI13[i,j],{i,1,Length[var]},{j,1,Length[var]}];
FullSimplify[Det[DI131]]
I14=a.C1.En
var={F11,En3};
DI14[i_,j_]:=D[D[I14,var[[i]]],var[[j]]]
DI141=IdentityMatrix[Length[var]];
Table[DI141[[i,j]]=DI14[i,j],{i,1,Length[var]},{j,1,Length[var]}];
FullSimplify[Det[DI141]]
I15=a.(C1 C1).En
var={F11,En3};
DI15[i_,j_]:=D[D[I15,var[[i]]],var[[j]]]
DI151=IdentityMatrix[Length[var]];
Table[DI151[[i,j]]=DI15[i,j],{i,1,Length[var]},{j,1,Length[var]}];
FullSimplify[Det[DI151]]
I16=b.C1.En
var={F11,En3};
DI16[i_,j_]:=D[D[I16,var[[i]]],var[[j]]]
DI161=IdentityMatrix[Length[var]];
Table[DI161[[i,j]]=DI16[i,j],{i,1,Length[var]},{j,1,Length[var]}];
FullSimplify[Det[DI161]]
I17=b.(C1 C1).En
var={F11,En3};
```

```
DI17[i_,j_]:=D[D[I17,var[[i]]],var[[j]]]
DI171=IdentityMatrix[Length[var]];
Table[DI171[[i,j]]=DI17[i,j],{i,1,Length[var]},{j,1,Length[var]}];
FullSimplify[Det[DI171]]
I18=Cross[a,b].C1.En
var={F11,En3};
DI18[i_,j_]:=D[D[I18,var[[i]]],var[[j]]]
DI181=IdentityMatrix[Length[var]];
Table[DI181[[i,j]]=DI18[i,j],{i,1,Length[var]},{j,1,Length[var]}];
FullSimplify[Det[DI181]]
I19=Cross[a,b].(C1 C1).En
var={F11,En3};
DI19[i_,j_]:=D[D[I19,var[[i]]],var[[j]]]
DI191=IdentityMatrix[Length[var]];
Table[DI191[[i,j]]=DI19[i,j],{i,1,Length[var]},{j,1,Length[var]}];
FullSimplify[Det[DI191]]
ClearAll[W1,W2,W4,W5,W6,W7,W8,W9,W10,W11,W12,W13,W14,W15,W16,W17,W18,W19]
(*γ=π/2;*)
D2WD2F=W1 DI11[[1,1]]+W2 DI22+W4 DI4[[1,1]]+W5 DI5[[1,1]]+W6 DI6[[1,1]]+W7 DI7[[1,1]]+W8
DI8[[1,1]]+W9 DI9[[1,1]]+W11 DI111E[[1,1]]+W12 DI121E[[1,1]]+W14 DI141[[1,1]]+W16 DI161[[1,1]]+W18
DI181[[1,1]]+W19 DI191[[1,1]];
D2WDFE=W11 DI111E[[1,2]]+W12 DI121E[[1,2]]+W14 DI141[[1,2]]+W16 DI161[[1,2]]+W18
DI181[[1,2]]+W19 DI191[[1,2]];
D2WD2E=2 W10+W11 DI111E[[2,2]]+W12 DI121E[[2,2]];
(*W4=W5=W6=W7=W8=W9=W14=W16=W18=W19=0;*)
(*W14=W16=W18=W19=0;*)
(*W5=W7=W12=W13=W15=W16=W17=W18=W19=0;*)
W5=W7=W9=W12=W19=0;
Sol1=Solve[D2WD2F D2WD2E-(D2WDFE)^2==0,En3];
```

Appendix B. Integrity Basis for the Proper and Full Orthogonal Set

The integrity basis is presented in the forms of typical invariants under the proper orthogonal group in terms of the symmetric tensor $\boldsymbol{G}$ and three generic vectors $\boldsymbol{u}$, $\boldsymbol{v}$ and $\boldsymbol{w}$:

(i)	$\mathrm{tr}\boldsymbol{G}^N$	(N = 1, 2, 3)
(ii)	$\boldsymbol{u}\boldsymbol{G}^N\boldsymbol{u}$, $[\boldsymbol{u},\boldsymbol{G}\boldsymbol{u},\boldsymbol{G}^2\boldsymbol{u}]$	(N = 1, 2, 3)
(iii)	$\boldsymbol{u}\boldsymbol{G}^N\boldsymbol{v}$	(N = 1, 2, 3)
	$[\boldsymbol{u},\boldsymbol{G}^M\boldsymbol{v},\boldsymbol{G}^N\boldsymbol{v}]$	(MN = 01, 02, 12)
	$[\boldsymbol{u},\boldsymbol{G}^M\boldsymbol{u},\boldsymbol{G}^N\boldsymbol{v}]$	(MN = 10, 11, 12, 20)
(iv)	$[\boldsymbol{u},\boldsymbol{G}^M\boldsymbol{v},\boldsymbol{G}^N\boldsymbol{w}]$	(MN = 00, 01, 02, 10, 11, 12, 20)

where $[\boldsymbol{u}, \boldsymbol{v}, \boldsymbol{w}]$ represents a triple scalar product of vectors $\boldsymbol{u}$, $\boldsymbol{v}$ and $\boldsymbol{w}$.

A table of typical invariants for the symmetric tensor $\boldsymbol{G}$, two polar vectors $\boldsymbol{u}$ and $\boldsymbol{v}$ and two axial vectors $\boldsymbol{r}$ and $\boldsymbol{s}$ under the full orthogonal group is presented:

(i)	$\mathrm{tr}\boldsymbol{G}^{N+1}$, $\boldsymbol{u}\boldsymbol{G}^N\boldsymbol{u}$, $\boldsymbol{v}\boldsymbol{G}^N\boldsymbol{v}$	(N = 0, 1, 2)
(ii)	$\boldsymbol{r}\boldsymbol{G}^N\boldsymbol{r},\boldsymbol{r}\boldsymbol{G}^N\boldsymbol{s}$, $[\boldsymbol{r},\boldsymbol{G}\boldsymbol{r},\boldsymbol{G}^2\boldsymbol{r}]$	(N = 1, 2, 3)
	$[\boldsymbol{r},\boldsymbol{G}^M\boldsymbol{s},\boldsymbol{G}^N\boldsymbol{s}]$, $[\boldsymbol{s},\boldsymbol{G}^M\boldsymbol{r},\boldsymbol{G}^N\boldsymbol{r}]$	(MN = 01, 02, 12)
(iii)	$[\boldsymbol{r},\boldsymbol{G}^M\boldsymbol{u},\boldsymbol{G}^N\boldsymbol{u}]$	(MN = 01, 02, 12)
	$(\boldsymbol{u}\boldsymbol{r})(\boldsymbol{u}\boldsymbol{G}^N\boldsymbol{r})$	(N = 1, 2, 3)
	$(\boldsymbol{u}\boldsymbol{r})[\boldsymbol{u},\boldsymbol{r},\boldsymbol{G}^N\boldsymbol{u}]$	(N = 1, 2)
(iv)	$(\boldsymbol{u}\boldsymbol{r})(\boldsymbol{v}\boldsymbol{G}^N\boldsymbol{r})+(\boldsymbol{v}\boldsymbol{r})(\boldsymbol{u}\boldsymbol{G}^N\boldsymbol{r})$	(N = 0, 1, 2)
	$(\boldsymbol{u}\boldsymbol{G}^N\boldsymbol{r})(\boldsymbol{v}\boldsymbol{G}^N\boldsymbol{r})-(\boldsymbol{v}\boldsymbol{G}^N\boldsymbol{r})(\boldsymbol{u}\boldsymbol{G}^N\boldsymbol{r})$	(MN = 01, 02, 12)
	$[\boldsymbol{r},\boldsymbol{G}^N\boldsymbol{u},\boldsymbol{v}]+[\boldsymbol{r},\boldsymbol{u},\boldsymbol{G}^N\boldsymbol{v}]$	(N = 0, 1, 2)
	$[\boldsymbol{r},\boldsymbol{G}^M\boldsymbol{u},\boldsymbol{G}^N\boldsymbol{v}]-[\boldsymbol{r},\boldsymbol{G}^N\boldsymbol{u},\boldsymbol{G}^M\boldsymbol{v}]$	(MN = 01, 02, 12)
	$(\boldsymbol{u}\boldsymbol{r})[\boldsymbol{v},\boldsymbol{r},\boldsymbol{G}^N\boldsymbol{r}]+(\boldsymbol{v}\boldsymbol{r})[\boldsymbol{u},\boldsymbol{r},\boldsymbol{G}^N\boldsymbol{r}]$	(N = 0, 1, 2)
(v)	$(\boldsymbol{u}\boldsymbol{G}^N\boldsymbol{r})(\boldsymbol{u}\boldsymbol{G}^N\boldsymbol{s})$	(MN = 00, 01, 02, 10, 20, 21)
	$(\boldsymbol{u}\boldsymbol{r})[\boldsymbol{v},\boldsymbol{G}^M\boldsymbol{r},\boldsymbol{G}^N\boldsymbol{u}]$, $(\boldsymbol{u}\boldsymbol{s})[\boldsymbol{u},\boldsymbol{G}^M\boldsymbol{s},\boldsymbol{G}^N\boldsymbol{u}]$	(MN = 00, 01, 10, 20)

(vi)

$(\boldsymbol{u}\boldsymbol{G}^{M}\boldsymbol{r})(\boldsymbol{v}\boldsymbol{G}^{N}\boldsymbol{s})+(\boldsymbol{v}\boldsymbol{G}^{M}\boldsymbol{r})(\boldsymbol{u}\boldsymbol{G}^{N}\boldsymbol{s})$	(MN = 00, 10, 20, 01, 02, 21)
$(\boldsymbol{u}\boldsymbol{G}^{M}\boldsymbol{r})(\boldsymbol{v}\boldsymbol{G}^{N}\boldsymbol{s})-(\boldsymbol{v}\boldsymbol{G}^{M}\boldsymbol{r})(\boldsymbol{u}\boldsymbol{G}^{N}\boldsymbol{s})$	(MN = 00, 10, 20, 01, 02, 12)
$(\boldsymbol{u}\boldsymbol{r})[\boldsymbol{s},\boldsymbol{G}^{M}\boldsymbol{r},\boldsymbol{G}^{N}\boldsymbol{v}]+(\boldsymbol{v}\boldsymbol{r})[\boldsymbol{s},\boldsymbol{G}^{M}\boldsymbol{r},\boldsymbol{G}^{N}\boldsymbol{u}]$	(MN = 00, 01, 10, 20)
$(\boldsymbol{s}\boldsymbol{r})[\boldsymbol{r},\boldsymbol{G}^{M}\boldsymbol{s},\boldsymbol{G}^{N}\boldsymbol{v}]+(\boldsymbol{v}\boldsymbol{s})[\boldsymbol{r},\boldsymbol{G}^{M}\boldsymbol{s},\boldsymbol{G}^{N}\boldsymbol{u}]$	(MN = 00, 01, 10, 20)

Appendix C. Tangent Modulus for Electro-Elastic Material

$$
\begin{aligned}
\boldsymbol{C} &= 4\{(W_{11}+2W_{12}I_1+W_2+W_{22}I_1^2)\boldsymbol{1}\otimes\boldsymbol{1}-(W_{12}+W_{22}I_1)(\boldsymbol{1}\otimes\boldsymbol{C}+\boldsymbol{C}\otimes\boldsymbol{1})+W_{22}\boldsymbol{C}\otimes\boldsymbol{C}\\
&-W_2\boldsymbol{I}+(W_{14}+W_{24}I_1)(\boldsymbol{1}\otimes\boldsymbol{a}\otimes\boldsymbol{a}+\boldsymbol{a}\otimes\boldsymbol{a}\otimes\boldsymbol{1})+(W_{16}+W_{26}I_1)(\boldsymbol{1}\otimes\boldsymbol{b}\otimes\boldsymbol{b}+\boldsymbol{b}\otimes\boldsymbol{b}\otimes\boldsymbol{1})\\
&+(W_{18}+W_{28}I_1)(\boldsymbol{1}\otimes\boldsymbol{a}\otimes\boldsymbol{b}+\boldsymbol{b}\otimes\boldsymbol{a}\otimes\boldsymbol{1})+(W_{1E_2}+W_{2E_2}I_1)(\boldsymbol{1}\otimes\boldsymbol{a}\otimes\boldsymbol{E}+\boldsymbol{E}\otimes\boldsymbol{a}\otimes\boldsymbol{1})\\
&+(W_{1E_3}+W_{2E_3}I_1)(\boldsymbol{1}\otimes\boldsymbol{b}\otimes\boldsymbol{E}+\boldsymbol{E}\otimes\boldsymbol{b}\otimes\boldsymbol{1})+(W_{1E_4}+W_{2E_4}I_1)(\boldsymbol{1}\otimes(\boldsymbol{a}\times\boldsymbol{b})\otimes\boldsymbol{E}\\
&+(\boldsymbol{a}\times\boldsymbol{b})\otimes\boldsymbol{E}\otimes\boldsymbol{1})-W_{24}(\boldsymbol{C}\otimes\boldsymbol{a}\otimes\boldsymbol{a}+\boldsymbol{a}\otimes\boldsymbol{a}\otimes\boldsymbol{C})-W_{26}(\boldsymbol{C}\otimes\boldsymbol{b}\otimes\boldsymbol{b}+\boldsymbol{b}\otimes\boldsymbol{b}\otimes\boldsymbol{C})\\
&-W_{28}(\boldsymbol{C}\otimes\boldsymbol{a}\otimes\boldsymbol{b}+\boldsymbol{b}\otimes\boldsymbol{a}\otimes\boldsymbol{C})-W_{2E_2}(\boldsymbol{C}\otimes\boldsymbol{a}\otimes\boldsymbol{E}+\boldsymbol{E}\otimes\boldsymbol{a}\otimes\boldsymbol{C})-W_{2E_3}(\boldsymbol{C}\otimes\boldsymbol{b}\otimes\boldsymbol{E}\\
&+\boldsymbol{E}\otimes\boldsymbol{b}\otimes\boldsymbol{C})-W_{2E_4}(\boldsymbol{C}\otimes(\boldsymbol{a}\times\boldsymbol{b})\otimes\boldsymbol{E}+\boldsymbol{E}\otimes(\boldsymbol{a}\times\boldsymbol{b})\otimes\boldsymbol{C})+W_{44}(\boldsymbol{a}\otimes\boldsymbol{a}\otimes\boldsymbol{a}\otimes\boldsymbol{a})\\
&+W_{66}(\boldsymbol{b}\otimes\boldsymbol{b}\otimes\boldsymbol{b}\otimes\boldsymbol{b})+W_{88}(\boldsymbol{a}\otimes\boldsymbol{b}\otimes\boldsymbol{a}\otimes\boldsymbol{b})+W_{E_2E_2}(\boldsymbol{a}\otimes\boldsymbol{E}\otimes\boldsymbol{a}\otimes\boldsymbol{E})\\
&+W_{E_3E_3}(\boldsymbol{b}\otimes\boldsymbol{E}\otimes\boldsymbol{b}\otimes\boldsymbol{E})+W_{E_4E_4}((\boldsymbol{a}\times\boldsymbol{b})\otimes\boldsymbol{E}\otimes(\boldsymbol{a}\times\boldsymbol{b})\otimes\boldsymbol{E})+W_{46}(\boldsymbol{a}\otimes\boldsymbol{a}\otimes\boldsymbol{b}\otimes\boldsymbol{b}\\
&+\boldsymbol{b}\otimes\boldsymbol{b}\otimes\boldsymbol{a}\otimes\boldsymbol{a})+W_{48}(\boldsymbol{a}\otimes\boldsymbol{a}\otimes\boldsymbol{a}\otimes\boldsymbol{b}+\boldsymbol{b}\otimes\boldsymbol{a}\otimes\boldsymbol{a}\otimes\boldsymbol{a})+W_{68}(\boldsymbol{b}\otimes\boldsymbol{b}\otimes\boldsymbol{a}\otimes\boldsymbol{b}\\
&+\boldsymbol{b}\otimes\boldsymbol{a}\otimes\boldsymbol{b}\otimes\boldsymbol{b})+W_{4E_2}(\boldsymbol{a}\otimes\boldsymbol{a}\otimes\boldsymbol{a}\otimes\boldsymbol{E}+\boldsymbol{E}\otimes\boldsymbol{a}\otimes\boldsymbol{a}\otimes\boldsymbol{a})+W_{4E_3}(\boldsymbol{a}\otimes\boldsymbol{a}\otimes\boldsymbol{b}\otimes\boldsymbol{E}\\
&\boldsymbol{E}\otimes\boldsymbol{b}\otimes\boldsymbol{a}\otimes\boldsymbol{a})+W_{4E_4}(\boldsymbol{a}\otimes\boldsymbol{a}\otimes(\boldsymbol{a}\times\boldsymbol{b})\otimes\boldsymbol{E}+\boldsymbol{E}\otimes(\boldsymbol{a}\times\boldsymbol{b})\otimes\boldsymbol{a}\otimes\boldsymbol{a})\\
&+W_{6E_2}(\boldsymbol{b}\otimes\boldsymbol{b}\otimes\boldsymbol{a}\otimes\boldsymbol{E}+\boldsymbol{E}\otimes\boldsymbol{a}\otimes\boldsymbol{b}\otimes\boldsymbol{b})+W_{6E_3}(\boldsymbol{b}\otimes\boldsymbol{b}\otimes\boldsymbol{b}\otimes\boldsymbol{E}+\boldsymbol{E}\otimes\boldsymbol{b}\otimes\boldsymbol{b}\otimes\boldsymbol{b})\\
&+W_{6E_4}(\boldsymbol{b}\otimes\boldsymbol{b}\otimes(\boldsymbol{a}\times\boldsymbol{b})\otimes\boldsymbol{E}+\boldsymbol{E}\otimes(\boldsymbol{a}\times\boldsymbol{b})\otimes\boldsymbol{b}\otimes\boldsymbol{b})+W_{8E_2}(\boldsymbol{a}\otimes\boldsymbol{b}\otimes\boldsymbol{a}\otimes\boldsymbol{E}\\
&+\boldsymbol{E}\otimes\boldsymbol{a}\otimes\boldsymbol{b}\otimes\boldsymbol{a})+W_{8E_3}(\boldsymbol{a}\otimes\boldsymbol{b}\otimes\boldsymbol{b}\otimes\boldsymbol{E}+\boldsymbol{E}\otimes\boldsymbol{b}\otimes\boldsymbol{b}\otimes\boldsymbol{a})\\
&+W_{8E_4}(\boldsymbol{a}\otimes\boldsymbol{b}\otimes(\boldsymbol{a}\times\boldsymbol{b})\otimes\boldsymbol{E}+\boldsymbol{E}\otimes(\boldsymbol{a}\times\boldsymbol{b})\otimes\boldsymbol{b}\otimes\boldsymbol{a})+W_{E_2E_3}(\boldsymbol{a}\otimes\boldsymbol{E}\otimes\boldsymbol{b}\otimes\boldsymbol{E}\\
&+\boldsymbol{E}\otimes\boldsymbol{b}\otimes\boldsymbol{E}\otimes\boldsymbol{a})+W_{E_2E_4}(\boldsymbol{a}\otimes\boldsymbol{E}\otimes(\boldsymbol{a}\times\boldsymbol{b})\otimes\boldsymbol{E}+\boldsymbol{E}\otimes(\boldsymbol{a}\times\boldsymbol{b})\otimes\boldsymbol{E}\otimes\boldsymbol{a})\\
&+W_{E_3E_4}(\boldsymbol{b}\otimes\boldsymbol{E}\otimes(\boldsymbol{a}\times\boldsymbol{b})\otimes\boldsymbol{E}+\boldsymbol{E}\otimes(\boldsymbol{a}\times\boldsymbol{b})\otimes\boldsymbol{E}\otimes\boldsymbol{b})-\boldsymbol{C}^{-1}(W_{E_11}+W_{E_12}(I_1\\
&+I))(\boldsymbol{1}\otimes\boldsymbol{F}^{-1}\boldsymbol{E}\otimes\boldsymbol{F}^{-1}\boldsymbol{E}+\boldsymbol{F}^{-1}\boldsymbol{E}\otimes\boldsymbol{F}^{-1}\boldsymbol{E}\otimes\boldsymbol{1})-W_{E_14}\boldsymbol{C}^{-1}(\boldsymbol{a}\otimes\boldsymbol{a}\otimes\boldsymbol{F}^{-1}\boldsymbol{E}\otimes\boldsymbol{F}^{-1}\boldsymbol{E}\\
&+\boldsymbol{F}^{-1}\boldsymbol{E}\otimes\boldsymbol{F}^{-1}\boldsymbol{E}\otimes\boldsymbol{a}\otimes\boldsymbol{a})-W_{E_16}\boldsymbol{C}^{-1}(\boldsymbol{b}\otimes\boldsymbol{b}\otimes\boldsymbol{F}^{-1}\boldsymbol{E}\otimes\boldsymbol{F}^{-1}\boldsymbol{E}+\boldsymbol{F}^{-1}\boldsymbol{E}\otimes\boldsymbol{F}^{-1}\boldsymbol{E}\otimes\boldsymbol{a}\\
&\otimes\boldsymbol{a})-W_{E_1E_1}\boldsymbol{C}^{-2}(\boldsymbol{F}^{-1}\boldsymbol{E}\otimes\boldsymbol{F}^{-1}\boldsymbol{E}\otimes\boldsymbol{F}^{-1}\boldsymbol{E}\otimes\boldsymbol{F}^{-1}\boldsymbol{E})-W_{E_1E_2}\boldsymbol{C}^{-1}(\boldsymbol{F}^{-1}\boldsymbol{E}\otimes\boldsymbol{F}^{-1}\boldsymbol{E}\otimes\boldsymbol{a}\otimes\boldsymbol{E}\\
&+\boldsymbol{E}\otimes\boldsymbol{a}\otimes\boldsymbol{F}^{-1}\boldsymbol{E}\otimes\boldsymbol{F}^{-1}\boldsymbol{E})-W_{E_1E_3}\boldsymbol{C}^{-1}(\boldsymbol{F}^{-1}\boldsymbol{E}\otimes\boldsymbol{F}^{-1}\boldsymbol{E}\otimes\boldsymbol{b}\otimes\boldsymbol{E}+\boldsymbol{E}\otimes\boldsymbol{b}\otimes\boldsymbol{F}^{-1}\boldsymbol{E}\otimes\boldsymbol{F}^{-1}\boldsymbol{E})\\
&-W_{E_1E_4}\boldsymbol{C}^{-1}(\boldsymbol{F}^{-1}\boldsymbol{E}\otimes\boldsymbol{F}^{-1}\boldsymbol{E}\otimes(\boldsymbol{a}\times\boldsymbol{b})\otimes\boldsymbol{E}+\boldsymbol{E}\otimes(\boldsymbol{a}\times\boldsymbol{b})\otimes\boldsymbol{F}^{-1}\boldsymbol{E}\otimes\boldsymbol{F}^{-1}\boldsymbol{E})\\
&-2W_{E_1E_1}(\boldsymbol{F}^{-1}\boldsymbol{E}\otimes\boldsymbol{F}^{-1}\boldsymbol{E})\otimes\frac{\partial\boldsymbol{C}^{-1}}{\partial\boldsymbol{C}}\}+P\frac{\partial\boldsymbol{C}^{-1}}{\partial\boldsymbol{C}},
\end{aligned}
$$

where

$$
\begin{aligned}
&W_{E_1}=\frac{\partial W}{\partial I_{11}},W_{E_2}=\frac{\partial W}{\partial I_{14}},W_{E_3}=\frac{\partial W}{\partial I_{16}},W_{E_4}=\frac{\partial W}{\partial I_{18}},W_{E_1E_1}=\frac{\partial^2 W}{\partial I_{11}^2},W_{E_1E_2}=\frac{\partial}{\partial I_{14}}\left(\frac{\partial W}{\partial I_{11}}\right),\\
&W_{E_1E_3}=\frac{\partial}{\partial I_{16}}\left(\frac{\partial W}{\partial I_{11}}\right),W_{E_1E_4}=\frac{\partial}{\partial I_{18}}\left(\frac{\partial W}{\partial I_{11}}\right),W_{E_2E_3}=\frac{\partial}{\partial I_{16}}\left(\frac{\partial W}{\partial I_{14}}\right),W_{E_2E_4}=\frac{\partial}{\partial I_{18}}\left(\frac{\partial W}{\partial I_{14}}\right),\\
&W_{E_3E_4}=\frac{\partial}{\partial I_{18}}\left(\frac{\partial W}{\partial I_{16}}\right).
\end{aligned}
$$

Appendix D. UMATs (User Subroutines for ABAQUS)

1. Mooney-Rivlin model + electrostatic energy function (E_MRmodel.f)

```
      SUBROUTINE UMAT(STRESS,STATEV,DDSDDE,SSE,SPD,SCD,
     1 RPL,DDSDDT,DRPLDE,DRPLDT,
     2 STRAN,DSTRAN,TIME,DTIME,TEMP,DTEMP,PREDEF,DPRED,CMNAME,
     3 NDI,NSHR,NTENS,NSTATEV,PROPS,NPROPS,COORDS,DROT,PNEWDT,
     4 CELENT,DFGRD0,DFGRD1,NOEL,NPT,LAYER,KSPT,KSTEP,KINC)
C
      INCLUDE 'ABA_PARAM.INC'
C
      CHARACTER*8 CMNAME
      DIMENSION STRESS(NTENS),STATEV(NSTATEV),
     1 DDSDDE(NTENS,NTENS),DDSDDT(NTENS),DRPLDE(NTENS),
     2 STRAN(NTENS),DSTRAN(NTENS),TIME(2),PREDEF(1),DPRED(1),
     3 PROPS(NPROPS),COORDS(3),DROT(3,3),DFGRD0(3,3),DFGRD1(3,3),
     4 Et(3),Stress_Max(3,3),EkEk(1),DFGRDM1_INV(3,3),En(3),
     5 TEMP(1),DTEMP(1),DFGRDP(3),DFGRDM1(3, 3),DFGRDM0(3, 3),
     6 CBAR(3,3),DDSDDE_Max(6,6)
C
      DIMENSION BBAR(6),DISTGR(3,3),BBARBBAR(6)
C
      PARAMETER(ZERO=0.D0, ONE=1.D0, TWO=2.D0, THREE=3.D0, FOUR=4.D0,
     1          FIVE=5.D0, SIX=6.D0, SEVEN=7.D0, EIGHT=8.D0)
C
C -------------------------------------------------------------
C    UMAT FOR COMPRESSIBLE MOONEY-RIVLIN MODEL
C    W=C10(I-3)+C01(I-3)+1/D1 (J-1)*(J-1)
C -------------------------------------------------------------
C    PROPS(1) - C10      C1
C    PROPS(2) - C01      C2
C    PROPS(3) - D1       Bulk modulus
C    PROPS(4) - E1       E-field in X direction
C    PROPS(5) - E2       E-field in Y direction
C    PROPS(6) - E3       E-field in Z direction
C    PROPS(7) - EPSILON  Vaccum permittivity*relative permittivity
C -------------------------------------------------------------
C
C   Read Material PROPERTIES
C
      C10=PROPS(1)
      C01=PROPS(2)
      D1 =PROPS(3)
      EPSILON=PROPS(7)
C
C    JACOBIAN AND DISTORTION TENSOR
C
      DET=DFGRD1(1, 1)*DFGRD1(2, 2)*DFGRD1(3, 3)
     1   -DFGRD1(1, 2)*DFGRD1(2, 1)*DFGRD1(3, 3)
      IF(NSHR.EQ.3) THEN
        DET=DET+DFGRD1(1, 2)*DFGRD1(2, 3)*DFGRD1(3, 1)
     1         +DFGRD1(1, 3)*DFGRD1(3, 2)*DFGRD1(2, 1)
     2         -DFGRD1(1, 3)*DFGRD1(3, 1)*DFGRD1(2, 2)
     3         -DFGRD1(2, 3)*DFGRD1(3, 2)*DFGRD1(1, 1)
      END IF
```

```
      SCALE=DET**(-ONE/THREE)
      DO K1=1, 3
        DO K2=1, 3
          DISTGR(K2, K1)=SCALE*DFGRD1(K2, K1)
        END DO
      END DO
C
C     CALCULATE LEFT CAUCHY-GREEN TENSOR (B=F.Ft)
C
      BBAR(1)=DISTGR(1, 1)**2+DISTGR(1, 2)**2+DISTGR(1, 3)**2
      BBAR(2)=DISTGR(2, 1)**2+DISTGR(2, 2)**2+DISTGR(2, 3)**2
      BBAR(3)=DISTGR(3, 3)**2+DISTGR(3, 1)**2+DISTGR(3, 2)**2
      BBAR(4)=DISTGR(1, 1)*DISTGR(2, 1)+DISTGR(1, 2)*DISTGR(2, 2)
     1       +DISTGR(1, 3)*DISTGR(2, 3)
      IF(NSHR.EQ.3) THEN
        BBAR(5)=DISTGR(1, 1)*DISTGR(3, 1)+DISTGR(1, 2)*DISTGR(3, 2)
     1         +DISTGR(1, 3)*DISTGR(3, 3)
        BBAR(6)=DISTGR(2, 1)*DISTGR(3, 1)+DISTGR(2, 2)*DISTGR(3, 2)
     1         +DISTGR(2, 3)*DISTGR(3, 3)
      END IF
C
C     CALCULATAE (B.Bt)
C
      BBARBBAR(1)=BBAR(1)*BBAR(1)+BBAR(4)*BBAR(4)+BBAR(5)*BBAR(5)
      BBARBBAR(2)=BBAR(4)*BBAR(4)+BBAR(2)*BBAR(2)+BBAR(6)*BBAR(6)
      BBARBBAR(3)=BBAR(5)*BBAR(5)+BBAR(6)*BBAR(6)+BBAR(3)*BBAR(3)
      BBARBBAR(4)=BBAR(1)*BBAR(4)+BBAR(4)*BBAR(2)+BBAR(5)*BBAR(6)
      BBARBBAR(5)=BBAR(1)*BBAR(5)+BBAR(4)*BBAR(6)+BBAR(5)*BBAR(3)
      BBARBBAR(6)=BBAR(4)*BBAR(5)+BBAR(2)*BBAR(6)+BBAR(6)*BBAR(3)
C
C     CALCULATE THE STRESS
C
      TRBBAR=(BBAR(1)+BBAR(2)+BBAR(3))
      TRBBAR1=(BBAR(1)+BBAR(2)+BBAR(3))/THREE
      TRBBAR2=(BBAR(1)**2+BBAR(2)**2+BBAR(3)**2)/THREE
      TRBBARBBAR=(BBARBBAR(1)+BBARBBAR(2)+BBARBBAR(3))/THREE
      EG1=TWO*C10/DET
      EG2=TWO*C01/DET
      EK=TWO/D1*(TWO*DET-ONE)
      PR=TWO/D1*(DET-ONE)
      DO K1=1,NDI
        STRESS(K1)=EG1*(BBAR(K1)-TRBBAR1)+PR
     1             +EG2*(TRBBAR*BBAR(K1)-TRBBAR2-BBARBBAR(K1)
     2             +TRBBARBBAR)
      END DO
      DO K1=NDI+1,NDI+NSHR
        STRESS(K1)=EG1*BBAR(K1)
     1             +EG2*(TRBBAR*BBAR(K1)-BBARBBAR(K1))
      END DO
C
C     CALCULATE THE STIFFNESS
C
      EG23=EG1*TWO/THREE
      EG24=EG2*TWO/THREE
      DDSDDE(1, 1)= EG23*(BBAR(1)+TRBBAR1)+EK
     1              +EG24*(-(BBAR(1)*(3*BBAR(1)+5*(BBAR(2)+BBAR(3))))/2
     2              +BBAR(4)**2+BBAR(5)**2)
```

```
 DDSDDE(2, 2)= EG23*(BBAR(2)+TRBBAR1)+EK
1              +EG24*(-(BBAR(2)*(5*BBAR(1)+3*BBAR(2)+5*BBAR(3)))/2
2              +BBAR(4)**2+BBAR(6)**2)
 DDSDDE(3, 3)= EG23*(BBAR(3)+TRBBAR1)+EK
1              +EG24*(-(BBAR(3)*(5*(BBAR(1)+BBAR(2))+3*BBAR(3)))/2
2              +BBAR(5)**2+BBAR(6)**2)
 DDSDDE(1, 2)=-EG23*(BBAR(1)+BBAR(2)-TRBBAR1)+EK
1             +EG24*((3*(2*BBAR(1)*BBAR(2)-(4*(BBAR(1)+BBAR(2))
2             *(BBAR(1)+BBAR(2)+BBAR(3)))/3-2*BBAR(4)**2))/2)
 DDSDDE(1, 3)=-EG23*(BBAR(1)+BBAR(3)-TRBBAR1)+EK
1             +EG24*((3*(2*BBAR(1)*BBAR(3)-(4*(BBAR(1)+BBAR(3))
2             *(BBAR(1)+BBAR(2)+BBAR(3)))/3-2*BBAR(5)**2))/2)
 DDSDDE(2, 3)=-EG23*(BBAR(2)+BBAR(3)-TRBBAR1)+EK
1             +EG24*((3*(2*BBAR(2)*BBAR(3)-(4*(BBAR(2)+BBAR(3))
2             *(BBAR(1)+BBAR(2)+BBAR(3)))/3-2*BBAR(6)**2))/2)
 DDSDDE(1, 4)= EG23*BBAR(4)/TWO
1             +EG24*(-((3*(BBAR(1)+BBAR(2))+5*BBAR(3))*BBAR(4))/4
2             +(BBAR(5)*BBAR(6))/2)
 DDSDDE(2, 4)= EG23*BBAR(4)/TWO
1             +EG24*(-((3*(BBAR(1)+BBAR(2))+5*BBAR(3))*BBAR(4))/4
2             +(BBAR(5)*BBAR(6))/2)
 DDSDDE(3, 4)=-EG23*BBAR(4)
1             +EG24*((-2*(BBAR(1)+BBAR(2))+BBAR(3))*BBAR(4)
2             -3*BBAR(5)*BBAR(6))
 DDSDDE(4, 4)= EG1*(BBAR(1)+BBAR(2))
1             +EG24*((13*BBAR(1)**2-6*BBAR(1)*BBAR(2)+13*BBAR(2)**2
2             +3*(BBAR(1)+BBAR(2))*BBAR(3)+2*(16*BBAR(4)**2
3             +5*(BBAR(5)**2+BBAR(6)**2)))/8)
 IF(NSHR.EQ.3) THEN
   DDSDDE(1, 5)= EG23*BBAR(5)/TWO
1               +EG24*(-((3*BBAR(1)+5*BBAR(2)+3*BBAR(3))*BBAR(5))/4
2               +(BBAR(4)*BBAR(6))/2)
   DDSDDE(2, 5)=-EG23*BBAR(5)
1               +EG24*((-2*BBAR(1)+BBAR(2)-2*BBAR(3))*BBAR(5)
2               -3*BBAR(4)*BBAR(6))
   DDSDDE(3, 5)= EG23*BBAR(5)/TWO
1               +EG24*(-((3*BBAR(1)+5*BBAR(2)+3*BBAR(3))*BBAR(5))/4
2               +(BBAR(4)*BBAR(6))/2)
   DDSDDE(1, 6)=-EG23*BBAR(6)
1               +EG24*(-3*BBAR(4)*BBAR(5)+(BBAR(1)-2*(BBAR(2)
2               +BBAR(3)))*BBAR(6))
   DDSDDE(2, 6)= EG23*BBAR(6)/TWO
1               +EG24*((2*BBAR(4)*BBAR(5)-(5*BBAR(1)+3*(BBAR(2)
2               +BBAR(3)))*BBAR(6))/4)
   DDSDDE(3, 6)= EG23*BBAR(6)/TWO
1               +EG24*((2*BBAR(4)*BBAR(5)-(5*BBAR(1)+3*(BBAR(2)
2               +BBAR(3)))*BBAR(6))/4)
   DDSDDE(5, 5)= EG1*(BBAR(1)+BBAR(3))/TWO
1               +EG24*((13*BBAR(1)**2+3*BBAR(1)*(BBAR(2)-2*BBAR(3))
2               +3*BBAR(2)*BBAR(3)+13*BBAR(3)**2+10*BBAR(4)**2
3               +32*BBAR(5)**2+10*BBAR(6)**2)/8)
   DDSDDE(6, 6)= EG1*(BBAR(2)+BBAR(3))/TWO
1               +EG24*((13*BBAR(2)**2-6*BBAR(2)*BBAR(3)
2               +13*BBAR(3)**2+3*BBAR(1)*(BBAR(2)+BBAR(3))
3               +10*(BBAR(4)**2+BBAR(5)**2)+32*BBAR(6)**2)/8)
   DDSDDE(4,5)= EG1*BBAR(6)/TWO
1               +EG24*((22*BBAR(4)*BBAR(5)+(-9*BBAR(1)+13*(BBAR(2)
```

```
     2               +BBAR(3)))*BBAR(6))/8)
        DDSDDE(4,6)= EG1*BBAR(5)/TWO
     1               +EG24*((-3*(BBAR(1)+3*BBAR(2)+BBAR(3))*BBAR(5))/8
     2               +(3*BBAR(4)*BBAR(6))/4)
        DDSDDE(5,6)= EG1*BBAR(4)/TWO
     1               +EG24*(((13*(BBAR(1)+BBAR(2))-9*BBAR(3))*BBAR(4)
     2               +22*BBAR(5)*BBAR(6))/8)
      END IF
      DO K1=1, NTENS
        DO K2=1, K1-1
          DDSDDE(K1, K2)=DDSDDE(K2, K1)
        END DO
      END DO
C
C     Calculate the inverse of deformation gradient
C
      DFGRDM1_INV(1,1)=DFGRD1(2,2)*DFGRD1(3,3)
     1 -DFGRD1(2,3)*DFGRD1(3,2)
      DFGRDM1_INV(1,2)=-DFGRD1(1,2)*DFGRD1(3,3)
     1 +DFGRD1(1,3)*DFGRD1(3,2)
      DFGRDM1_INV(1,3)=DFGRD1(1,2)*DFGRD1(2,3)
     1 -DFGRD1(1,3)*DFGRD1(2,2)

      DFGRDM1_INV(2,1)=-DFGRD1(2,1)*DFGRD1(3,3)
     1 +DFGRD1(2,3)*DFGRD1(3,1)
      DFGRDM1_INV(2,2)=DFGRD1(1,1)*DFGRD1(3,3)
     1 -DFGRD1(1,3)*DFGRD1(3,1)
      DFGRDM1_INV(2,3)=-DFGRD1(1,1)*DFGRD1(2,3)
     1 +DFGRD1(1,3)*DFGRD1(2,1)

      DFGRDM1_INV(3,1)=DFGRD1(2,1)*DFGRD1(3,2)
     1 -DFGRD1(2,2)*DFGRD1(3,1)
      DFGRDM1_INV(3,2)=-DFGRD1(1,1)*DFGRD1(3,2)
     1 +DFGRD1(1,2)*DFGRD1(3,1)
      DFGRDM1_INV(3,3)=DFGRD1(1,1)*DFGRD1(2,2)
     1 -DFGRD1(1,2)*DFGRD1(2,1)

      DO I=1,3
      DO J=1,3
      DFGRDM1_INV(I,J)=DFGRDM1_INV(I,J)/DET
      END DO
      END DO
C
C     Calculate the current true electric field
C
      En(1)=PROPS(14)
      En(2)=PROPS(15)
      En(3)=PROPS(16)
      DO I=1,3
      Et(I)=0
      END DO
      DO I=1,3
      DO J=1,3
      Et(J)=Et(J)+En(I)*DFGRDM1_INV(I,J)
      END DO
      END DO
      EkEk=0.0D0
```

```
      DO I=1, 3
         EkEk=EkEk+Et(I)*Et(I)
      ENDDO
      DO I=1,3
        DO J=1,3
        Stress_Max(I,J)=0.0D0
        ENDDO
      ENDDO
C
C     Update the true stress due to polarization
C
      DO I=1,3
        DO J=1,3
        IF (I==J) THEN
        Stress_Max(I,J)=EPSILON*Et(I)*Et(J)-0.50D0*EPSILON*EkEk(1)
        ELSE
        Stress_Max(I,J)=EPSILON*Et(I)*Et(J)
        ENDIF
        ENDDO
      ENDDO
      STRESS(1)=STRESS(1)+Stress_Max(1,1)
      STRESS(2)=STRESS(2)+Stress_Max(2,2)
      STRESS(3)=STRESS(3)+Stress_Max(3,3)
      STRESS(4)=STRESS(4)+Stress_Max(1,2)
      STRESS(5)=STRESS(5)+Stress_Max(1,3)
      STRESS(6)=STRESS(6)+Stress_Max(2,3)
      RETURN
      END
```

2. *Neo*-Hookean+Gasser-Ogden-Holzapfel model + electrostatic energy function (E_Anisomodel.f)

```
      SUBROUTINE UMAT(STRESS,STATEV,DDSDDE,SSE,SPD,SCD,
     1 RPL,DDSDDT,DRPLDE,DRPLDT,
     2 STRAN,DSTRAN,TIME,DTIME,TEMP,DTEMP,PREDEF,DPRED,CMNAME,
     3 NDI,NSHR,NTENS,NSTATEV,PROPS,NPROPS,COORDS,DROT,PNEWDT,
     4 CELENT,DFGRD0,DFGRD1,NOEL,NPT,LAYER,KSPT,KSTEP,KINC)
C
      INCLUDE 'ABA_PARAM.INC'
C
      CHARACTER*8 CMNAME
      DIMENSION STRESS(NTENS),STATEV(NSTATEV),
     1 DDSDDE(NTENS,NTENS),DDSDDT(NTENS),DRPLDE(NTENS),
     2 STRAN(NTENS),DSTRAN(NTENS),TIME(2),PREDEF(1),DPRED(1),
     3 PROPS(NPROPS),COORDS(3),DROT(3,3),DFGRD0(3,3),DFGRD1(3,3),
     4 Et(3),Stress_Max(3,3),EkEk(1),DFGRDM1_INV(3,3),En(3),
     5 TEMP(1),DTEMP(1),DFGRDP(3),DFGRDM1(3, 3),DFGRDM0(3, 3),
     6 CBAR(3,3),DDSDDE_Max(6,6)
C
      DIMENSION BBAR(6),DISTGR(3,3),BBARBBAR(6), MM(6), M(3), D(6),
     1          NN(6), N(3)

C
      PARAMETER(ZERO=0.D0, ONE=1.D0, TWO=2.D0, THREE=3.D0, FOUR=4.D0,
     1          FIVE=5.D0, SIX=6.D0, SEVEN=7.D0, EIGHT=8.D0)
```

```
C
C -------------------------------------------------------------
C    GASSER & HOLZAPFEL STRAIN ENERGY FUNCTION
C    W=C10(I-3)+k1/2k2 exp[k2{K I1+(1-3K) I4i-1}**2-1]
C -------------------------------------------------------------
C    PROPS(1) - C10
C    PROPS(2) - D1
C    PROPS(3) - k1
C    PROPS(4) - K2
C    PROPS(5) - k
c    PROPS(6) - cos (fiber angle1)
C    PROPS(7) - sin (fiber angle1)
C    PROPS(8) - cos (fiber angle2)
C    PROPS(9) - sin (fiber angle2)
C -------------------------------------------------------------
C
C   Read Material PROPERTIES
C
      C10=PROPS(1)
      D1 =PROPS(2)
      P =PROPS(3)
      PP =PROPS(4)
      PK = PROPS(5)
      COS=PROPS(6)
      SIN=PROPS(7)
      Q =PROPS(8)
      QQ =PROPS(9)
      QK =PROPS(10)
      COSS=PROPS(11)
      SINN=PROPS(12)
      EPSILON=PROPS(13)
C    JACOBIAN AND DISTORTION TENSOR
      DET=DFGRD1(1, 1)*DFGRD1(2, 2)*DFGRD1(3, 3)
     1   -DFGRD1(1, 2)*DFGRD1(2, 1)*DFGRD1(3, 3)
      IF(NSHR.EQ.3) THEN
        DET=DET+DFGRD1(1, 2)*DFGRD1(2, 3)*DFGRD1(3, 1)
     1         +DFGRD1(1, 3)*DFGRD1(3, 2)*DFGRD1(2, 1)
     2         -DFGRD1(1, 3)*DFGRD1(3, 1)*DFGRD1(2, 2)
     3         -DFGRD1(2, 3)*DFGRD1(3, 2)*DFGRD1(1, 1)
      END IF
      SCALE=DET**(-ONE/THREE)
      DO K1=1, 3
        DO K2=1, 3
          DISTGR(K2, K1)=SCALE*DFGRD1(K2, K1)
        END DO
      END DO
C    CALCULATE LEFT CAUCHY-GREEN TENSOR (B=F.Ft)
      BBAR(1)=DISTGR(1, 1)**2+DISTGR(1, 2)**2+DISTGR(1, 3)**2
      BBAR(2)=DISTGR(2, 1)**2+DISTGR(2, 2)**2+DISTGR(2, 3)**2
      BBAR(3)=DISTGR(3, 3)**2+DISTGR(3, 1)**2+DISTGR(3, 2)**2
      BBAR(4)=DISTGR(1, 1)*DISTGR(2, 1)+DISTGR(1, 2)*DISTGR(2, 2)
     1       +DISTGR(1, 3)*DISTGR(2, 3)
      IF(NSHR.EQ.3) THEN
        BBAR(5)=DISTGR(1, 1)*DISTGR(3, 1)+DISTGR(1, 2)*DISTGR(3, 2)
     1         +DISTGR(1, 3)*DISTGR(3, 3)
        BBAR(6)=DISTGR(2, 1)*DISTGR(3, 1)+DISTGR(2, 2)*DISTGR(3, 2)
     1         +DISTGR(2, 3)*DISTGR(3, 3)
```

```
      END IF
C     CALCULATAE (B.Bt)
      BBARBBAR(1)=BBAR(1)*BBAR(1)+BBAR(4)*BBAR(4)+BBAR(5)*BBAR(5)
      BBARBBAR(2)=BBAR(4)*BBAR(4)+BBAR(2)*BBAR(2)+BBAR(6)*BBAR(6)
      BBARBBAR(3)=BBAR(5)*BBAR(5)+BBAR(6)*BBAR(6)+BBAR(3)*BBAR(3)
      BBARBBAR(4)=BBAR(1)*BBAR(4)+BBAR(4)*BBAR(2)+BBAR(5)*BBAR(6)
      BBARBBAR(5)=BBAR(1)*BBAR(5)+BBAR(4)*BBAR(6)+BBAR(5)*BBAR(3)
      BBARBBAR(6)=BBAR(4)*BBAR(5)+BBAR(2)*BBAR(6)+BBAR(6)*BBAR(3)
C     CALCULATE INVARIANT I1 I4
      TRBBAR=BBAR(1)+BBAR(2)+BBAR(3)
      M(1)=DISTGR(1,1)*COS+DISTGR(1,2)*SIN
      M(2)=DISTGR(2,1)*COS+DISTGR(2,2)*SIN
      M(3)=DISTGR(3,1)*COS+DISTGR(3,2)*SIN
      N(1)=DISTGR(1,1)*COSS+DISTGR(1,2)*SINN
      N(2)=DISTGR(2,1)*COSS+DISTGR(2,2)*SINN
      N(3)=DISTGR(3,1)*COSS+DISTGR(3,2)*SINN
      TRBBARR=M(1)**2+M(2)**2+M(3)**2
      TRBBARRR=N(1)**2+N(2)**2+N(3)**2
C    CALCULATE ORIENTATION mimj
      MM(1)=M(1)*M(1)
      MM(2)=M(2)*M(2)
      MM(3)=M(3)*M(3)
      MM(4)=M(1)*M(2)
      MM(5)=M(1)*M(3)
      MM(6)=M(2)*M(3)
      NN(1)=N(1)*N(1)
      NN(2)=N(2)*N(2)
      NN(3)=N(3)*N(3)
      NN(4)=N(1)*N(2)
      NN(5)=N(1)*N(3)
      NN(6)=N(2)*N(3)
C     CALCULATE DW/DI
      A=(-1+TRBBARR*(1-3*PK)+TRBBAR*PK)
      AA=PP*A**2
      B=(-1+TRBBARRR*(1-3*QK)+TRBBAR*QK)
      BB=QQ*B**2
      WO=C10+exp(AA)*PK*A*P+exp(BB)*QK*B*Q
      WFA=exp(AA)*(1-3*PK)*A*P
      WFB=exp(BB)*(1-3*QK)*B*Q
      WOO=(P*(2*exp(AA)*PK**2*PP+4*exp(AA)*PK**2*A**2*PP**2))/(2*PP)
     1   +(Q*(2*exp(BB)*QK**2*QQ+4*exp(BB)*QK**2*B**2*QQ**2))/(2*QQ)
      WFFA=(P*(2*exp(AA)*(1-3*PK)**2*PP+4*exp(AA)*(1-3*PK)**2*A**2
     1    *PP**2))/(2*PP)
      WFFB=(Q*(2*exp(BB)*(1-3*QK)**2*QQ+4*exp(BB)*(1-3*QK)**2*B**2
     1    *QQ**2))/(2*QQ)
      WOFA=exp(AA)*(1-3*PK)*PK*P+2*exp(AA)*(1-3*PK)*PK*A**2*P*PP
      WOFB=exp(BB)*(1-3*QK)*QK*Q+2*exp(QQ)*(1-3*QK)*QK*B**2*Q*QQ
C     CALCULATE THE STRESS
      TRBBART=TRBBAR/THREE
      TRBBARRT=TRBBARR/THREE
      TRBBARRRT=TRBBARRR/THREE
      EG=TWO/DET
      EK=TWO/D1*(TWO*DET-ONE)
      PR=TWO/D1*(DET-ONE)
      DO K1=1,NDI
        STRESS(K1)=EG*WO*(BBAR(K1)-TRBBART)+EG*WFA*(MM(K1)-TRBBARRT)
     1             +EG*WFB*(NN(K1)-TRBBARRRT)+PR
```

```
      END DO
      DO K1=NDI+1,NDI+NSHR
        STRESS(K1)=EG*WO*BBAR(K1)+EG*WFA*(MM(K1))+EG*WFB*(NN(K1))
      END DO
C     CALCULATE THE STIFFNESS
      DDSDDE(1, 1)=(8*(2*TRBBAR*WO+2*TRBBARR*WFA+2*TRBBARRR*WFB))
     1          /(9*DET)-(2*(4*WO*BBAR(1)+4*WFA*(M(1))**2+4*WFB
     2          *(N(1))**2))/(3*DET)+(4*(WOO*(-TRBBART+BBAR(1))**2
     3          +2*WOFA*(-TRBBART+BBAR(1))*(-TRBBARRT+(M(1))**2)
     4          +2*WOFB*(-TRBBART+BBAR(1))*(-TRBBARRRT+(N(1))**2)
     5          +WFFA*(-TRBBARRT+(M(1))**2)**2)+WFFB*(-TRBBARRRT
     6          +(N(1))**2)**2)/DET+EK
      DDSDDE(2, 2)=(8*(2*TRBBAR*WO+2*TRBBARR*WFA++2*TRBBARRR*WFB))
     1          /(9*DET)-(2*(4*WO*BBAR(2)+4*WFA*(M(2))**2+4*WFB
     2          *(N(2))**2))/(3*DET)+(4*(WOO*(-TRBBART+BBAR(2))**2
     3          +2*WOFA*(-TRBBART+BBAR(2))*(-TRBBARRT+(M(2))**2)
     4          +2*WOFB*(-TRBBART+BBAR(2))*(-TRBBARRRT+(N(2))**2)
     5          +WFFA*(-TRBBARRT+(M(2))**2)**2)+WFFB*(-TRBBARRRT
     6          +(N(2))**2)**2)/DET+EK
      DDSDDE(3, 3)=(8*(2*TRBBAR*WO+2*TRBBARR*WFA++2*TRBBARRR*WFB))
     1          /(9*DET)-(2*(4*WO*BBAR(3)+4*WFA*(M(3))**2+4*WFB
     2          *(N(3))**2))/(3*DET)+(4*(WOO*(-TRBBART+BBAR(3))**2
     3          +2*WOFA*(-TRBBART+BBAR(3))*(-TRBBARRT+(M(3))**2)
     4          +2*WOFB*(-TRBBART+BBAR(3))*(-TRBBARRRT+(N(3))**2)
     5          +WFFA*(-TRBBARRT+(M(3))**2)**2)+WFFB*(-TRBBARRRT
     6          +(N(3))**2)**2)/DET+EK
      DDSDDE(1, 2)=(2*(2*TRBBAR*WO+2*TRBBARR*WFA+2*TRBBARRR*WFA))
     1         /(9*DET)-(2*(2*WO*BBAR(1)+2*WO*BBAR(2)+2*WFA*(M(1))**2
     2         +2*WFA*(M(2))**2+2*WFB*(N(1))**2+2*WFB*(N(2))**2))
     3         /(3*DET)+(4*(WOO*(-TRBBART+BBAR(1))*(-TRBBART+BBAR(2))
     4         +WFFA*(-TRBBARRT+(M(1))**2)*(-TRBBARRT+(M(2))**2)+WFFB
     5         *(-TRBBARRRT+(N(1))**2)*(-TRBBARRRT+(N(2))**2)+WOFA
     4         *((-TRBBART+BBAR(2))*(-TRBBARRT+(M(1))**2)+(-TRBBART
     5         +BBAR(1))*(-TRBBARRT+(M(2))**2))+WOFB*((-TRBBART
     6         +BBAR(2))*(-TRBBARRRT+(N(1))**2)+(-TRBBART+BBAR(1))
     7         *(-TRBBARRRT+(N(2))**2))))/DET+EK
      DDSDDE(1, 3)=(2*(2*TRBBAR*WO+2*TRBBARR*WFA+2*TRBBARRR*WFA))
     1         /(9*DET)-(2*(2*WO*BBAR(1)+2*WO*BBAR(3)+2*WFA*(M(1))**2
     2         +2*WFA*(M(3))**2+2*WFB*(N(1))**2+2*WFB*(N(3))**2))
     3         /(3*DET)+(4*(WOO*(-TRBBART+BBAR(1))*(-TRBBART+BBAR(3))
     4         +WFFA*(-TRBBARRT+(M(1))**2)*(-TRBBARRT+(M(3))**2)+WFFB
     5         *(-TRBBARRRT+(N(1))**2)*(-TRBBARRRT+(N(3))**2)+WOFA
     4         *((-TRBBART+BBAR(3))*(-TRBBARRT+(M(1))**2)+(-TRBBART
     5         +BBAR(1))*(-TRBBARRT+(M(3))**2))+WOFB*((-TRBBART
     6         +BBAR(3))*(-TRBBARRRT+(N(1))**2)+(-TRBBART+BBAR(1))
     7         *(-TRBBARRRT+(N(3))**2))))/DET+EK
      DDSDDE(2, 3)=(2*(2*TRBBAR*WO+2*TRBBARR*WFA+2*TRBBARRR*WFA))
     1         /(9*DET)-(2*(2*WO*BBAR(2)+2*WO*BBAR(3)+2*WFA*(M(2))**2
     2         +2*WFA*(M(3))**2+2*WFB*(N(2))**2+2*WFB*(N(3))**2))
     3         /(3*DET)+(4*(WOO*(-TRBBART+BBAR(2))*(-TRBBART+BBAR(3))
     4         +WFFA*(-TRBBARRT+(M(2))**2)*(-TRBBARRT+(M(3))**2)+WFFB
     5         *(-TRBBARRRT+(N(2))**2)*(-TRBBARRRT+(N(3))**2)+WOFA
     4         *((-TRBBART+BBAR(3))*(-TRBBARRT+(M(2))**2)+(-TRBBART
     5         +BBAR(2))*(-TRBBARRT+(M(3))**2))+WOFB*((-TRBBART
     6         +BBAR(3))*(-TRBBARRRT+(N(2))**2)+(-TRBBART+BBAR(2))
     7         *(-TRBBARRRT+(N(3))**2))))/DET+EK
      DDSDDE(1, 4)=(-2*(2*WO*BBAR(4)+2*WFA*(M(1))*(M(2))+2*WFB*(N(1))
```

```
1          *(N(2))))/(3*DET)+(4*(WOO*(-TRBBART+BBAR(1))*BBAR(4)
2          +WFFA*(M(1))*(-TRBBARRT+(M(1))**2)*(M(2))+WFFB*(N(1))
3          *(-TRBBARRRT+(N(1))**2)*(N(2))+WOFA*(BBAR(4)*(-TRBBARRT
4          +(M(1))**2)+(-TRBBART+BBAR(1))*(M(1))*(M(2)))+WOFB
5          *(BBAR(4)*(-TRBBARRRT+(N(1))**2)+(-TRBBART+BBAR(1))
6          *(N(1))*(N(2)))))/DET
 DDSDDE(2, 4)=(-2*(2*WO*BBAR(4)+2*WFA*(M(1))*(M(2))+2*WFB*(N(1))
1          *(N(2))))/(3*DET)+(4*(WOO*(-TRBBART+BBAR(2))*BBAR(4)
2          +WFFA*(M(1))*(M(2))*(-TRBBARRT+(M(2))**2)+WFFB*(N(1))
3          *(N(2))*(-TRBBARRRT+(N(2))**2)+WOFA*((-TRBBART+BBAR(2))
4          *(M(1))*(M(2))+BBAR(4)*(-TRBBARRT+(M(2))**2))+WOFB
5          *((-TRBBART+BBAR(2))*(N(1))*(N(2))+BBAR(4)*(-TRBBARRRT
6          +(N(2))**2))))/DET
 DDSDDE(3, 4)=(-2*(2*WO*BBAR(4)+2*WFA*(M(1))*(M(2))+2*WFB*(N(1))
1          *(N(2))))/(3*DET)+(4*(WOO*(-TRBBART+BBAR(3))*BBAR(4)
2          +WFFA*(M(1))*(M(2))*(-TRBBARRT+(M(3))**2)+WFFB*(N(1))
3          *(N(2))*(-TRBBARRT+(M(3))**2)+WOFA*((-TRBBART+BBAR(3))
4          *(M(1))*(M(2))+BBAR(4)*(-TRBBARRT+(M(3))**2))+WOFB
5          *((-TRBBART+BBAR(3))*(N(1))*(N(2))+BBAR(4)*(-TRBBARRRT
6          +(N(3))**2))))/DET
 DDSDDE(4, 4)=(2*TRBBAR*WO+2*TRBBARR*WFA+2*TRBBARRR*WFB)/(3*DET)
1          +(4*(WOO*BBAR(4)**2+2*WOFA*BBAR(4)*(M(1))*(M(2))+2*WOFB
2          *BBAR(4)*(N(1))*(N(2))+WFFA*(M(1))**2*(M(2))**2+WFFB
3          *(N(1))**2*(N(2))**2))/DET
 IF(NSHR.EQ.3) THEN
   DDSDDE(1, 5)=(-2*(2*WO*BBAR(5)+2*WFA*(M(1))*(M(3))+2*WFB
1       *(N(1))*(N(3))))/(3*DET)+(4*(WOO*(-TRBBART+BBAR(1))
2       *BBAR(5)+WFFA*(M(1))*(-TRBBARRT+(M(1))**2)*(M(3))+WFFB
3       *(N(1))*(-TRBBARRRT+(N(1))**2)*(N(3))+WOFA*(BBAR(5)
4       *(-TRBBARRT+(M(1))**2)+(-TRBBART+BBAR(1))*(M(1))*(M(3)))
5       +WOFB*(BBAR(5)*(-TRBBARRRT+(N(1))**2)+(-TRBBART+BBAR(1))
6       *(N(1))*(N(3)))))/DET
   DDSDDE(2, 5)=(-2*(2*WO*BBAR(5)+2*WFA*(M(1))*(M(3))+2*WFB
1       *(N(1))*(N(3))))/(3*DET)+(4*(WOO*(-TRBBART+BBAR(2))
2       *BBAR(5)+WFFA*(M(1))*(-TRBBARRT+(M(3))**2)*(M(3))+WFFB
3       *(N(1))*(-TRBBARRRT+(N(3))**2)*(N(3))+WOFA*(BBAR(5)
4       *(-TRBBARRT+(M(2))**2)+(-TRBBART+BBAR(2))*(M(1))*(M(3)))
5       +WOFB*(BBAR(5)*(-TRBBARRRT+(N(2))**2)+(-TRBBART+BBAR(2))
6       *(N(1))*(N(3)))))/DET
   DDSDDE(3, 5)=(-2*(2*WO*BBAR(5)+2*WFA*(M(1))*(M(3))+2*WFB
1       *(N(1))*(N(3))))/(3*DET)+(4*(WOO*(-TRBBART+BBAR(3))
2       *BBAR(5)+WFFA*(M(1))*(M(3))*(-TRBBARRT+(M(3))**2)+WFFB
3       *(N(1))*(N(3))*(-TRBBARRRT+(N(3))**2)+WOFA*((-TRBBART
4       +BBAR(3))*(M(1))*(M(3))+BBAR(5)*(-TRBBARRT+(M(3))**2))
5       +WOFB*((-TRBBART+BBAR(3))*(N(1))*(N(3))+BBAR(5)
6       *(-TRBBARRRT+(N(3))**2))))/DET
   DDSDDE(1, 6)=(-2*(2*WO*BBAR(6)+2*WFA*(M(2))*(M(3))+2*WFB
1       *(N(2))*(N(3))))/(3*DET)+(4*(WOO*(-TRBBART+BBAR(1))*BBAR(6)
2       +WFFA*(-TRBBARRT+(M(1))**2)*(M(2))*(M(3))+WFFB*(-TRBBARRRT
3       +(N(1))**2)*(N(2))*(N(3))+WOFA*(BBAR(6)*(-TRBBARRT
4       +(M(1))**2)+(-TRBBART+BBAR(1))*(M(2))*(M(3)))+WOFB*(BBAR(6)
5       *(-TRBBARRRT+(N(1))**2)+(-TRBBART+BBAR(1))*(N(2))
6       *(N(3)))))/DET
   DDSDDE(2, 6)=(-2*(2*WO*BBAR(6)+2*WFA*(M(2))*(M(3))+2*WFB*(N(2))
1       *(N(3))))/(3*DET)+(4*(WOO*(-TRBBART+BBAR(2))*BBAR(6)+WFFA
2       *(M(2))*(-TRBBARRT+(M(2))**2)*(M(3))+WFFB*(N(2))
3       *(-TRBBARRRT+(N(2))**2)*(N(3))+WOFA*(BBAR(6)*(-TRBBARRT
```

```
     4       +(M(2))**2)+(-TRBBART+BBAR(2))*(M(2))*(M(3)))+WOFB*(BBAR(6)
     5       *(-TRBBARRRT+(N(2))**2)+(-TRBBART+BBAR(2))*(N(2))
     6       *(N(3)))))/DET
        DDSDDE(3, 6)=(-2*(2*WO*BBAR(6)+2*WFA*(M(2))*(M(3))+2*WFB*(N(2))
     1       *(N(3))))/(3*DET)+(4*(WOO*(-TRBBART+BBAR(3))*BBAR(6)+WFFA
     2       *(M(2))*(M(3))*(-TRBBARRT+(M(3))**2)+WFFB*(N(2))*(N(3))
     3       *(-TRBBARRRT+(N(3))**2)+WOFA*((-TRBBART+BBAR(3))*(M(2))
     3       *(M(3))+BBAR(6)*(-TRBBARRT+(M(3))**2))+WOFB*((-TRBBART
     4       +BBAR(3))*(N(2))*(N(3))+BBAR(6)*(-TRBBARRRT
     5       +(N(3))**2))))/DET
        DDSDDE(5, 5)=(2*TRBBAR*WO+2*TRBBARR*WFA+2*TRBBARRR*WFB)/(3*DET)
     1       +(4*(WOO*BBAR(5)**2+2*WOFA*BBAR(5)*(M(1))*(M(3))+2*WOFB
     2       *BBAR(5)*(N(1))*(N(3))+WFFA*(M(1))**2*(M(3))**2+WFFB
     3       *(N(1))**2*(N(3))**2))/DET
        DDSDDE(6, 6)=(2*TRBBAR*WO+2*TRBBARR*WFA+2*TRBBARRR*WFB)/(3*DET)
     1       +(4*(WOO*BBAR(6)**2+2*WOFA*BBAR(6)*(M(2))*(M(3))+2*WOFB
     2       *BBAR(6)*(N(2))*(N(3))+WFFA*(M(2))**2*(M(3))**2+WFFB
     3       *(N(2))**2*(N(3))**2))/DET
        DDSDDE(4,5)=(4*(WOO*BBAR(4)*BBAR(5)+WFFA*(M(1))**2*(M(2))*(M(3))
     1       +WFFB*(N(1))**2*(N(2))*(N(3))+WOFA*(BBAR(5)*(M(1))*(M(2))
     2       +BBAR(4)*(M(1))*(M(3)))+WOFB*(BBAR(5)*(N(1))*(N(2))+BBAR(4)
     3       *(N(1))*(N(3)))))/DET
        DDSDDE(4,6)=(4*(WOO*BBAR(4)*BBAR(6)+WFFA*(M(1))*(M(2))**2*(M(3))
     1       +WFFB*(N(1))*(N(2))**2*(N(3))+WOFA*(BBAR(6)*(M(1))*(M(2))
     2       +BBAR(4)*(M(2))*(M(3)))+WOFB*(BBAR(6)*(N(1))*(N(2))+BBAR(4)
     3       *(N(2))*(N(3)))))/DET
        DDSDDE(5,6)=(4*(WOO*BBAR(5)*BBAR(6)+WFFA*(M(1))*(M(2))*(M(3))**2
     1       +WFFB*(N(1))*(N(2))*(N(3))**2+WOFA*(BBAR(6)*(M(1))*(M(3))
     2       +BBAR(5)*(M(2))*(M(3)))+WOFB*(BBAR(6)*(N(1))*(N(3))+BBAR(5)
     3       *(N(2))*(N(3)))))/DET
      END IF
      DO K1=1, NTENS
        DO K2=1, K1-1
          DDSDDE(K1, K2)=DDSDDE(K2, K1)
        END DO
      END DO
C     Calculate the inverse of deformation gradient
      DFGRDM1_INV(1,1)=DFGRD1(2,2)*DFGRD1(3,3)
     1 -DFGRD1(2,3)*DFGRD1(3,2)
      DFGRDM1_INV(1,2)=-DFGRD1(1,2)*DFGRD1(3,3)
     1 +DFGRD1(1,3)*DFGRD1(3,2)
      DFGRDM1_INV(1,3)=DFGRD1(1,2)*DFGRD1(2,3)
     1 -DFGRD1(1,3)*DFGRD1(2,2)

      DFGRDM1_INV(2,1)=-DFGRD1(2,1)*DFGRD1(3,3)
     1 +DFGRD1(2,3)*DFGRD1(3,1)
      DFGRDM1_INV(2,2)=DFGRD1(1,1)*DFGRD1(3,3)
     1 -DFGRD1(1,3)*DFGRD1(3,1)
      DFGRDM1_INV(2,3)=-DFGRD1(1,1)*DFGRD1(2,3)
     1 +DFGRD1(1,3)*DFGRD1(2,1)

      DFGRDM1_INV(3,1)=DFGRD1(2,1)*DFGRD1(3,2)
     1 -DFGRD1(2,2)*DFGRD1(3,1)
      DFGRDM1_INV(3,2)=-DFGRD1(1,1)*DFGRD1(3,2)
     1 +DFGRD1(1,2)*DFGRD1(3,1)
      DFGRDM1_INV(3,3)=DFGRD1(1,1)*DFGRD1(2,2)
     1 -DFGRD1(1,2)*DFGRD1(2,1)
```

```
      DO I=1,3
      DO J=1,3
      DFGRDM1_INV(I,J)=DFGRDM1_INV(I,J)/DET
      END DO
      END DO
C     Calculate the current true electric field
      En(1)=PROPS(14)
      En(2)=PROPS(15)
      En(3)=PROPS(16)
      DO I=1,3
      Et(I)=0
      END DO
      DO I=1,3
      DO J=1,3
      Et(J)=Et(J)+En(I)*DFGRDM1_INV(I,J)
      END DO
      END DO
      EkEk=0.0D0
      DO I=1, 3
         EkEk=EkEk+Et(I)*Et(I)
      ENDDO
      DO I=1,3
        DO J=1,3
        Stress_Max(I,J)=0.0D0
        ENDDO
      ENDDO
C     Update the true stress due to polarization
      DO I=1,3
        DO J=1,3
        IF (I==J) THEN
        Stress_Max(I,J)=EPSILON*Et(I)*Et(J)-0.50D0*EPSILON*EkEk(1)
        ELSE
        Stress_Max(I,J)=EPSILON*Et(I)*Et(J)
        ENDIF
        ENDDO
      ENDDO
      STRESS(1)=STRESS(1)+Stress_Max(1,1)
      STRESS(2)=STRESS(2)+Stress_Max(2,2)
      STRESS(3)=STRESS(3)+Stress_Max(3,3)
      STRESS(4)=STRESS(4)+Stress_Max(1,2)
      STRESS(5)=STRESS(5)+Stress_Max(1,3)
      STRESS(6)=STRESS(6)+Stress_Max(2,3)
      RETURN
      END
```

Appendix E. Input File for the Anisotropic Material (Define the Orientation of Fibers)

```
*Heading
** Job name: Cuttlefish_test2 Model name: Model-1
** Generated by: Abaqus/CAE 6.10-1
*Preprint, echo=NO, model=NO, history=NO, contact=NO
**
** PARTS
**
*Part, name=Part-1
*Node
      1, -0.140000001, 0.0199999996, 0.00164000003
      2, -0.140000001, 0.0260000005, 0.00164000003
      3, -0.140000001, 0.0320000015, 0.00164000003
      4, -0.140000001, 0.0379999988, 0.00164000003
      5, -0.140000001, 0.0439999998, 0.00164000003
      6, -0.140000001, 0.0500000007, 0.00164000003
       …
    250, -0.00999999978, 0.0379999988,          0.
    251, -0.00999999978, 0.0439999998,          0.
    252, -0.00999999978, 0.0500000007,          0.
*Element, type=C3D8
  1,  13,  14,  20,  19,   1,   2,   8,   7
  2,  14,  15,  21,  20,   2,   3,   9,   8
  3,  15,  16,  22,  21,   3,   4,  10,   9
  4,  16,  17,  23,  22,   4,   5,  11,  10
  5,  17,  18,  24,  23,   5,   6,  12,  11
  6,  25,  26,  32,  31,  13,  14,  20,  19
  …
 95, 233, 234, 240, 239, 221, 222, 228, 227
 96, 241, 242, 248, 247, 229, 230, 236, 235
 97, 242, 243, 249, 248, 230, 231, 237, 236
 98, 243, 244, 250, 249, 231, 232, 238, 237
 99, 244, 245, 251, 250, 232, 233, 239, 238
100, 245, 246, 252, 251, 233, 234, 240, 239
*Nset, nset=_PickedSet2, internal, generate
```

```
  1,  252,    1
*Elset, elset=_PickedSet2, internal, generate
  1,  100,    1
** Section: UMAT
*orientation,name=ori-1,local directions=2
 1.0,0.0,0.0,0.0,1.0,0.0
 3,0.0
 0.707107,  0.707107, 0.0
 0.707107,  -0.707107, 0.0
*Solid Section, elset=_PickedSet2, material=UMAT, orientation=ori-1
*End Part
**
**
** ASSEMBLY
**
*Assembly, name=Assembly
**
*Instance, name=Part-1-1, part=Part-1
*End Instance
**
*Nset, nset=_PickedSet4, internal, instance=Part-1-1, generate
  1,  247,    6
*Elset, elset=_PickedSet4, internal, instance=Part-1-1, generate
 1,  96,   5
*Elset, elset=__PickedSurf5_S3, internal, instance=Part-1-1, generate
  1,  100,    1
*Surface, type=ELEMENT, name=_PickedSurf5, internal
__PickedSurf5_S3, S3
*End Assembly
**
** MATERIALS
**
*Material, name=UMAT
*User Material, constants=16
16000.,   4.19e-09,    200000.,        0.2,        0.1,   0.707107,    0.707107,    200000.
       0.2,        0.1,  0.707107,    -0.707107, 3.2745e-11,         0.,         0.,      1.0e06
** ----------------------------------------------------------------
```

```
**
** STEP: disp
**
*Step, name=disp, nlgeom=YES
*Static
1., 1., 1e-05, 1.
**
** OUTPUT REQUESTS
**
*Restart, write, frequency=0
*Output, field, frequency=0
*Output, history, frequency=0
*End Step
** ----------------------------------------------------------------
**
** STEP: Load
**
*Step, name=Load, nlgeom=YES
*Static
0.01, 1., 1e-05, 1.
**
** BOUNDARY CONDITIONS
**
** Name: Fixed Type: Symmetry/Antisymmetry/Encastre
*Boundary
_PickedSet4, ENCASTRE
**
** LOADS
**
** Name: Load-1   Type: Pressure
*Dsload
_PickedSurf5, P, 30.
**
** OUTPUT REQUESTS
**
*Restart, write, frequency=0
**
```

```
** FIELD OUTPUT: F-Output-1
**
*Output, field, variable=PRESELECT
**
** HISTORY OUTPUT: H-Output-1
**
*Output, history, variable=PRESELECT
*End Step
```